NEAR-FIELD ANALYSIS OF FREQUENCY SELECTIVE SURFACES AND APPLICATION IN DIRECTIVE ANTENNAS

by

Carolina Mateo Segura

Submitted for the degree of Doctor of Philosophy

Heriot-Watt University

School of Engineering and Physical Science

Edinburgh, October 2010

Abstract

Near-field analysis of frequency selective surfaces and application in directive antennas

Carolina Mateo Segura

Doctorate of Philosophy

Department of Engineering and Physical Science

Heriot-Watt University

2010

A near-field characterisation of two dimensional metallo-dielectric frequency selective surfaces either in a single or double layer configuration is presented in this thesis. Motivated by the current attention of the electromagnetic properties of near-fields, an in-house periodic MoM-based computational tool is developed for the efficient and rigorous estimation of the near-fields in frequency selective surfaces (FSS) illuminated by a plane wave. For this purpose a thorough convergence study related to the calculation of the near fields is initially presented. The near-field estimation allows us to calculate the power stored in an FSS at resonance which, in turn, can be used in the calculation of the loaded quality factor of the FSS. Based on the characterisation of various topologies, new techniques for the analysis of highly-directive and broadband leaky wave antennas are proposed. An initial design based on a perturbed FSS results in a structure with multiband response and near-fields enhanced by more than 70 fold, which can be relevant to sensor applications. Subsequently, the near-field technique is used in combination with reciprocity for the extraction of the radiation patterns in Fabry-Perot cavity antennas formed between a FSS and a metamaterial ground plane. In combination with traditional array theory the complex dispersion characteristics of high-gain sub-wavelength 2-D Fabry-Perot leaky-wave antennas (LWA) consisting of two periodic metallodielectric arrays over a ground plane are extracted. This yields a fast and rigorous tool for the characterisation of this type of antennas. Design guidelines are given throughout to synthesize a highly-directive antenna and a broadband leaky-wave antenna.

This thesis was fully funded by the Joint Research Institute for Integrated Systems in Edinburgh, Scotland.

A mis queridos padres,

To my soulmate Andy,

ACADEMIC REGISTRY
Research Thesis Submission

Name*:*	Carolina Mateo Segura		
School/PGI:	School of Engineering and Physical Science		
Version: *(i.e. First, Resubmission, Final)*	FINAL	Degree Sought (Award **and** Subject area)	Doctorate of Philosophy (Electrical Engineering)

Declaration

In accordance with the appropriate regulations I hereby submit my thesis and I declare that:

1) the thesis embodies the results of my own work and has been composed by myself
2) where appropriate, I have made acknowledgement of the work of others and have made reference to work carried out in collaboration with other persons
3) the thesis is the correct version of the thesis for submission and is the same version as any electronic versions submitted*.
4) my thesis for the award referred to, deposited in the Heriot-Watt University Library, should be made available for loan or photocopying and be available via the Institutional Repository, subject to such conditions as the Librarian may require
5) I understand that as a student of the University I am required to abide by the Regulations of the University and to conform to its discipline.

* *Please note that it is the responsibility of the candidate to ensure that the correct version of the thesis is submitted.*

Signature of Candidate*:*	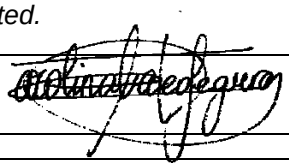	Date:	15/11/2010

Submission

Submitted By *(name in capitals):*	CAROLINA MATEO SEGURA
Signature of Individual Submitting:	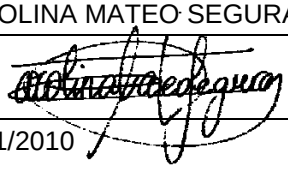
Date Submitted:	15/11/2010

For Completion in Academic Registry

Received in the Academic Registry by *(name in capitals):*			
Method of Submission *(Handed in to Academic Registry; posted through internal/external mail):*			
*E-thesis Submitted (**mandatory for final theses from January 2009**)*			
Signature:		Date:	

Please note this form should bound into the submitted thesis.

Acknowledgments

My doctorate studies at Heriot-Watt University have been a greatly enriching experience which has allowed me to grow not only from a scientific and academic point of view but also a personal one. I have had the chance to collaborate with high calibre researchers and academics who have contributed in one way or another to the completion of this work. Now, I would like to say a huge GRACIAS to all of them from the heart.

First of all, for his constant educational and technical support, his patience, understanding, the exceptional advising and mentoring and encouragement throughout these years I would like to gratefully thank my supervisor and friend Dr. George Goussetis.

I would also like to thank the faculty members of the School of Engineering and Physical Science at Heriot-Watt University together with Edinburgh University including Juanjo, Enrico, Raul, Stratos and Loren for the interaction we had during the past four years.

I would like to particularly acknowledge the financial support from the Joint Research Institute for Integrated Systems without which none of this would have been possible, especially Prof. Alan Greenaway, Prof. Anthony Walton and Prof. Colin Cunningham for having put your faith in me.

From Aalto University, Constantin Simovski, Sergei Tretyakov and Olli Lukkonnen. Thank you for your warm welcome, nice discussions and guidance process through the time I spent with you.

I would like also to fully acknowledge Dr. Alexandros Feresidis for the technical support of this last year, for the in depth discussions on many related topics of research, and for the availability in using the facilities at Loughborough University. To the technicians of the Department of Electronic and Electrical Engineering and to my fellows Chinwe, Nerijus, Emma, Ajid, Noren, Alford and Will.

I am also very grateful to the Electromagnetic Radiation Group of the Technical University of Cartagena (UPCT). Thanks to their help and friendship the workload has been lighter! Dr. Jose Gomez-Tornero for his constant jokes, friendship, advice and support in the period he shared with us at Heriot-Watt. Maria Garcia-Vigueras to whom I am deeply grateful for her help, trust and friendship during these years. I have always considered her an excellent team partner.

I would like to acknowledge as well my mentor Prof. Vicente Boria Esbert from Polytechnic University of Valencia for the great personal interaction that he has always shown. Prof. Benito Gimeno for the time spent together studying papers, for the support and help in the early stages of this work.

I especially want to show my gratitude to my parents, for their unconditional support not only these years but always. They have taught me that every important achievement in life needs effort and dedication. Thank you for giving me the chance to prove and improve myself through all my walks of life and to allow me to be where I am today. Also, thank you to my Spanish and new Scottish family and friends who kept my mind off this arduous work when I really needed it.

Finally, I want to thank my beloved Andy for his infinite patience, his constant support, trust and encouragement. You have always been with me, overcoming the difficulties, willing to undergo personal sacrifices in order for me to finish my research. Nene, thank you for being by my side, without you indeed this work could not have been completed.

List of Publications

Journal papers:

J1. **C. Mateo-Segura**, C. Simovski, G. Goussetis, and S. Tretyakov, "*Subwavelength resolution for horizontal and vertical polarization by coupled arrays of oblate nanoellipsoids,*" Optics Letters, Vol. 34, Iss. 15, pp. 2333–2335 (2009).

J2. **C. Mateo-Segura**, George Goussetis, and Alexandros P. Feresidis, "*Resonant Effects and Near Field Enhancement in Perturbed Arrays of Metal Dipoles,*" *IEEE Trans. Antennas and Propagation*, Vol. 58 No. 8, pp. 2523-2530, Aug. 2010.

J3. JJ. Sanz-Fernandez, **C. Mateo-Segura**, G. Goussetis, and R.Cheung, *"Quality Factor of Frequency Selective Surfaces at Infrared," IEEE Trans. Antennas and Propagation*, September 2009 (minor revisions).

J4. **C. Mateo-Segura**, George Goussetis, and Alexandros P. Feresidis, *"Analysis of Thin 2-D Leaky-Wave Antennas Employing Two Periodic Layers," IEEE Trans. Antennas and Propagation*, in press.

J5. **C. Mateo-Segura**, M. García-Vigueras, G. Goussetis, A. P. Feresidis and J.L. Gómez-Tornero *"Fast and Rigorous Dispersion Calculation of Thin Fabry-Perot Leaky-Wave Antennas," IEEE Trans. Antennas and Propagation*, February 2010 (awaiting).

J6. **C. Mateo-Segura**, Alexandros P. Feresidis, and George Goussetis, *"Broadband Highly Directive 2-D Leaky-Wave Antennas Based on Double-Layer Meta-Surfaces," IEEE Trans. Antennas and Propagation*, (in preparation).

International conferences:

C11. C. Mateo-Segura, A. P. Feresidis and G. Goussetis *"Analysis of Broadband Highly-Directive Fabry-Perot Cavity Leaky-Wave Antennas with Two Periodic Layers,"* IEEE Antennas and Propagation Symposium 2010, Toronto, Ontario, Canada 11-17 July 2010.

C10. C. Mateo-Segura, A. P. Feresidis and G. Goussetis *"Highly directive 2-D Leaky-Wave Antennas based on double layer meta-surfaces,"* invited paper, special session

European Conference on Antennas & Propagation 2010, Barcelona, Spain, 12-16 April, 2010.

C9. C. Mateo-Segura, M. García-Vigueras, G. Goussetis, J.L. Gómez-Tornero and A. Feresidis *"Efficient dispersion analysis of 2D High-Gain Leaky-Wave Antennas,"* European Conference on Antennas & Propagation 2010, Barcelona, Spain, 12-16 April, 2010.

C8. C. Mateo-Segura, M. García-Vigueras, G. Goussetis, J.L. Gómez-Tornero and A. Feresidis *"Analysis of Sub-wavelength Cavity Leaky-Wave Antennas with High-Impedance Surfaces,"* Loughborough Antennas & Propagation Conference 2009, Loughborough, UK, 16-17 November, 2009.

C7. M. García-Vigueras, C. Mateo-Segura, J.L. Gómez-Tornero, G. Goussetis and A. Feresidis *"Analysis and Design of 1D and 2D High-Gain Leaky-Wave A-tennas using Metallodielectric FSS and AMC,"* 3rd International Congress on Advanced Electromagnetic Materials in Microwaves and Optics, London, UK, 30-4 September, 2009.

C6. C. Mateo-Segura, G. Goussetis and A. Feresidis, *"Analysis of 2D periodic leaky wave antennas with subwavelength profile,"* IEEE Antennas and Propagation Symposium 2009, North Charleston, USA 1-5 June 2009.

C5. C. Mateo-Segura, G. Goussetis, *"Miniaturised double periodic arrays exhibiting strong bianisotropy,"* 2nd International Congress on Advanced Electromagnetic Materials in Microwaves and Optics, Pamplona, Spain , 21-26 September, 2008.

C4. C. Mateo-Segura, J. Sanz-Fernandez, G. Goussetis, R. Cheung, *"Structured Planar Surfaces Exhibiting Strong Near Field Enhancement at FIR,"* Optics and Photonics 2008, Edinburgh, UK, 26-29 August 2008.

C3. C. Mateo-Segura, G. Goussetis, *"Near and far fields for a doubly periodic array of metal strips,"* IEEE Antennas and Propagation Symposium 2008, San Diego, USA 7-12 July 2008.

C2. G. Goussetis, C. Mateo-Segura, J.-L. Gomez-Tornero, N. Uzunoglu, *"Waveguide Loaded with Metamaterial Surface for Dispersion Linearization: Numerical and Experimental Results,"* IEEE Antennas and Propagation Symposium 2008, San Diego, USA 7-12 July 2008.

C1. C. Mateo-Segura, G. Goussetis, *"Near field calculation for a doubly periodic array of metal strips,*" Annual International Conference, Days on Diffraction 2008, St. Petersburg, Russia, 3-6 June 2008.

Contents

List of Tables

List of Figures

Chapter 1

Introduction

"The work of James Clerk Maxwell changed the world forever"

Albert Einstein

1.1 Introduction

Engineers have always had to face the challenges of modern technology and the demands of modern society. The field of telecommunications is a clear example of this continuous development in which engineers worldwide work to meet the global demands for the welfare of mankind. Since classical electromagnetism, which finds its origin in the 19^{th} century when James Clerk Maxwell set the foundations of electromagnetism theory, scientists have made important progress in numerous disciplines, in which telecommunications, sensor systems and antenna design are of interest in the present thesis. In particular, understanding the interaction of electromagnetic waves with the matter is an active, interdisciplinary area of research which serves as the basis of a more complex electromagnetic problem.

In general, electromagnetic waves entering a material cause electrons to move around exchanging electromagnetic energy. This can be used to control and manipulate electromagnetic waves, forming the basis for electromagnetic devices. Materials, as they can be found in nature, exhibit only a subset of electromagnetic properties. However, by engineering the geometry of macroscopic objects material properties can be extended beyond what is known as natural, giving to the new born concept of '*metamaterial'*.

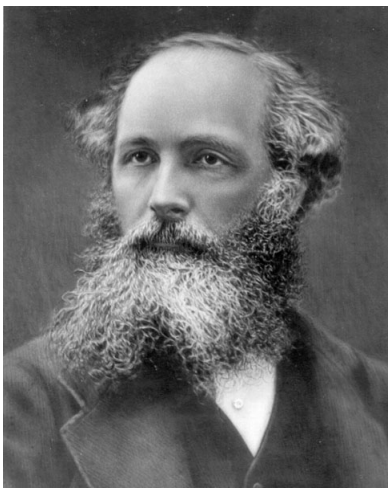

Fig. 1-1 From **James Clerk Maxwell** (1831-1879) the famous Scottish physicist, who discovered the theory of electromagnetism and forever changed our views on the nature of light to the topology of modern metamaterials concept.

The pursuit of these "artificial" materials for electromagnetic applications is not new; their history dates from more than 100 years ago. Many references in the literature can be found on materials exhibiting unusual properties; it is believed that probably the first experiments date from 1898 by Jagagish Chandra Bose on twisted elements presenting what is known today as chiral properties [1]. Artificial dielectrics were also explored in the forties by Kock for lightweight microwave antenna lenses [2] and in the sixties by W. Rotman [3] who proposed an artificial dielectric, composed of periodic arrays of wires, that simulated plasma[1] operation. The idea of complex media was widely

[1] Plasma is any gas that contains certain quantities of charged (ionized) particles. From an electromagnetic point of view, in the absence of DC magnetic fields, plasma can be considered as an isotropic lossy dielectric with magnetic permeability of unity and dispersive electric permittivity $\varepsilon_p = 1 - \frac{w_p^2}{\nu^2 + w^2} + j\frac{w_p^2 \nu / w}{\nu^2 + w^2}$, where w_p is known as the plasma frequency and ν is the collision frequency.

investigated. In particular, in 1967 V.G. Veselago [4] examined the electromagnetic properties of an ideal medium with both negative electric permittivity ε and magnetic permeability μ. He showed that the direction of the Poynting vector and the direction of the phase velocity for a uniform plane wave in such a medium are antiparalell. This kind of materials are known today under different terminology such as Left Handed (LH) media [5-6], media with Negative Refractive Index (NRI) [7-8], backward wave media (BW) [9] and double negative (DNG) metamaterials [10]. More than 30 years elapsed until the pioneering work by Prof. J. Pendry [11] revitalised the interest in this area of research. Pendry's work in combination with the studies presented in [3] led to the UCSD group proving the first experimental demonstrations of such media, [12].

The unusual and promising properties of these artificial structures rapidly expanded the interest for metamaterials. This has resulted in a broadening of the context in which the term *metamaterial* is used. Nowadays, it includes many research areas such as photonic crystals (PC) [13-15] electromagnetic/photonic bandgap structures (EBG/PGB) [16-18], frequency selective surfaces (FSS) [19-20], chiral media [21-23], plasmonic structures [25], NRI media [7-8] or LH materials [5-6]. In this broad context the term metamaterial has been also utilised to define almost any periodic structure that is employed as a substrate or superstrate to enhance the performance or the properties of conventional microwave and antenna structures. Many engineers working in areas of electromagnetism and microwave engineering such as microwave filters [25] and FSS [26] have been wary of this emerging field stating that classical electromagnetic theory could be used to explain the performance of metamaterial.

Periodic structures, such as FSS, consisting of elements varying from simple straight wires to very elaborate concoctions have received much attention due to their myriad of practical applications in the microwave, near IR and optical frequencies. The study of periodic surfaces and their interaction with electromagnetic waves received significant attention in the mid-1960s because of the great potential for military applications; however, there are older references dating from 1919 to the famous Marconi and Franklin reflector for use in wireless telegraphy and telephony.

Normally, resonant FSSs exhibit perfect reflection (capacitive arrays) or transmission (inductive arrays) only at resonance. However, many applications require a different

response. Several properties of planar two-dimensional periodic metallic arrays have been exploited in the last few years. On one hand, the concept of Electromagnetic Band Gap (EBG) material with respect to surface waves propagating along the array [16-18] has been studied. Metallo-dielectric EBG (MEBG) surfaces have been designed and employed for suppression of surface waves in the microwave and millimeter-wave bands and a wide number of applications such as improved microstrip patch antennas, compact resonators and filters [27] have been proposed.

More recently, engineers and scientists worldwide had been working on the synthesis and development of artificial dielectrics possessing properties resembling those of what would be magnetic conductors in the existence of magnetic charges. As a result, a special type of periodic surfaces based on FSSs, called either Artificial Magnetic Conductors (AMC) or High Impedance Surfaces (HIS), emulating the inexistent magnetic conductor have been shown. They are grounded periodic arrays exhibiting a HIS within a specific frequency range for incident plane waves [28-30], so that the average tangential magnetic field is small even with a large electric field along the surface. Due to this unusual boundary condition, AMC structures reflect incident plane waves in–phase to the incident field and can be used as ground planes for low-profile highly directive resonant cavity antennas.

Electromagnetic periodic structures are certainly an interesting and challenging area of study and research. The richness of the electromagnetic phenomena associated with their operation, the great variety of their properties and potential applicability in the design of novel applications or alternative implementations of conventional applications with enhanced performance have motivated several engineers to perform research in this area.

1.2 Framework of the research

This Ph. D. research has been carried out within the Radio Frequency and Microwave Group of the School of Engineering and Physical Science (EPS) at Heriot-Watt University, Edinburgh. The work has been fully financially supported by a prize scholarship awarded by the Edinburgh Research Partnership, from the Institute for

Integrated Systems. Moreover, several of the designs presented in the Ph. D. dissertation have been fabricated in collaboration with the state of the art Scottish Microelectronic Centre.

When this research started, back in 2006, the conceptual aspects related to the operation of electromagnetic periodic surfaces had been well studied and understood, the analysis techniques based on electromagnetic modelling tools for the far-field characterisation of these structures were well studied. However, the near-field characterisation of these structures which reveals interesting properties inherent in certain configurations was missing in the literature. The main objective of this Ph. D. dissertation is to serve as a general guide for the near-field analysis of two dimensional periodic structures in diverse configurations which in turn can be used for the calculation of the power stored and subsequently the quality factor of FSSs. It will also be shown that the near-field analysis can be used as a design tool in antenna systems. Significant novel applications of 2-D periodic surfaces in Antenna Design are presented and sensing applications are proposed.

To accomplish this objective, a method based on the Floquet modal analysis is employed for the formulation of the Electric Field Integral Equation, which is subsequently solved by using the spectral domain Method of Moments (MoM). Particularly, a derivation of the near field excited at different structures is carried out all through this work. Collaborations with experts in different research areas of other institutions including Loughborough University (UK), Aalto University School of Science and Technology (Finland) and Polytechnic University of Cartagena (Spain) have been completed.

The main contribution of each institute to the development of this dissertation was:

- Loughborough University (Nov 2009-2010): fabrication facilities and far-field measurements of broadband highly-directive 2-D periodic Leaky-Wave antennas with two periodic layers.

- Aalto University School of Science and Technology, Department of Radio Science and Engineering (Jul-Sept 2008): theoretical and numerical analysis of two coupled

arrays of oblate nanoellipsoids which exhibit near-field enhancement and subwavelength imaging in the optical regime. This study extends the frequency range presented in this thesis from the microwave to the optical region and can be found as a full paper in the list of publications.

- Polytechnic University of Cartagena: theoretical and numerical analysis of highly-directive 2-D periodic Leaky-Wave antennas with two periodic layers using a different approach based on a Transmission Equivalent Network model which serves as a comparison to the technique presented here.

This Ph. D. research has been awarded the "*Mention of Excellence in Metamaterials*" by the Metamorphose Network of Excellence.

1.3 Scope of the thesis and survey of its contents

This dissertation deals with the modelling of planar periodic structures based on the near-field calculation when they are placed either in a free-standing configuration or in close proximity to other periodic surfaces. The study focuses on different configurations where the periodic surface is acting as an FSS/PRS or acting as a metamaterial ground plane (HIS). Based on these results applications related to highly-directive leaky wave antennas and broadband LWA are proposed, designed and manufactured.

The dissertation is structured in six chapters, including this introductory chapter, as follows:

In chapter 2, Floquet modal analysis is employed for the fast and efficient formulation of the far and near fields in a two layer infinite periodic array of conducting elements printed either on a grounded or ungrounded dielectric substrate. Although this kind of analysis is well documented for arrays in stratified dielectric layers, the formulation for the near fields of a two layer periodic array on a grounded dielectric substrate has not been explicitly reported in the past. An outline of the method is revisited in this chapter. Beginning with the Electric Field Integral Equation (EFIE) which is formed by applying the boundary condition on the conducting elements, the problem is subsequently reduced into a matrix form using Galerkin's Method of Moments (MoM). Finally, the

reflection coefficient, the currents excited on the elements and the near scatter fields under plane wave incidence are determined.

In chapter 3, the reflection and transmission response of different frequency selective surfaces designs and the near-fields excited in the proximity of different structures is examined. A thorough convergence study related to the calculation of the far and near fields of different FSS configurations is presented. The equivalent self impedance of a perturbed array of metal dipoles is derived and the resonant effects upon plane wave illumination are studied. Here, perturbation is understood as a change in the length of every other dipole element in the array. In this configuration it is revealed that the scattering within a frequency range is dominated by the excitation of the odd mode. It is demonstrated that within this frequency range, very strong near fields are excited in the vicinity of the array. The near fields are calculated using the spectral domain periodic Method of Moments, the near fields for a number of perturbed array designs are calculated and an increase in the near-field strength of more than 70 times compared with the incidence is demonstrated. This observation can be particularly interesting for sensing applications. Finally, a miniaturized geometry is proposed and the results are corroborated with HFSS.

In chapter 4, a fast and accurate analysis and synthesis technique for high-gain subwavelength two dimensional Fabry-Pérot leaky-wave antennas (LWA) consisting of two periodic metallo-dielectric arrays over a ground plane is presented. Full-wave MoM together with reciprocity is employed for the estimation of the near fields upon plane wave illumination and the radiation patterns of the LWA. This yields a fast and rigorous tool for the characterisation of this type of antennas. The operation principles of these antennas as well as the radiation characteristics are discussed. Moreover, design guidelines to tailor the antenna profile, the dimensions of the arrays as well as the antenna directivity and bandwidth are provided. A study on the radiation efficiency for antennas with different profiles is also presented and the trade off between directivity and radiation bandwidth is discussed. Numerical examples are given throughout to demonstrate the technique. Furthermore, a simple and rigorous analysis technique to extract the complex dispersion of the antenna is shown. The analysis procedure is based on a combination of array theory as well as the reciprocity technique from which the leaky-mode complex propagation constant is obtained. To demonstrate this technique

some working examples based on half-wavelength and subwavelength profiles are given. The results are compared to a Transverse Equivalent Network (TEN) analysis.

In chapter 5, the same technique as the one employed in the previous chapter is used to investigate the directivity pattern of double layer two-dimensional periodic arrays acting as partially reflective surfaces (PRS) over a ground plane in the leaky-wave antenna design. The technique proposed for the analysis of these antennas is compared to a ray optics model based on multiple reflections between the PRS and the ground plane to produce the radiation pattern. By modifying the features of the elements of the arrays high gain and wide-band antenna performance can be achieved. An optimised double layer dipole and patch leaky wave antenna design is presented, fabricated and measured.

Finally, in chapter 6 conclusions of the work will be presented, and some guidelines for further work will be proposed.

References

[1] J.C. Bose, "On the rotation of plane of polarization of electric waves by a twisted structure", *Proc. Roy. Soc.*, vol. 63, pp. 146-152, 1898.

[2] W.E. Kock, "Metallic delay lenses," *Bell Sys. Tech. J.*, vol. 27, pp. 58-82, 1948.

[3] W. Rotman, "Plasma simulation by artificial dielectrics and parallel-plate media,"*IRE Trans. on Ant. and Propag.*, vol. 10, no. 1, pp. 82–95, Jan. 1962.

[4] V.G. Veselago, "The electrodynamics of substances with simultaneously negative values of ε and μ," *Soviet Physics Uspekhi*, vol. 10, no. 4, pp. 509–514, Jan-Feb1968.

[5] D.R. Smith, W. J. Padilla, D.C. Vier, S.C. Nemat-Nasser and S. Schultz, "Composite medium with simultaneously negative permeability and permittivity," *Phys. Rev. Lett.*, vol. 84, no. 18, pp. 4184-4187, May 2000.

[6] J.B. Pendry, "Negative refraction makes a perfect lens," *Phys. Rev. Lett.*, vol. 85, no. 18, pp. 3966-3969, Oct. 2000.

[7] D. R. Smith and N. Kroll, "Negative refractive index in left-handed materials," *Phys. Rev. Lett.*, vol. 85, pp. 2933-2936, Oct. 2000.

[8] A.K. Iyer, and G.V. Eleftheriades, "Negative refractive index metamaterials supporting 2-D waves," *IEEE MTT International Microwave Symposium (IMS) Digest*, Seattle, WA, June 2-7, 2002, pp. 1067-1070.

[9] I. V. Lindell, S.A. Tretyakov, K.I. Nikoskinen, and S. Ilvonen, "BW media – Media with negative parameters, capable of supporting backward waves," *Microwave Opt. Tech. Lett.*, vol. 31, no. 2, pp. 129-133, Oct. 2001.

[10] R. W. Ziolkowski and A. Kipple, "Application of double negative metamaterials to increase the power radiated by electrically small antennas," *IEEE Trans. Antennas Propag.*, vol. 51, no 10, pp. 2626-2640, Oct. 2003.

[11] J.B. Pendry, A.J. Holden, W.J. Stewart, and I. Youngs, "Extremely Low Frequency Plasmons in Metallic Mesostructures," *Phys. Rev. Lett.*, vol. 76, p. 47734776, Jun. 1996.

[12] R.A. Shelby, D.R. Smith, and S. Schultz, "Experimental verification of a negative index of refraction," *Science Magazine*, vol. 292, pp. 77–79, Apr. 2001.

[13] E. Yablonovitch, "Photonic band-gap crystals," *Journal of Physics: Condensed Matter*, vol. 5, pp. 2443- 2460, 1993.

[14] J. B. Pendry, "Calculating photonic band structure," *J. Phys. : Condens. Matter*, vol. 9, Feb. 1996.

[15] E. Yablonovitch, "Photonic Crystals: Semiconductors of Light," *Scientific American*, pp. 47–55, Dec. 2001.

[16] M.M. Sigalas, C.T. Chan, K.M. Ho, and C.M. Soukoulis, "Metallic photonic bandgap materials," *Phys. Rev. B*, vol. 52, no. 16, pp. 11 744–11 752, Oct. 1995.

[17] A.S. Barlevy, D. Sievenpiper, and Y. Rahmat-Samii, "Photonic bandgap (PBG) structures of multiple metallic periodic screens: efficient electromagnetic characterization," in *Proc. IEEE Antennas and Propagation International Symposium (AP-S)*, vol. 2, Jun. 1998, pp. 1216–1219.

[18] D. Sievenpiper and E. Yablonovitch, "Eliminating surface currents with metallodielectric photonic crystals," in *Proc. IEEE International Microwave Symposium (MTT-S)*, vol. 2, Jun. 1998, pp. 663–666.

[19] B.A. Munk, Frequency Selective Surfaces: Theory and Design, 1st ed. New York: John Wiley and Sons, Ltd., 2000.

[20] J.C. Vardaxoglou, Frequency Selective Surfaces: Analysis and Design , 1st ed. Research Studies Press Ltd, 1997.

[21] F. Mariotte, S.A. Tretyakov, and B. Sauviac, "Modeling effective properties of chiral composites," *IEEE Antennas Propagat. Mag.*, vol. 38, no. 2, pp. 22 – 32, Apr. 1996.

[22] N. Engheta, D.L. Jaggard, and M.W. Kowarz, "Electromagnetic waves in Faraday chiral media," *IEEE Trans. Antennas Propagat.*, vol. 40, no. 4, pp. 367 – 374, Apr. 1992.

[23] F. Mariotte and N. Engheta, "Reflection and transmission of guided electromagnetic waves at an air-chiral interface and at a chiral slab in a parallel-plate waveguide," *IEEE Trans. Microwave Theory Tech.*, vol. 41, no. 11, pp. 1895–1906, Nov.1993.

[24] D.R. Smith, D.C. Vier, W. Padilla, Nemat-Nasser, C. Syrus, S. Schultz, "Loop-wire medium for investigating plasmons at microwave frequencies," *App. Phys. Lett.*, vol. 75, no. 10, pp. 1425-1427, 1999.

[25] B.E. Spielman, S. Amari, C. Caloz, G.V. Eleftheriades, T. Itoh, D.R. Jackson, R. Levy, J.D. Rhodes, and R.V. Snyder, "Metamaterials: A Rich Opportunity for Discovery or an Overhyped Gravy Train," *IEEE Microwave Magaz.*, vol. 10, no. 3, pp. 8–42, May 2009.

[26] B.A. Munk, *Metamaterials: Critique and Alternatives*. Hoboken, NJ: John Wiley and Sons, Inc., 2009.

[27] N. Llombart, A. Neto, G. Gerini, and P. de Maagt, "Planar circularly symmetric EBG structures for reducing surface waves in printed antennas," *IEEE Transactions on Antennas and Propagation*, vol. 53, no. 10, pp. 3210-3218, Oct. 2005.

[28] R.W. Ziolkowski and F. Auzanneau, "Artificial molecule realization of a magnetic wall," *J. Appl. Phys*, vol. 82, no. 7, pp. 3192 – 3194, Oct. 1997.

[29] D. Sievenpiper, Z. Lijun, R.F.J. Broas, N.G. Alexopolous, and E. Yablonovitch, "High-impedance electromagnetic surfaces with a forbidden frequency band," *IEEE Trans. Microwave Theory Tech.*, vol. 47, no. 11, pp. 2059–2074, Nov. 1999.

[30] A. P. Feresidis, G. Goussetis, S. Wang, and J. C. Vardaxoglou, "Artificial magnetic conductor surfaces and their application to low profile high-gain planar antennas," *IEEE Trans. Antennas Propagat.*, vol. 53, no. 1, pp. 209–215, Jan. 2005.

Chapter 2

Electromagnetic modelling of Periodic Surfaces

"The mathematical sciences particularly exhibit order, symmetry, and limitation; and these are the greatest forms of the beautiful."

Ἀριστοτέλης, Aristotélēs

2.1 Introduction

Modelling periodic planar structures is essential for the analysis and design of many microwave devices [1-7]. Therefore, it is necessary to have efficient tools readily available in order to characterise its behaviour. There are a substantial number of numerical methods that have been investigated in the analysis of periodic arrays, all of them deriving from Maxwell's equations [8].

The most important qualities of these tools are related to the robustness and simplicity of implementation, accuracy and computational efficiency. Robustness and simplicity are necessary so that the tool is simple and performs well even under unusual conditions that stress the initial assumptions. Computational efficiency is required so that both

execution time as well as memory requirements are feasible. Finally accuracy is important so the simulation matches well with the real measured results. However, there is no one tool which can satisfy all of these characteristics. Users will have to prioritise, in accordance with their needs, which quality is more important in order to solve their electromagnetic problem.

Many methods have been adopted to analyse periodic surfaces [9-13]. The most popular combinations are Time domain-Differential equation methods such as Finite Element Method (FEM) [9], Finite Difference Time Domain (FDTD) [10-11] or Transmission Line Matrix (TLM) method [12] and Frequency domain- Integral Equation methods such as Method of Moments (MoM) [6, 13]. Throughout the present thesis, a numerical electromagnetic modelling technique based on MoM to solve the Electric Field Integral Equation (EFIE) has widely been used. Specific modelling tools for particular periodic planar structures have been developed and employed. However, commercial software packages such as High Frequency Structure Simulator (HFSS) based on full-wave FEM and CST Microstripes^{TM} based on TLM method has also been utilised as modelling tools mostly to corroborate the results. The major drawback of the tools, compared to the software developed here, is related to memory and time consumption.

In this chapter the transmission/reflection plane wave performance of double layer periodic planar surfaces with metallizations laying on a grounded dielectric substrate is presented. The method can be easily amended for single layer arrays. The arrays are assumed to be infinitely thin and of perfect conducting area. Nevertheless, the technique shown here can be applied to determine the fields in aperture arrays with simple modifications [14-16]. In the following we will be focused with full-wave solutions of periodic planar surfaces modelled using spectral domain MoM. The method requires calculating only boundary values, rather than values throughout the space defined by a partial differential equation. It is significantly more efficient in terms of computational resources for problems that involved electrically small surfaces/volumes.

The main tasks of the developed software are:

- Solve the electric field integral equation to obtain the currents excited on the elements upon plane wave illumination.

- Determine the corresponding reflection and transmission coefficients in each interface for each Floquet Space Harmonic.
- Obtain the reflected and transmitted field amplitude in each layer.
- Obtain the near electric and magnetic field excited in the vicinity of the structure under investigation.

The chapter starts with a brief introduction on electromagnetism; it includes an introduction of basic electromagnetic theory, solution of boundary problems as well as mode propagation. Section 2.3 presents the theory of propagation in periodic structures. The formulation of MoM for the solution of a grounded double layer two dimensional periodic surface is shown as an example in section 2.4.

2.2 Periodic Surfaces in Electromagnetics

The approach adopted in this work for the analysis of periodic surfaces is based on the electromagnetic field expansion and matching at the different interfaces of the structure to be studied [2, 15-17]. The electromagnetic field expansion is related to the basic formulation of electromagnetic equations as applied in homogeneous source free media. In this section an overview of electromagnetism for the analysis of periodic arrays is presented. The theory presented here does not aim to be complete and exhaustive, since we would like to give a simple overview of the subject with special emphasis on the topic which concerns this work. For more details please refer to [6-8]. Initially, a brief overview of electromagnetic theory and the basic laws of electromagnetism are presented. The derivation of the boundary conditions associated with the electric and magnetic field behaviour are also shown. At the end of the section the different transverse electromagnetic field modes and plane wave excitation are introduced.

2.2.1 Overview of electromagnetism

Maxwell equations represent a concise way to state the fundamentals of electromagnetism. The general differential form of Maxwell's equations is given in 2.2-

1-2.2-4 [8]. This representation is used to relate the electric and magnetic field vectors, current densities and charge densities in space and time. The first is Faraday's law of induction; the second is Ampère's law as amended by Maxwell to include the displacement current $\partial\mathbf{D}/\partial t$, the third and fourth are Gauss' laws for the electric and magnetic fields [8, 18].

The displacement current term $\partial\mathbf{D}/\partial t$ in Ampère's law is essential in predicting the existence of propagating electromagnetic waves. The quantities **E** and **H** are the electric and magnetic field intensities and are measured in units of [volt/m] and [ampere/m], respectively. The quantities **D**, which is equal to $\varepsilon_r \cdot \varepsilon_o \cdot \mathbf{E}$, and **B**, calculated as $\mu_r \cdot \mu_o \cdot \mathbf{H}$, are the electric and magnetic flux densities and are in units of [coulomb/m^2] and [weber/m^2] or [tesla]. **B** is also called the magnetic induction. The relative permittivity/ permeability of the medium where the waves propagate are ε_r/ μ_r and ε_o / μ_o is the permittivity/permeability of vacuum. The quantities ρ and **J** are the volume charge density and electric current density (charge flux) of any external charges (that is, not including any induced polarization charges and currents.) They are measured in units of [coulomb/m^3] and [ampere/m^2].

$$\nabla \times \boldsymbol{E} = -\frac{\partial \boldsymbol{B}}{\partial t} \tag{2.2-1}$$

$$\nabla \times \boldsymbol{H} = \frac{\partial \boldsymbol{D}}{\partial t} + \boldsymbol{J} \tag{2.2-2}$$

$$\nabla \cdot \boldsymbol{D} = \rho \tag{2.2-3}$$

$$\nabla \cdot \boldsymbol{B} = 0 \tag{2.2-4}$$

In order to solve these equations it is often sufficient to consider the steady state solution, with sinusoidal time dependence of the fields. Replacing the time derivatives by $\partial t \rightarrow j\omega$, we may rewrite the previous set of equations in the form,

$$\nabla \times \boldsymbol{E} = -j\omega \boldsymbol{B} \tag{2.2-5}$$

$$\nabla \times \boldsymbol{H} = j\omega \boldsymbol{D} + \boldsymbol{J} \tag{2.2-6}$$

$$\nabla \cdot \boldsymbol{D} = \rho \tag{2.2-7}$$

$$\nabla \cdot \boldsymbol{B} = 0 \tag{2.2-8}$$

The basic field equations may be expressed in equivalent integral form also. They have limited applications and are usually used only to solve electromagnetic boundary problems that posses complete symmetry. By application of the Stokes' theorem to (2.2-5) and (2.2-6) gives,

$$\begin{aligned} \iint_S \nabla \times \boldsymbol{E} \cdot dS &= \oint_C \boldsymbol{E} \cdot dl = -j\omega \iint_S \boldsymbol{B} \cdot dS \\ \oint_C \boldsymbol{H} \cdot dl &= \iint_S \left(-j\omega \boldsymbol{D} + \boldsymbol{J}\right) \cdot dS \end{aligned} \tag{2.2-9}$$

Using the divergence theorem, the remaining equations become,

$$\oiint_S \boldsymbol{D} \cdot dS = \iiint_V \rho \cdot dV \tag{2.2-10}$$

$$\oiint_S \boldsymbol{B} \cdot dS = 0 \tag{2.2-11}$$

The expressions in (2.2-9) refers to an open surface S bounded by a closed contour C, while in (2.2-10) the surface S is closed surface with an interior volume V. The vector element dS is directed outward.

Observing Eq. (2.2-1-4), it can be seen that each equation presents more than one unknown field which makes it difficult to solve. This dependence can be detached by raising the order of the differential equation to second order. For the particular case of source free media and time harmonic fields, the *uncoupled* equations, also known as vector wave equations, reduce to [8, 18]:

$$\nabla^2 \boldsymbol{E} = -\omega^2 \mu\varepsilon \boldsymbol{E} \tag{2.2-12}$$

$$\nabla^2 \boldsymbol{H} = -\omega^2 \mu\varepsilon \boldsymbol{H} \tag{2.2-13}$$

2.2.2 Boundary Conditions

The differential form of Maxwell's equations represent derivatives of the electric and magnetic field vectors with respect to the space coordinates. If the electromagnetic problem under consideration is presented in a media whose electrical properties are discontinuous at certain points, the behaviour of the electric and magnetic field vectors

across these discontinuous boundaries must be studied. In particular, to find the solution of the boundary problem one needs to find the relationship between the components of the electric and magnetic fields on both sides of the boundaries. The integral form of Maxwell's equations can be used to obtain the boundary conditions associated with various interfaces.

Fig. 2-1 depicts a surface S which separates two regions along which there are no charges or sources, one with permittivity ε_1 and permeability μ_1 and the other one with permittivity ε_2 and permeability μ_2. The surface normal ***n*** is directed from medium 2 into medium 1, and the contour C runs parallel to the surface S. There is a closed surface also parallel to S.

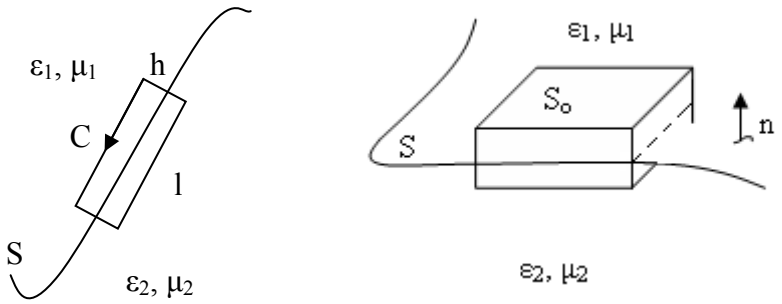

Fig. 2-1 Geometry for boundary conditions of the electric and magnetic field components.

The line integral equation of the electric field around C will be equal to the negative time rate of change of the total magnetic flux through the contour. As h goes to zero the total flux through C vanishes since ***B*** is a bounded function. Therefore, the tangential components of the electric field will be equal at both sides. Likewise, the line integral of ***H*** around the same contour yields a similar result, [18].

If actual electric sources and charges exist along the interface between the two regions, or if either of the two regions forming the interface is a perfect electric conductor, the boundary conditions of the magnetic field must be modified to include the sources and charges or the induced linear electric current density $\boldsymbol{J_s}$. The boundary condition on the tangential magnetic field becomes:

$$\left(H_1 - H_2\right) = -n \times J_s \tag{2.2-20}$$

This last equation states that the tangential components of the magnetic field across an interface, along which there exists a surface electric current density J_s (Amp/m) are discontinuous by an amount equal to the electric current density. Moreover, if either of the two media is a perfect electric conductor the total electric field is zero over the conducting area.

In a similar fashion, the BCs shown in Table 2-1 can be obtained. At a discontinuity surface it is enough to match the tangential field components. Only when the fields satisfy Maxwell's equations will the normal components of the flux vectors satisfy the boundary conditions of the problem.

TABLE 2-1
BOUNDARY CONDITIONS ON TIME-HARMONIC ELECTROMAGNETIC FIELDS

Field	**General**	**Finite-conductivity media, no sources or charges**	**Medium 1 of infinite electric conductivity**
Tangential electric field intensity	$\hat{n}\times(E_2-E_1)=-M_s$	$\hat{n}\times(E_2-E_1)=0$	$\hat{n}\times(E_2)=0$
Tangential magnetic field intensity	$\hat{n}\times(H_2-H_1)=J_s$	$\hat{n}\times(H_2-H_1)=0$	$\hat{n}\times(H_2)=J_s$
Normal electric flux density	$\hat{n}\cdot(D_2-D_1)=q_{es}$	$\hat{n}\cdot(D_2-D_1)=0$	$\hat{n}\cdot(D_2)=q_{es}$
Normal magnetic flux density	$\hat{n}\cdot(B_2-B_1)=q_{ms}$	$\hat{n}\cdot(B_2-B_1)=0$	$\hat{n}\cdot(B_2)=0$

2.2.3 Transverse Electromagnetic modes and Plane Wave excitation of 2-D periodic surfaces

For a given electromagnetic boundary problem many field configurations which satisfy the vector wave equation (Maxwell's equations) (2.2-12-13) together with the boundary conditions exist. All the different field pattern configurations that are solution of Maxwell's equations are usually referred to as *modes*. The periodic surfaces analysed in this work are excited by a uniform incident plane wave. A *uniform plane wave* is a particular solution of the vector wave equation in free space for which electric and magnetic field phasors are contained in the same plane and whose magnitude and phase are independent of the position of the plane, [8]. This is demonstrated in the following

where a lossless medium (ε and μ are real numbers, so the propagation constant k is also real) is considered.

A basic plane wave solution of (2.2-12) can be found by considering an electric field with only a $\hat{y}$ component and uniform (no variation) in the x and y direction. Then $\partial/\partial x = \partial/\partial y = 0$ and (2.2-12) reduces to,

$$\frac{\partial^2 E_y}{\partial z^2} + k^2 E_y = 0 \tag{2.2-21}$$

where the propagation constant, k, is defined as $k = \omega^2 \cdot \varepsilon \cdot \mu$. The time harmonic solutions to this equation can be easily derived [8] and have the form,

$$E_y(z) = E^+ e^{-jkz} + E^- e^{+jkz} \tag{2.2-22}$$

where E^+ and E^- are arbitrary (and in general complex) constants that must be determined by the boundary conditions. The first term in (2.2-22) represents a wave travelling in the +z direction. Similarly, the second term in (2.2-22) represents a wave travelling in the negative z direction; hence, the notation E^+ and E^- for these wave amplitudes.

The velocity of the wave in this sense is called phase velocity as it is the velocity at which a fixed phase point on the wave travels. It is given by,

$$v_p = \frac{\omega}{k} = \frac{1}{\varepsilon\mu} \tag{2.2-23}$$

in free-space $v_p = c$, the speed of light.

The wavelength, λ, is defined as the distance the wave must propagate to suffer a change in phase of 2π,

$$\lambda = \frac{2\pi}{k} = \frac{2\pi v_p}{\omega} = \frac{v_p}{f} \tag{2.2-24}$$

A complete specification of the plane wave electromagnetic field must include the magnetic field. In general, whenever ***E*** or ***H*** is known, the other field vector can be readily found by using one of Maxwell's curl equations. Thus, applying (2.2-5) to the electric field of (2.2-22) gives H_y=H_z=0, and

$$H_x = \frac{1}{\eta}\left(E^+ e^{-jkz} - E^- e^{+jkz}\right) \tag{2.2-25}$$

where $\eta = \omega \cdot \mu / k = \sqrt{\mu / \varepsilon}$ is the wave impedance for the plane wave, defined as the ratio of the ***E*** and ***H*** fields. For plane waves, this impedance is also the intrinsic impedance of the medium. In free-space we have $\eta_o = \sqrt{\mu_o / \varepsilon_o}$ =377 Ω. We can note by observation of (2.2-22) and (2.2-25) that ***H*** is perpendicular to ***E*** and that both are transverse to the direction of propagation, $\hat{z}$. Therefore, uniform plane waves are a particular case of a *transverse electromagnetic* (TEM) *wave*.

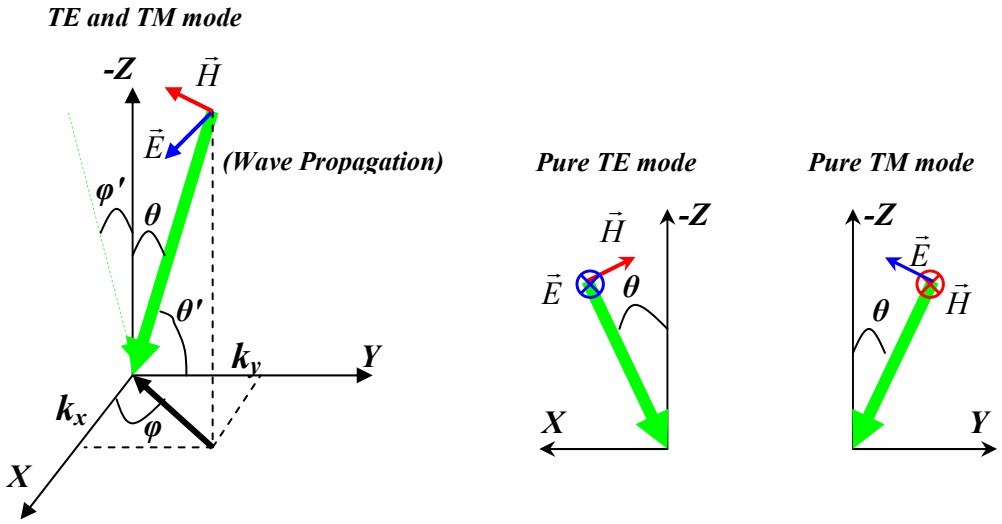

a) b) c)

Fig. 2-2 Spherical coordinate system for an incoming incident plane wave from a particular angle of incident.

In the following we consider a surface laying on the XY plane in free-space. Such a surface is excited by an incident plane wave with propagation constant ***k*** defined as,

$$\bar{k} = k_o\left((\sin\theta\cos\varphi)\hat{x} + (\sin\theta\sin\varphi)\hat{y} + \cos\theta\hat{z}\right) \tag{2.2-26}$$

where θ is defined as the angle between propagation vector ***k*** and Z-axis and φ is the angle formed between the projection of vector k in the XY-plane and X-axis. Please refer to Fig. 2-2a.

Initially consider the incident plane wave travelling in the XZ-plane, φ=0, (Fig.2-2b) the propagation vector becomes,

$$\bar{k} = k_o\left(-\sin\theta\hat{x} + \cos\theta\hat{z}\right) \tag{2.2-27}$$

electric and magnetic field components are orthogonal between them and to ***k,*** as demonstrated above. The electric field components at this plane are defined as,

$$E_y = E^+ e^{-j\boldsymbol{k}\cdot\boldsymbol{r}} \qquad E_x = E_z = 0 \tag{2.2-28}$$

where $r = x\hat{x} + z\hat{z}$. By application of (2.2-5) and the previous definition of the intrinsic impedance the magnetic field components are,

$$H_x = E^+/\eta_o \cos(\theta)\, e^{-j\boldsymbol{k}\cdot\boldsymbol{r}} \qquad H_z = E^+/\eta_o \sin(\theta)\, e^{-j\boldsymbol{k}\cdot\boldsymbol{r}} \qquad H_y = 0 \tag{2.2-29}$$

This specific field configuration is known as transverse electric field mode (TE) since the electric field components are transverse to the direction of propagation, E_z=0, Fig. 2.2b.

Likewise, considering the incident wave travelling along the YZ- plane, φ=π, (Fig.2-2c) the propagation vector becomes,

$$\bar{k} = k_o\left(-\sin\theta\hat{y} + \cos\theta\hat{z}\right) \tag{2.2-30}$$

The magnetic field components in this plane are defined as,

$$H_x = -E^+/\eta_o\, e^{-j\boldsymbol{k}\cdot\boldsymbol{r}} \qquad H_y = H_z = 0. \tag{2.2-31}$$

where $r = y\hat{y} + z\hat{z}$. By application of (2.2-6) the electric field components are,

$$E_y = E^+ cos(\theta)\, e^{-j\boldsymbol{k}\cdot\boldsymbol{r}} \qquad E_z = E^+ sin(\theta)\, {}^{+}e^{-j\boldsymbol{k}\cdot\boldsymbol{r}} \qquad E_x = 0 \tag{2.2-32}$$

This field pattern is known as transverse magnetic mode (TM) where the magnetic field components are transverse to the direction of propagation, H_z=0, Fig. 2.2c.

For any other angle of incident, *(θ,φ),* the propagation vector takes the form of (2.2-26). In this case the expression of the electric field can be expressed as function of the angle *θ'*, Fig 2-2a, [19]

$$E_y = \sin(\theta') \tag{2.2-33}$$

The following transformation needs to be carried out in order to express the field in terms of the common spherical angles θ and φ (Fig.2-2).

$$\begin{aligned}
&\cos(\theta') = \hat{r}\cdot\hat{y} = \hat{y}\cdot(\sin\theta\cdot\cos\varphi\hat{x} + \sin\theta\cdot\sin\varphi\hat{y} + \cos\varphi\hat{z}) = \sin\theta\cdot\sin\varphi \\
&\sin^2(\theta') + \cos^2(\theta') = 1 \\
&\sin(\theta') = \sqrt{1-\cos^2(\theta')} = \sqrt{1-\sin^2\theta\cdot\sin^2\varphi}
\end{aligned} \tag{2.2-34}$$

The y-component of the incident electric field can be expressed in terms of θ and φ as follows,

$$E_y = \sin(\theta') = \sqrt{1-\sin^2(\theta)\sin^2(\varphi)} \tag{2.2-35}$$

The projection of the propagation wave vector of an incident plane wave in the XZ plane is given in (2.2-36),

$$k_{xz} = \sin(\theta)\cos(\varphi)\hat{x} + \cos(\theta)\hat{z} \tag{2.2-36}$$

The normalised wave vector is,

$$\hat{k}_{xz} = \frac{\sin(\theta)\cos(\varphi)\hat{x} + \cos(\theta)\hat{z}}{\sqrt{\sin^2(\theta)\cos^2(\varphi) + \cos^2(\theta)}} \tag{2.2-37}$$

So that *cos(φ')* can be written as in Eq. (2.2-38)

$$\cos(\varphi') = \hat{k}_{xz}\cdot\hat{z} = \frac{\cos(\theta)}{\sqrt{\sin^2(\theta)\cos^2(\varphi) + \cos^2(\theta)}} \tag{2.2-38}$$

The x- and z- components of the incidence are described in (2.2-39) and (2.2-40),

$$E_x = \cos(\theta')\sin(\varphi') = \sin(\theta)\sin(\varphi)\sqrt{1-\frac{\cos^2(\theta)}{\sin^2(\theta)\cos^2(\varphi)+\cos^2(\theta)}} =$$
$$\sin(\theta)\sin(\varphi)\sqrt{\frac{\sin^2(\theta)\cos^2(\varphi)+\cos^2(\theta)-\cos^2(\theta)}{\sin^2(\theta)\cos^2(\varphi)+\cos^2(\theta)}} = \frac{\sin(\theta)\sin(\varphi)\sin(\theta)\cos(\varphi)}{\sqrt{\sin^2(\theta)\left[1-\sin^2(\varphi)\right]+\cos^2(\theta)}} =$$
$$\frac{\sin(\theta)\sin(\varphi)\sin(\theta)\cos(\varphi)}{\sqrt{\sin^2(\theta)-\sin^2(\theta)\sin^2(\varphi)+\cos^2(\theta)}} = \frac{\sin(\theta)\sin(\varphi)\sin(\theta)\cos(\varphi)}{\sqrt{1-\sin^2(\theta)\sin^2(\varphi)}} =$$
$$\frac{\sin(\theta)\sin(\varphi)\sin(\theta)\cos(\varphi)\sqrt{1-\sin^2(\theta)\sin^2(\varphi)}}{1-\sin^2(\theta)\sin^2(\varphi)} \tag{2.2-39}$$

Applying orthogonality of the electric field and the propagation vector k, the z-component of the electric field can be derived,

$$E_z = -\frac{E_x \cdot k_x + E_y \cdot k_y}{k_z} \tag{2.2-40}$$

The magnetic field components can be readily derived using (2.2-5). This field configuration is characterised for a non zero electric and magnetic field in the direction of propagation, E_z, $H_z \neq 0$ and are known as hybrid modes which can be expressed as a superposition of TE and TM modes, Fig. 2-2a.

2.3 Propagation in Periodic Surfaces

A periodic structure can be obtained as a combination of infinite replica of a unit cell shifted by translation vectors. In accordance with the number of vectors used in the translation, a periodic structure can be uni-, bi- or tri- dimensional. Specifically, a uni-dimensional periodic structure is commonly a lineal uniform array of identical elements [20]; bi-dimensional periodic structures are typically organized in the form of plane array elements in a grid with double periodicity [6]; and tri-dimensional periodic array structures are arranged in a grid with triple periodicity [21]. An example of 1-D, 2-D and 3-D periodic structures is shown in Fig. 2-3.

Real structures are finite and therefore ideal periodic structures cannot exist. Nevertheless, if an array is large enough it can be approximated by an infinite periodic

structure. By considering an infinite array model the complexity in computational analysis is reduced. In this case the electromagnetic field inside a uniformly excited periodic structure is the same for each cell, except for a phase displacement [7, 22]. This means that the analysis of the whole structure is simplified to the analysis of one unit cell as it will be introduced in the following. From the computational point of view, this suggests significant gains in memory requirements and computational time.

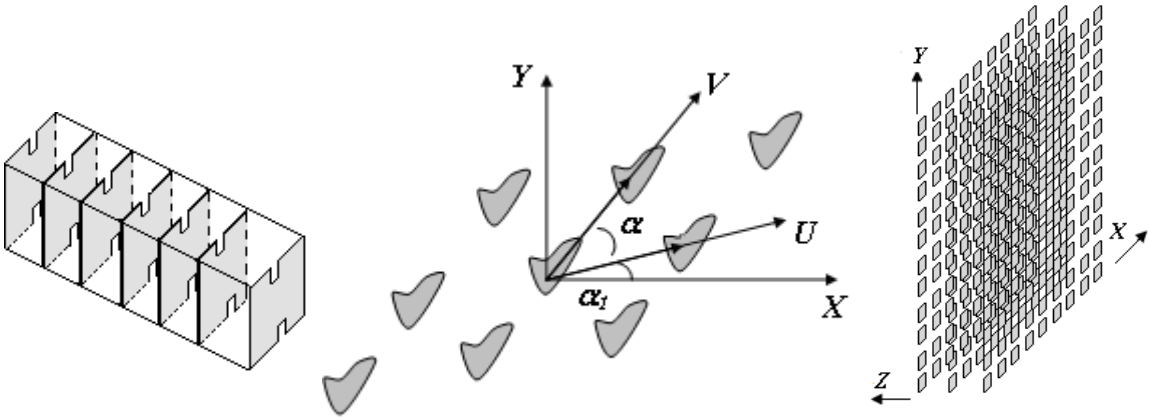

Fig. 2-3. Example of a 1-D, 2-D and 3-D periodic metamaterial surface.

In the remainder of this chapter we will give special attention to one type of periodic surfaces (e.g. Frequency Selective Surfaces (FSS)) due to the interest in the present thesis.

2.3.1 Frequency Selective Surfaces

Frequency Selective Surfaces have been the subject of extensive studies [4-7, 23-30]. Due to their selectivity in frequency, polarization and angle of incidence, FSS have been widely employed in frequency separation in quasi optical beam splitters [23] dual or multi-banding Cassegrain reflectors [4, 24], radomes [25, 26], dual band arrays [27-30], filters [7], sensors [31] and absorbers for radar, satellite and antenna systems [7] in the microwaves, Near Infrared (NI) and optical regime.

FSSs typically consist of printed arrays of conducting elements, an example of a free-standing array of conducting dipoles is shown in Fig. 2-4, or a periodic set of apertures in a conducting plane which is the Babinet's complement of the former. The behaviour

of both configurations is complementary. Unless otherwise stated from this point onwards only conducting elements either in a free-standing configuration or printed on a dielectric substrate will be considered.

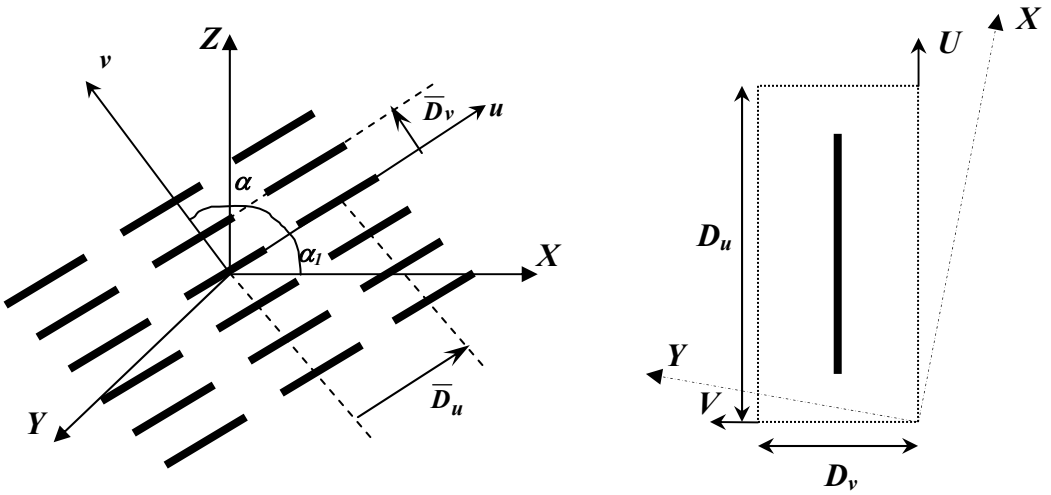

Figure 2-4 Geometry of a free standing 2-D periodic array of dipoles and unit cell of an arbitrary lattice geometry.

The elements that compose the array can be shaped in order to accommodate different applications. A dipole FSS is shown in figure 2-4 and other examples of common FSS unit cells are presented in Fig 2-5. The elements of the array are periodically arranged on a given *lattice geometry*. In a 2-D periodic structure, the lattice geometry, which holds each element, is described by a pair of translation vectors namely, $\vec{D}_u$ and $\vec{D}_v$. These vectors can be either orthogonal or separated by an angle α and in general are described as,

$$\begin{aligned} \vec{D}_u &= D_u\left(\cos\alpha_1\hat{x} + \sin\alpha_1\hat{y}\right) \\ \vec{D}_v &= D_v\left(\cos\alpha_2\hat{x} + \sin\alpha_2\hat{y}\right) \end{aligned} \tag{2.3-1}$$

where α_1 is the angle between unitary vector $\hat{u}$ and axis $\hat{x}$, and α_2 is the angle between unitary vector $\hat{v}$ and axis $\hat{x}$. Lattice dimensions play an important role in the design of the array as they are mainly responsible for the appearance of grating lobes[1].

When a plane wave is incident on an FSS array it is partly transmitted in the forward direction $\overline{E}^t$ and partly reflected in the specular direction $\overline{E}^r$. The specular reflection

[1] Grating lobes will be introduced in section 2.3.3

coefficient is defined as the relation between the reflected and incident amplitudes; likewise the transmission coefficient is defined as the relation between the transmitted and incident amplitudes.

$$R = \frac{E_r}{E_i} \tag{2.3-2}$$

$$T = \frac{E_t}{E_i} \tag{2.3-3}$$

It is usually desirable that the surface has minimum sensitivity to the variation of angles of illumination. However, depending on the application it may be required that the reflection and transmission spectral responses vary. The elements and the lattice geometries chosen decisively contribute in improving the angular sensibility or varying the influence of the grating lobes.

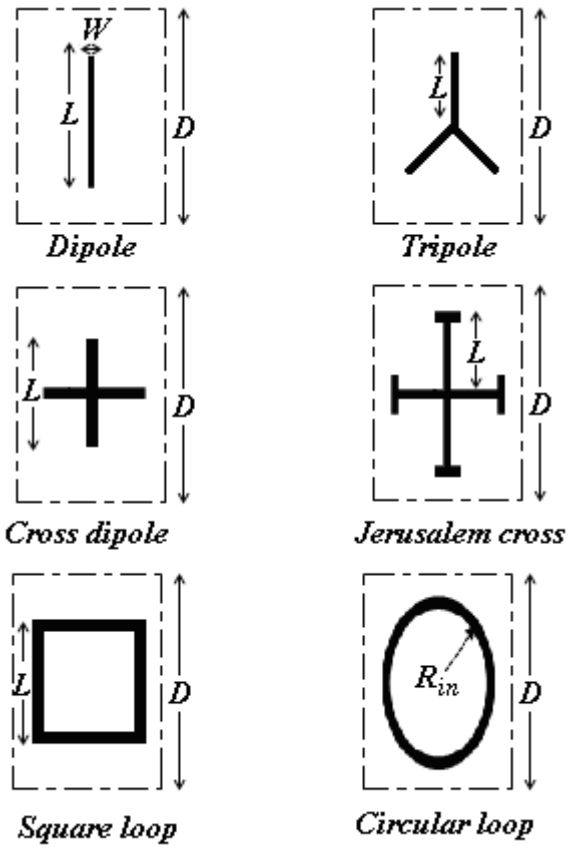

Figure 2-5 Square unit cells of different geometries of Frequency Selective Surfaces.

2.3.2 Propagation in a periodic structure

In formulating the problem of electromagnetic scattering from a periodic surface, firstly the scattered fields from the surface have to be related to the surface currents induced on the screen by the incident plane wave. In order to obtain this relation in the following the fundamentals of the propagation in a periodic structure are explained.

The basis of the analysis of any type of periodic structure is Floquet's theorem [22], named after the French mathematician G. Floquet whose work on the periodic solution of differential equations instigated the theorem. To introduce Floquet's theorem consider initially an electromagnetic plane wave incident on a 1-D array of metallic patches such as the one depicted in Fig. 2-6. This wave induces some currents over the metallic patches which at the same time radiate a scattered field to the surrounding space. If the angle of incidence is not normal to the screen then the wave will excite successive elements of the screen with a different phase, which can be understood using a geometrical optics model. This is represented in Fig. 2-6. The currents on successive unit cells have a phase difference that is dependant on the frequency of the incident wave, k, and the periodicity of the structure, D_y.

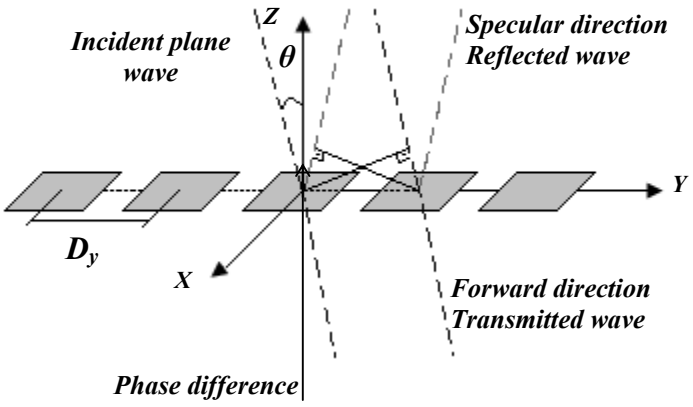

Figure 2-6 Difference between paths of the incident plane wave.

In fact, according to Floquet's theorem, if $\vec{E}(x,y,z)$ and $\vec{H}(x,y,z)$ are the phasors of the electric and magnetic field at a certain point, z=0, in the unit cell between $-D_y/2 \leq z \leq D_y/2$, then the phasors of the fields at $z=D_y$ in the unit cell located in the region $D_y/2 \leq z \leq 3D_y/2$ should be $\vec{E}(x,y,z)e^{-j\beta_o D_y}$ and $\vec{H}(x,y,z)e^{-j\beta_o D_y}$, where β_o stands for propagation constant in free-space. The phase $e^{-j\beta_o D_y}$ corresponds to the phase added

to a wave after travelling a distance D_y. Consequently, everywhere in the periodic structure, the fields at two different points, being one period apart, are related according to Eq. (2.3-4)

$$\vec{E}(x,y,z+D_y)=\vec{E}(x,y,z)e^{-j\beta_o D_y}$$
$$\vec{H}(x,y,z+D_y)=\vec{H}(x,y,z)e^{-j\beta_o D_y} \tag{2.3-4}$$

Likewise, the fields everywhere in a periodic surface are given by (2.3-5),

$$\vec{E}(x,y,z)=\vec{E}_{periodic}(x,y,z)e^{-j\beta_o z}$$
$$\vec{H}(x,y,z)=\vec{H}_{periodic}(x,y,z)e^{-j\beta_o z} \tag{2.3-5}$$

where $\vec{E}_{periodic}(x,y,z)$ and $\vec{H}_{periodic}(x,y,z)$ are periodic functions with period D_y. These functions can be expanded as an infinite sum of Fourier series (2.3-6)

$$\vec{E}_{periodic}(x,y,z)=\sum_{p=-\infty}^{\infty}\vec{E}_{periodic_p}(x,y,z)e^{-j\frac{2\pi}{D_y}p\cdot z}$$
$$\vec{H}_{periodic}(x,y,z)=\sum_{p=-\infty}^{\infty}\vec{H}_{periodic_p}(x,y,z)e^{-j\frac{2\pi}{D_y}p\cdot z} \tag{2.3-6}$$

Using (2.3-5) and (2.3-6), the total electromagnetic field scattered by an infinite periodic structure illuminated by a plane wave can be expressed as,

$$\vec{E}(x,y,z)=\sum_{p=-\infty}^{\infty}\vec{E}_{periodic_p}(x,y,z)e^{-j\left(\beta_o+\frac{2\pi}{D_y}p\right)z}$$
$$\vec{H}(x,y,z)=\sum_{p=-\infty}^{\infty}\vec{H}_{periodic_p}(x,y,z)e^{-j\left(\beta_o+\frac{2\pi}{D_y}p\right)z} \tag{2.3-7}$$

where $\beta_p=\beta_o+\frac{2\pi}{D_y}p$ represents the unique wavenumber (and therefore phase velocity) along the direction of periodicity (y) of all the possible supported modes (Floquet Space Harmonics -FSH). For low frequencies, all but the 0^{th} order harmonic (p=0), represent slow waves in the direction of periodicity, and therefore are evanescent in the direction normal to the plane of the array since $\beta_p > \beta_o$.

Consider now the 2-D case presented in Fig.2-4. In order to look into the total scattered field the wave equation needs to be solved for this structure. Allow for a coordinate system defined as (***u,v,Z***), which is a rotation of the rectangular coordinate system (***X,Y,Z***), as seen in Fig. 2-4, we can described a scalar potential $\phi(u,v,z)$ which should satisfy the vector wave equation (2.2-12),

$$\nabla^2\phi(u,v,z)+k^2\phi(u,v,z)=0 \tag{2.3-8}$$

Due to the periodic nature of the surface along both u and v axes, the scalar potential $\phi(u,v,z)$ should also satisfy the condition of periodicity,

$$\phi(u+D_u,v+D_v,z)=e^{-j(k_uD_u+k_vD_v)}\phi(u,v,z) \tag{2.3-9}$$

where, k_u and k_v are the phase displacement between elements along the $\hat{u}$ and $\hat{v}$ axis. Similarly to standard waveguides, the behaviour along the direction of propagation (e.g. positive $\hat{z}$ - axis) is,

$$\phi(u,v,z)=e^{-\gamma z}\phi(u,v) \tag{2.3-10}$$

where $\gamma=j\beta$ for propagative modes in lossless structures. Therefore, taking (2.3-10) into (2.3-8), the vector wave equation is written as,

$$\nabla_T{}^2\phi(u,v)+\left(k^2+\beta^2\right)\phi(u,v)=0 \tag{2.3-11}$$

$\nabla_T{}^2$ is the transversal laplacian operator, and β is defined as $\beta^2=k^2-k_u{}^2-k_v{}^2$. In order to solve this equation the separation of variable technique is utilised [8]. This means that the scalar potential can be expressed as the product of two independent variable functions, named here as $f(u)$ and $g(v)$.

$$\phi(u,v)=f(u)g(v) \tag{2.3-12}$$

Therefore, the wave equation can be written separately for the $\hat{u}$ and $\hat{v}$ component. Likewise, the boundary conditions can be independently applied for each component and the problem reduces to know the phase displacement between elements along the $\hat{u}$ direction, k_u, and $\hat{v}$ direction, k_v.

$$\frac{\partial^2}{\partial u^2} f(u) + k_u{}^2 f(u) = 0$$
$$\frac{\partial^2}{\partial v^2} g(v) + k_v{}^2 g(v) = 0 \tag{2.3-13}$$

Firstly, the function $f(u)$ is considered. Since $\phi(u,v)$ is periodic $f(u)$ should also be periodic, this yields,

$$f(u + D_u) = f(u) e^{-jk_u^i D_u} \tag{2.3-14}$$

where k_u^i is the wavenumber of the incident plane wave along the u axis. It is possible to define a new periodic function $f_{periodic}(u)$ of the form,

$$f_{periodic}(u) = f(u) e^{jk_u^i u} \tag{2.3-15}$$

It can be easily demonstrated that this is a periodic function by simple substitution at $u=u+D_u$,

$$f_{periodic}(u + D_u) = f(u + D_u) e^{jk_u^i (u + D_u)} = f(u + D_u) e^{jk_u^i u} e^{jk_u^i D_u} =$$
$$f(u) e^{jk_u^i u} = f_{periodic}(u) \tag{2.3-16}$$

Due to the periodicity of $f_{periodic}(u)$, this function can be expressed as an infinite sum or Fourier series,

$$f_{periodic}(u) = \sum_{p=-\infty}^{+\infty} a' e^{-\frac{j2\pi p}{D_u} u} \tag{2.3-17}$$

where a' are scalar coefficients. Substituting (2.3-17) into (2.3-15) the expression for $f(u)$ is readily obtained as,

$$f(u) = \sum_{p=-\infty}^{+\infty} a' e^{-\frac{j2\pi}{D_u} p \cdot u} \cdot e^{-jk_u^i u} = \sum_{p=-\infty}^{+\infty} a' e^{-j\left(\frac{2\pi}{D_u} p + k_u^i\right) u} = \sum_{p=-\infty}^{+\infty} a' e^{-jk_{pu} u} \tag{2.3-18}$$

where k_{pu} is the phase displacement for each Floquet harmonic at each element of the array along the u- axis,

$$k_{pu} = k_u^i + \frac{2\pi}{D_u} p \tag{2.3-19}$$

Using the same outlined procedure, the function $g(v)$ can also be derived, being its expression,

$$g(v) = \sum_{q=-\infty}^{+\infty} a'' e^{-jk_{qv}v} \tag{2.3-20}$$

where k_{qv} is the phase displacement for each Floquet harmonic at each element of the array along the v- axis,

$$k_{qv} = k_v^i + \frac{2\pi}{D_v} q \tag{2.3-21}$$

where k_v^i is the wavenumber of the incident plane wave along the v axis. Hence, the modal field solution of the vector wave equation for a 2-D periodic array has the form,

$$\phi_{pq}(u,v,z) = e^{-j\left(k_{pu}u + k_{qv}v\right)} e^{-j\beta_{pq}z} \tag{2.3-22}$$

and the eigenvalues are,

$$k_{pq} = \sqrt{{k_{pu}}^2 + {k_{qv}}^2} \tag{2.3-23}$$

Any component of the electric and magnetic field can be expressed in terms of a Fourier series of the form of Eq. (2.3-24)

$$E_{pq}(u,v,z) = \sum_{pq} a_{pq} e^{-j(k_u u + k_n v)} e^{-j\left(k_u^i u + k_v^i v\right)} e^{-j\beta_{pq}z} \tag{2.3-24}$$

where $k_u = \frac{2\pi p}{D_u}$ and $k_v = \frac{2\pi q}{D_v}$ represents the unique wavenumbers along the direction of periodicity *u* and *v*.

2.3.3 Grating Lobes

Grating lobes are undesired secondary beams which appear at certain angles as a result of higher order constructive interference when the size of the unit cell becomes electrically large. The physical understanding of grating lobes is fundamental for the analysis of planar periodic surfaces. Consider a plane wave incident upon the 1-D structure shown in Fig. 2-6 with interspacing between the patches D_y. Referring to the angle of incidence by θ it is clear that the excitation phase of an individual element will be delayed by a factor $\beta \cdot D_y \cdot \sin\theta$ with respect to the element located immediately to the left. At the same time, the reflected/transmitted phase of the same element will be ahead by the same amount with respect to the element located immediately to the left; hence the total reflected/transmitted field by the array at a certain direction, θ, is the superposition of the reflected/transmitted waves from all the elements since at this direction the waves will always be in phase. Now, it is possible that at other directions propagation takes place.

In section 2.3.2 it was presented that in periodic surfaces each excited Space Floquet Harmonic has a distinct wavenumber, β_p, and therefore phase velocity. A higher order FSH can therefore be propagating provided that its transverse propagation constant, β_p (k_y), is smaller than that of free-space, β_o. In other words, the transverse wavenumber of the p FSH is,

$$k_y = k_o \sin\theta + p\frac{2\pi}{D_y} \tag{2.3-25}$$

Grating lobe will appear when, $k > k_y \Rightarrow k_o \sin\theta_g > k_o \sin\theta + p\frac{2\pi}{D_y}$

$$\theta_g = a\sin\left(\sin\theta + p\frac{2\pi}{k_o D_y}\right) \tag{2.3-26}$$

where θ_g is the angle of the grating lobe. From Eq. (2.3-26) it can be observed that the first FSH able to propagate is the -1FSH. Moreover, from 2.3-26 it can be seen that grating lobes mainly depend on the periodicity and the angle of incidence. The maximum size of the unit cell to avoid grating lobes should obey the same rule as conventional antenna arrays [19]. Generally, in order to avoid grating lobes the size of the unit cell must be smaller than a wavelength for normal incidence (θ=0º). For other

values of the angle of incidence the periodicity must be lower than half-wavelength in free-space.

By simple work on Eq. 2.3-26 the frequency where the grating lobe appears can be readily obtained,

$$f_g = \frac{c}{\lambda_g} = \frac{pc}{D_y\left(\sin\theta + \sin\theta_g\right)} \tag{2.3-27}$$

2.4 Analysis Technique for 2-D Periodic Surfaces: Method of Moment Formulation

The modelling technique employed in this work for the analysis of 2-D periodic surfaces is based on formulating the EFIE and subsequently solving it by using the MoM [13]. In order to present the technique, here we employ an example involving two layers of 2-D dipole array embedded in a grounded dielectric substrate. Commencing with an example the structure depicted in Fig. 2-7, the EFIE is derived and subsequently solved by using periodic spectral domain MoM. The currents excited on the elements and the reflection and transmission coefficient are obtained. Subsequently, the expressions of the electric and magnetic near-field are derived.

2.4.1 Vector Field TE and TM modes for rectangular geometry lattice

Allowing for a rectangular lattice distribution of the elements that composed the array, the translation vectors of (2.3-1) take the form,

$$\vec{D}_u = D_x\hat{x} \tag{2.4-1}$$

$$\vec{D}_v = D_y\hat{y} \tag{2.4-2}$$

In the following Eq. 2.3-24 is expressed in the common cartesian coordinates. Initially, the rotational transformation of *(u,v)* onto *(x,y)* is considered which allows to express

any component of the electric field in terms of a Fourier series in the rectangular coordinate,

$$E_{pq}(x,y,z) = e^{-j\frac{2\pi}{\sin\alpha}\left(\frac{p}{D_u}\sin\alpha_2 - \frac{q}{D_v}\sin\alpha_1\right)\cdot x} \cdot e^{j\frac{2\pi}{\sin\alpha}\left(-\frac{p}{D_u}\cos\alpha_2 + \frac{q}{D_v}\cos\alpha_1\right)\cdot y}$$
$$\cdot e^{-j\left(k_x^i x + k_y^i y\right)} \cdot e^{-j\beta_{pq} z} = e^{-j\frac{2\pi p}{D_x}x} e^{-j\frac{2\pi q}{D_y}y} e^{-j\left(k_x^i x + k_y^i y\right)} e^{-j\beta_{pq} z} \tag{2.4-3}$$

when α_1=0 and α=α_2=90º. The phase displacement along the rotated coordinate system expressed in terms of the cartesian coordinate system can be denoted as,

$$\vec{k}_{x_1} = -\frac{2\pi}{A}\hat{z}\times D_v = \frac{2\pi}{A}D_v\left(\sin\alpha_2\hat{x} - \cos\alpha_2\hat{y}\right) = \frac{2\pi}{D_u\sin\alpha}\left(\sin\alpha_2\hat{x} - \cos\alpha_2\hat{y}\right) = \frac{2\pi}{D_x}\hat{x}$$
$$\vec{k}_{y_1} = -\frac{2\pi}{A}\hat{z}\times D_u = \frac{2\pi}{A}D_u\left(-\sin\alpha_1\hat{x} + \cos\alpha_1\hat{y}\right) = \frac{2\pi}{D_v\sin\alpha}\left(-\sin\alpha_1\hat{x} + \cos\alpha_1\hat{y}\right) = \frac{2\pi}{D_y}\hat{y} \tag{2.4-4}$$

The term A represents the area of the Unit Cell whose value is $\left|\vec{D}_u \times \vec{D}_v\right|$

$$A = \left|\vec{D}_u \times \vec{D}_v\right| = D_u D_v \cos\alpha_1 \sin\alpha_2 - D_u D_v \sin\alpha_1 \cos\alpha_2 =$$
$$= D_u D_v \sin(\alpha_2 - \alpha_1) = D_u D_v \sin\alpha = D_x D_y \tag{2.4-5}$$

As it can be observed from Eq. (2.4-3) the wavenumber for each harmonic is formed by the fundamental (e.g. indicent - k_x^i and k_y^i), which in the following will be denoted as $\vec{k}_{t00}$, and that due to periodicity. Therefore, the wavenumber of the 2-D periodic of Fig. 2-7 is,

$$\vec{k}_{tpq} = \vec{k}_{t00} + p\vec{k}_{x1} + q\vec{k}_{y1} = k_x\hat{x} + k_y\hat{y} \tag{2.4-6}$$

Traditional definition of spherical coordinates can be found in Appendix A.1.

$$k_{t00} = k\sin\theta^i\cos\varphi^i\hat{x} + k\sin\theta^i\sin\varphi^i\hat{y} = k_{00x}\hat{x} + k_{00y}\hat{y}$$
$$k = k_0\sqrt{\varepsilon_r} = \frac{2\pi}{\lambda_0}\sqrt{\varepsilon_r} \tag{2.4-7}$$

The subscripts p and q in Eq. (2.4-6) take values from 0 to $\pm$1,$\pm$2,… and the wavenumber referred to the periodic Floquet Harmonics are those represented in (2.4-

5). The solution of the wave equation (2.4-3) for a 2-D periodic array in the Cartesian coordinate system is therefore,

$$E_{pq}(x,y,z) = e^{-jk_x x} e^{-jk_y y} e^{-j\beta_{pq} z} = \psi_{pq}(x,y) e^{-j\beta_{pq} z} \tag{2.4-7}$$

where $\psi_{pq}(x,y)$represents the Floquet's phasors and where β_{pq} is the z-component of the propagation vector defined as:

$$\beta_{pq} = \left(\varepsilon_r k_0^2 - k_x^2 - k_y^2\right)^{1/2} \tag{2.4-8}$$

The Floquet phasors $\psi_{pq}(x,y)$ are orthogonal between them over the array's unit cell. In the vector space the inner product notation can be utilised which yields,

$$\left\langle \psi_{pq}, \psi_{\ln} \right\rangle_A = \iint\limits_{\substack{Unit \\ Cell}} \psi_{pq} \cdot \psi_{\ln}^* dxdy = A\delta_{pl}\delta_{qn} = \begin{cases} A & p = l \quad q = n \\ 0 & otherwise \end{cases} \tag{2.4-9}$$

Once the set of solutions of the wave equation are determined in the rectangular coordinate system, it only remains to seek the solutions of higher order modes (other than traverse electromagnetic) which are also solutions of the wave equation and which will determine the electromagnetic field configuration. The TE and TM modes propagate along $\hat{z}$ -axis with a propagation constant γ_{mn} which is,

$$\gamma_{mn} = \begin{cases} \sqrt{k_{mn}{}^2 - k^2} & k < k_{mn} \quad \text{Evanescent mode} \\ \sqrt{k^2 - k_{mn}{}^2} & k > k_{mn} \quad \text{Propagating mode} \end{cases} \tag{2.4-10}$$

TM_z Case *(H_z =0)*

The magnetic vector is parallel to the plane of the array, H_z=0. The longitudinal component of the electric field obtained by solution of the vector wave equation takes the form of Eq. (2.4-11). The transverse component of electric and magnetic field are calculated according to [18] as in (2.4-12) and (2.4-13),

$$E_{z\,pq} = \frac{k_{tpq}}{\beta_{pq}} \Psi_{pq}(x,y) \tag{2.4-11}$$

$$\overline{E}_{t\,pq} = -j \frac{\beta_{pq}}{k_{tpq}^2} \nabla_t E_{z\,pq} = \frac{k_x \hat{x} + k_y \hat{y}}{k_{tpq}} \Psi_{pq}(x,y) \tag{2.4-12}$$

where $\frac{k_x\hat{x}+k_y\hat{y}}{k_{tpq}}$ is the unitary vector of TM modes named $\bar{\kappa}_{1pq}$. Likewise, the transverse magnetic components,

$$\begin{aligned}\overline{H}_{t\,pq} &= -j\frac{w\varepsilon}{k_{tpq}^2}\hat{z}\times\nabla_t E_{z\,pq} \\ &= \frac{w\varepsilon}{\beta_{pq}}\hat{z}\times\frac{k_x\hat{x}+k_y\hat{y}}{k_{tpq}}\Psi_{pq}(x,y)=\frac{k\eta}{\beta_{pq}}\Psi_{pq}(x,y)\frac{-k_y\hat{x}+k_x\hat{y}}{k_{tpq}}\end{aligned} \tag{2.4-13}$$

where η is the free-space admittance, which value is $\eta=\sqrt{\frac{\varepsilon}{\mu}}$ and the term $\frac{k\eta}{\beta_{pq}}$ represents the TM modal admittance η_{1pq}.

TE$_z$ Case *(E_z=0)*

The same procedure can be followed to study the Transverse Electric modes. In this case the electric vector is parallel to the plane of the array, E_z=0. The transverse components of the electric and magnetic field can be derived from the longitudinal component of the magnetic field H_z which takes the form [18],

$$H_{z\,pq}=\frac{\eta k_{tpq}}{k}\Psi_{pq}(x,y) \tag{2.4-14}$$

According to [18] the transverse electric and magnetic field components are as in (2.4-15) and (2.4-16),

$$\overline{E}_{t\,pq}=-j\frac{w\mu}{k_{tpq}^2}\hat{z}\times\nabla_t H_{z\,pq}=\frac{-k_y\hat{x}+k_x\hat{y}}{k_{tpq}}\Psi_{pq}(x,y) \tag{2.4-15}$$

where $\frac{-k_y\hat{x}+k_x\hat{y}}{k_{tpq}}$ is the unitary vector of TE modes named $\bar{\kappa}_{2pq}$. In the same fashion, the transverse magnetic components are calculated as,

$$\overline{H}_{t\,pq}=-j\frac{\beta_{pq}}{k_{tpq}^2}\nabla_t H_{z\,pq}=\frac{\beta_{pq}\eta}{k}\cdot\frac{k_x\hat{x}+k_y\hat{y}}{k_{tpq}}\Psi_{pq}(x,y) \tag{2.4-16}$$

where the term $\frac{\beta_{pq}\eta}{k}$ represents the TE modal admittance η_{2pq}. From the expressions of $\bar{\kappa}_{1pq}$ and $\bar{\kappa}_{2pq}$ one can see that both are orthogonal.

The field expansion tangential to the array can now be written in a compact form in terms of the Floquet modes for TM and TE components.

$$\begin{aligned}\bar{E}(\bar{r},z) &= \sum_{pq} a_{1pq}\Psi(x,y)e^{-j\beta_{pq}z}\bar{\kappa}_{1pq} + \sum_{pq} a_{2pq}\Psi(x,y)e^{-j\beta_{pq}z}\bar{\kappa}_{2pq} \\ &= \sum_{mpq} a_{mpq}\Psi(x,y)e^{-j\beta_{pq}z}\bar{\kappa}_{mpq}\end{aligned} \tag{2.4-17}$$

$$\bar{H}(\bar{r},z) = -\sum_{mpq}\eta_{mpq}a_{mpq}\Psi(x,y)e^{-j\beta_{pq}z}\hat{z}\times\bar{\kappa}_{mpq}$$

The different modes are represented by the index *m*, so that m=1 is the Transverse Magnetic Mode and m=2 is the Transverse Electric Mode.

2.4.2 Theoretical field analysis of 2 layer FSS embedded in a grounded dielectric surface structure

The electric and magnetic field expressed as vector Floquet modes for TE and TM components have been presented. In the following these expressions will be used in conjunction with the boundary conditions of the specific problem in order to derive the currents excited on the elements as well as the fields near the surface. As an example, two layers of an array of metal dipoles embedded in a grounded dielectric media is presented, the cross-section of the structure is shown in Fig. 2-7.

The surface is excited by a plane wave incident as previously explained in section 2.2.3. The incident electric and magnetic field are represented as in 2.4-18 where T^{inc}_{m00} is the amplitude of the incident wave,

$$\vec{E}_{inc}(\vec{r},z) = \sum_{m=1}^{2} T^{inc}_{m00}e^{-j\beta^0_{00}z}\psi_{00}(\vec{r})\bar{\kappa}_{m00} \tag{2.4-18}$$

$$\vec{H}_{inc}(\vec{r},z)=\sum_{m=1}^{2}\eta_{m00}^{0}T_{m00}^{inc}e^{-j\beta_{00}^{0}z}\psi_{00}(\vec{r})\vec{z}\times\vec{\kappa}_{m00}$$

The fundamental mode or the lowest mode is that whose p and q are equal to 0. This fundamental mode is in fact a plane wave as it can be observed by substitution of the indexes p and q in 2.4-6. Indeed, when p and q equal 0 the direction of propagation according to 2.4-6 becomes equal to the direction of the incident field (forward scattering) and the specular reflected field. These directions will always be present in any periodic surface. Assuming no grating lobes, higher values of p and q will produce imaginary values of the propagation constant corresponding to waves being attenuated as the observation point moves away from the array. These waves are called *evanescent waves* (2.4-10) and while their magnitude are insignificant compared to the propagating modes as the observation points move away from the array they are strong and extremely important close to the array. They represent electromagnetic energy stored around the elements.

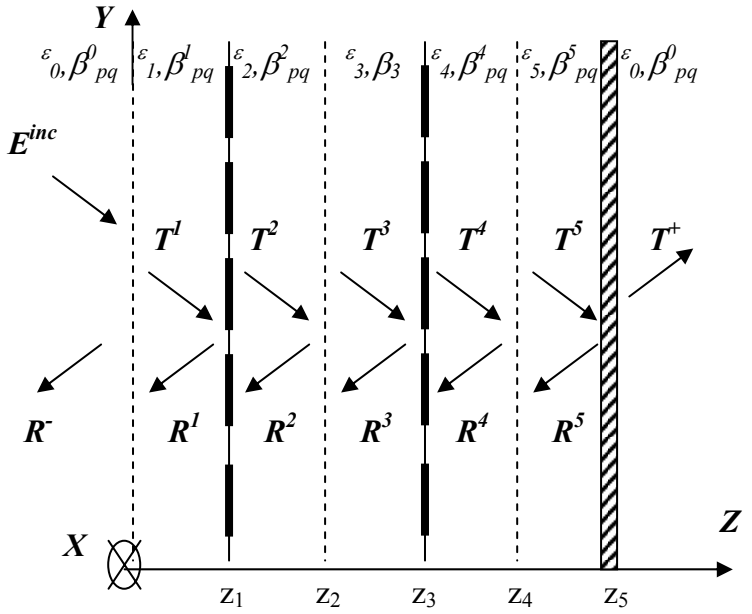

Figure 2-7 Cross section of dipole array embedded in dielectrics and sketch of incident, transmitted and reflected waves in each interface (T^+ only will be considered when there is no ground plane otherwise $T^+=0$).

Next, starting from the diagram showed in Fig. 2-7 which represents qualitatively the reflected and transmitted fields at each region, the electric and magnetic field expressions can be written. A summary of these expressions is collected in table 2-2.

TABLE 2-2
TANGENTIAL ELECTRIC AND MAGNETIC FIELD EXPRESSIONS FOR THE DIFFERENT MEDIA OF FIG. 2-7

REGION (n)	*ELECTRIC/MAGNETIC FIELD*
0 (z<0)	$\overline{E}^{-}(x,y,z)=\sum_{mpq}\overline{E}^{inc}+R^{-}_{mpq}e^{j\beta^{0}_{pq}z}e^{-j\bar{k}_{tpq}(x\hat{x}+y\hat{y})}\overline{\kappa}_{mpq}$ $\overline{H}^{-}(x,y,z)=\sum_{mpq}\overline{H}^{inc}-\eta^{0}_{mpq}R^{-}_{mpq}e^{j\beta^{0}_{pq}z}e^{-j\bar{k}_{tpq}(x\hat{x}+y\hat{y})}\hat{z}\times\overline{\kappa}_{mpq}$
1(0<z<z_1) *2 (z_1<z<z_2)* *3 (z_2<z<z_3)* *4 (z_3<z<z_4)* *5 (z_4<z<z_5)*	$\overline{E}^{n}(x,y,z)=\sum_{mpq}\left(T^{n}_{mpq}e^{-j\beta^{n}_{pq}z}+R^{n}_{mpq}e^{j\beta^{n}_{pq}z}\right)e^{-j\bar{k}_{tpq}(x\hat{x}+y\hat{y})}\overline{\kappa}_{mpq}$ $\overline{H}^{n}(x,y,z)=\sum_{mpq}\eta^{n}_{mpq}\left(T^{n}_{mpq}e^{-j\beta^{n}_{pq}z}+R^{n}_{mpq}e^{j\beta^{n}_{pq}z}\right)e^{-j\bar{k}_{tpq}(x\hat{x}+y\hat{y})}\hat{z}\times\overline{\kappa}_{mpq}$
(if no ground plane) *6 (z_5<z)*	$\vec{E}^{+}(\vec{r},z)=\sum_{mpq}\left(T^{6}_{mpq}e^{-j\beta^{6}_{pq}z}\right)e^{-j\bar{k}_{tpq}(x\hat{x}+y\hat{y})}\overline{\kappa}_{mpq}$ $\vec{H}^{+}(\vec{r},z)=\sum_{mpq}\eta^{6}_{mpq}\left(T^{6}_{mpq}e^{-j\beta^{6}_{pq}z}\right)e^{-j\bar{k}_{tpq}(x\hat{x}+y\hat{y})}\vec{z}\times\overline{\kappa}_{mpq}$

The incident electric and magnetic field are assumed in (2.4-18). Region 0 concerns free-space. Region n assumes the n^{th} dielectric with thickness z_n-z_{n-1} and relative permittivity ε_n. The propagation constant along this medium for each Floquet mode is β^{n}_{pq}. Region 6 is only considered when no ground plane is placed at $z=z_5$ and it is free-space (permittivity ε_0 and propagation constant for each Floquet mode β^{0}_{pq}) one should note that no reflected wave is considered.

The next step in the analysis is the application of the boundary conditions at each interface in order to match both the electric and magnetic fields, as explained in section 2.2.2. This analysis conveniently commences from the last interface which refers to $z=z_5$ and moves towards successively lower values z_n. The corresponding relationships between the reflected and transmitted field amplitudes in each region can be derived and are summarized in Table 2-3. In Appendix A.2, a more detailed description of the derivation of the fields is provided.

TABLE 2-3
REFLECTED AND TRANSMITTED FIELD EXPRESSIONS FOR THE DIFFERENT MEDIA OF FIG. 2-7

Interface	*REFLECTED AND TRANSMITTED FIELD AMPLITUDE RELATIONSHIP*
0 (z=0)	$R^{-}_{mpq} = \rho^{0}_{m00} T^{inc}_{m00} \delta_{p0}\delta_{0q} - \frac{\eta^{1}_{mpq}\left(1+\zeta^{1}_{mpq}\right)}{\left(\eta^{0}_{mpq}+\eta^{1}_{mpq}\zeta^{1}_{mpq}\right)}\left(K^{12}_{mpq}\tilde{J}^{2}_{mpq} + K^{1}_{mpq}\tilde{J}^{1}_{mpq}\right)$
1 (z=z1)	$R^{1}_{mpq} = \rho^{1}_{mpq} T^{1}_{mpq} - K^{12}_{mpq}\tilde{J}^{2}_{mpq} - K^{1}_{mpq}\tilde{J}^{1}_{mpq}$
2 (z=z2)	$R^{2}_{mpq} = \rho^{2}_{mpq} T^{2}_{mpq} - K^{2}_{mpq}\tilde{J}^{2}_{mpq}$
3 (z=z3)	$R^{3}_{mpq} = \rho^{3}_{mpq} T^{3}_{mpq} - K^{3}_{mpq}\tilde{J}^{2}_{mpq}$
4 (z=z4)	$R^{4}_{mpq} = \rho^{4}_{mpq} T^{4}_{mpq}$
5 (z=z5)	$R^{5}_{mpq} = \rho^{5}_{mpq} T^{5}_{mpq}$

The expression of the reflection coefficients, ρ^{n}_{mpq}, that appear in table 2-3 are defined in table 2-4. For a complete derivation of these coefficients please review Appendix A.2.

The expressions of the coefficient ζ of table 2-4 are gathered in table 2-5. For a complete derivation of these coefficients please review Appendix A.2.

TABLE 2-4
REFLECTION COEFFICIENTS AT EACH INTERFACE OF FIG. 2-7

Interface (n)	*REFLECTION COEFFCIENT (ρ)*
0 (z=0)	$\rho^{0}_{m00} = \frac{\left(\eta^{0}_{m00} - \eta^{1}_{m00}\zeta^{1}_{m00}\right)}{\left(\eta^{1}_{m00}\zeta^{1}_{m00} + \eta^{0}_{m00}\right)}$
1 (z=z1)	
2 (z=z2)	$\rho^{n}_{mpq} = \frac{\left(\eta^{n}_{mpq} - \eta^{n+1}_{mpq}\zeta^{n+1}_{mpq}\right)}{\left(\eta^{n}_{mpq} + \eta^{n+1}_{mpq}\zeta^{n+1}_{mpq}\right)} e^{-2j\beta^{n}_{pq} z_n}$
3 (z=z3)	
4 (z=z4)	
5 (z=z5)	$\rho^{5}_{mpq} = -e^{-2j\beta^{5}_{pq} z_5}$

TABLE 2-5

COEFFICIENT ζ AT EACH INTERFACE OF FIG. 2-7

Interface	*COEFFICIENT ζ*
0 (z=0)	
1 (z=z1)	$\zeta_{mpq}^{n} = \dfrac{e^{-j\beta_{pq}^{n} z_{n-1}} - \rho_{mpq}^{n} e^{j\beta_{pq}^{n} z_{n-1}}}{e^{-j\beta_{pq}^{n} z_{n-1}} + \rho_{mpq}^{n} e^{j\beta_{pq}^{n} z_{n-1}}}$
2 (z=z2)	
3 (z=z3)	
4 (z=z4)	
5 (z=z5)	$\zeta_{mpq}^{6} = 0$

Finally, the coefficients of the current that appear in the expressions of table 2-3 are defined in table 2-6. For a complete derivation of these coefficients please review Appendix A.2.

TABLE 2-6

CURRENT COEFFICIENTS OF FSS1 AND FSS2 AT EACH INTERFACE OF FIG. 2-7

REGION	*CURRENT COEFFICIENT K*
Interface 1 – z=0	---
Interface 2 – z=z1	$K_{mpq}^{12} = \dfrac{\left(1+\zeta_{mpq}^{2}\right)\eta_{mpq}^{2} e^{j\left(\beta_{pq}^{2}-\beta_{pq}^{1}\right)z_1}}{\left(\eta_{mpq}^{1}+\eta_{mpq}^{2}\zeta_{mpq}^{2}\right)} K_{mpq}^{2} \quad FSS_2$
	$K_{mpq}^{1} = \dfrac{1}{\left(\eta_{mpq}^{1}+\eta_{mpq}^{2}\zeta_{mpq}^{2}\right)} e^{-j\beta_{pq}^{1} z_1} \quad FSS_1$
Interface 3 – z=z2	$K_{mpq}^{2} = \dfrac{\left(1+\zeta_{mpq}^{3}\right)}{\left(\eta_{mpq}^{2}+\eta_{mpq}^{3}\zeta_{mpq}^{3}\right)} \eta_{mpq}^{3} K_{mpq}^{3} e^{j\left(\beta_{pq}^{3}-\beta_{pq}^{2}\right)z_2} \quad FSS_2$
Interface 4 – z=z3	$K_{mpq}^{3} = \dfrac{\tilde{J}_{mpq}^{2}}{A_2\left(\eta_{mpq}^{3}+\eta_{mpq}^{4}\zeta_{mpq}^{4}\right)} e^{-j\beta_{pq}^{3} z_3} \quad FSS_2$
Interface 5 – z=z4	---
Interface 6 – z=z5	---

Once the amplitude of the reflected field in region 0 (R^{-}_{mpq}) is obtained in terms of the incident field , T^{inc}_{m00}, and the coefficients of the current, J^{1}_{mpq} and J^{2}_{mpq}. The remaining reflected and transmitted fields can be found algebraically. For instance, the amplitude

of the transmitted field in region 1 (T^{l}_{mpq}) can be expressed in terms of the incidence and the current on both arrays by taking the boundary condition at interface 1(please refer to Appendix A.2 Eq. A.2-39). After some algebra (2.4-19) is obtained,

$$T^1_{mpq} = \frac{\left(1+\rho^0_{m00}\right)T^{inc}_{m00}\delta_{p0}\delta_{0q} - \frac{\eta^1_{mpq}-\eta^0_{mpq}}{\left(\eta^0_{mpq}+\eta^1_{mpq}\zeta^1_{mpq}\right)}\left(K^{12}_{mpq}\tilde{J}^2_{mpq}+K^1_{mpq}\tilde{J}^1_{mpq}\right)}{\left(1+\rho^1_{mpq}\right)} \tag{2.4-19}$$

The amplitude of the reflected field in region 1 by using the relations of table 2-3 is,

$$R^1_{mpq} = \rho^1_{mpq}\frac{\left(1+\rho^0_{m00}\right)T^{inc}_{m00}\delta_{p0}\delta_{0q}}{\left(1+\rho^1_{mpq}\right)} - \left(\frac{\left(\eta^1_{mpq}-\eta^0_{mpq}\right)\rho^1_{mpq}}{\left(\eta^1_{mpq}\zeta^1_{mpq}+\eta^0_{mpq}\right)}+1\right)\left(K^{12}_{mpq}\tilde{J}^2_{mpq}+K^1_{mpq}\tilde{J}^1_{mpq}\right) \tag{2.4-20}$$

The last step to derive the Electric Field Integral Equation is imposing the boundary condition of the electric field being zero on the metallic elements of FSS_1 and FSS_2 and applying the orthogonality of the Floquet phasors. Two coupled Electric Field Integral Equations are readily obtained one for each array,

Frequency Selective Surface 1 (FSS_1) at $z=z_1$

The electric field in region 1 is matched to be zero over the conducting area of FSS1,

$$\bar{E}^1\left(\bar{r},z_1\right)=0 \qquad \bar{r}\in A_1 \tag{2.4-21}$$

$$\sum_{mpq}\left(T^1_{mpq}e^{-j\beta^1_{pq}z_1}+R^1_{mpq}e^{j\beta^1_{pq}z_1}\right)\psi_{pq}\left(\bar{r}\right)\bar{\kappa}_{mpq}=0$$

$$\sum_{mpq}\left(T^1_{mpq}e^{-j\beta^1_{pq}z_1}+\left(\rho^1_{mpq}T^1_{mpq}-K^{12}_{mpq}\tilde{J}^2_{mpq}-K^1_{mpq}\tilde{J}^1_{mpq}\right)e^{j\beta^1_{pq}z_1}\right)\psi_{pq}\left(\bar{r}\right)\bar{\kappa}_{mpq}=0$$

$$\sum_{mpq}\left(e^{-j\beta^1_{pq}z_1}+\rho^1_{mpq}e^{j\beta^1_{pq}z_1}\right)T^1_{mpq}\psi_{pq}\left(\bar{r}\right)\bar{\kappa}_{mpq}=$$

$$\sum_{mpq}\left(K^{12}_{mpq}\tilde{J}^2_{mpq}+K^1_{mpq}\tilde{J}^1_{mpq}\right)e^{j\beta^1_{pq}z_1}\psi_{pq}\left(\bar{r}\right)\bar{\kappa}_{mpq} \tag{2.4-22}$$

Substitution of (2.4-19) in (2.4-22) yields the first Electric Field Integral Equation $EFIE_1$,

$$\sum_{mpq}\left(e^{-j\beta^1_{mpq}z_1}+\rho^1_{mpq}e^{j\beta^1_{mpq}z_1}\right)\left(\frac{\left(1+\rho^0_{m00}\right)T^{inc}_{m00}\delta_{p0}\delta_{0q}}{\left(1+\rho^1_{mpq}\right)}\right)\psi_{00}(\bar{r})\bar{\kappa}_{m00}$$
$$=\sum_{mpq}\left(\frac{\left(\eta^1_{mpq}-\eta^0_{mpq}\right)}{\left(\eta^1_{mpq}\zeta^1_{mpq}+\eta^0_{mpq}\right)}\cdot\frac{\left(e^{-j\beta^1_{mpq}z_1}+\rho^1_{mpq}e^{j\beta^1_{mpq}z_1}\right)}{\left(1+\rho^1_{mpq}\right)}+e^{j\beta^1_{mpq}z_1}\right)\cdot \tag{2.4-23}$$
$$\left(K^{12}_{mpq}\tilde{J}^2_{mpq}+K^1_{mpq}\tilde{J}^1_{mpq}\right)\psi_{pq}(\bar{r})\bar{\kappa}_{mpq}$$

Where the only unknowns are the currents excited on both FSSs.

Eq. (2.4-19) and (2.4-20) allows to express the R and T coefficients as functions of the incident field, $T^{inc}{}_{m00}$, and the coefficients of the current, $J^1{}_{mpq}$ and $J^2{}_{mpq}$. These coefficients are gathered in table 2-7

TABLE 2-7
REFLECTED AND TRANSMITTED FIELDS IN TERMS OF THE FIELDS IN REGION 1

REGION (n)	***ELECTRIC/MAGNETIC FIELD AMPLITUDE***
2 ($z_1<z<z_2$)	$R^2_{mpq}=\rho^2_{mpq}\dfrac{T^1_{mpq}e^{-j\beta^1_{pq}z_1}+R^1_{mpq}e^{j\beta^1_{pq}z_1}}{\left(e^{-j\beta^2_{pq}z_1}+\rho^2_{mpq}e^{j\beta^2_{pq}z_1}\right)}$
	$T^2_{mpq}=\dfrac{T^1_{mpq}e^{-j\beta^1_{pq}z_1}+R^1_{mpq}e^{j\beta^1_{pq}z_1}}{\left(e^{-j\beta^2_{pq}z_1}+\rho^2_{mpq}e^{j\beta^2_{pq}z_1}\right)}$
3 ($z_2<z<z_3$)	$R^n_{mpq}=\rho^n_{mpq}\dfrac{\left(e^{-j\beta^{n-1}_{pq}z_{n-1}}+\rho^{n-1}_{mpq}e^{j\beta^{n-1}_{pq}z_{n-1}}\right)}{\left(e^{-j\beta^n_{pq}z_{n-1}}+\rho^n_{mpq}e^{j\beta^n_{pq}z_{n-1}}\right)}T^{n-1}_{mpq}$
4 ($z_3<z<z_4$)	
5 ($z_4<z<z_5$)	$T^n_{mpq}=\dfrac{\left(e^{-j\beta^{n-1}_{pq}z_{n-1}}+\rho^{n-1}_{mpq}e^{j\beta^{n-1}_{pq}z_{n-1}}\right)}{\left(e^{-j\beta^n_{pq}z_{n-1}}+\rho^n_{mpq}e^{j\beta^n_{pq}z_{n-1}}\right)}T^{n-1}_{mpq}$

Now that all the reflection and transmission fields are known in terms of the incident field , $T^{inc}{}_{m00}$, and the coefficients of the current, $J^1{}_{mpq}$ and $J^2{}_{mpq}$, the second Electric Field Integral Equation is derived,

Frequency Selective Surface 2 (FSS$_2$) at $z=z_3$

The electric field in region 3 is matched to be zero over the conducting area of FSS2,

$$\bar{E}^3(\bar{r}, z_3) = 0 \qquad \bar{r} \in A_2 \tag{2.4-24}$$

$$\sum_{mpq}\left(T^3_{mpq} e^{-j\beta^3_{pq} z_3} + R^3_{mpq} e^{j\beta^3_{pq} z_3} \right) \psi_{pq}(\bar{r}) \bar{\kappa}_{mpq} = 0$$

$$\sum_{mpq}\left(T^3_{mpq} e^{-j\beta^3_{pq} z_3} + \left(\rho^3_{mpq} T^3_{mpq} - K^3_{mpq} \tilde{J}^2_{mpq} \right) e^{j\beta^3_{pq} z_3} \right) \psi_{pq}(\bar{r}) \bar{\kappa}_{mpq} = 0$$

$$\sum_{mpq}\left(e^{-j\beta^3_{pq} z_3} + \rho^3_{mpq} e^{j\beta^3_{pq} z_3} \right) T^3_{mpq} \psi_{pq}(\bar{r}) \bar{\kappa}_{mpq} =$$

$$\sum_{mpq}\left(K^3_{mpq} \tilde{J}^2_{mpq} \right) e^{j\beta^3_{pq} z_3} \psi_{pq}(\bar{r}) \bar{\kappa}_{mpq} \tag{2.4-25}$$

Defining the coefficient ξ as,

$$\xi^n_{mpq} = \frac{e^{-j\beta^{n-1}_{pq} z_{n-1}} + \rho^{n-1}_{mpq} e^{j\beta^{n-1}_{pq} z_{n-1}}}{\left(e^{-j\beta^n_{pq} z_{n-1}} + \rho^n_{mpq} e^{j\beta^n_{pq} z_{n-1}} \right)} \tag{2.4-26}$$

and taking coefficient T^3_{mpq} from Table 2-7, Eq. (2.4-25) yields the second Electric Field Integral Equation *EFIE$_2$* after some algebra,

$$\sum_{mpq}\left(e^{-j\beta^3_{pq} z_3} + \rho^3_{mpq} e^{j\beta^3_{pq} z_3} \right) \xi^3_{mpq} \xi^2_{mpq} \left(\frac{\left(1 + \rho^0_{m00}\right) I^{inc}_{m00} \delta_{p0} \delta_{0q}}{\left(1 + \rho^1_{mpq}\right)} \right) \psi_{00}(\bar{r}) \bar{\kappa}_{m00} =$$

$$\sum_{mpq} \xi^3_{mpq} \left(\xi^2_{mpq} \frac{\left(\eta^1_{mpq} - \eta^0_{mpq}\right)}{\left(\eta^1_{mpq} \zeta^1_{mpq} + \eta^0_{mpq}\right)} - \frac{1}{e^{-j\beta^2_{pq} z_1} + \rho^2_{mpq} e^{-j\beta^2_{pq} z_1}} \right)$$

$$\left(K^{12}_{mpq} \tilde{J}^2_{mpq} + K^1_{mpq} \tilde{J}^1_{mpq} \right) + \left(K^3_{mpq} \tilde{J}^2_{mpq} \right) e^{j\beta^3_{pq} z_3} \psi_{pq}(\bar{r}) \bar{\kappa}_{mpq} \tag{2.4-27}$$

As a final step the currents are calculated using Method of Moments. Once the currents are obtained the near fields excited in the structure of Fig. 2.7 can be calculated by simple substitution in the set of Equations that describe the near fields, table 2-2.

2.4.2.a Method of Moments, derivation of the currents

The currents excited in both FSSs are the unknowns in the electric field integral equations, which can be solved using MoM. Applying MoM allows us to expand the currents as a summation of a series of functions which after some manipulations allow us to express the EFIE in a matrix form (2.4-28). An overview of this method is presented in Appendix A.3. The matrix form of the EFIE takes the form,

$$[Z_{in}][c_n]=\left[\widetilde{E}^1\right] \tag{2.4-28}$$

Taking for instance $EFIE_1$, $\widetilde{E}^1$ represents the LHS of the $EFIE_1$ and Z_{in} is described as,

$$Z^1_{in}=\sum_{mpq}\left(\frac{\left(\eta^1_{mpq}-\eta^0_{mpq}\right)}{\left(\eta^1_{mpq}\zeta^1_{mpq}+\eta^0_{mpq}\right)}\cdot\frac{\left(e^{-j\beta^1_{mpq}z_1}+\rho^1_{mpq}e^{j\beta^1_{mpq}z_1}\right)}{\left(1+\rho^1_{mpq}\right)}+e^{j\beta^1_{mpq}z_1}\right)$$
$$K^1_{mpq}\widetilde{h}_i^{1^*}\left(\bar{k}_{tpq}\right)\widetilde{h}^1_n\left(\bar{k}_{tpq}\right)$$
$$Z^2_{in\,in}=\sum_{mpq}\left(\frac{\left(\eta^1_{mpq}-\eta^0_{mpq}\right)}{\left(\eta^1_{mpq}\zeta^1_{mpq}+\eta^0_{mpq}\right)}\cdot\frac{\left(e^{-j\beta^1_{mpq}z_1}+\rho^1_{mpq}e^{j\beta^1_{mpq}z_1}\right)}{\left(1+\rho^1_{mpq}\right)}+e^{j\beta^1_{mpq}z_1}\right)$$
$$K^{12}_{mpq}\widetilde{h}_i^{2^*}\left(\bar{k}_{tpq}\right)\widetilde{h}^2_n\left(\bar{k}_{tpq}\right) \tag{2.4-29}$$

where the coefficients $\widetilde{h}_i^*\left(\bar{k}_{tpq}\right)$ and $\widetilde{h}_n\left(\bar{k}_{tpq}\right)$ represent the Floquet transformation of the basis functions and test functions (here we use Galerkin MoM and therefore the test functions are equal to the basis functions) at each array. For more details refer to Appendix A.3.

2.4.2.b Basis Functions

The efficiency in the derivation of an accurate solution of (2.4-28) critically depends upon the choice of the basis functions. Several factors need to be considered in choosing them:

1) The functions must satisfy the edge condition so that the number of basis functions is small and therefore the matrix size is manageable.

2) This functions should be analytically Fourier transformable so they can be easily derive for its substitution in (2.4-29)
3) It must decay reasonably rapidly for large k_{tpq} so that the computational time is viable when calculating the scalar product that appear in (2.4-29)

Currents on the elements that compose the periodic array are typically expressed either by using entire-domain or sub-domain basis functions [6]. The former spans the entire support of the unknown, the metallic element in the unit cell, and are typically tailored for the specific geometry of the region over which the unknown is being expanded. The main advantage of choosing entire domain basis function is that the size of the resulting matrix is usually much smaller than that for the sub-domain functions; however, for arbitrary shape elements suitable entire domain basis functions are not available in general.

The most popular sub-domain basis functions is the roof-top [32-33], which has a triangular or piecewise-linear dependence in the direction of the current and a pulse or stepwise-constant dependence in the orthogonal direction. The number of sub-domain basis functions required to accurately represent the current is usually larger and their Fourier transforms do not decay very rapidly.

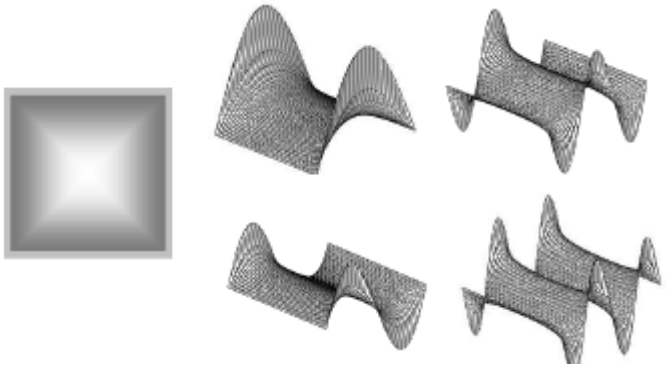

Figure 2-8 Representation of the typical entire domain current functions for a square patch element.

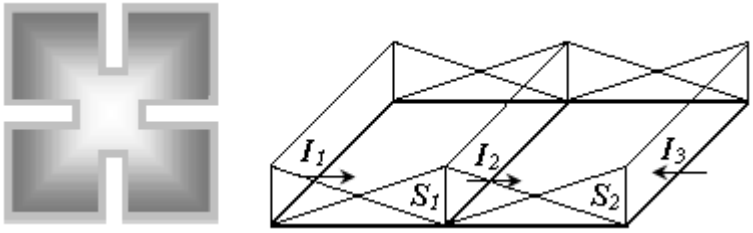

Figure 2-9 1-D Representation of surface current using rooftop basis functions.

As the elements characterised through this work consist of either metallic dipoles or patches the basis functions utilised only involve entire domain basis functions. For the purpose of this example let us assume dipoles as the perfect conductor elements on the array. The current distribution on a dipole can be considered a zero ended sinusoidal or cosinusoidal functions at the ends of the length of the dipole and no variation along the width. The basis functions in this case are,

$$\begin{aligned} h_n^c &= \sqrt{\frac{2}{WL}}\cos\left(\frac{n\pi}{L}y\right) \quad n=1,3,5 \\ h_n^s &= \sqrt{\frac{2}{WL}}\sin\left(\frac{n\pi}{L}y\right) \quad n=2,4 \end{aligned} \tag{2.4-30}$$

In the developed code, 5 basis functions are considered to model the elements. Thus, n=1,2,3,4,5.

The Floquet transformation of these currents is,

$$\begin{aligned} \tilde{h}_n^c &= \iint_A \bar{h}_n^c(\bar{r})\psi_{pq}^*(\bar{r})dS = \sqrt{\frac{2W}{L}}\frac{\sin\left(k_x\frac{W}{2}\right)}{k_x\frac{W}{2}}\cdot\left\{\frac{\sin\left[\left(\frac{n\pi}{L}-k_y\right)\frac{L}{2}\right]}{\left(\frac{n\pi}{L}-k_y\right)}+\frac{\sin\left[\left(\frac{n\pi}{L}+k_y\right)\frac{L}{2}\right]}{\left(\frac{n\pi}{L}+k_y\right)}\right\}\hat{y} \\ h_n^s &= \iint_A \bar{h}_n^c(\bar{r})\psi_{pq}^*(\bar{r})dS = j\cdot\sqrt{\frac{2W}{L}}\frac{\sin\left(k_x\frac{W}{2}\right)}{k_x\frac{W}{2}}\cdot\left\{\frac{\sin\left[\left(\frac{n\pi}{L}-k_y\right)\frac{L}{2}\right]}{\left(\frac{n\pi}{L}-k_y\right)}-\frac{\sin\left[\left(\frac{n\pi}{L}+k_y\right)\frac{L}{2}\right]}{\left(\frac{n\pi}{L}+k_y\right)}\right\}\hat{y} \end{aligned} \tag{2.4-31}$$

With all these equations the code specific for modelling the structures analysed in this work is developed.

2.5 Summary

This chapter aims to describe the theory and the formulation of the electromagnetic simulator for 2-D periodic structures that was developed during this work. Section 2.2 presents the electromagnetic theory as described by Maxwell's equations as well as the solution of the wave equation for electric and magnetic fields. The description of the boundary conditions for time harmonic electromagnetic fields in the presence of discontinuities is discussed. This section concludes with an explanation of the transverse electromagnetic modes and plane wave excitation of 2-D periodic surfaces.

Section 2.3 briefly describes the different types of periodic surfaces. After an overview on the different periodic surfaces, we focus on 2-D structures and in particular frequency selective surfaces. The section concludes describing the basic of the propagation on infinite periodic array.

Section 2.4 presents the general formulation of the analysis of frequency selective surfaces based on MoM. This method is employed in order to develop full wave analysis of periodic surfaces. An example involving two 2-D periodic surfaces embedded in a grounded dielectric media is presented. The derivation of the fields, the reflected and transmitted coefficients in each region as well as the formulation of the EFIE is provided.

References

[1] B. Munk, and R.J. Lubber, "Reflection properties of two-layer dipole arrays", *IEEE Trans. Antennas Propagat.*, vol. AP-22, pp.766-773, Nov. 1974.

[2] J.P. Montgomery, "Scattering by an infinite periodic array of thin conductors on a dielectric sheet", *IEEE Trans. Antennas Propagat.*, vol. AP-23, no.1, pp.70-75, Jan. 1975.

[3] T. Itoh, "Spectral domain immitance approach for dispersion characteristics of generalized printed transmission lines," *IEEE Trans. Microwave Theory Tech.*, vol. MTT-28, pp.733-736, July. 1980.

[4] C.H. Tsao and R. Mittra, "Spectral-domain analysis of frequency selective surfaces comprised of periodic arrays of cross-dipoles and Jerusalem crosses", *IEEE Trans. Antennas Propagat.*, vol AP-32, no.5, pp. 478-486, May 1984.

[5] W. Changhua, J.A. Encinar, "Efficient computation of generalized scattering matrix for analyzing multilayered periodic structures," *IEEE Trans. Antennas Propag.*, vol.43, no. 11, pp. 1233 – 1242, Nov. 1995.

[6] R. Mittra, C.H. Chan, T. Cwik, "Techniques for analyzing frequency selective surfaces-a review," *Proceedings of the IEEE*, Vol. 76, pp.593- 615, Dec. 1988.

[7] B. Munk, *Frequency Selective Surfaces: Theory and Design*, John Wiley and Sons, 2000.

[8] C. A. Balanis, "Advanced Engineering electromagnetics," New York: John Wiley & Sons Inc, 1989.

[9] M.N.O. Sadiku, "A simple introduction to finite element analysis of electromagnetic problems," *IEEE Trans. Educ.,* vol. 32, no. 2, May 1989, pp. 85–93.

[10] K.S. Yee, "Numerical Solutions of Initial Boundary Value Problems Involving Maxwell's Equations in Isotropic Media", *IEEE Trans. Antennas Propag.*, vol. 14(5), pp. 302-307, May 1966.

[11] A. Monorchio, and R. Mittra, "Time-Domain (FE/FDTD) technique for solving complex electromagnetic problems", *IEEE Microw. and guided waves Lett.*, vol 8, no. 2, pp. 93-95, Feb. 1998.

[12] C. Christopoulos, "The Transmission-Line Modeling Method in Electromagnetics," Morgan & Claypool publishers, 2006.

[13] R.F. Harrington, *Field Computation by Moment Method*, New York, NY: Macmillan, 1968.

[14] R. B. Kieburtz and A. Ishimaru, "Scattering by a periodically apertured conducting screen", *IRE Trans. Antennas Propagat.*, vol. AP-9, no 6, Nov. 1961.

[15] C.C. Chen, "Transmissions through a conducting screen of perforated periodically with apertures," *IEEE Trans. Microwave Theory Tech.*, vol. MTT-18, no.9, pp.627-632, Sep. 1970.

[16] C.C. Chen, "Transmissions of microwaves through perforated flat plates," *IEEE Trans. Microwave Theory Tech.*, vol. MTT-21, no.1, pp.1-6, Jan. 1973.

[17] J.C. Vardaxoglou, Frequency Selective Surfaces Analysis and Design, John Wiley, 1997.

[18] D. M. Pozar, Microwave Engineering, 2nd edition, New York: John Wiley & Sons Inc, 1998.

[19] C. A. Balanis, "Antenna Theory: Analysis and Design," Second edition, New York: John Wiley & Sons Inc, 1997.

[20] G. Goussetis, A. P. Feresidis, and P. Kosmas, "Efficient Analysis, Design, and Filter Applications of EBG Waveguide with Periodic Resonant Loads," *IEEE Trans. Microw. Theory and Tech.*, Vol. 54, No. 11, Nov. 2006.

[21] N. Liu, H. Guo, L. Fu, S. Kaiser, H. Schweizer, and H. Giessen, "Three Dimensional photonic metamaterials at optical frequencies," Nature materials 7, 31-37, 2008.

[22] M. G. Floquet, "Sur les équations différentielles linéaires à coefficients périodiques," Annales scientifiques de l'École Normale Supérieure, pp. 47-88, 1883

[23] R. Ulrich, "Far-infrared properties of metallic mesh and its complementary structure," Infrared Physics, vol. 7, pp.37-55, 1967.

[24] V. D. Agrawal, and F.A. Pelow, "Design of a dischroic Casegrain subreflector," *IEEE Trans. Antennas Propag.,* AP-27, no. 4, pp.466-473, July 1979.

[25] S.W. Lee, "Scattering by dielectric loaded screen," *IEEE Trans. Antennas Propag.,* AP-19, no. 5, pp.656-665, Sep. 1971.

[26] C. J. Larson, "Modified Center Layer Metallic Biplanar Radome Design," Tech. Rept. AFAL-TR-78-28, Ohio State Univ. ElectroScience Lab. Rept. RF 4346-2, Columbus, March 1978.

[27] R.A. Hill, and B. A. Munk, "The Effect of Perturbating a Frequency Selective Surface and its Relation to the Design of a Dual-Band Surface," *IEEE Trans. Antennas and Propagat.*, vol. 44, no. 3, pp. 368-374, Mar. 1996

[28] A.D. Chuprin, E.A. Parker and J.C. Batchelor, "Convoluted double square: single layer FSS with close band spacings," *IEE Elect. Lett.*, Vol. 36, No. 22, pp. 1830-1831, Oct. 2000

[29] J. Romeu, and Y. Rahmat-Samii, "Fractal FSS: A Novel Dual-Band Frequency Selective Surface," *IEEE Trans. Antennas and Propagat.*, Vol. 48, no. 7, pp. 1097-1105, July 2000

[30] G.Q. Luo, W. Hong, H.J. Tang, J.X. Chen, K. Wu, "Dualband frequency-selective surfaces using substrate-integrated waveguide technology," *IET Proc. Microwaves Antenna Propagat.*, Vol. 1, No. 2, pp. 408–413, Jan. 2007.

[31] C. Debus, and P. H. Bolivar, "Frequency Selective Surfaces for High-Sensitivity Terahertz Sensors," *Conference on Lasers and Electro-Optics*, 2007.

[32] A.W. Glisson, and D.R. Wilton, "Simple and efficient numerical methods for problems of electromagnetic radiation and scattering from surfaces," *IEEE Trans. Antennas and Propagat.*, vol. AP-28, no. 5, pp. 593-603, Sep. 1980.

[33] B.J.Rubin, and H.L. Bertoni, "Reflection from a periodically perforated plane using a subsectional current approximation," *IEEE Trans. Antennas and Propagat.*, vol. AP-31, no. 6, pp. 829-836, Nov. 1983.

Chapter 3

Near-Field calculation on Frequency Selective Surfaces. FSS with enhanced Near-Fields.

"Computer power is a supplement, not a substitute of brain power"

Benedikt A. Munk

3.1 Introduction

In this chapter, the technique outlined in chapter 2 is employed in order to examine the reflection and transmission response of different frequency selective surface designs and to study the near-fields excited in the proximity of these structures. In particular, a thorough convergence study related to the calculation of the far and, especially, near fields of different FSS configurations is presented. The motivation behind this work is due to the increased attention that electromagnetic properties of near-fields are currently receiving in the physics and engineering communities [1-6]. Near-fields allow overcoming limits that in the far-field are fundamental. Theoretical and experimental results in the past decade have demonstrated the possibilities to produce artificial magnetism at THz and optical frequencies [1-2], transfer sub-wavelength images [3],

focus electromagnetic waves beyond the diffraction limit [4], and enhance near fields [3-5] for imaging or sensor applications. Moreover, the near-field estimation allows us to calculate the power stored in an FSS at resonance which can be directly used in the calculation of the loaded quality factor of FSS. By finding the loaded quality factor the level of coupling of the FSS to its environment can be readily observed.

Following the description of the near-fields on FSS we propose an FSS structure with multiband response and enhanced near-fields. This property may easily lead to applications such as a near-field chemical or biochemical sensor [6]. The resonant effects as well as the near-fields of the proposed structure, which consists of a perturbed[1] planar periodic array of metal dipoles, is carefully studied in this chapter. The analysis commences with the derivation of the equivalent self impedance of the array and a study of the resonant effects and the excited near-fields upon plane wave illumination. Deriving from this study, it is revealed that as a result of the perturbation, the scattering within a frequency range is dominated by the excitation of the odd mode which is a drastic departure from the unperturbed case. Moreover, it is demonstrated that within this frequency range, very strong currents are excited on the array elements and thus very strong near fields are excited in the vicinity of the array.

Furthermore, by using the aforementioned technique a careful study related to the calculation of the far and near fields is carried out for a number of perturbed array designs. It is demonstrated that an increase in the longitudinal magnetic near-field strength of more than 70 times compared with the incidence can be achieved. The results obtained in this chapter are corroborated with HFSS results to validate the accuracy of the method.

3.2 Near-Field Calculation on Frequency Selective Surfaces

In this section, the calculation of the far as well as near fields upon plane wave incidence by using the software developed in chapter 2 is presented for both a free-

[1] Perturbation here refers to the alteration of the length of every second dipole that composed the array.

standing perturbed planar periodic array of metal dipoles and a grounded double layer 2-D periodic planar array of patches. For each design essential convergence considerations need to be taken into account on the estimation of the far and near-field. The minimum number of Floquet Space Harmonics terms as well as Basis Functions needed to obtain an accurate solution are investigated. This allows for a correct representation of the near-fields which yields an accurate estimation of the power stored and consequently loaded quality factor of an FSS.

3.2.1 Convergence study in the Far- and Near-Field Calculation

According to the Floquet expansion of the fields for a doubly periodic surface, electromagnetic fields can be expressed as a superposition of an infinite set of Floquet Space Harmonics (FSH) with a unique wavenumber along each direction of periodicity as it was discussed in chapter 2. For a 2-D periodicity, FSH are characterized by wavenumbers,

$$k_x = k_{oox} + \frac{2\pi}{D_x} p$$
$$k_y = k_{ooy} + \frac{2\pi}{D_y} q \qquad (3.2\text{-}1)$$

D_x/D_y are the length of the unit cell along x and y respectively and β_o is the wavenumber of the 0 order.

For low frequencies, higher order harmonics ($p, q \neq 0$), represent slow waves in the direction of periodicity, and therefore are evanescent in the direction normal to the plane of the array. Thus, they do not contribute to the far field. However, they need to be taken into account in a rigorous full-wave formulation of the EFIE in the spectral domain. Moreover, in layered configurations of periodic arrays when the distance between the arrays is smaller than half-wavelength, higher order evanescent FSH can increasingly interact and therefore become increasingly important in the calculation of the near fields. Additionally, the interaction becomes more and more significant as the distance between the arrays reduces.

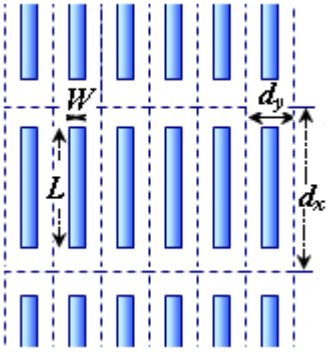

Fig. 3-1 Layout of the free-standing capacitive FSS based on parallel metallic dipoles with dimensions in mm L=7.9, W=0.5, D_x=3.85 and D_y=10.6.

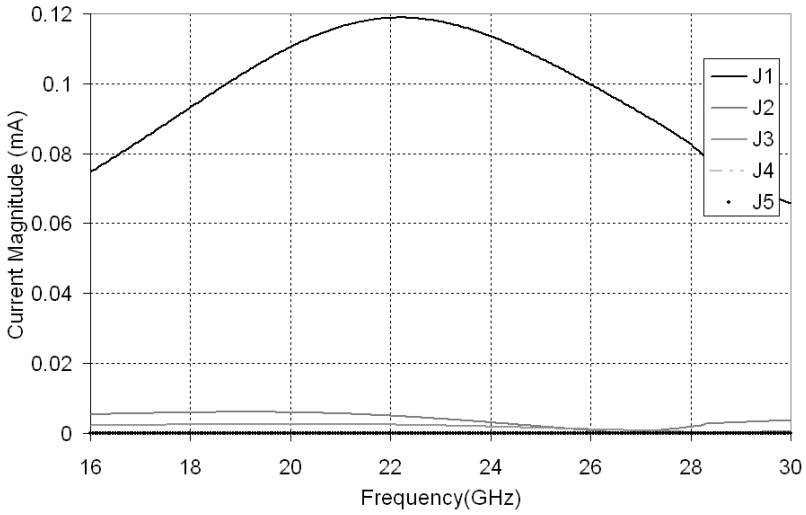

Fig. 3-2 Unknown coefficients {c} that represent the currents used to solve the EFIE by MoM for a free-standing FSS based on parallel metallic dipoles with dimensions in mm L=7.9, W=0.5, D_x=3.85 and D_y=10.6.

3.2.1.a Convergence analysis on a free-standing planar periodic array

Initially the method developed in chapter 2 is employed to model a free-standing array of metallic dipoles, such as the one shown in Fig. 3-1, with dimensions D_x= 3.85 mm, D_y= 10.6mm, L= 7.9mm and W= 0.5m. A convergence study related to the number of basis functions, which better represent the current coefficients, is carried out. This study is shown in Fig.3-2 which shows that 5 basis functions suffice to achieve a very good convergence in the results.

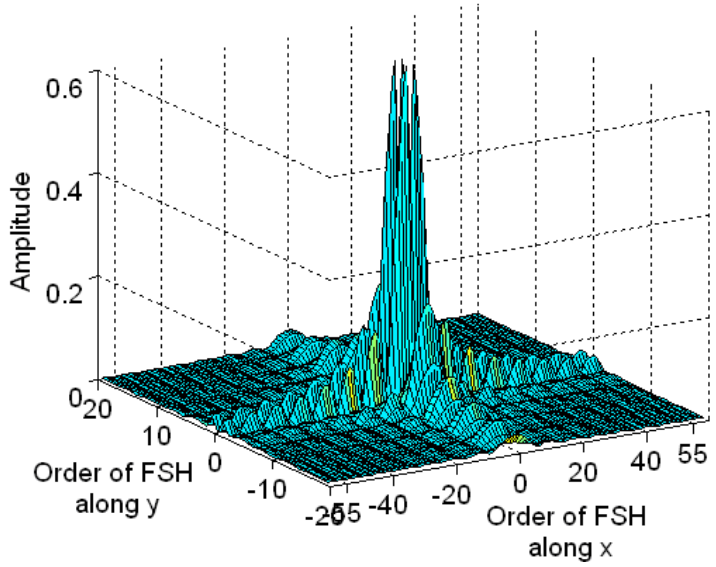

a)

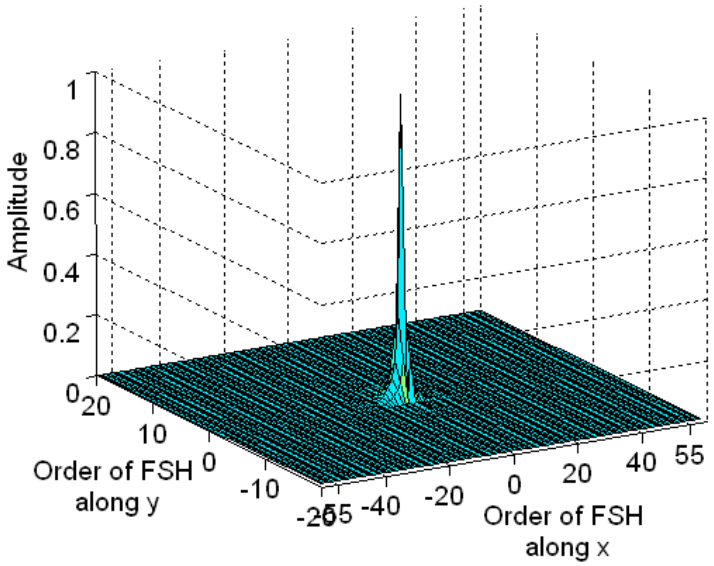

b)

Fig. 3-3 Amplitude (normalised) of the excitation of the fundamental and higher order (a) TM and (b) TE Floquet Space Harmonics (FSH) upon normal plane wave incidence for the perturbed array of Fig. 3-1 at 22.15GHz.

In order to ensure a relative good convergence in the near-field calculation, the relative excitation of TE and TM FSH was calculated and it is shown in Fig. 3-3 at resonance 22.15 GHz. Despite some observed oscillation, lower order harmonics in general are more strongly excited and hence contribute more to the electromagnetics of the scattering. This allows for truncation of the infinite dimensions of the problem to a finite set of space harmonics, which are typically employed to model the transmission and reflection coefficient upon plane wave incidence. This graph is instructive in

determining the number of FSH that need to be considered for calculation of the near fields. For a typical capacitive array, such as the one in Fig. 3-1, 400 FSH (20FSH in x and y direction) suffice to obtain results that have converged with an accuracy of more than 5% in the far-field. This can be seen by observation of Fig.3-4 which shows the transmission coefficient of the structure in Fig. 3-1.

TABLE 3-1 FLOQUET SPACE HARMONICS NEEDED FOR CONVERGENCE IN ORDER TO OBTAIN A SPECIFIC ACCURACY

ACCURACY	Far Field-FSH	Near-Field-FSH			
	TM/TE	TM		TE	
		FSH_x	FSH_y	FSH_x	FSH_y
1%	30	120	60	60	8
5%	20	90	40	40	-
10%	17	70	20	20	-
15%	15	60	10	10	-
20%	10	50	8	8	-

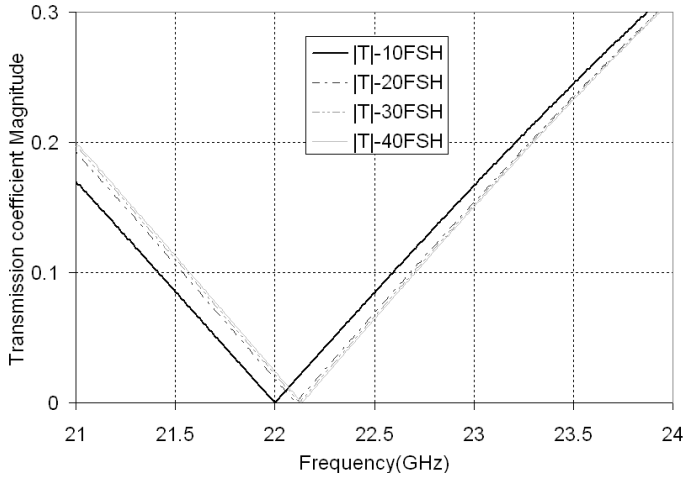

Fig. 3-4 Far field transmission coefficient (magnitude) for the FSS of Fig. 3-1 upon plane wave incidence considering 10, 20, 30 and 40 Floquet Space Harmonics in both x and y directions

In order to calculate the near-fields in the vicinity of the array, contributions by each FSH have to be summed, each weighted according to Fig. 3-3. According to this graph, to account for FSH that contribute up to 5% of the maximum, we need to consider 90FSH in x direction and 40FSH in y direction, to the total of 3600 FSH. This conclusion has been confirmed by our simulations and is shown in Fig. 3-5, where fictitious ripples and reduced amplitudes in the near field distributions were observed if

the same number of FSH that are required for convergence in the far field were employed. The necessary number of FSH in order to obtain a specific accuracy is shown in table 3.1.

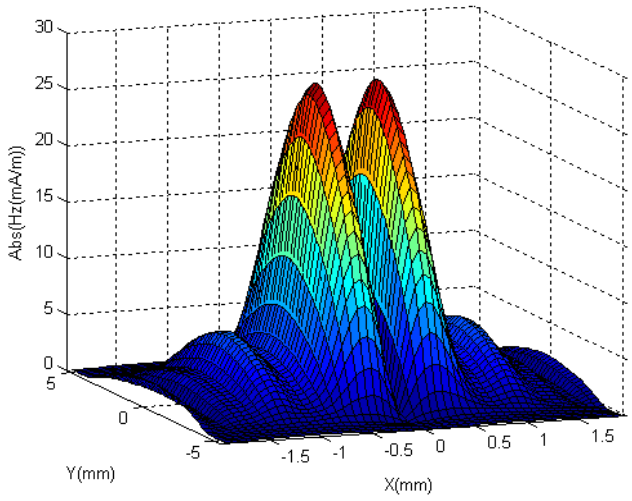

a)

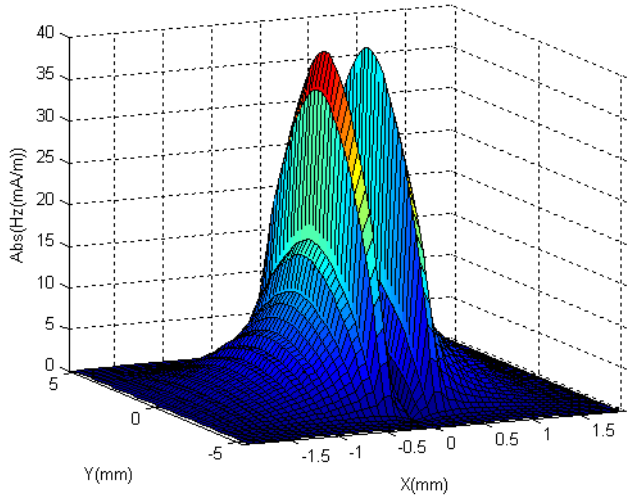

b)

Fig. 3-5 Magnitude of the z-component of the magnetic field in the unit cell of the FSS of Fig. 3-1 at z= 0 for normal plane wave incidence with E_y= 1V/m as calculated using MoM and a) 20 FSH in both x and y directions and b) 40 FSH along y and 90 FSH along x at resonance (f= 22.15GHz).

3.2.1.b Convergence analysis on a grounded double layer 2-D periodic planar array

The convergence study of the near-fields excited in the cavity formed by a grounded two layers of 2-D periodic array of patches is presented here. This section does not aim

to explain the structure (which will be introduced and studied in detail in the next chapter) rather focuses on the convergence of near-field calculation. A careful convergence analysis is necessary due to some features specific to the structure under consideration. In this respect, it is important to mention that the lower array is acting as a High Impedance Surface (HIS) with closely pack elements working far from its resonance. Therefore, it is expected that more basis functions are necessary to accurately weight the {c} coefficients of the current. Moreover, at distances more than a wavelength from the array a limited number of FSH (typically in the order of 20 in each direction for 2-D periodic arrays) is required to predict the interaction of the incoming plane wave with the periodic array. In contrast to that case, here we are interested in the estimation of the fields in the proximity of the periodic array in particular at the middle point of the cavity formed by the two arrays. Evanescent FSH, that describe reactive fields, can contribute significantly to the overall field in the proximity of the array. It is therefore plausible to expect that more FSH are required for the estimation of the fields at distances increasingly close to the periodic arrays.

An example involving a periodic array consisting of patches with edge 8.0 mm and periodicity 9.0 mm printed on a dielectric slab of thickness 1.5 mm and relative permittivity 2.55 is employed. This array is located at a distance h= 5.45 mm (~λ/4 at 14GHz) above another array, which consists of patches with edge 4.15 mm and is printed on a dielectric slab of thickness 1.15mm and relative permittivity 2.2. Fig. 3-6 shows a 3-D view of the structure's layout.

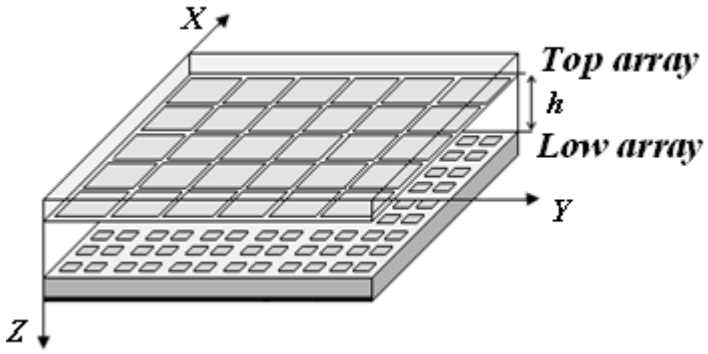

Fig. 3-6 3-D view of a resonant cavity formed by a metamaterial ground plane (low array of patches + ground plane) and a 2-D periodic array of patches (top array) at a distance h.

The first 5 coefficients of the current, {c}in $j = \sum_{i=1}^{n} c_i j_i$ where n=5, that represent the current excited in the HIS patches as well as the first 5 coefficients of the current excited in the patches of the upper array (FSS - no ground plane) are presented in Fig.3-7. The ratio between the fifth order, c_5, and the first order, c_1, current coefficient in the case of the HIS (lower array+ground plane) is about 600 times higher than the ratio between the fifth order, c_5, and first order, c_1, current coefficient of the FSS array. This clearly shows the requirement of including more basis function on the analysis of this kind of structures. From the figure it can be appreciated that for this particular configuration of the array (HIS: array + ground plane) the elements are closely packed and non resonant which make higher order basis functions contribute greatly in the modelling of the current excited on the patch elements.

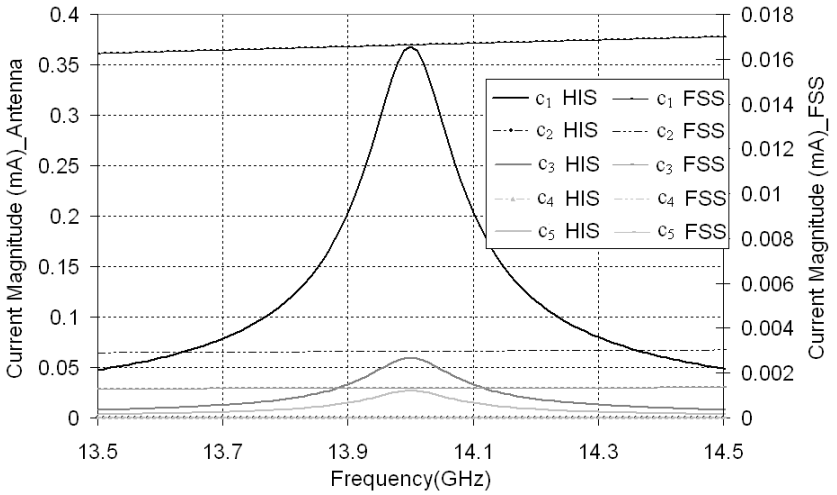

Fig. 3-7 Unknown coefficients {c} that represent the currents used to solve the EFIE by MoM for the structure in Fig. 3-6 with dimensions (in mm) D= 9.0, h=5.45, for the top array: square patches L=8, $h_{dielectric1}$=1.5 and ε_r=2.55 and for the low array: square patches L=4.15, $h_{dielectric2}$=1.15 and ε_r=2.2 as calculated with MoM.

As the number of basis functions considered for convergence increases so does the number of FSH. In order to complete a careful investigation of both parameters, the near field at $z=h/2$ (e.g. centre of the cavity) and at the centre of the unit cell, as estimated with increasing number of basis functions and FSH in both directions, is shown in Fig. 3-8a and b respectively. The structure has been excited by a normally incident plane wave polarized along the horizontal direction (E_y). From this figure it can be observed that the total number of basis functions for a convergence in terms of frequency shift

lower than 1% level is 30. Furthermore, convergence is achieved at about 120 FSH in each direction, which is about thrice as many as commonly used in the far-field estimation of the reflection characteristics from this type of arrays. The total number increases with the square of the required FSH in each direction, which for this case is 14400 FSH for a convergence better than 1%.

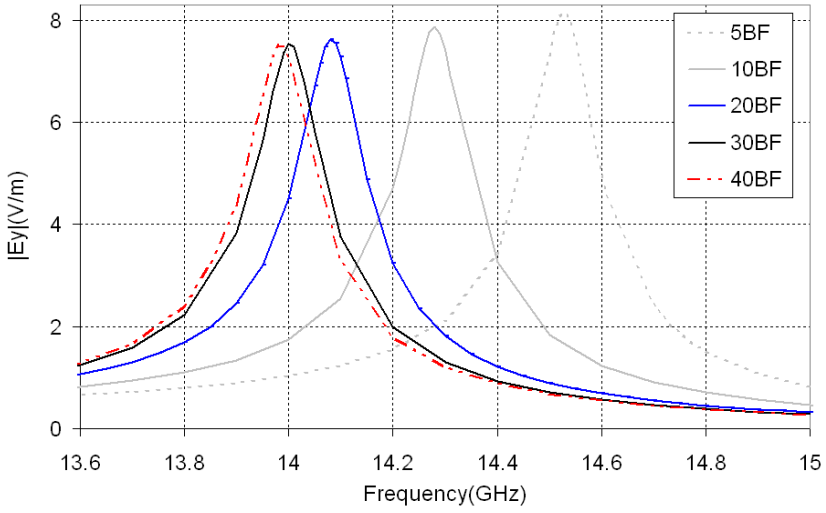

a)

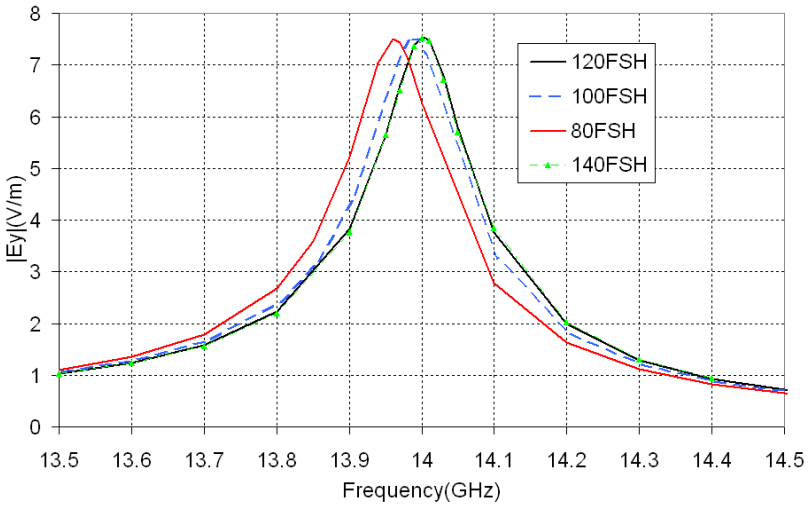

b)

Fig. 3-8 Magnitude of the y-component of the electric field at the centre of the cavity and the centre of the unit cell (x= y= 0, z=h/2) for the structure of Fig. 3-6 with dimensions (in mm) D= 9.0, h=5.45, for the top array: square patches L=8, $h_{dielectric1}$=1.5 and ε_r=2.55 and for the low array: square patches L=4.15, $h_{dielectric2}$=1.15 and ε_r=2.2 as calculated with MoM for a) increasing number of basis functions of the lower array (the number of BF for the PRS is 5) and 120 FSH and b) increasing number of Floquet Space Harmonics and 30 entire domain basis functions for the lower array (HIS) when the number of BF to model the current of each element of the PRS is 5.

In order to demonstrate the important role of higher order FSH when the distance between the arrays (*h*) becomes smaller we employ a series of examples with different *h*. For a fair comparison, all the cavities have been designed to resonate at the same frequency, 14GHz. Detailed design guidelines for these structures will be given in the next chapter. The top array is the same for all of them and five different low arrays are employed each of them at a distance *h* equal to λ/3, λ/4, λ/5, λ/7 and λ/12.

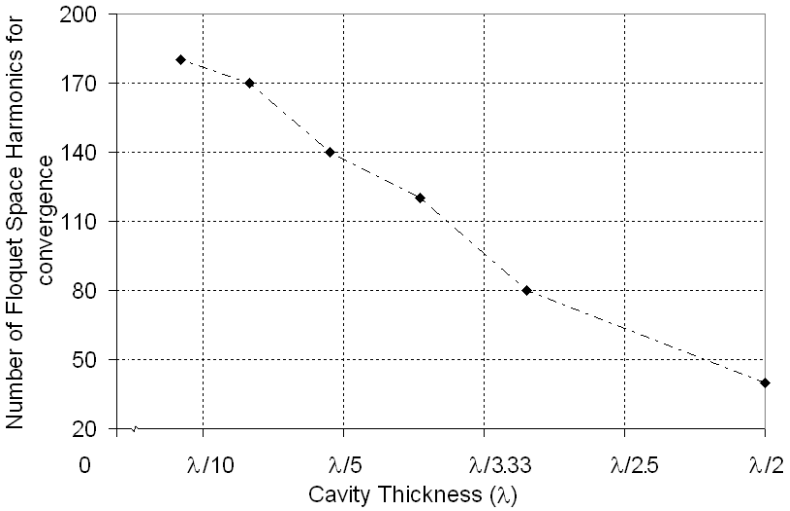

Fig. 3-9 Minimum number of Floquet Space Harmonics required for convergence (within 1%) in the calculation of the fields at z=h/2 for structures similar to Fig. 3-6 but different values of h (here shown as a fraction of the wavelength). All of them resonate at 14GHz.

The number of FSH in each direction required for a converged estimation of the near fields (within 1%) for increasingly thinner cavities is shown in Fig. 3-9. From this figure we see that for h= λ/2, 1600FSH (40FSH in x and y direction) suffice to achieve convergence, while for instance, for h=λ/7 a total of 28900 (170FSH in x and y direction) must be considered. As expected, more FSH are required to achieve convergence for closely located arrays. This is because for thinner cavities (smaller *h*), higher order FSH excited at the two periodic arrays can increasingly interact while the observation point (point where the fields are calculated) is closer to the periodic arrays.

3.2.2 Power stored in Frequency Selective Surfaces

Following the detailed investigation of the near-fields, the power stored in the vicinity of an FSS can be readily obtained and as a result the quality factor of the FSS is

determined. In this section, the doubly periodic array of metal dipoles presented in Fig. 3-1 is employed as a working example for a rigorous study of the reactive power stored in the FSS. In the following the 2-D periodic structure is excited by a normal incident plane wave with a 1V/m amplitude. At resonance (e.g. 22.15GHz) this structure will fully reflect the incident wave as shown in Fig. 3-10. It can also be observed that at 28.25GHz grating lobes appear manifesting as dips in the reflection response. As a result of this, from this frequency part of the energy is directed to other angles, leading to an apparent power loss at the direction of incidence.

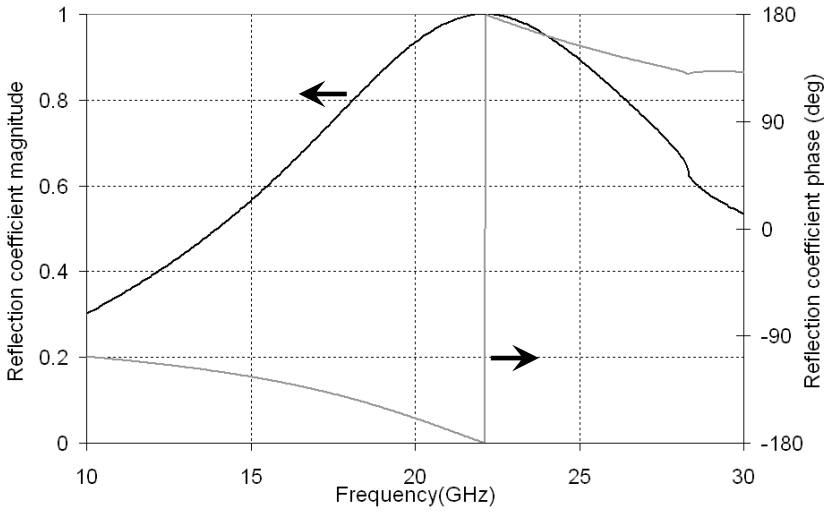

Fig. 3-10 Far field reflection coefficient (magnitude) for the FSS of Fig. 3-1 upon plane wave incidence considering 20 Floquet Space Harmonics in both x and y directions.

The reactive energy stored by a lossless, isotropic, homogeneous, linear media can be calculated from Eq. (3.2-2).

$$W_{stored} = 2 \cdot W_E = \frac{1}{2}\varepsilon_0 \iiint_V \overline{E} \cdot \overline{E}^* dV \tag{3.2-2}$$

where E represents the reactive field in the vicinity of the array at resonance assuming operation below the grating lobe regime. The total power stored by a 2-D periodic structure is the energy stored per unit of time and it can be easily determined from (3.2-3),

$$P_{stored} = \frac{W}{t} = W \cdot f_{resonance}$$

$$P_{stored} = f_{resonance} \cdot \varepsilon_0 \iiint_V \left| \sum_{mpq} R^{-}_{mpq} \bar{\kappa}_{mpq} \psi_{pq}(\bar{r}) e^{j\beta^0_{pq} z} \right|^2 dV \tag{3.2-3}$$

where subscript m represent TM (m=1) or TE (m=2) modes, *p* and *q* refer to each higher order FSH in each direction of propagation (neglecting the propagating FSH- *p*=*q*=0), *dV*=*dx*·*dy*·*dz* and $\bar{\kappa}_{mpq}$ and $\psi_{pq}(\bar{r})$ are as in Chapter 2. Therefore, according to (3.2-3) the evanescent electric field needs to be integrated along a specific volume (*V*). The volume, *V*, is defined in the transverse plane by the size of the unit cell and in the direction normal to the array is truncated to the distance where the contribution from the slowest decaying Floquet Space Harmonic (usually the p=0, q=-1) drops below 1% from its maximum value. This condition is written in Eq. (3.2-4)

$$e^{-\beta_z z} \leq 1\% \tag{3.2-4}$$

where β_z is the propagation constant defined in the previous chapter as,

$$\beta_z = \sqrt{\beta^2_{pq} - k_0^2} \tag{3.2-5}$$

In expression (3.2-5), β_{pq} is the propagation of every Floquet Space Harmonic along x and y-axis and k_0 is the propagation constant of the incident wave. As normal incidence is assumed,

$$\beta^2_{pq} = \left(\frac{2\pi}{dx} p\right)^2 + \left(\frac{2\pi}{dy} q\right)^2 \tag{3.2-6}$$

with these assumptions the height of the volume (d_z) considered in the calculation of the power stored in this particular example is 12.5 mm. Moreover, in the near field estimation, FSH which contribute up to 5% of the maximum of the -1 harmonic at the level of the array are considered in order to ensure convergence. The number of higher order FSH has been calculated from figures such as the one shown in Fig 3-3. The average power stored in the near-field of the FSS unit cell at resonance has been calculated giving to a value of 0.15157677μW.

3.2.3 Loaded Quality Factor of Frequency Selective Surfaces

At microwave frequencies the elements in the FSS can be assumed to be nearly perfect conductors, this means that no ohmic losses are considered because dielectric losses are the main source of thermal absorption [10]. In resonant systems, such as FSSs, the thermal absorption is conveniently described by the quality factor, which represents the ratio between the average reactive energy stored over the energy dissipated in a resonator in a period of oscillation and is defined in Eq. (3.2-7).

$$Q = w\frac{Energy_{stored}}{Energy_{loss}\,per\ \sec ond} \tag{3.2-7}$$

In the absence of power dissipation (e.g. lossless case) the loaded quality factor, Q_L, is employed to characterise the degree of coupling of the FSS to its environment, and it is also defined by Eq. (3.2-7). It can be demonstrated that within certain approximations, the loaded quality factor, Q_L, can be obtained from the 3dB fractional bandwidth, eq. (3.2-8) [11-12].

$$Q_L = \frac{f_{resonance}}{\Delta f_{-3dB}} \tag{3.2-8}$$

In this section, the loaded quality factor is calculated based on the results of section 3.2.2 and its value is compared to the 3dB fractional bandwidth in order to check the agreement of both methods. The average power stored in the near-field of the FSS unit cell calculated in the previous section is 0.15157677μW. The next step is to calculate the total complex power transferred by the 2-D periodic structure (power loss). This is defined in terms of the Poynting vector as follows,

$$P_0 = \frac{1}{2}\oint \overline{S}\cdot d\overline{s} = \frac{1}{2}\oint \left(\overline{E}\times\overline{H}^*\right)\cdot d\overline{s} \tag{3.2-9}$$

The value of the power transferred to free-space by the FSS's unit cell at resonance can be numerically calculated. The reflection coefficient at resonance in the lossless case exactly equal to -1, the power transferred from the FSS unit cell to the environment at resonance is equal to the power incident on it. This can be obtained through a surface integral of the Poynting vector along the unit cell as defined in (3.2-9). For free space

plane wave incidence with electric field strength 1V/m, the amplitude of the magnetic field can be calculated considering the medium impedance (e.g. $\frac{1}{120\pi}$). By substitution of these values in (3.2-9) and considering a 2-D periodic structure with a periodic unit cell d_x=3.85mm and d_y=10.6mm P_0 is equal to 0.054126 μW.

On the other hand, this value can also be estimated by using the developed MoM tool for the calculation of the near-fields excited in the vicinity of this structure and subsequent solution of the surface integral within the unit cell. The obtained value of the integral of the near-fields in Eq. (3.2-9) is 0.055564045 μW which is in excellent agreement with the numerical result.

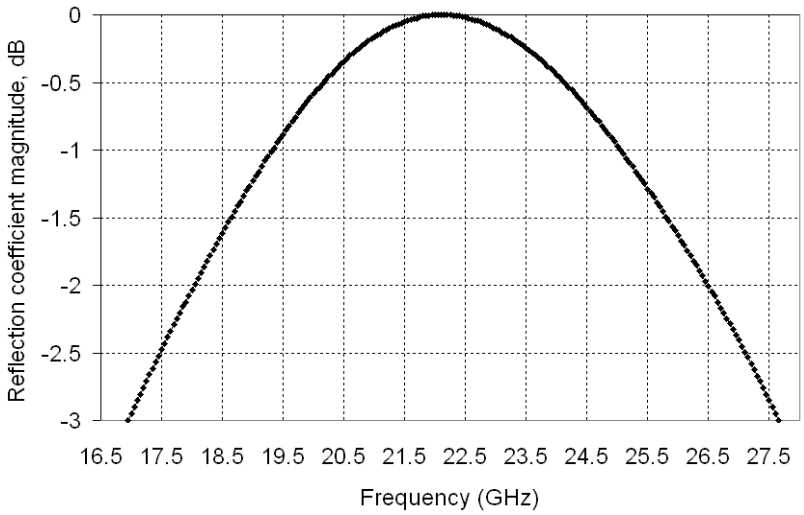

Fig. 3-11 Reflection coefficient from a free-standing planar periodic array of metallic dipoles upon normally incident plane wave as calculated from method of moments. The dimensions of the unit cell and the dipoles are in mm L=7.9, W=0.5, D_x=3.85 and D_y=10.6.

The loaded quality factor as obtained using MoM for the estimation of the near-fields after substitution in Eq. (3.2-7) has a value of 2.7242. Moreover, Fig. 3-11 shows the 3dB bandwidth of the array (27.65GHz-16.95GHz) and a resonant frequency of 22.15 GHz. The value of the loaded quality factor according to Eq. (3.2-8) is 2.07 which shows a fairly good agreement with the value obtained by the near-field estimation.

Identical studies have been performed for variable periodicity along the x axis, d_x, table 3-2 summarizes the calculated values of the resonance frequency, power stored and the loaded quality factor for each of this values.

TABLE 3-2 RESONANCE FREQUENCY, POWER RADIATED, STORED AND QUALITY FACTOR OF THE LOSSLESS 2D PERIODIC STRUCTURE CONSISTING OF PARALLEL METAL STRIPS.

d_x (mm)	$f_{resonance}$ (GHz)	P_{stored} (μW)	P_{rad}-MoM (μW)	P_{rad}-Numerical (μW)	Q_{MOM}	Q_{3Db}
3.85	22.15	0.151576768	0.05564045	0.054125989	2.724	2.074
5	20.9	0.27943718	0.072257361	0.070293493	3.218	2.580
5.9	20.25	0.382768702	0.086828857	0.082946321	3.784	3.139
7	19.6	0.53909955	0.101154511	0.09841089	5.329	3.852
8	19.15	0.711061644	0.115614266	0.112469588	6.150	4.506

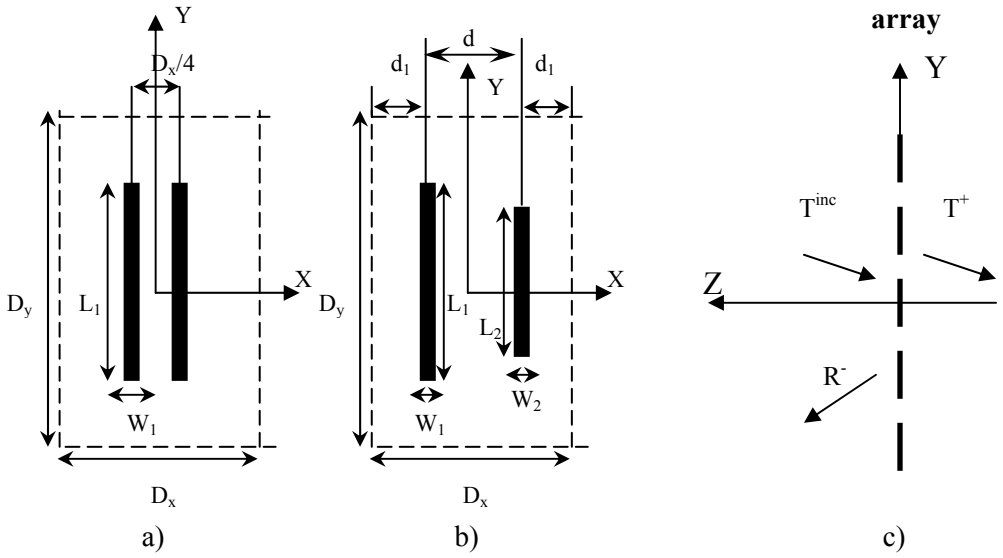

Fig. 3-12 a) unperturbed and b) perturbed planar unit cell of the periodic array of metal dipoles c) side view of the array.

3.3 Frequency Selective Surfaces with Enhanced Near-Fields

In [22] it was recognized that there are limitations associated with the far-field performance of multiband arrays. In particular, it was argued that for plane wave incidence, dual-band arrays at a certain frequency exhibit the so-called "modal interaction null". For a dual band capacitive screen consisting of a periodic array of metallic dipoles, such as the structure shown in Fig. 3-1, this refers to a frequency point

where the array appears transparent to incident plane waves in the far field. This point always emerges between two full reflection points, thus posing limitations in the bandwidth of the stopbands. However a detailed investigation into the resonant effects and associated near-fields of perturbed arrays has yet to appear [31].

In the remainder of the chapter a particular design of an FSS with unit cell shown in Fig. 3-12b is investigated. This structure shows particular characteristics which cause it to be interesting not only for multiband designs but also in multiple applications where enhancement of the near-fields is needed. We demonstrate that small perturbations give rise to strong near-field enhancement within a frequency range where the underlying physics are dominated by the odd mode, which is a drastic departure from the unperturbed case, Fig. 3-12a. Moreover, we show that within this frequency range, very strong currents are excited on the array elements.

3.3.1 Resonant Effects of the Perturbed array

We commence by deriving the equivalent self impedance of a perturbed array. The pole and zeros of the equivalent reactance are identified and the resonant effects exhibited by the perturbed array are discussed. Subsequently, by means of an example the nature of the resonant effects is demonstrated.

3.3.1.a Equivalent Impedance of a Perturbed array

Consider a planar periodic array of metal dipoles with self impedance $Z_A=R_A+jX_A$. An equivalent circuit for this array is presented in [13] and is reproduced in Fig. 3-13 when $X_P= X_A$. The reflection coefficient, Γ, from this array upon plane wave illumination can be calculated as indicated in (3.3-1). At resonance, the imaginary part of the self impedance goes to zero, corresponding to a full reflection for incident plane waves.

$$\Gamma = -\frac{R_A}{Z_A} = -\frac{R_A}{R_A + jX_A} \tag{3.3-1}$$

Next, a perturbation is introduced by changing the length of every other dipole element in the array. Consider an array with a unit cell consisting of two dipoles, Fig. 3-12.

Commencing from the nominal length of the dipoles, one is lengthened, and therefore inductively loaded, and the other is shortened, and therefore capacitively loaded. The modification of the length in both cases is such that the magnitude of the inductive and capacitive loading respectively is equal to ΔX. The combined structure can be conveniently modeled as two coupled unperturbed sub-arrays, an inductively loaded (sub-array 1) and a capacitively loaded (sub-array 2) [13].

For small perturbations, ΔX can be assumed independent of the frequency. Moreover, the real part of the self and mutual impedance of the sub-arrays can, to a good approximation, be assumed equal to that of the nominal array, R_A [13]. Let $Z_{11,22}$ and $Z_{12,21}$ be the self and mutual impedance of the two sub-arrays. For simplicity, the analysis is restricted to the case of plane waves normally incident on the array. In this case the two mutual impedances/admittances are equal, i.e. $Z_{12}= Z_{21}$. In accordance with the above, the impedance matrix for the combined perturbed array can be written as:

$$\begin{bmatrix} Z_{11} & Z_{12} \\ Z_{21} & Z_{22} \end{bmatrix} = \begin{bmatrix} R_A + j\cdot(X_A + \Delta X) & R_A + j\cdot X_M \\ R_A + j\cdot X_M & R_A + j\cdot(X_A - \Delta X) \end{bmatrix} \tag{3.3-2}$$

where the subscript M is employed to denote the mutual reactance of the two arrays.

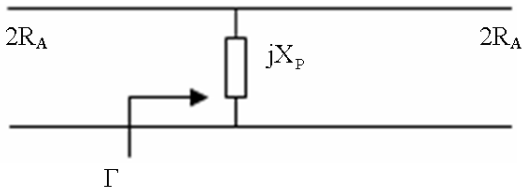

Fig. 3-13 Equivalent circuit for the scattering of plane waves by the periodic array shown in Fig.3-12 in the absence of grating lobes.

The reflection coefficient can be calculated as the ratio of the scattered over the incident field. The former can be expressed as a function of the currents excited on the dipole elements while the latter determines the equivalent voltage applied. The definition of the voltage and how this can be obtained is found in chapter 4 of [13]. The reflection coefficient of a normally incident plane wave by the entire array in terms of the self and mutual impedances of the sub-arrays is given by [22]

$$\Gamma = -R_A \frac{Z_{22} - Z_{12} - Z_{21} + Z_{11}}{Z_{22}\cdot Z_{11} - Z_{12}\cdot Z_{21}} \tag{3.3-3}$$

By substitution of the impedance values indicated in (3.3-2) into (3.3-3) we obtain,

$$\Gamma = -R_A \frac{2j\left(X_A - X_M\right)}{R_A^2 - X_A^2 + \Delta X^2 + 2jR_A X_A - R_A^2 + X_M^2 - 2jR_A X_M} \tag{3.3-4}$$

Simple algebraic manipulation yields:

$$\Gamma = \frac{-R_A}{R_A + \dfrac{X_M^2 - X_A^2 + \Delta X^2}{2j\left(X_A - X_M\right)}} \tag{3.3-5}$$

Eq. (3.3-5) can be expressed as,

$$\Gamma = \frac{-R_A}{R_A + jX_P} \tag{3.3-6}$$

where

$$X_P = \frac{X_M^2 - X_A^2 + \Delta X^2}{2\left(X_M - X_A\right)} \tag{3.3-7}$$

An equivalent circuit that yields the reflection in (3.3.6) is shown in Fig. 3-13. By simple comparison of (3.3-1) and (3.3-6), the equivalent impedance of the perturbed array is,

$$Z_A^{eq} = R_A + jX_P = R_A + j\frac{X_M^2 - X_A^2 + \Delta X^2}{2\left(X_M - X_A\right)} \tag{3.3-8}$$

The reactive part of (3.3-8) yields two zeros when X_A is,

$$X_A = \pm\sqrt{X_M^2 + \Delta X^2} \tag{3.3-9}$$

and a pole when,

$$X_A = X_M \tag{3.3-10}$$

Considering the equivalent circuit of Fig. 3-13, one can conclude that at the two reactance zeros, the reflection coefficient is equal to $\Gamma = -1$, while at the pole, $\Gamma = 0$, i.e.

the array appears transparent to an incident plane wave. The zeros and poles of X_P correspond to the resonances of the perturbed array.

Let I_1 and I_2 be the amplitude of the current flowing in each sub-array element. The current vector [I] can then be obtained upon solution of the matrix Eq. (3.3-11),

$$[Z]\cdot[I]=[V] \tag{3.3-11}$$

For small perturbations, we can assume that the voltage applied to each sub-array is equal to the nominal value, i.e. $V_1= V_2= V_0$. The solution of the linear equation system defined in (3.3-11) produce the currents,

$$I_1=\frac{Z_{22}-Z_{12}}{Z_{11}Z_{22}-Z_{12}Z_{21}}V_0 \tag{3.3-12}$$

$$I_2=\frac{Z_{11}-Z_{21}}{Z_{11}Z_{22}-Z_{12}Z_{21}}V_0 \tag{3.3-13}$$

After substituting the values of the impedances and the value of the currents at the two reactance zeros are,

$$I_1^{n1,n2}=\frac{V_0}{2R_A}\left[1+\frac{\Delta X}{\mp\sqrt{X_M^2+\Delta X^2}+X_M}\right] \tag{3.3-14}$$

$$I_2^{n1,n2}=\frac{V_0}{2R_A}\left[1+\frac{\Delta X}{\pm\sqrt{X_M^2+\Delta X^2}-X_M}\right] \tag{3.3-15}$$

and at the reactance pole,

$$I_1^p=-j\frac{V_0}{\Delta X} \tag{3.3-16}$$

$$I_2^p=j\frac{V_0}{\Delta X} \tag{3.3-17}$$

Since X_M is typically negative and ΔX is assumed small [13], the second term in the square brackets in (3.3-14 and 3.3-15) is, to a first approximation, negligible for the top sign of the square roots. To this approximation, the current flowing in the perturbed array is equal to $I_0=V_0/(2R_A)$. A simple comparison shows that this is the current at the resonance of the unperturbed array. Therefore for the positive value of the square root in

(3.3-9), the underlying physics for the resonances of the perturbed and unperturbed array are similar. The currents I_1^{n1} and I_2^{n1} excited in the two sub-arrays are flowing in parallel and, to a first approximation, are equal to those excited on the elements of the unperturbed array at resonance.

On the contrary, the negative sign of the square root in (3.3-9) as well as the reactance pole (3.3-10) emerge as a result of the perturbation and correspond to significantly different physics. From Eq. (3.3-16 and 3.3-17) it is evident that the currents in the two sub-arrays flow in opposite directions and at $\pm 90^o$ from the incidence, i.e. the sub-arrays at the reactance pole exhibit purely inductive and capacitive behaviour. Moreover, significantly larger magnitudes of the currents are expected in this case since ΔX is small (e.g. compared to R_A). Similar observation of (3.3-14-3.3-15) for the bottom sign of the square root reveals significant deviation from the resonance of the unperturbed array.

3.3.1.b Numerical example of the Resonant Effects in a Perturbed array

In the last section the reflection coefficient, the equivalent impedance and the induced currents on the two sub-arrays were derived for both cases perturbed and unperturbed periodic planar array. Next, the resonant effects discussed above are probed into by means of an example involving a plane wave normally incident on a free-standing periodic array of metallic dipoles. Referring to Fig. 3-12, the dimensions of the unperturbed array are D_x= 7.7mm, D_y= 10.6mm, L_1= L_2= 7.9mm, W_1= W_2= 0.5m. Unless otherwise mentioned, the dipoles are assumed symmetrically located in the unit cell, so that d= $2d_1$. The reflection characteristics upon normally incident plane wave have been calculated using the code developed in chapter 2, [7].

The magnitude of the reflection coefficient vs. frequency was calculated and it is shown in Fig. 3-14. This plot shows a peak at 22.15GHz, corresponding to the resonance of the unperturbed array. Following this calculation, perturbation is introduced by respectively lengthening and shortening the dipoles within the unit cell. The reflection characteristics from an array with L_1= 8.2mm, L_2= 7.5mm are shown in Fig. 3-14 with a black solid line. In the vicinity of 22.15GHz, the response matches well that of the unperturbed

array. Nevertheless, in accordance with the discussion above and [22], another full reflection point emerges at 17.2GHz followed by a reflection null at 17.34GHz.

The reflection responses of Fig. 3-14 have also been reproduced using Eq. (3.3-6 and 3.3-7). A rigorous description of the procedure that yields the self and mutual impedances for the sub-arrays is given in chapter 4 of [13]. For the structure under consideration the values indicated in Table 3.3 have been used (in Ohm),

TABLE 3-3 ARRAY PARAMETERS FOR THE CALCULATION OF THE REFLECTION COEFFICIENT BY USING EQ. IN 3.3-5

Array self-resistance R_A	**Array self-reactance X_A**	**Array mutual-reactance X_M**	**Perturbation ΔX**
53·f(GHz)+1048	145	-131	45

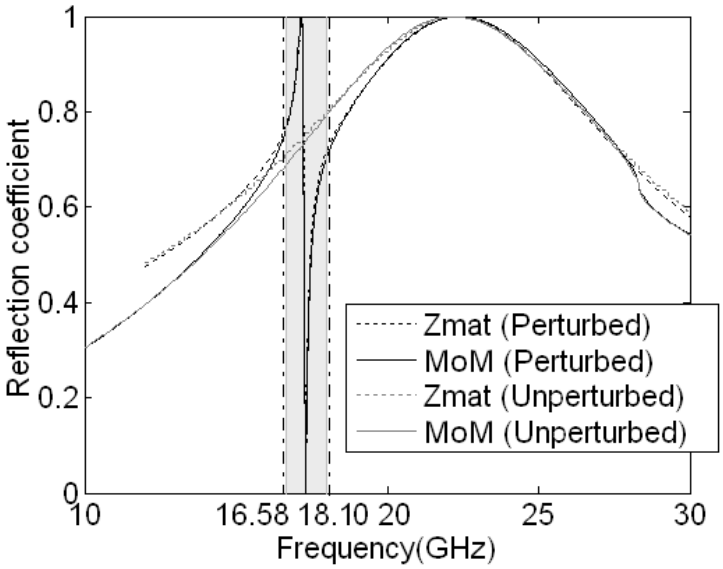

Fig. 3-14 Reflection coefficient from a free-standing planar periodic array of metallic dipoles (Fig.3-1) upon normally incident plane wave as calculated from the impedance matrix and the method of moments for the perturbed (L_1=8.2, L_2=7.5, W_1= W_2=0.5, D_x=7.7, D_y=10.6) and unperturbed (L1= L2=7.9) case. In both cases d=2d1. Dimensions in mm.

The response obtained for the unperturbed array can be calculated setting ΔX= 0. The reflection response obtained by these parameters is shown with a dotted line in Fig. 3-14. The good agreement with the full-wave validates the impedance matrix model

within a range of frequencies from about 15GHz to about 28GHz, where the grating lobes emerge and manifest as a sudden dip in the MoM results.

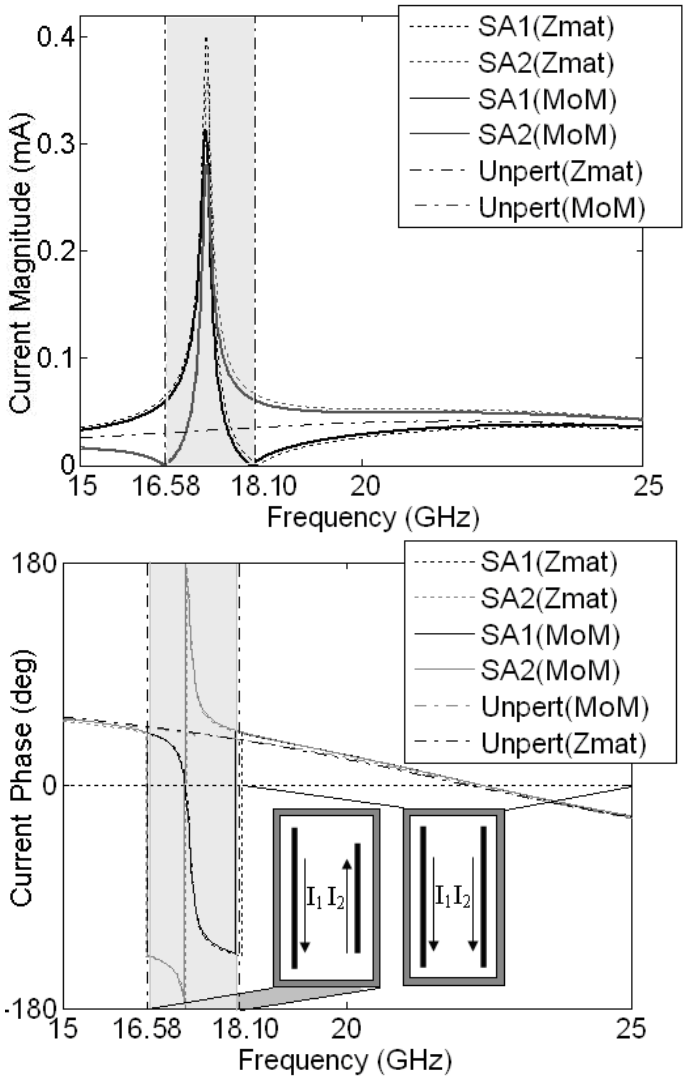

Fig. 3-15 Currents induced on the free-standing planar periodic array of metallic dipoles (Fig. 3-12) upon normally incident plane wave with E_y= 1V/m as calculated from the impedance matrix and the method of moments for the perturbed (SA1: inductive sub-array 1 and SA2: capacitive sub-array 2) and unperturbed case. Dimensions as in Fig. 3-14.

Subsequently, the magnitude and phase of the current induced on the dipoles, as calculated by (3.3-12 and 3.3-13) and with MoM upon a normally incident plane wave for the perturbed as well as the unperturbed array were calculated. Their values are shown in Fig. 3-15. The good agreement further validates the accuracy of both methods. From this figure it can be seen that in the vicinity of 22.15GHz, the currents excited on the elements of the perturbed array converge to those of the unperturbed case, revealing analogous underlying physics in both cases. In particular, the currents in both dipoles flow in parallel with comparable magnitudes and are in phase with the incidence at

exactly 22.15GHz. This frequency is associated to the resonance of the array, indicated by the purely ohmic behaviour as well as the full reflection of the incident field.

In the case of the perturbed array, the currents induced on the capacitively loaded sub-array 2 are zero at 16.58GHz and increase rapidly with frequency. Similarly, the currents induced on the inductively loaded sub-array 1 reduce rapidly to a zero value at 18.10GHz. In contrast with the unperturbed case, between these frequencies the currents in the two sub-arrays are out-of-phase and obtain very large values. At 17.34GHz, where the perturbed array appears transparent to an incident plane wave, the currents on the two sub-arrays are equal in magnitude and in $\pm 90^{o}$ phase difference from the incident field (purely reactive). As a result their contributions to the total far field cancel out. Below this frequency, the current on sub-array 1 is stronger than that on sub-array 2 while above this frequency the situation swaps. At 17.20GHz, the currents on sub-array 1 are real, positive and higher in magnitude than those on sub-array 2, which are real and negative. As a result, the perturbed array appears fully reflective to the incident plane wave. Away from the 16.58GHz- 18.10GHz frequency range the currents on the two sub-arrays converge to those of the unperturbed case.

This study reveals that within the frequency range 16.58GHz-18.10GHz the physical effects are dominated by the excitation of the anti-symmetric (odd) resonant mode. The excitation of the anti-symmetric mode is known for the case of horizontally spaced layers of vertically stacked pairs of metallic strips [32-33], where it gives rise to an effective magnetic permeability. However, this is a drastically different case, since the uniplanar features of the array suggest excitation of this mode by the electric rather than the magnetic field. Excitation of the odd mode in this case is possible due to the asymmetry introduced in the perturbed array. This corresponds to drastically different physics compared to the unperturbed case. For small perturbations, the coupling of the odd mode to the incident plane wave is weak. As a result, the external quality factor is large, leading to narrowband and strong resonant effects, manifested here as strong induced currents. These are expected to give rise to strong near fields, which are calculated in the following section.

3.3.2 Enhanced Near Fields

In section 3.3.1b the current flowing in the two sub-arrays was determined. The opposing currents flowing in the two dipoles within the unit cell can be associated with a current loop, where continuity of the current between the two open ends is provided by the displacement current. It is therefore expected that this resonance is associated with strong magnetic fields in the direction normal to the surface. To illustrate this, Fig. 3-16a shows the longitudinal component of the magnetic field at the plane of the array and frequency 17.34GHz. The number of FSH considered for an accuracy of more than 5% in the near-field according to section 3.2.1 is 90FSH in the x-direction and 40FSH in the y-direction. The illumination is a normally incident plane wave linearly polarized along the y-axis and of amplitude 1V/m. For comparison, Fig. 3-16b also shows the same field component for the same illumination at 22.15GHz. Interestingly, although in the former case the array appears transparent to the incident wave, significantly higher energy is stored in its vicinity in the form of reactive near fields. It is interesting to note that since a loop element provides a longer current path, the odd (anti-symmetric) mode is associated with a lower resonant frequency compared to the even mode. As a result, the odd mode resonance appears at lower frequencies than the even mode resonance. The rest of the electric and magnetic field components at both frequencies (even mode: 22.15GHz and odd mode: 17.34GHz) are shown in Fig. 3-17.

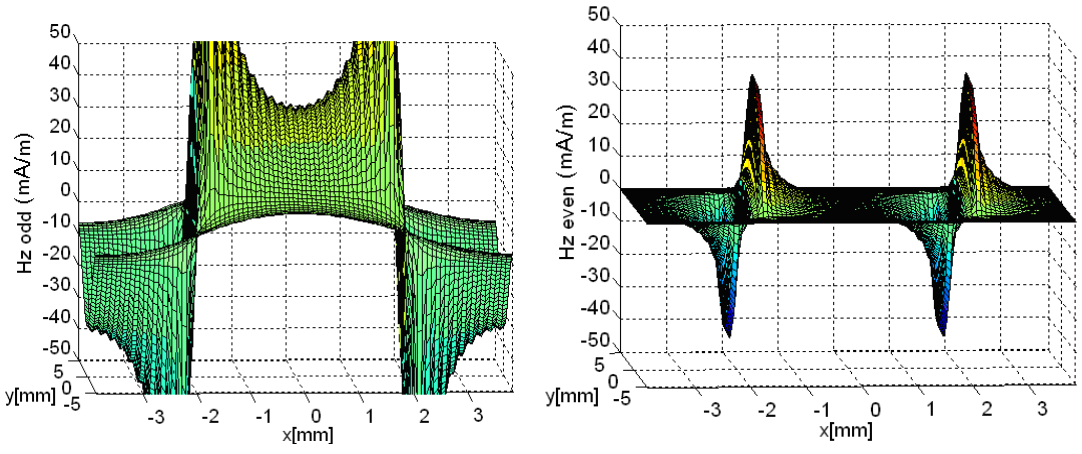

a) b)

Fig. 3-16 z-component of the magnetic field in the unit cell of the perturbed FSS of Fig. 3-14 at z= 0 as calculated using MoM for normal plane wave incidence with E_y= 1V/m at (a) 17.34GHz and (b) 22.15GHz.

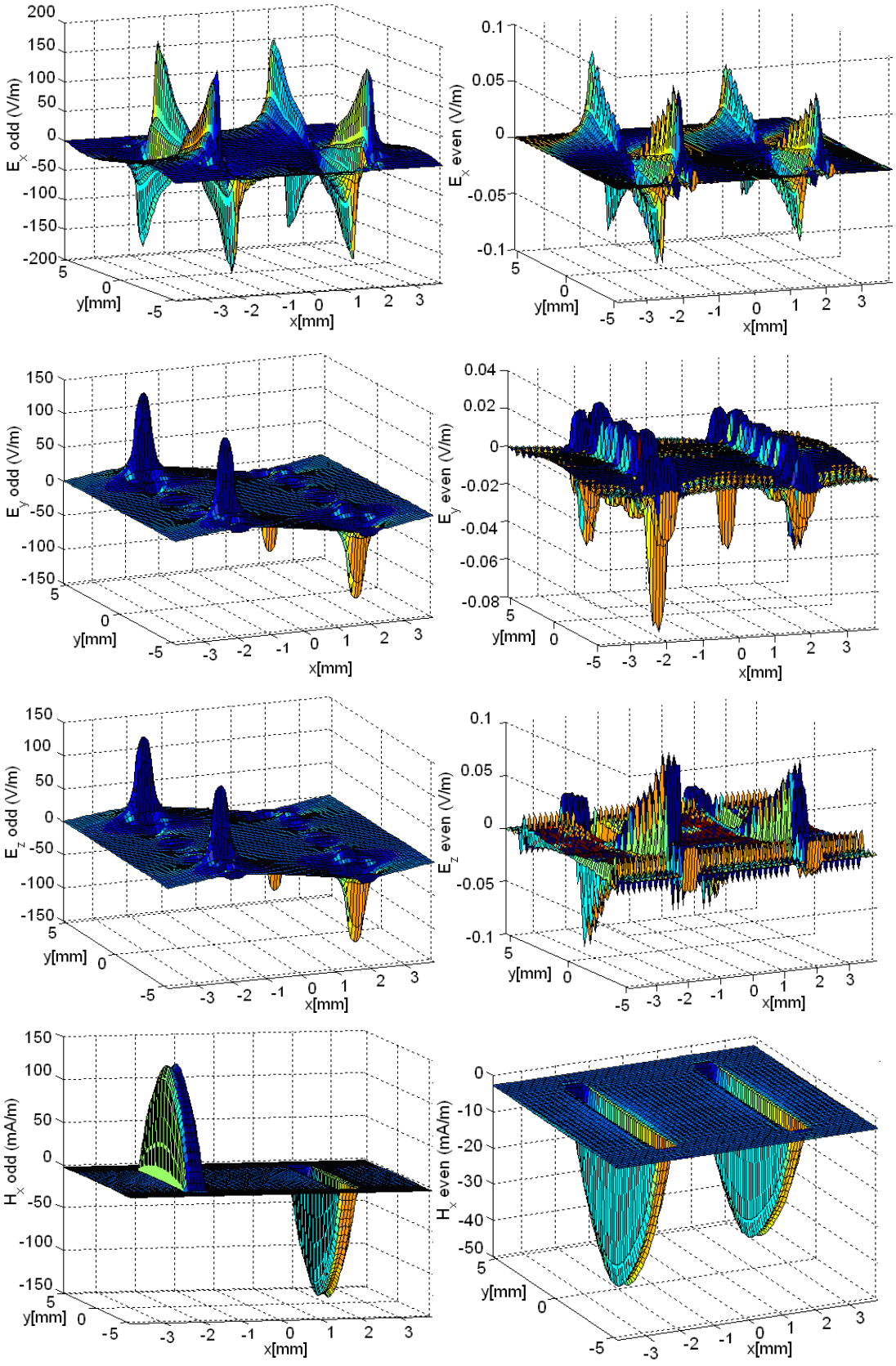

Fig. 3-17 x,y and z-component of the electric and magnetic field in the unit cell of the perturbed FSS of Fig. 3-14 at z= 0 as calculated using MoM for normal plane wave incidence with E_y= 1V/m at (left column) 17.34GHz and (right column) 22.15GHz.

A vectorial representation of the magnetic field at the XZ-plane at both frequencies is depicted in Fig. 3-18. At 22.15GHz, the parallel currents in the two dipoles produce circulation of the magnetic field in the same direction (Fig. 3-18b). Thus, the normal magnetic field in the centre of the unit cell goes to zero. On the contrary, at 17.34GHz, due to the antiparallel flow of the currents, the magnetic field produced by the dipoles circulates in opposite directions, leading to constructive interference in the area between the dipoles (Fig. 3-18a). The field distributions shown in Fig. 3-18 have also been validated using HFSS, Floquet boundary conditions (master and slave) were used across the opposing walls of the unit cell, and radiation boundary conditions were imposed on the top and the bottom of the unit cell. The structure was excited by a 1V/m electric field polarised along the y-axis. Fig. 3-19a shows the circulation of the magnetic field at the XZ-plane at 17.34GHz, and b) at 22.15GHz, showing good qualitative agreement with the results of Fig. 3-18. Note that the scale of the magnetic field in Fig. 3-19a, corresponding to the even mode, has been increased by a factor of 10 compared to that in Fig. 3-19b in order to make it discernable for comparison.

To quantify the comparison, Fig. 3-20 shows the magnitude of the z-component of the magnetic field at the centre of the unit cell as obtained with HFSS and the in-house MoM (90 FSH in x and 40 FSH in y have been employed for the calculation). Good agreement between the two results is observed. The discrepancy of the location of the maxima of |Hz| is due to the lack of convergence of HFSS. The incident magnetic field, polarised along the x-axis, has an amplitude of 2.65mA/m. On the other hand, the magnitude of the normal magnetic field (z-component), at the centre of the unit cell, shown in Fig. 3-20 is 35.7mA/m, showing a more than ten-fold near field enhancement.

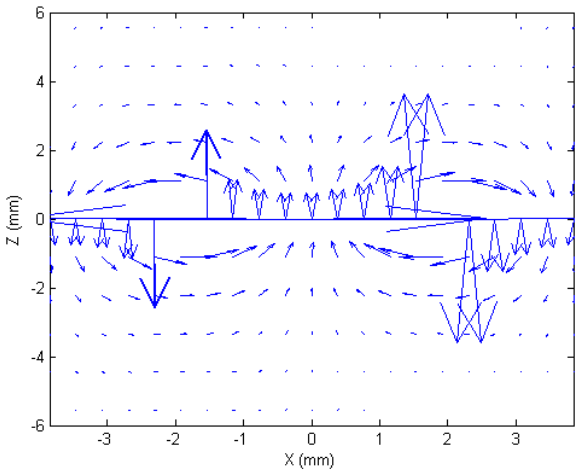

a)

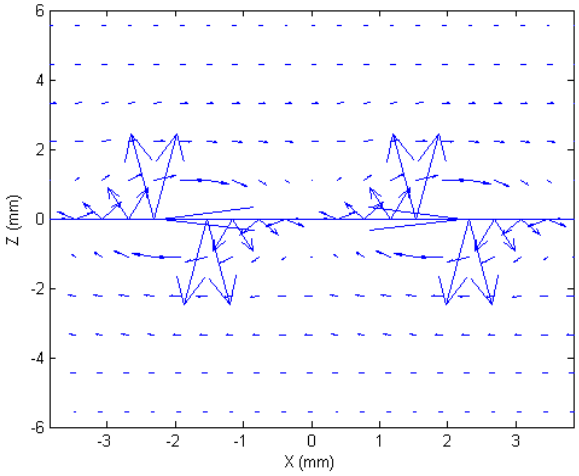

b)

Fig. 3-18 Vectorial representation of the magnetic field in the unit cell of the perturbed FSS of Fig. 3-14 at the xz-plane as calculated using MoM for normal plane wave incidence at (a) 17.34GHz (odd mode) and (b) 22.15GHz (even mode).

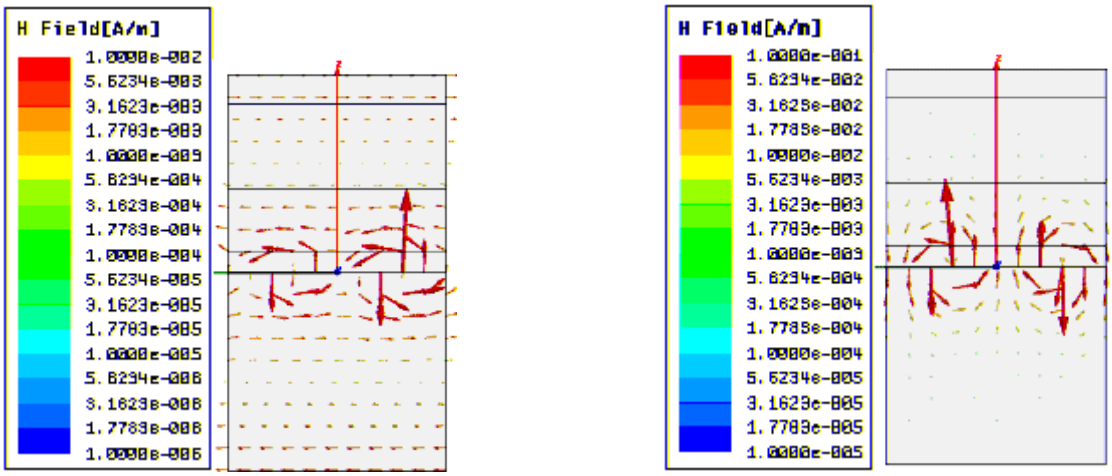

a) b)

Fig. 3-19 Vectorial representation of the magnetic field in the unit cell of the perturbed FSS of Fig. 3-14 at the xz-plane calculated using HFSS for normal plane wave incidence at (a) 22.15GHz and (b) 17.34GHz.

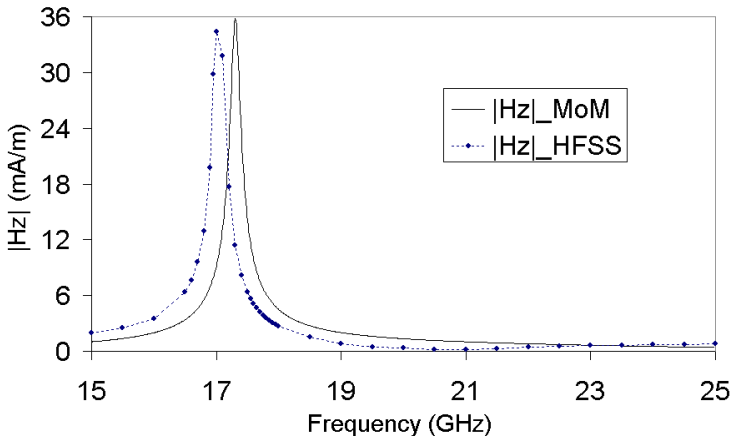

Fig. 3.20 Magnitude of the z-component of the magnetic field at the centre of the unit cell for normal plane wave incidence with E_y= 1V/m as calculated using MoM and HFSS. Dimensions are as in Fig. 3-14.

3.3.3 Geometrical Considerations

After having demonstrated the excitation of the odd mode and validated our simulation tool, a more detailed study of the effect of the geometrical parameters on the excitation of the odd mode and the near field enhancement is subsequently presented. The parameters studied include the periodicity along x, D_x, the level of perturbation, the distance between the elements and the angle of incidence.

TABLE 3-4 MAXIMUM VALUE OF THE CURRENTS EXCITED ON THE ELEMENTS AND VALUE OF THE CURRENTS AT THE FREQUENCY WHERE Γ=0 FOR DIFFERENT VALUES OF THE PERIODICITY, D_x

I_1(mA)	I_2(mA)	I_1=I_2 (mA)	D_x (mm)
0.248084	0.255467	0.240141	1.8
0.26424	0.266897	0.24209	2.8
0.287431	0.271779	0.235854	5.3
0.29892	0.272891	0.229487	6.8
0.306278	0.272925	0.224611	7.7
0.322532	0.273639	0.214202	9.2
0.374088	0.289865	0.195485	12.4

TABLE 3-5 MAXIMUM VALUE OF THE CURRENTS EXCITED ON THE ELEMENTS AND VALUE OF THE CURRENTS AT THE FREQUENCY WHERE Γ=0 FOR DIFFERENT VALUES OF THE PERIODICITY, D_y

I_1 (mA)	I_2 (mA)	$I_1=I_2$ (mA)	D_y (mm)
0.241994	0.217685	0.18919	8.9
0.271771	0.244498	0.208213	9.5
0.314289	0.280949	0.229311	10.6
0.34287	0.296433	0.230838	12.4
0.359641	0.305241	0.231298	13.6

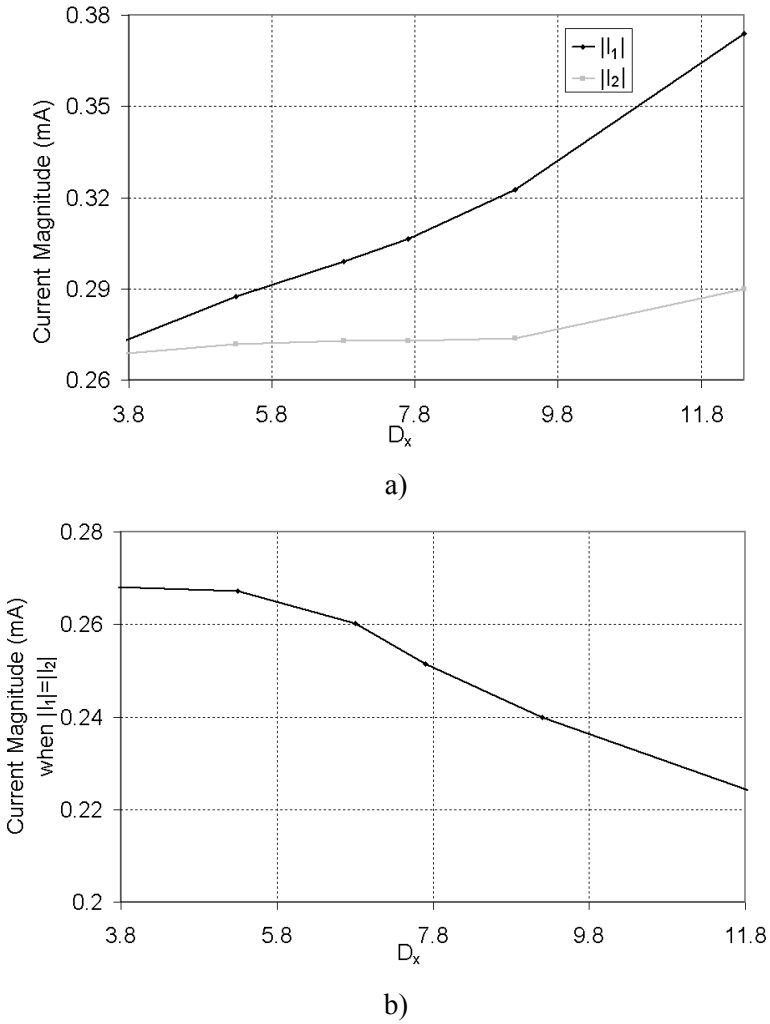

Fig. 3-21 a) Maximum value of the current for the two dipoles at the odd mode for increasing periodicity D_x. b) Current magnitude value at the point where the array appears transparent to incident coming waves (the currents on the two dipoles are equal and at phase $\pm 90^o$ from the incidence). All dimensions except D_x are as in Fig. 3-14.

Effect of the periodicity along x and y

The effect of periodicity along x, D_x, on the currents excited at the odd mode is summarised in Fig. 3-21. Fig. 3-21a depicts the amplitude of the current at the frequency where this is maximum for both dipoles as the periodicity, D_x, is varied. The dipoles are located symmetrically within the unit cell, so that $d= 2d_1$, please refer to Fig. 3-12. The maximum of the odd mode current increases with increasing periodicity. This is also the case for the even mode and the unperturbed array. Fig. 3-21b shows the point where the currents at the two dipoles are at $\pm 90^o$ from the incidence, equal in magnitude and the array appears transparent to incident waves. Interestingly, despite the increased value of the peak current, Fig. 3-21b shows a decreasing trend for the cross-over point. This results in reduced near fields at the cross-over point. Table 3-4 and 3-5 summarize the values of the currents on the elements at its maximum value as well as when both currents are equal (array appears transparent to incident waves) for different values of D_x and D_y.

Effect of the level of perturbation

The level of perturbation is known to affect the frequency separation between the two full reflection points as well as the modal interaction null [22]. It is therefore reasonable to expect the bandwidth of the odd mode excitation to be broader for larger levels of perturbation. This is depicted in Fig. 3-22a which shows the lower and upper frequency points where the currents excited on the two dipoles are out of phase as the length of the second dipole varies. Interestingly, the maximum frequency of the odd mode increases almost linearly with the level of perturbation, while the lower frequency remains almost constant.

The broader bandwidth observed for greater perturbations suggests that the external quality factor is reduced, and therefore less reactive energy is stored at resonance. This is indeed confirmed in Fig. 3-22b, which shows the common current value at the point where the array appears transparent to incident plane waves (cross-over point as in Fig.3-21b). Clearly, the excitation of the odd mode is stronger for smaller perturbation levels. However attention should be paid to the fact that very narrow resonances will also experience very high thermal absorption.

Table 3-6 summarizes the values of the currents on the elements at its maximum value as well as when both currents are equal (array appears transparent to incident waves) for different values of L_2 (e.g. different perturbation values).

TABLE 3-6 MAXIMUM VALUE OF THE CURRENTS EXCITED ON THE ELEMENTS AND VALUE OF THE CURRENTS AT THE FREQUENCY WHERE Γ=0 FOR DIFFERENT PERTURBATION VALUES, L_2

I_1 (mA)	I_2 (mA)	$I_1=I_2$ (mA)	L_2 (mm)
0.13846	0.096328	0.17655	6.5
0.185684	0.147523	0.318533	7
0.314289	0.280949	0.784842	7.5
0.526582	0.4941	1.892884	7.8
2.081806	2.052311	12.17477	8.1

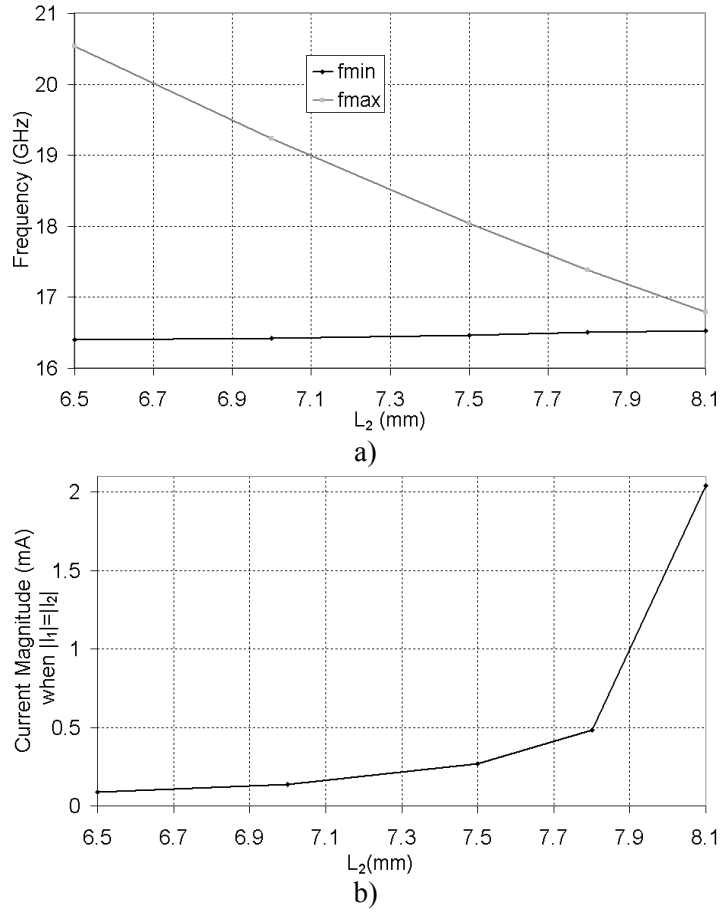

Fig. 3-22 a) Lower and upper frequency points where the currents excited on the two dipoles are out of phase as L_2 varies. b) Current value at the point where the array appears transparent to incident coming waves (the currents on the two dipoles are equal and at phase $\pm 90^o$ from the incidence). All dimensions except L_2 are as in Fig. 3-14.

Effect of the separation between elements

For applications that require strong and localised near-fields, our study reveals that the two dipoles of the unit cell should preferably be arranged in closely located pairs, e.g. so that $d<d_1$. Fig. 3-23 shows the normal component of the magnetic field at the plane of the array and frequency 18.32GHz, which corresponds to the frequency that the array appears transparent to incident plane waves. The dimensions are as in Fig. 3-14, except for the fact that d=0.9mm and d_1=3.4mm. As shown, significant localized field enhancement is observed. Compared to Fig. 3-20, the magnetic field component normal to the array at the centre of the unit cell is enhanced by a factor of about 6, resulting in an overall near-field enhancement of more than 70 times, when compared to the incidence. This observation can be particularly interesting for sensing applications, such as those proposed in [6]. In table 3-7 the values of the currents on the elements at its maximum value as well as when both currents are equal (array appears transparent to incident waves) for different values of d (e.g. distance between elements) are collected.

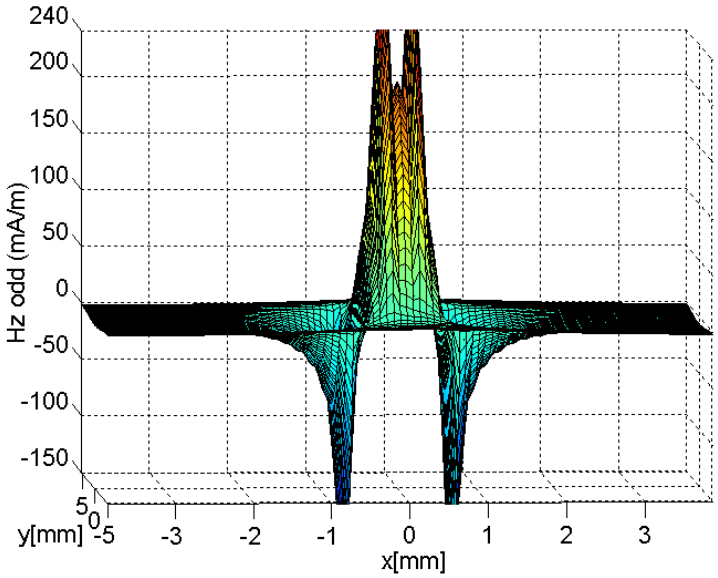

Fig. 3-23 Z-component of the magnetic field in the unit cell of the perturbed FSS of Fig. 3-14, where the distance between the dipoles, d, has been reduced to $D_x/9$, at z= 0 as calculated using MoM for normal plane wave incidence with E_y= 1V/m at 18.32GHz.

Furthermore, the linear geometry of the strips, parallel to the E-field polarization, suggests that the current – and therefore the strong longitudinal magnetic field - is excited due the presence of the electric field. We can therefore conclude that the expected enhancement of the magnetic field emerges as a result of electric-to-magnetic coupling (i.e. bi-anisotropy) [34]. The evanescent nature of the higher order Floquet

modes and the longitudinal polarization of the excited magnetic field suggest that it is confined in the evanescent near field of the grid. Fig. 3-23 has also been validated using HFSS, the results are plotted in Fig. 3-24.

TABLE 3-7 MAXIMUM VALUE OF THE CURRENTS EXCITED ON THE ELEMENTS AND VALUE OF THE CURRENTS AT THE FREQUENCY WHERE Γ=0 FOR DIFFERENT DISTANCES BETWEEN ELEMENTS, d

I_1 (mA)	I_2 (mA)	I_1=I_2 (mA)	d (mm)
0.373202	0.415531	0.374098	0.125
0.289222	0.290002	0.277348	0.225
0.278975	0.266039	0.252086	0.355
0.28178	0.261821	0.241913	0.525
0.2883	0.260954	0.232466	0.825
0.306981	0.275613	0.234139	1.225
0.311848	0.279207	0.233083	1.525
0.314289	0.280949	0.229311	1.925

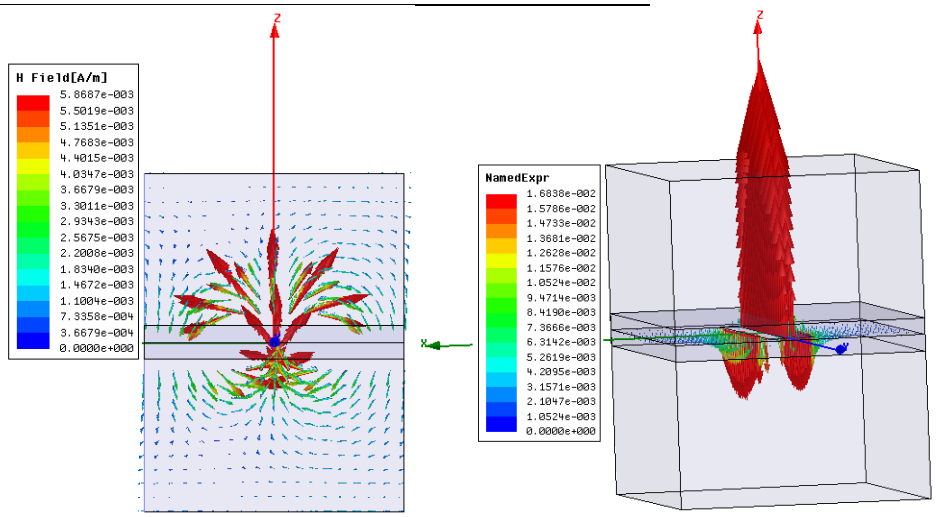

Fig. 3-24 Magnetic field at the array of Fig. 3-23 for normal plane wave incident Ey=1V/m as calculated with commercial software HFSS, where the distance between the dipoles, d, has been reduced to $D_x/9$, at z= 0 and f=18.32GHz.

Effect of the angle of incidence

The effect of the angle of incidence (θ,φ), on the currents excited at the odd mode is summarised in Table 3-8. This table also presents the amplitude of the current at the

frequency where this is maximum for both dipoles as the angles are varied. The dipoles are located symmetrically within the unit cell so that d= $2d_1$. The maximum of the odd mode current as well as the currents at the cross-over point decreases with increasing angle of incidence. This results in reduced near fields at the cross-over point when the incident is not normal.

TABLE 3-8 MAXIMUM VALUE OF THE CURRENTS EXCITED ON THE ELEMENTS AND VALUE OF THE CURRENTS AT THE FREQUENCY WHERE Γ=0 FOR DIFFERENT ANGLE OF INCIDENCES, θ AND φ

I_1 (mA)	I_2 (mA)	I_1=I_2 (mA)	θ=φ (deg)
0.314289	0.280949	0.229311	0
0.294155	0.266209	0.228547	25
0.231437	0.20835	0.183815	45
0.102034	0.099967	0.094838	65
0.020135	0.018258	0.017346	85

3.3.4 Miniaturization of doubly periodic arrays

The far and near field properties of perturbed arrays of metal strips have been studied in the previous sections. It was demonstrated that they produce two full reflection points separated by a reflection null (modal interaction null) and that the currents excited on the metallic elements are strong and out-of-phase in the vicinity of this point. In all the cases, the unit cell size is comparable to the wavelength, which suggests that extraction of homogenised parameters is not possible. In this section we present new results on 2-D periodic planar structures including designs with miniaturised unit cell. The proposed structures maintain compatibility with single layer printed metamaterials while the reduced unit cell compared to the wavelength reflects progress towards extracting equivalent homogenised parameters [35].

In order to miniaturise the unit cell, meander shaped metallic dipoles are employed that are known to condense longer electrical length in smaller physical dimensions [36]. Fig. 3-25a shows the miniaturised elements within a unit cell of the same dimensions as Fig. 3-12. The far-field reflection response is also shown in Fig 3-25b, where the response of

Fig. 3-14 is reproduced for comparison. The frequency, where the modal interaction null occurs, decreases from 17.34 GHz to 5.3GHz for the same unit cell, corresponding to a miniaturisation factor of more than 3 and a unit cell less than λ/5.

Fig. 3-26 shows the near magnetic fields excited by a linearly polarised plane wave incident at 0º and of strength 1V/m. As shown, a strong average longitudinal magnetic field is produced in the vicinity of the array as a result of the opposing magnetic field circulation around the two elements. Although the miniaturised structure is more pertinent to ohmic losses, the structure reproduces the same underlying physics with the unperturbed case within a miniaturised unit cell.

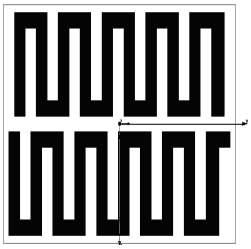

a)

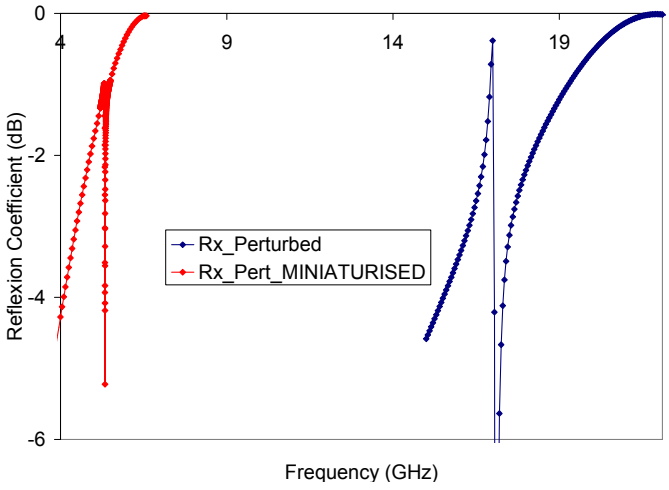

b)

Fig.3-25 Proposed unit cell and reflection response of metal strips (blue) and meander dipole (red).

A second design consisting of a different shape of the metallic dipoles is studied. Similarly to the meander shape dipole the longer electrical length results in smaller physical dimensions [36]. Fig. 3-27a shows the miniaturised elements within a unit cell of the same dimensions as before. The frequency, where the modal interaction null occurs, decreases to 3.8 GHz for the same unit cell, corresponding to a miniaturisation

factor of approximate 5 and a unit cell less than λ/7, Fig. 3-27b. Fig. 3-28 shows the near magnetic fields excited by a linearly polarised plane wave incident at 0º and of strength 1V/m. A strong average longitudinal magnetic field is produced in the vicinity of the array as a result of the opposing magnetic field circulation around the two elements.

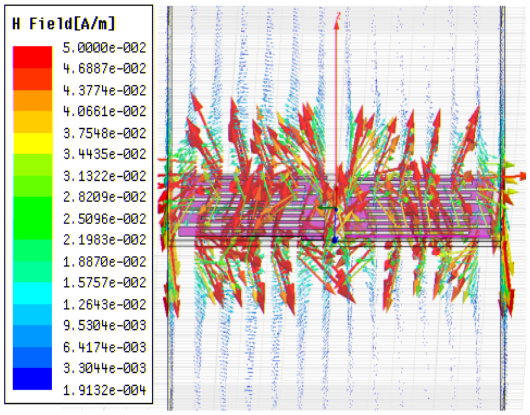

a)

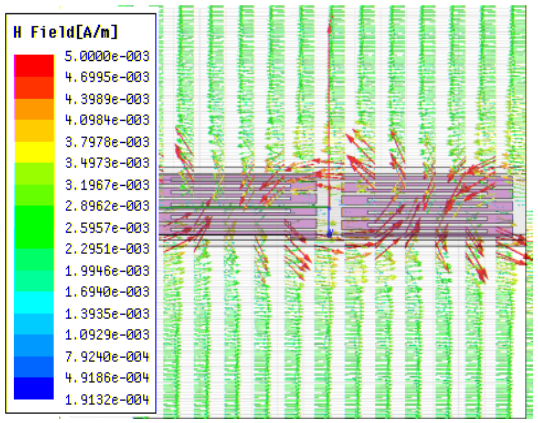

b)

Fig.3-26 Magnetic field at the array of Fig. 3-25 for normal plane wave incident Ey=1V/m as calculated with commercial software HFSS a) at 5.3 GHz and b) at 6.1 GHz

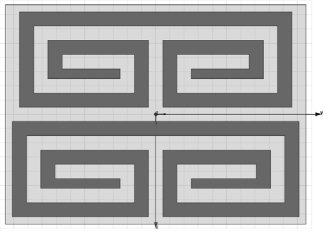

a)

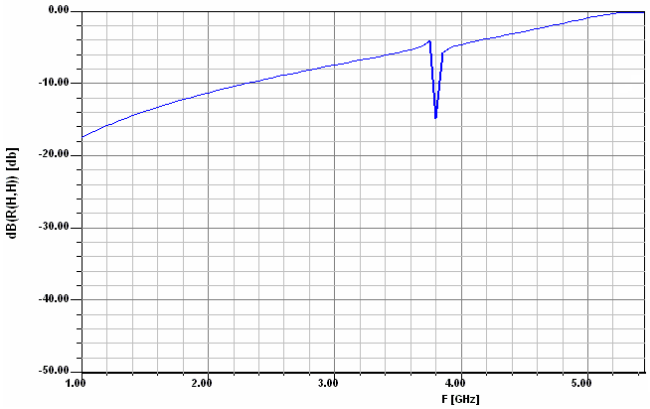

b)

Fig.3-27 a) Proposed unit cell and b) reflection response of the array of dipoles such as the one in (a).

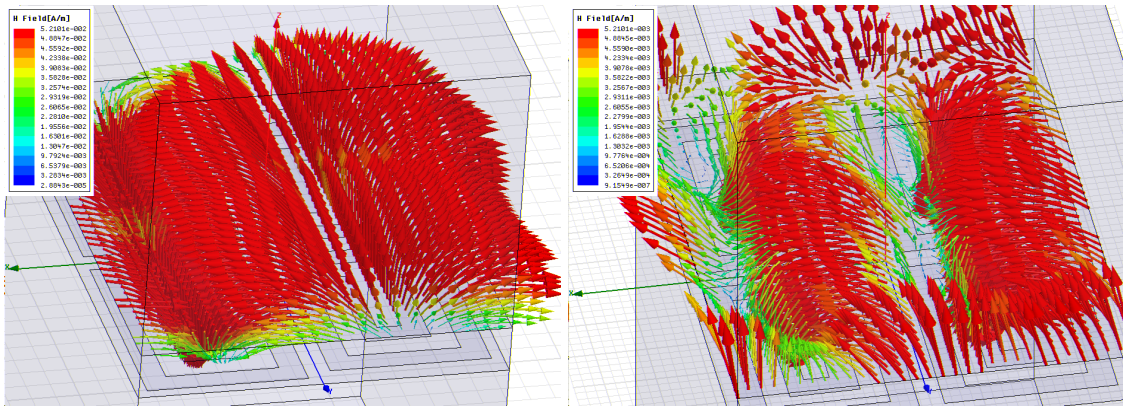

a) b)

Fig.3-28 Magnetic field at the array (a) for normal plane wave incident Ey=1V/m as calculated with commercial software HFSS b) at 3.8 GHz and c) at 5.4 GHz

3.4 Summary

In this chapter, a thorough study related to the calculation of the far and near fields of different FSS configurations has been presented by means of using the modelling technique outline in Chapter 2. Important considerations related to the convergence of the calculations have been carefully analysed in section 3.2. Furthermore, in this section the power stored in an FSS has been calculated following the estimation of the near-fields and as a result the loaded quality factor has been obtained.

A perturbed FSS structure with multiband response and enhanced near-fields has been proposed and analysed in section 3.3. The impedance of the perturbed periodic array of metal dipoles has been derived and the resonant effects have been studied. It has been demonstrated that as a result of the perturbation the scattering of plane waves within a frequency range is dominated by the excitation of the odd mode, with currents flowing antiparallel between successive dipoles.

The electric and magnetic near field excited on the structure under investigation has also been calculated in this section. After the calculation, it has been shown that at the frequency range dominated by the odd mode strong reactive fields are stored in the vicinity of the array. The results have been corroborated by HFSS. A study on the geometrical parameters on the excitation of the odd mode and the near field enhancement was also presented. The section concluded with miniaturised structures exhibiting the same characteristics.

3.5 References

[1] A.N. Lagarkov, A.K. Sarychev, "Electromagnetic properties of composites containing elongated conducting inclusions," *Phys. Rev. B.*, Vol. 53, No. 10, pp. 6318-6336, March 1996.

[2] T. J. Yen, W. J. Padilla, N. Fang, D. C. Vier, D. R. Smith, J. B. Pendry, D. N. Basov, and X. Zhang, "Terahertz magnetic response from artificial materials," *Science*, pp. 1494–1496, Mar. 2004.

[3] P. Belov, C. Simovski, P. Ikonen, "Canalization of subwavelength images by electromagnetic crystals," *Phys. Rev. B* 71, 193105, 2005.

[4] G.V. Eleftheriades, A.K. Iyer and P.C. Kremer, "Planar negative refractive index media using periodically L-C loaded transmission lines," *IEEE Trans. on Microwave Theory and Techniques*, vol. 50, no. 12, pp. 2702-2712, Dec. 2002

[5] P. Alitalo, S. Maslovski, S. Tretyakov, "Near-field enhancement and imaging in double cylindrical polariton-resonant structures: Enlarging superlens," *Phys. Lett. A*, Vol. 357, No. 4-5, pp. 397-400, 2006

[6] C. Debus, P.H. Bolivar, "Frequency selective surfaces for high sensitivity terahertz sensing," *Applied Physics Letters*, Vol. 91, 184102, Oct. 2007.

[7] R. Mittra, C.H. Chan, T. Cwik, "Techniques for analyzing frequency selective surfaces-a review," *Proceedings of the IEEE*, Vol. 76, pp.593-1615, Dec. 1988.

[8] J.C. Vardaxoglou, Frequency Selective Surfaces Analysis and Design, John Wiley, 1997.

[9] W. Changhua, J.A. Encinar, "Efficient computation of generalized scattering matrix for analyzing multilayered periodic structures," *IEEE Trans. Antennas Propag.*, vol.43, no. 11,Nov. 1995, pp. 1233 - 1242.

[10] G. Goussetis, A.P. Feresidis, J.C. Vardaxoglou, "Tailoring the AMC and EBG Characteristics of Periodic Metallic Arrays Printed on Grounded on Grounded Dielectric Substrate," *IEEE Trans. Antennas and Propagat.*, Vol. 54, No. 1, pp. 82-89, Jan. 2006.

[11] D. M. Pozar, Microwave Engineering, 2nd edition, New York: John Wiley & Sons Inc, 1998.

[12] G. Matthai, E. M. T. Jones and L. Young, Microwave Filters, Impedance-Matching Networks, and Coupling Structures, Artech House, 1980.

[13] Munk, *Frequency Selective Surfaces: Theory and Design*, John Wiley and Sons, 2000.

[14] D. Sievenpiper, Z. Lijun, R.F. Broas, N.G. Alexopoulos, and E. Yablonovitch, "High-impedance electromagnetic surfaces with a forbidden frequency band," *IEEE Trans. Microwave Theory and Techniques*, Vol. 47 , No. 11, pp. 2059-2074, Nov. 1999

[15] S. Maci, M. Caiazzo, A. Cucini and M. Casaletti, "A pole-zero matching method for EBG surfaces composed of a dipole FSS printed on a grounded dielectric slab," *IEEE Antennas and Propagat*., Vol. 53, No. 1, pp. 70-81, Jan. 2005.

[16] G. Goussetis, A.P. Feresidis and P. Kosmas, "Efficient Analysis, Design and Filter Applications of EBG Waveguide with Periodic Resonant Loads," *IEEE Trans. on Microwave Theory and Techniques*, Vol. 54, No. 11, pp. 3885-3892, November 2006

[17] A.P. Feresidis, G. Goussetis, S. Wang and J.C. Vardaxoglou, "Artificial magnetic conductor surfaces and their application to low-profile high-gain planar antennas," *IEEE Trans. on Antennas and Propagat.*, vol. 53, no 1, pp. 209-215, Jan. 2005

[18] O. Luukkonen, C. Simovski, G. Granet, G. Goussetis, D. Lioubtchenko, A. V. Raisanen, and S. A. Tretyakov, "Simple and Accurate Analytical Model of Planar Grids and High-Impedance Surfaces Comprising Metal Strips or Patches," *IEEE Trans. Antenna and Propagat.*, Vol. 56, No. 6, pp. 1624-1632, June 2008

[19] Y. Guo, G. Goussetis, A. P. Feresidis, and J. C. Vardaxoglou, "Efficient Modeling of Novel Uniplanar Left-Handed Metamaterials," *IEEE Trans. on Microwave Theory and Techniques*, Vol. 53, No 4, pp. 1462-1468, April 2005

[20] M. Beruete, I. Campillo, J.E. Rodríguez-Seco, E. Perea, M. Navarro-Cía, I. J. Núñez-Manrique, M. Sorolla, "Enhanced Gain by Double-Periodic Stacked Subwavelength Hole Array," *IEEE Microw. Wireless Comp.* Lett., Vol. 17, No. 12, pp. 831- 833, Dec 2007

[21] J. Huang, T.-K. Wu, S.W. Lee, "Tri-Band Surface with Frequency Selective Circular Ring Elements," *IEEE Trans. Antennas and Propagat.,* Vol. 42, No. 2, pp. 166-175, Feb. 1994

[22] R.A. Hill, and B. A. Munk, "The Effect of Perturbating a Frequency Selective Surface and its Relation to the Design of a Dual-Band Surface," *IEEE Trans. Antennas and Propagat.*, vol. 44, no. 3, pp. 368-374, Mar. 1996

[23] A.D. Chuprin, E.A. Parker and J.C. Batchelor, "Convoluted double square: single layer FSS with close band spacings," *IEE Elect. Lett.*, Vol. 36, No. 22, pp. 1830-1831, Oct. 2000

[24] J. Romeu, and Y. Rahmat-Samii, "Fractal FSS: A Novel Dual-Band Frequency Selective Surface," *IEEE Trans. Antennas and Propagat.*, Vol. 48, No. 7, pp. 1097-1105, July 2000

[25] J. P. Gianvittorio, J. Romeu, S. Blanch, Y. Rahmat-Samii, "Self-Similar Prefractal Frequency Selective Surfaces for Multiband and Dual-Polarized Applications," *IEEE Trans. Antennas and Propagat.*, Vol. 51, No. 11, pp. 3088-3096, Nov. 2003

[26] M. Ohira, H. Deguchi, M. Tsuji, H. Shigesawa, "Multiband Single-Layer Frequency Selective Surface Designed by Combination of Genetic Algorithm and Geometry-Refinement Technique," *IEEE Trans. Antennas and Propagat.*, Vol. 52, No. 11, pp. 2925-2931, Nov. 2004

[27] D.J. Kern, D.H. Werner, A. Monorchio, L. Lanuzza, M.J. Wilhelm, "The Design Synthesis of Multiband Artificial Magnetic Conductors Using High Impedance Frequency Selective Surfaces," *IEEE Trans. Antennas and Propagat.*, Vol. 53, No. 1, pp. 8-17, Jan. 2005

[28] M.A. Hiranandani, A.B. Yakovlev and A.A. Kishk, "Artificial magnetic conductors realised by frequency-selective surfaces on a grounded dielectric slab for antenna applications," *IEE Proc. Microwaves Antenna Propagat.*, Vol. 153, No. 5, pp. 487–493, Oct. 2006

[29] G.Q. Luo, W. Hong, H.J. Tang, J.X. Chen, K. Wu, "Dualband frequency-selective surfaces using substrate-integrated waveguide technology," *IET Proc. Microwaves Antenna Propagat.*, Vol. 1, No. 2, pp. 408–413, Jan. 2007

[30] G.Q. Luo, W. Hong, H.J. Tang, J.X. Chen, L.L. Sun, "Triband Frequency Selective Surface With Periodic Cell Perturbation," *IEEE Microw. And Wireless Comp. Lett.*, Vol. 17, No. 6, pp. 436, June 2007

[31] Ben Munk, private communication

[32] V. A. Podolskiy, A. Sarychev, V. Shalaev, "Plasmon modes and negative refraction in metal nanowire composites". *Optics Express*, Vol. 11, pp. 735-745, March 2003.

[33] G. Shvets and Y. A. Urzhumov, "Negative index meta-materials based on two-dimensional metallic structures", *Journal of Optics A: Applied and Pure Optics*, Vol. 8, S122, March 2006.

[34] R. Marques, F. Medina and R.R El-Idrissi, Role of bianisotropy in negative permeability and left-handed metamaterials, Physical Review B, pp. 144440, 2002.

[35] A.N. Serdyukov, I.V. Semchenko, S.A. Tretyakov, A. Sihvola, Electromagnetics of bi-anisotropic materials: Theory and applications, Amsterdam: Gordon and Breach Science, 2001.

[36] G. Goussetis, A. Feresidis, and J.C. Vardaxoglou, "Periodically Loaded 1D Metallodielectric EBG Structures," IEE Proceedings Microwaves Antenna and Propagation, Vol. 151, No. 6, pp. 481-485, Dec 2004.

Chapter 4

Analysis of 2-D Leaky-Wave Antennas with two periodic layers

"Doing easy what others find difficult is talent; doing what is impossible for talent is genius."

Henry-Frederic Amiel

4.1 Introduction

In this chapter, the technique presented in Chapter 2 is utilised for two different purposes. On one hand, it is used for the first time as a fast and accurate analysis and synthesis technique for the characterisation of high-gain sub-wavelength 2-D Fabry-Perot leaky-wave antennas (LWA) consisting of two periodic metallodielectric arrays over a ground plane. On the other hand, the same technique in combination with array theory is employed as a simple and rigorous analysis method to extract the complex dispersion characteristics of this LWA.

A complete description of the analysis technique is described in section 4.2. Full-wave method of moments (MoM) is initially used to determine the currents induced on the

patches. Reciprocity is subsequently employed to calculate the far-field radiation patterns, by reducing the calculations to the sampling of the near field excited within the antenna cavity upon plane wave illumination. Finally, the phase constant as obtained by MoM and reciprocity is used to estimate the radiation patterns for different values of the leakage rate using array theory. The correct value for the leakage rate is identified by matching the corresponding radiation pattern to that obtained using the full-wave method. Following the convergence analysis presented in chapter 3, the operation principles of these antennas as well as the radiation characteristics are discussed.

In section 4.3 design guidelines to tailor the antenna profile, the dimensions of the arrays as well as the antenna directivity and bandwidth are provided. A study on the radiation efficiency for antennas with different profiles is also presented and the trade off between directivity and radiation bandwidth is discussed. Numerical examples are given throughout to demonstrate the technique. A finite size antenna model is simulated using commercial software (Microstripes^{TM} 2009) which validates the technique.

Following these results, in section 4.4 we present results for the estimation of the complex dispersion of sub-wavelength LWA. A comparison with the Transverse Equivalent Network (TEN) method is provided. Unlike the transverse equivalent network method, the proposed technique maintains its accuracy on the calculation of the leaky-mode complex propagation even for antennas with low profile.

4.1.1 Highly Directive Leaky-Wave Antennas

The motivation behind the study of periodic planar 2-D Leaky Wave Antennas (LWA) is due to the significant interest that these antennas have attracted in recent years. This is mainly caused by their high gain and efficiency performance in conjunction with the advantages in terms of the low fabrication complexities in the microwave and millimeter-wave region [1-4]. Typical implementations of high-gain 2-D LWAs consist of a single layer periodic metallo-dielectric array acting as a partially-reflecting surface (PRS) and forming a resonant cavity with a ground plane positioned at a distance of about half-wavelength [5-9]. The bandwidth and gain of such antennas depend on the reflection (amplitude and phase) of the PRS, which in turn is determined from the PRS

geometrical characteristics [6]. Uniform 2-D LWAs have also been presented in the past [10-14] consisting of dielectric layers of alternating thickness and material constants, stacked over a ground plane. However, to achieve high-gain a number of layers or particularly high dielectric constants are required. Therefore, periodic metallodielectric PRS, which are compatible with commonly employed printed circuit techniques, are the best solution to minimize the number of required layers and offer increased design flexibility.

An efficient analysis of periodic 2-D LWAs has been recently presented based on the principle of reciprocity and full-wave spectral domain analysis [8, 9]. Highly directive planar antennas were achieved for PRSs consisting of both metallic patches or apertures etched in a fully conducing sheet. Other techniques have also been presented. An approximate ray-optics model was employed in [5] to extract the radiation pattern and the resonance condition. In [10] a transmission line model was introduced in order to predict the radiation characteristics and resonance conditions of antennas formed using multiple layers of dielectrics. However, in all cases the antenna profile, which is mainly determined by the resonance condition of the cavity, has always been approximately half-wavelength.

Over the last few years, planar periodic metallic arrays placed on a grounded dielectric substrate have been shown to behave as high impedance surfaces (HIS). Due to the effective high surface impedance, such surfaces reflect incident plane waves in–phase and are termed artificial magnetic conductors (AMC) [15-18]. Recently, a planar HIS ground plane [19-21] has been proposed as a means to reduce the profile of the high-gain resonant cavity 2-D LWA from approximately half wavelength to quarter wavelength [17] or to lower sub-wavelength values [22] as shown in Fig. 4-1. More recently, the LW analysis of thin subwavelength antennas based on a PRS and a HIS has been carried out using FDTD [23].

The radiation characteristics of infinite LWAs can also be obtained by the complex wavenumber of the associated leaky mode [12, 24]. The wavenumber dispersion allows estimation of the antenna radiating aperture profile, which in turn can be used to obtain the far-field radiation patterns, their beamwidths and associated bandwidths, as well as the variation of the antenna pointing angle with frequency [1]. Knowledge of the

complex dispersion relation is also helpful in the synthesis of practical LWAs. For example, the leakage rate allows estimation of the power radiated within a finite antenna length, which is essential in designing finite LWAs with high radiation efficiency. The complex wavenumber is also required for the systematic design of a non-uniform LWA, which can produce tapered illumination patterns that avoid phase aberration [1, 25-26], leading to far-field patterns with reduced side-lobes and antenna systems prone to reduce interference.

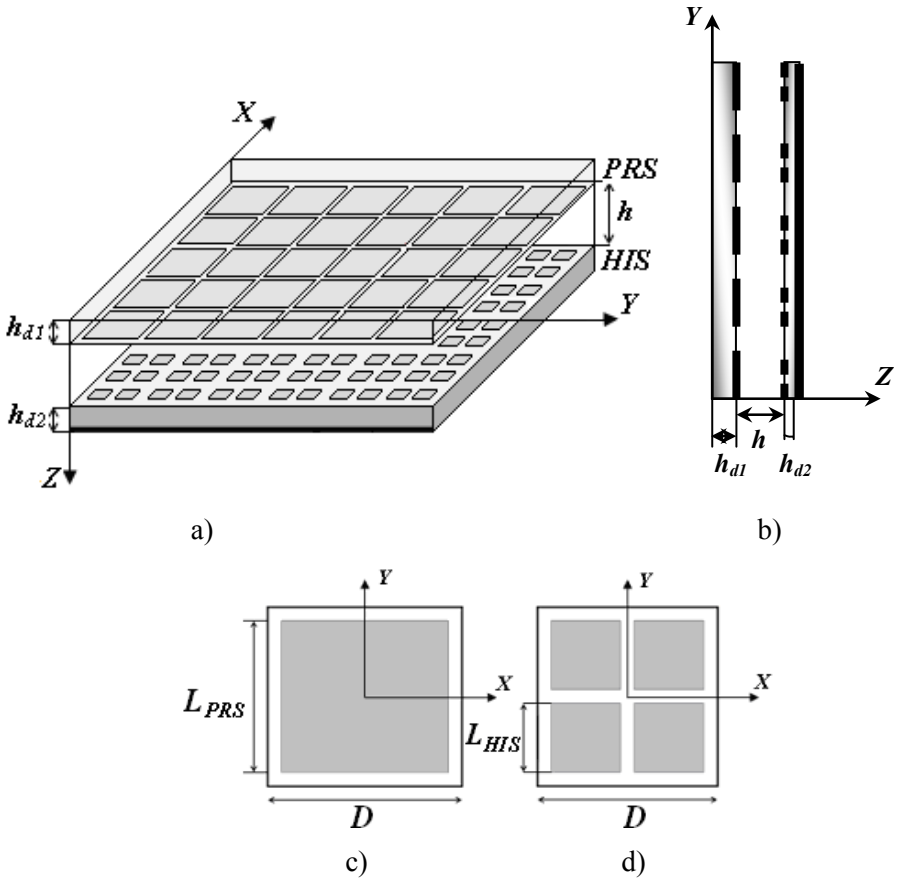

Fig.4-1. a) 3-D view and b) cross-section of the resonant cavity formed by metamaterial ground plane (HIS) and partially reflective surface (PRS) with excitation source inside the cavity c) Unit cell of a square patch PRS array and d) HIS array.

The complex dispersion of Fabry-Pérot LWAs with a PRS consisting of 2-D periodic metallodielectric arrays was first extracted in [27] employing a TEN and a pole-zero method to estimate the equivalent impedance of the array. Since a single mode TEN is employed, the accuracy of this technique is reduced for sub-wavelength profile antennas. Although it is possible to produce multiport TEN [28] and other formulations of the eigenvalue problem using full-wave techniques, such as MoM [27], the associated eigenvalue equations typically take non-canonical form [29], which is

cumbersome to solve numerically in the complex plane. Techniques based on the Finite-Difference Time-Domain (FDTD) method have also been developed in order to extract the dispersion of the complex wavenumber for this type of antennas [30-31]. These techniques can be time consuming, particularly for a fine discretization of the geometry and have limited accuracy for large values of the leakage rate.

4.2 Analysis Technique of Highly-Directive 2-D LWA

The analysis technique utilised to study 2-D LWA such as the one shown in Fig. 4-1 is presented next. We employ working examples where both arrays are capacitive and consist of metallic square patches. The periodicities of the two arrays are assumed commensurate (Fig. 4-1), this ensures that the set of Floquet Space Harmonics (FSH) associated with the PRS array is also suitable for expanding the fields at the HIS array. Despite introducing some redundancy in the expansion of the fields related to the latter, this allows modelling of the overall structure using well-established spectral domain techniques as described in chapter 2 and [32-34]. In order to provide high reflectivity, the PRS typically operates close to the array resonance. For this reason, square patches of the order of half wavelength are employed. The HIS operation resembles that of an artificial magnetic conductor [17], which can be achieved with smaller unit cells. Here the periodicity of the HIS ground plane is half of that of the PRS array in both directions.

4.2.1 MoM and Reciprocity

Reciprocity is invoked for the analysis of this LWA, which reduces the estimation of the far-field radiation characteristics to the calculation of the fields at an observation point inside the antenna when illuminated by a plane wave of fixed magnitude and a varying angle of incidence. The technique is described in [8] for antennas consisting of a single periodic layer and exploits the fact that the receiving and transmitting field patterns for an antenna are identical [35]. Without loss of generality, in the following we assume that the antenna is fed by a Hertzian dipole parallel to the y-axis and located at the

aforementioned observation point inside the cavity. By scanning the relative field strength, E_y, at the observation point, the (receiving) radiation pattern of the antenna can be obtained. In a practical implementation, a half wavelength dipole can be utilized as in [22] without significant perturbation in the antenna directivity. Moreover, once the 3-D radiation pattern is determined the integration of the obtained values can be used as reference in order to obtain the directivity pattern, so that,

$$D(\theta,\varphi)=\frac{4\pi\cdot|E(\theta,\varphi)|^2}{\iint\limits_{\theta,\varphi}|E(\theta,\varphi)|^2\cdot\sin(\theta)\cdot d\theta\cdot d\varphi} \tag{4.2-1}$$

where D(θ, φ) is the directivity of the antenna in the direction (θ, φ) and E(θ, φ) is the electric field (E_y) at the observation point excited by a plane wave incident from (θ, φ). The theoretical background is well documented in [8] and therefore not further expanded here.

Using reciprocity allows for a fast and accurate analysis using periodic spectral domain method of moments (MoM) technique as described in chapter 2, [32-34]. To express the current on the patches a finite summation of zero-ended orthogonal entire domain basis functions is employed, hence ensuring further computational efficiency. The in-house software developed in chapter 2 is used for the computation of the near fields excited at a point inside the antenna cavity under plane wave illumination. Moreover, the results derived from the convergence study related to the number of basis functions and the number of FSH carried out in chapter 3 is considered throughout.

4.2.1.a Influence of the observation point location in the near-field calculation

The aim here is to analyse the influence of selecting the point where the near-fields are calculated. In order to do so the near-fields are calculated considering the source (e.g. Hertzian dipole) displaced at different points within the unit cell. The antenna under consideration –antenna#2- (Fig. 4-1) involves a PRS consisting of patches with edge 8.0 mm and periodicity 9.0 mm printed on a dielectric slab of thickness 1.5 mm and relative permittivity 2.55. In the remaining, this will be referred to as PRS1. This PRS is located

at a distance h= 5.45 mm (~λ/4 at f=14GHz) above the HIS array, which consists of patches with edge 4.15 mm and is printed on a dielectric slab of thickness 1.15mm and relative permittivity 2.2.

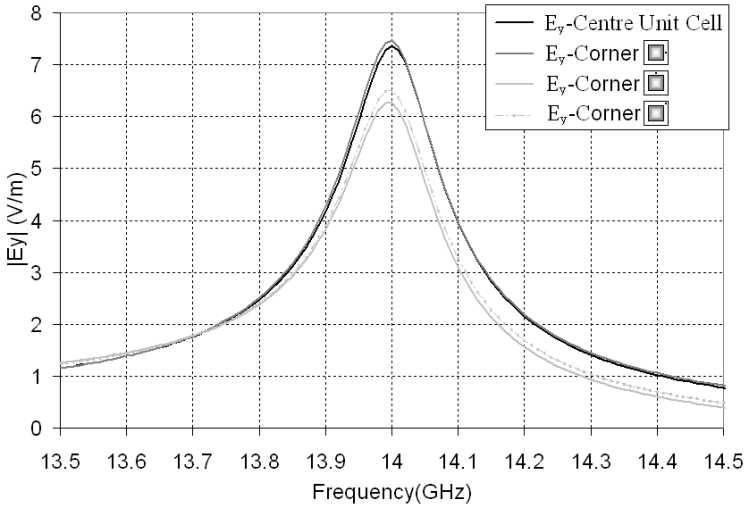

Fig. 4-2 Magnitude of the y-component of the electric field in the centre of the unit cell (x= y= 0), (x=4.25mm, y= 0), (x=0, y= 4.25mm) and (x=4.25mm, y= 4.25mm) at z=h/2 for antenna#2. The dimensions (in mm) D= 9.0, h=5.45, for PRSs: square patches L_{PRS1}=8, h_{d1}=1.5 and ε_r=2.55 For the HIS: square patches L_{HIS}=4.15, h_{d2}=1.15 and ε_r=2.2.

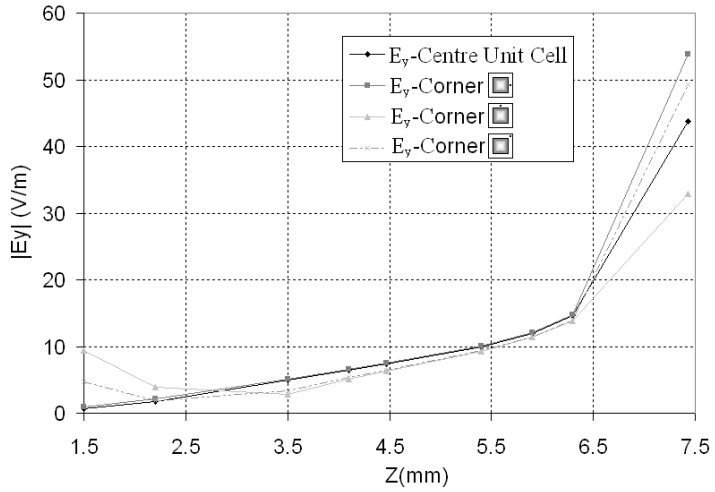

Fig. 4-3 Magnitude of the y-component of the electric field in the centre of the unit cell (x= y= 0), (x=4.25mm, y= 0), (x=0, y= 4.25mm) and (x=4.25mm, y= 4.25mm) at different points inside the cavity for antenna#2. The dimensions (in mm) D= 9.0, h=5.45, for PRSs: square patches L_{PRS1}=8, h_{d1}=1.5 and ε_r=2.55 For the HIS: square patches L_{HIS}=4.15, h_{d2}=1.15 and ε_r=2.2.

Fig. 4-2 shows the near-field excited in the middle of the cavity and at different points within the unit cell ((x=0, y=0), (x=4.25mm, y=0), (x=0mm, y=4.25) and

(x=4.25mm,y=4.25)). In the calculation of the near-field, the convergence analysis presented in chapter 3 is kept in mind. It can be observed that the maximum appears at the same frequency of operation but the value of the field is lower when the dipole is displaced from the centre of the unit cell. This conclusion can also be corroborated by the results presented in Fig. 4-3 where the near-field calculated considering the source (e.g. Hertzian dipole) displaced at different points within the unit cell ((x=0, y=0), (x=4.25mm, y=0), (x=0mm, y=4.25) and (x=4.25mm,y=4.25mm)) and at different points inside the cavity (different Z values) are shown. Despite the similarity of the fields at central points in the cavity as the observation point is closer to either array the value of the fields are more dissimilar depending on the (x, y) position within the unit cell.

4.2.1.b Operation Principle of the antenna

The high-gain 2-D LWA is known to operate at a mode which is a perturbation of the first order TE and TM modes of the parallel plate waveguide formed between the PRS and the ground plane [23, 36]. By substituting one of the two parallel plates by a PRS, the fast waveguide modes are allowed to radiate. For broadside radiation, the antenna operates close to the cut-off of the parallel plate waveguide TE/TM mode. At this frequency the distance between the parallel plates is equal to half wavelength, and a standing wave in the transverse direction is formed. This leads to a resonant Fabry-Perot type cavity model for this type of antennas. For this reason, antennas formed with a single periodic array (only as PRS, [6]) typically have a profile of half wavelength.

This is demonstrated in Fig. 4-4, where the y-component of the electric field is plotted against the z-axis for an antenna employing PRS1 and with profile λ/2 at the centre of the unit cell. The introduction of a HIS ground plane modifies the reflection characteristics and hence the transverse resonance condition [17]. In this way, the HIS reduces the cut-off frequency of the parallel plate waveguide and eventually the antenna profile. Fig. 4-4 also shows similar field distributions for antennas all producing a pencil beam at boresight at 14GHz with different profiles λ/3, λ/4, λ/5, λ/7 and λ/12 (detailed design guidelines will be introduced in the next section.). It is important to mention that on the calculation of the near-field component (E_y) the convergence study carried out in the previous chapter has been kept in mind, meaning that the number of FSH considered

for each antenna profile is the one depicted in Fig. 3-7 from chapter 3. From Fig. 4-4 one can note that thinner antennas increasingly deviate from the typical half wavelength field distribution, exhibiting a field maximum at the plane of the HIS array. Moreover, significant near field enhancement is observed for thinner antennas which can be useful in e.g. sensor applications.

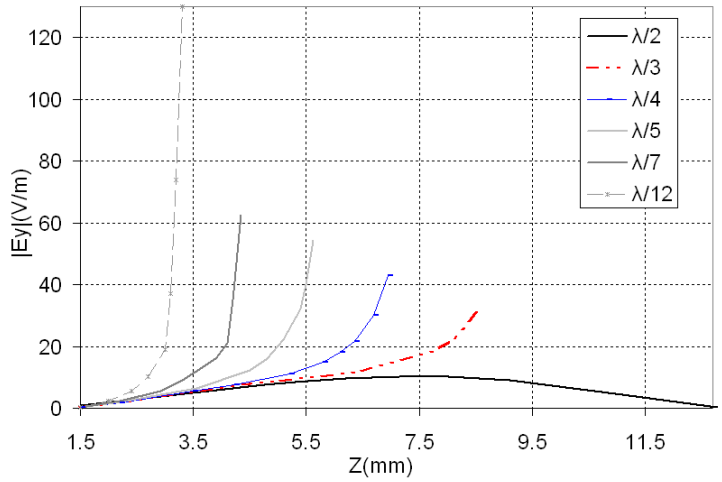

Fig. 4-4 Distribution of the y-component of the electric field at the centre of the unit cell (x= y= 0) and varying z for six different antennas with different profile (shown in the legend as a function of the wavelength, λ) all operating at 14 GHz.

4.2.1.c Radiation Characteristics of sub-wavelength 2-D LWA

The application of near-field calculation and reciprocity in the calculation of the 3-D directivity pattern, by using Eq. (4.2-1), for low-profile 2-D LWA with two periodic arrays is demonstrated next. As an example antenna#2 is considered. Fig. 4-5 shows the 3-D directivity pattern calculated by estimation of the near-fields at $z=h/2$ (e.g. centre of the cavity) and at the centre of the unit cell considering 120 FSH in both directions (Fig. 3-7) when the antenna is excited by a normally incident plane wave polarized along the horizontal direction (E_y). As shown, a pencil beam with directivity of about 20.9 dB at broadside is produced. Since the analysis is based on an infinite array assumption, no sidelobes emerge below the grating lobe frequencies for a single fast propagating mode.

To demonstrate the frequency dependence of this radiation pattern, Fig. 4-6 shows the H- and E-plane cuts of this radiation pattern for three frequency points. In agreement

with the performance of half-wavelength antennas, as the frequency increases from that of broadside radiation, a conical pattern is obtained.

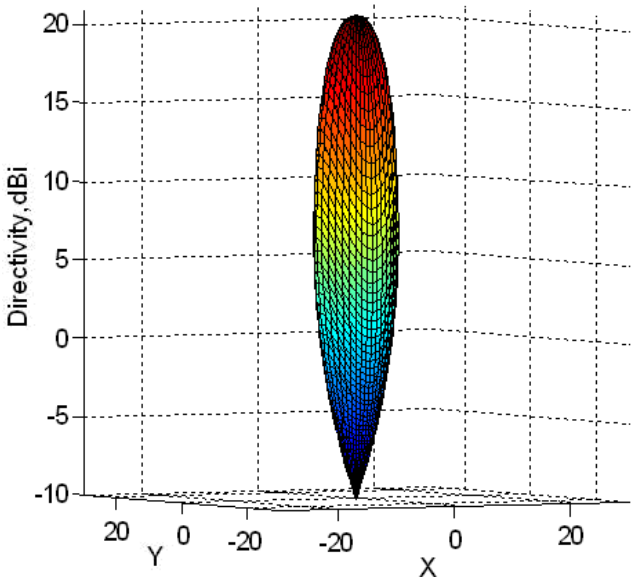

Fig. 4-5 3-D directivity pattern of a LWA formed by PRS1, L_{HIS}=4.15mm and profile h= 5.45mm (~λ/4) at 14GHz (antenna#2).

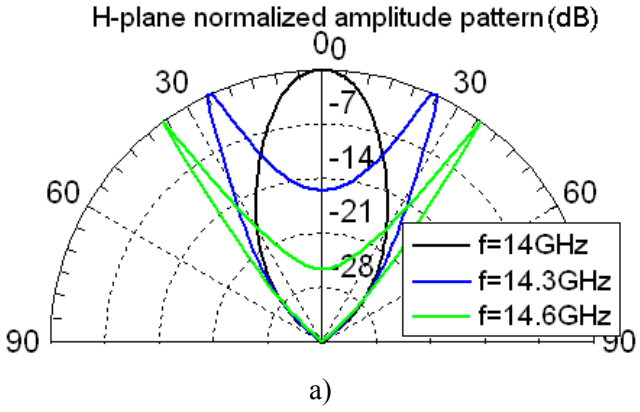

a)

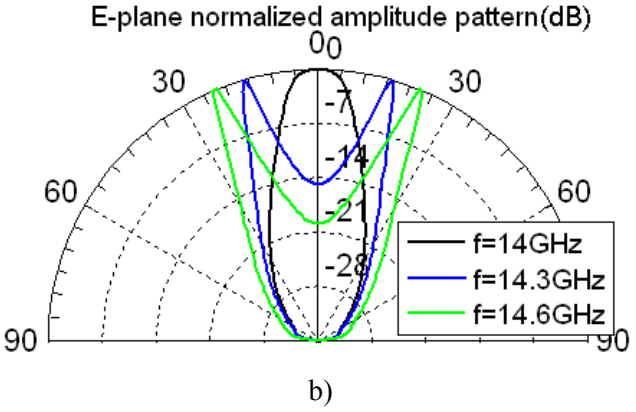

b)

Fig. 4-6 a) H- plane and b) E-plane cuts of antenna#2 at different frequencies. The dimensions (in mm) D= 9.0, h=5.45, for PRSs: square patches L_{PRS1}=8, h_{d1}=1.5 and ε_r=2.55 For the HIS: square patches L_{HIS}=4.15, h_{d2}=1.15 and ε_r=2.2

4.2.2 Complex dispersion estimation of Fabry-Perot LWA

A new fast and rigorous technique for the estimation of the complex dispersion of sub-wavelength periodic 2-D LWAs is proposed in the following. The complex wavenumber, $\boldsymbol{k}$, of a leaky-mode in general takes the form,

$$k = \beta - j\alpha\left(m^{-1}\right) \tag{4.2-2}$$

where β is the phase constant and α is the leakage rate. The complex nature of $\boldsymbol{k}$ expresses the decrease of the amplitude of the leaky wave as it propagates due to radiation. In the absence of other sources of radiation, the phase constant, β, determines the pointing angle, θ, of the antenna's main lobe and the leakage rate, α, determines the illumination of the radiating aperture. Significantly, the radiation pattern of a LWA can be obtained analytically for a uniform LWA with a given complex wavenumber [1, 37]. The method that we propose here is based on the following procedure; the radiation pattern of a particular infinite-size LWA is initially obtained using the analysis technique explained in section 4.2.1. Subsequently an iterative procedure is employed based on array theory [35, 37] in order to reproduce this pattern from pairs of β and α. Since the calculations involved in this iterative process are analytical, and since prior knowledge of the propagation constant, β, can be obtained by the angle of maximum radiation, the proposed technique is fast and computationally efficient. In the following we present the method and the analytical expressions involved in the calculation of the radiation patterns.

4.4.2.a Array Factor approach

The array factor (AF) approach serves as an alternative method to calculate the radiation characteristics of periodic LWAs [35, 37]. The array factor for a 2-D planar array is given by the following expression [35],

$$AF(\theta,\varphi) = \left[\sum_{m=-\frac{M}{2}}^{m=\frac{M}{2}} I_{m1} e^{j(m-1)(k_0 D_x \sin\theta\cos\varphi)+j\xi_m}\right] \cdot \left[\sum_{n=-\frac{N}{2}}^{n=\frac{N}{2}} I_{1n} e^{j(n-1)(k_0 D_y \sin\theta\sin\varphi)+j\xi_n}\right] \tag{4.2-3}$$

where D_x / D_y is the periodicity and M / N is the number of unit cells along the x- / y-axis respectively. For an infinitely long antenna there is no contribution to the radiation by edge effects. The phase ξ_m /ξ_n in Eq. (4.2-3) represents the relative phase shift of the excitation for the m / n order element referenced to the element at the origin. Assuming that all higher Floquet space harmonic (FSHs) are evanescent and only the fundamental can radiate, then the relative phase shift is determined by the propagation constant, $\beta_{x/y}$, of the fundamental FSH in the x- / y- directions:

$$\xi_m = -(m-1)\beta_x D_x \qquad \xi_n = -(n-1)\beta_y D_y \tag{4.2-4}$$

The relevant excitation strength of the m^{th} / n^{th} array element, I_{m1} / I_{1n} in Eq. (4.2-3), can be obtained from the attenuation rate, α_x / α_y, due to the leakage, as well as the magnitude of the reference element, I_o. Since for a uniformly periodic array the leakage rate, α, is constant along the antenna, the excitation strength drops exponentially for elements away from the excitation point. To a step approximation, we can therefore write for the m^{th} / n^{th} element along the x- / y-axis,

$$I_{m1} = I_0 e^{-\alpha_x (m-1) D_x} \qquad I_{1n} = I_0 e^{-\alpha_y (n-1) D_y} \tag{4.2-5}$$

The radiation pattern of the antenna under consideration can be obtained as the product of the array factor with the radiation pattern of the PRS array element. In this example we assume a free-standing PRS consisting of square patches with edge L (Fig. 4-1) whose radiation intensity, U , at every (θ,φ) can be obtained using Babinet's principle from that of a rectangular aperture [35],

$$U(\theta,\varphi) = \frac{\pi^2 \eta_0 (L\cdot L)^2 |E_0|^2}{8\lambda_0^2} \left[\frac{\cos\left(\frac{k_0 L}{2}\sin\theta\cos\varphi\right)}{\left(\frac{k_0 L}{2}\sin\theta\cos\varphi\right)^2 - \left(\frac{\pi}{2}\right)^2} \right]^2 \cdot \left[\frac{\sin\left(\frac{k_0 L}{2}\sin\theta\sin\varphi\right)}{\frac{k_0 L}{2}\sin\theta\sin\varphi} \right]^2 \cdot \left(\sin^2\varphi + \cos^2\theta\cos^2\varphi\right) \tag{4.2-6}$$

where k_0 is the free space wavenumber, η_0 is the intrinsic impedance and E_o is a constant. By combining Eq. (4.2-3) and (4.2-6), the radiation pattern of a LWA such as the one depicted in Fig. 4-1 can be analytically obtained for a given wavenumber $\boldsymbol{k}$.

4.4.2.b Derivation of the complex propagation constant

As shown above, the estimation of the radiation pattern following an array factor approach requires prior knowledge of both the real, β, and imaginary, α, part of the wavenumber, $\boldsymbol{k}$. In order to reduce the complexity of the problem, the former can be obtained by tracking the angle of maximum directivity in the full-wave radiation pattern as in Fig. 4-6. In particular, in order to extract the dispersion of the propagation constant in a particular direction the radiation pattern of the antenna under consideration is obtained at different frequencies. The angle, θ, corresponding to the direction of maximum directivity for each frequency is then related with β by means of simple trigonometry [1] (Fig. 4-7),

$$\beta = k_0 \cdot \sin\theta \tag{4.2-7}$$

where k_0 is the free-space wavenumber, β_x / β_y correspond to the phase constants along the H- / E-plane and can be obtained by varying the angle of the incident wave along the xz- / yz-planes respectively.

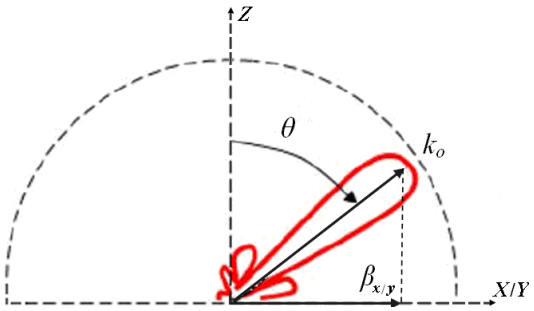

Fig. 4-7 Estimation of the propagation constant from the angle of maximum gain at the H-plane (β_x) and the E-plane (β_y) for a LWA.

Subsequently, the AF approach is employed to obtain the dispersion of the leakage rate, α. This can be estimated using an inverse and iterative procedure. For each frequency point, we use the corresponding value of the propagation constant, β, and the radiation pattern is successively estimated according to Eq. 4.2-3 for different values of the leakage rate, α. For each value of α, the corresponding radiation pattern is compared with the one derived using the technique in section 4.2.1. This is done by calculating an error function which is expressed as the mean-square error between the two normalised patterns. The value of α for which the error function is minimized corresponds to the actual value of the leakage rate at the particular frequency. For a new frequency point,

estimations of the leakage rate at nearby frequencies can be used as starting values, also considering that higher frequencies typically produce lower leakage rates. Since the calculations involved in the iterative procedure are analytical, the proposed method is fast and efficient.

4.3 Design Considerations

A series of broadside LWAs with different profiles, all designed to produce broadside radiation at 14 GHz are employed as examples. Detailed design guidelines for these LWAs will follow in the next section. An antenna formed using PRS1 and no HIS array has a profile of approximately equal to half wavelength (h=11.28 mm) and in the following will be referred to as antenna #0. Antennas with profile, h, approximately equal to λ/3, λ/4, λ/5, λ/7 and λ/12 have also been designed using the same PRS1 and HISs with varying patch size, L_{HIS}. In the following these will be referred to as antennas #1-#5 respectively and the corresponding HISs are numbered accordingly. All HISs are printed on a dielectric substrate of thickness h_{d2}=1.15 mm and ε_r=2.2. The patch dimensions for the HISs are (in mm) L_{HIS1}= 4.0, L_{HIS2}= 4.15, L_{HIS3}= 4.25, L_{HIS4}= 4.35 and L_{HIS5}= 4.45 respectively. The thickness of the cavities, h, for antennas #1-#5 are (in mm) h_1= 7.05, h_2= 5.45, h_3= 4.12, h_4= 2.85 and h_5= 1.81 respectively. Design guidelines for these antennas follow next.

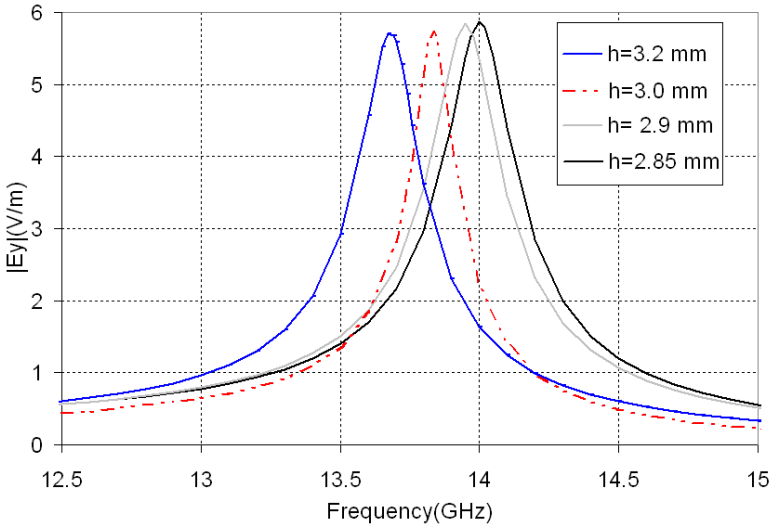

Fig. 4-8 Magnitude of the y-component of the electric field in the centre of the unit cell (x= y= 0) and at z=h/2 for an antenna with PRS1 and HIS4 for varying profile, h.

4.3.1 Antenna Profile

To a first approximation the profile of 2-D LWA with two periodic layers (Fig. 4-1) can be determined employing a ray optics model[1] [17]. However for thinner cavities the single mode approximation becomes less accurate and therefore this model provides a worse estimation. Calculation of the near-fields inside the cavity in conjunction with reciprocity arguments can be employed towards a more accurate procedure for determining the antenna profile. Reciprocity suggests that at the central operating frequency of broadside antennas, the fields at the observation points are maximised for a given normally incident wave. Therefore, scanning the fields over the frequency yields the central operating frequency of the antenna at the peak of the observed curve. By modifying the antenna profile, it is then possible to tune the design to the specified frequency.

This is shown here by means of an example involving an antenna formed by PRS1 and HIS4. The ray optics model suggests that for broadside operating frequency at 14 GHz, the antenna profile should be 3.0 mm. Commencing from this value, Fig. 4-8 shows the near fields at the centre of the antenna cavity for different antenna profiles, h. As expected from the ray optics model, lower cavity profiles yield operation at higher frequencies. The optimal profile for this antenna for broadband operation at 14GHz is determined to be h=2.85 mm (this is approximately $\lambda/7$). This value varies by 5% compared to the value obtained through the ray optics model where 30BF were employed to model the currents on the elements of the HIS4, 5 BF to model the currents on the elements of the PRS and 170FSH have been considered in order to calculate the reflection phase of HIS4.

4.3.2 HIS dimensions

For a design procedure that commences from a given operating frequency, as well as antenna profile and a fixed PRS, reciprocity can be employed to determine the required HIS dimensions to meet the radiation requirements. The antenna composed of PRS1 above HIS2 at a distance 5.45mm, which operates at 14GHz, is employed as an example. The fields at the observation point in the centre of the cavity and the unit cell

[1] This model will be briefly introduced in chapter 5.

are shown versus frequency for five different values of the lower array element size (HIS1, HIS2, HIS3, HIS4 and HIS5) for normal incidence in Fig. 4-9. As shown, by increasing the lower array element size, the operating frequency of the antenna for broadside radiation reduces. This is in agreement with previous results [22] and to a ray optics approximation can be attributed to the reduced reflection phase provided by HIS arrays with larger element size (plotted in the inset of Fig. 4-9). This graph suggests that it is possible to design an antenna that operates at a specified frequency with a specific profile and a given PRS solely by modifying the lower array dimensions. Since the reflectivity of the PRS is typically directly associated with the directivity of the antenna, this process can be useful in the design of antennas that meet a required gain specification.

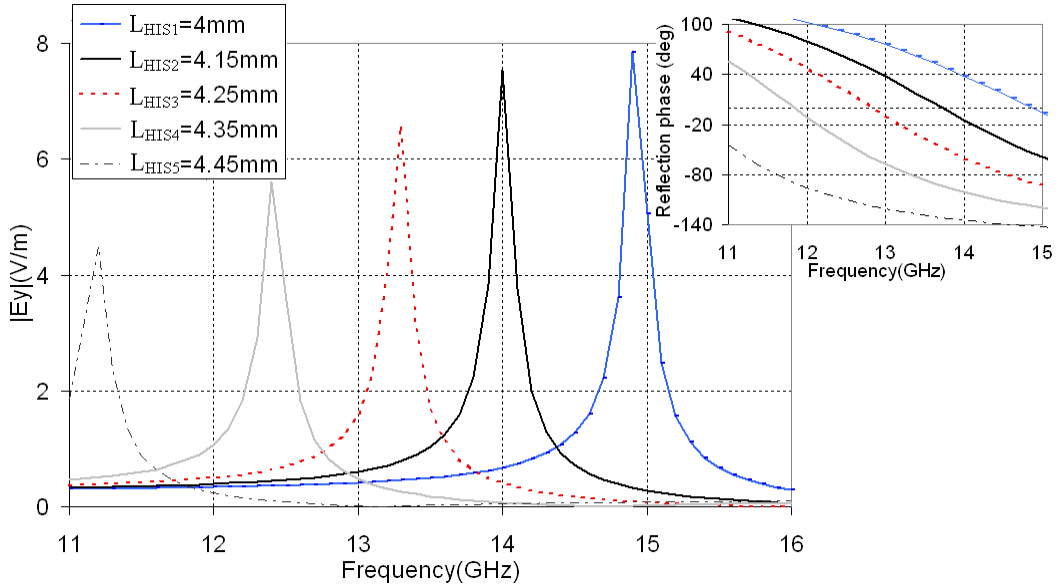

Fig. 4-9 Magnitude of the y-component of the electric field in the centre of the unit cell (x= y= 0) and at z=h/2 for an antenna with PRS1 for varying HIS element, L_{HIS}. Inset: Reflection phase by HIS1, HIS2, HIS3, HIS4 and HIS5 with D=9 mm, ε_r=2.2, h_{d2}=1.15 mm and L_{HIS1}= 4.0 mm, L_{HIS2}= 4.15 mm, L_{HIS3}= 4.25 mm, L_{HIS4}= 4.35 mm and L_{HIS5}= 4.45 mm.

4.3.3 Directivity

Leaky wave theory suggests that among electrically large LWAs, those with lower leakage rates produce larger radiating apertures and therefore more directive patterns. Intuitively, it is plausible to expect that antennas formed by more reflective PRSs will produce lower leakage rates. Indeed, simple ray optics model predicts that a more reflective PRS results in a higher directivity [5]. A method to extract the directivity of

the LWA under consideration was discussed in the previous section. Here by means of an example employing two LWAs with the same profile that operate at the same frequency, we demonstrate the possibility to tailor the directivity by modifying the PRS.

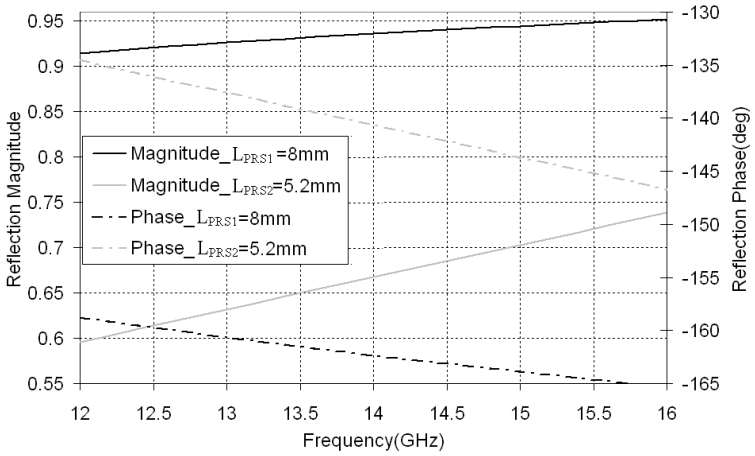

Fig. 4-10 Reflection coefficient (magnitude and phase) by two PRSs with dimensions (in mm) D=9.0, L_{PRS1}=8.0 and L_{PRS2} =5.2.

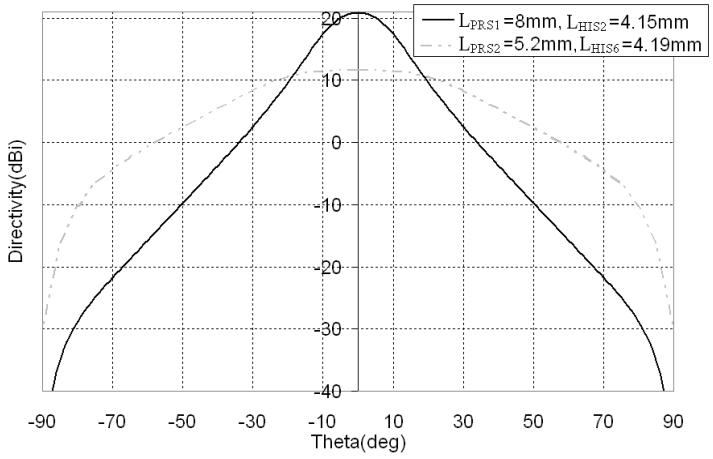

a)

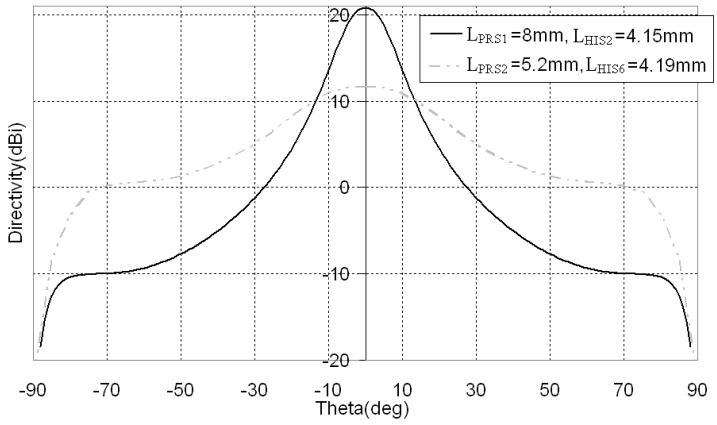

b)

Fig. 4-11 Directivity pattern at a) H-plane and b) E-plane of two LWA formed with a PRS: square patches L_{PRS}=8 and 5mm, h_{d1}=1.5 mm and ε_r=2.55, and an HIS: square patches L_{HIS}=4.15

and 4.19mm respectively, h_{d2}=1.15 mm and ε_r=2.2, with profile 5.45 mm operating both at 14 GHz.

Following the technique outlined above, we design two antennas for broadband radiation at 14 GHz with thickness of the cavity, h=5.45 mm (profile ~λ/4) employing two PRSs, namely PRS1 and PRS2, with different reflectivity at 14 GHz. In particular, we employ as an example antenna #2 (composed by PRS1) from the previous section. The reflection magnitude and phase of PRS1 is shown in Fig. 4-10. Fig. 4-10 also shows the reflection magnitude and phase of PRS2, which shares the same geometrical features with PRS1, but the patch size is L_{PRS2}= 5.2 mm. As shown, a capacitive square patch PRS with fixed periodicity becomes increasingly reflective below resonance for larger patches. The antennas can be designed by tuning the HIS dimensions to 4.15 mm and 4.19 mm respectively, as discussed above. The E and H plane cuts of the antennas directivity are shown in Fig. 4-11. As shown, the antenna formed using PRS1 produces directivity approximately 9.2 dB greater than that formed using PRS2. This is mainly attributed to the higher reflectivity of PRS1 at 14 GHz (Fig. 4-10). This result implies that it is possible to design a tailored directivity simply by modifying the reflectivity of the PRS. As will be discussed in the following subsection, increased directivity however comes at a cost of reduced bandwidth.

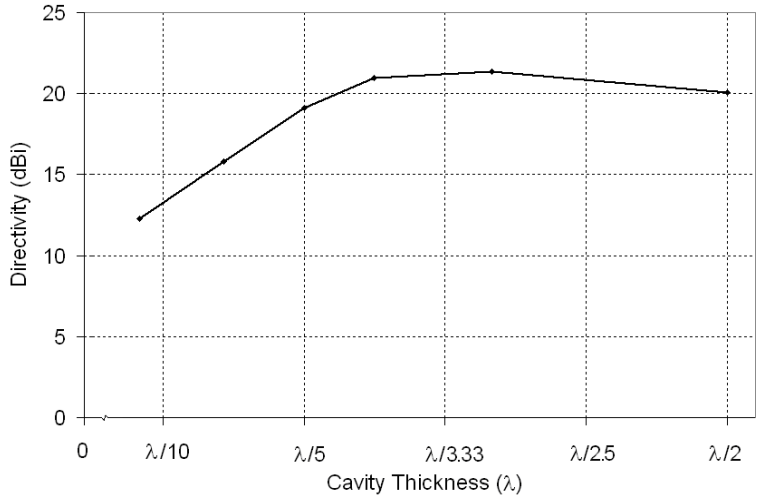

Fig. 4-12 Directivity at boresight of antenna#0-antenna#5 at the operating frequency, 14GHz.

It is further instructive to study the directivity of antennas with a fixed PRS and varying profile. Fig. 12 shows the directivity of antennas #0-#5, all of which employ the same PRS but have increasingly reduced profile. As shown, antennas with increasingly lower

profile produce reduced directivity for a given PRS. This is in agreement with the observations in [23], where full wave simulations of finite antennas were employed to demonstrate a reduced illuminating aperture for thinner arrays.

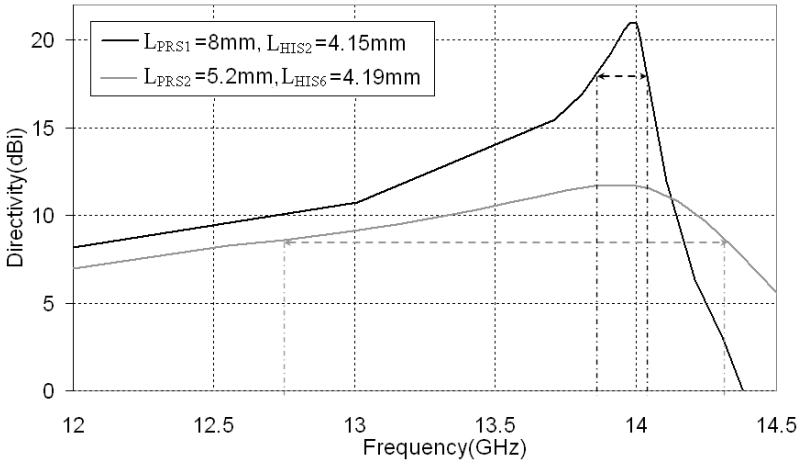

a)

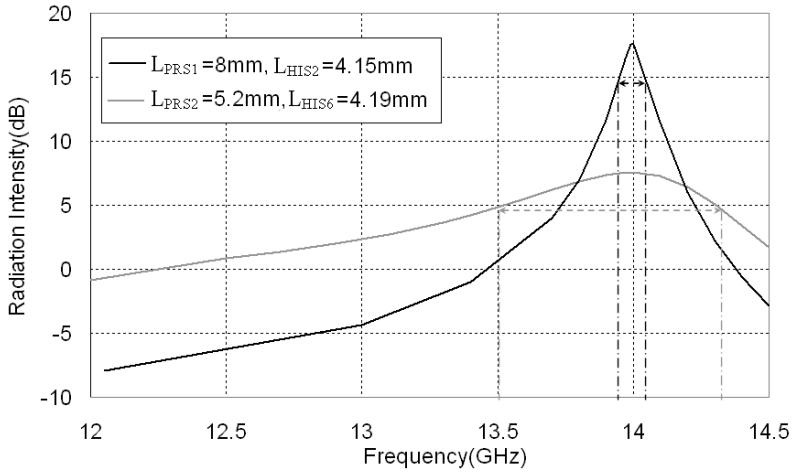

b)

Fig. 4-13 a) Directivity and b) radiation intensity at boresight vs. frequency of the two antenna designs, PRS1-HIS2 and PRS2-L_{HIS}=4.19 mm, operating both at 14GHz.

4.3.4 Bandwidth

In section 4.2 it was shown that commonly to all LWA, the radiation patterns of the antennas under investigation change with frequency due to the dispersion of the radiating mode. Beyond matching considerations, the 3 dB pattern bandwidth of the antenna can be obtained as the bandwidth within which the fields at the observation point drop within 3 dB of their peak value. The directivity bandwidth is similarly defined as the frequency range within which the directivity of the antenna at a certain

direction (typically broadside) varies within 3 dB of its maximum value. The pattern and directivity bandwidth for the two antennas of Fig. 4-10 have been calculated and are plotted in Fig. 4-13. As shown, the 3 dB directivity and pattern bandwidths for antenna # 2 formed with PRS1 are 90% and 88% narrower than those formed with PRS2, respectively. In agreement with the observation made in [38], the directivity bandwidth for each antenna is wider than the pattern bandwidth.

Since PRS1 is more reflective than PRS2, the cavity formed by PRS1 is more weakly coupled to the incoming plane wave and therefore produces a higher external quality factor than the cavity formed by PRS2. As the external quality factor (in case of no ohmic losses) is inversely proportional to the 3 dB fractional bandwidth, a higher external quality factor implies that the 3 dB fractional bandwidth is narrower [39]. We note that in this case the reactive power stored in the resonator is also higher. The technique described in this and the previous subsections provide the designer with tools to address the trade off between bandwidth and directivity.

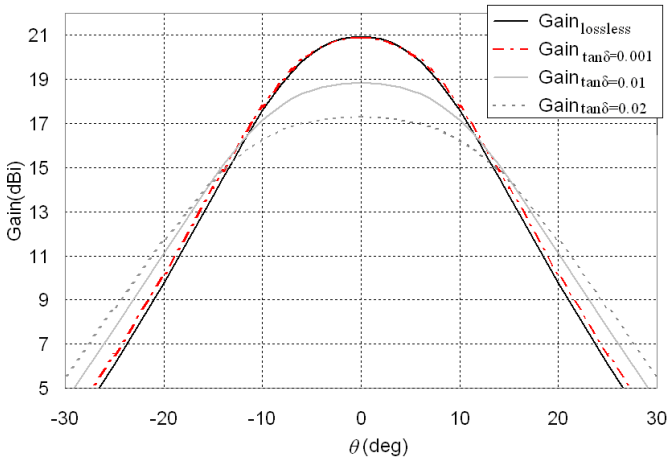

Fig. 4-14 Gain of the LWA formed with PRS1 and HIS2 operating at 14 GHz for different dielectric substrates.

4.3.5 Antenna Efficiency

So far this study has been undertaken assuming zero thermal losses. In practice, losses reduce the antenna efficiency. The radiation efficiency, e, (i.e. antenna efficiency neglecting the mismatch) can be obtained as the ratio of the total radiated power in the presence of thermal losses over the total radiated power in the absence of thermal

losses,

$$e = \frac{\iint_{\theta,\varphi} \left|E_{lossy}(\theta,\varphi)\right|^2 \cdot \sin(\theta) \cdot d\theta \cdot d\varphi}{\iint_{\theta,\varphi} \left|E_{lossless}(\theta,\varphi)\right|^2 \cdot \sin(\theta) \cdot d\theta \cdot d\varphi} \tag{4.3-1}$$

where E_{lossy} / $E_{lossless}$ are the fields at the observation point for a given plane wave incidence assuming/neglecting thermal losses. If the effect of losses is introduced in the MoM formulation, then the antenna radiation efficiency can be readily obtained for the LWA under consideration. In practice, the main source of thermal losses for this type of antennas in the microwave regime arises from the dielectrics [23]. To a good approximation, we have therefore assumed that the metallization is perfectly conducting.

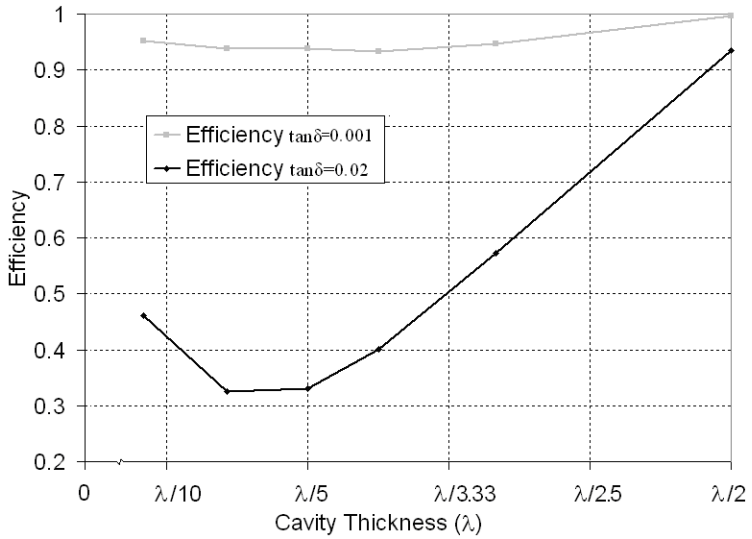

Fig. 4-15 Antenna efficiency for the antennas in Fig.4-2 considering a dielectric substrate with tanδ=0.02 (equal to that of FR4) and a dielectric substrate with tanδ=0.001 (equal to that of TEFLON).

The gain obtained for antenna #2 (PRS1 and HIS2) by increasing the loss tangent of the dielectric substrates involved is depicted in Fig. 4-14. As shown, losses of about 3.6 dB are incurred when the loss tangent value increases to 0.02 (e.g. FR4 substrate). This is because part of the near field stored in the antenna is dissipated as heating in the dielectric substrates. As it was shown in Fig. 4-4, the near fields stored in the vicinity of the antenna cavity are generally increasing for cavities of reduced profile. Increased thermal losses are therefore predicted in the presence of non-perfect dielectrics for antennas of lower profile. This is presented in Fig. 4-15 showing the efficiency of the

antennas involved in Fig. 4-4 when the loss tangent of the dielectrics is either 0.02 (equal to that of FR4) or 0.001 (equal to that of Teflon). As a result of the dielectric losses, antenna#4 with profile λ/7 exhibits efficiency reduced by 54% and 4.8% respectively compared to the λ/2 antenna. It is worth noting that the efficiency appears to increase for very thin antennas in the order of λ/12, which is in agreement with the observations in [23].

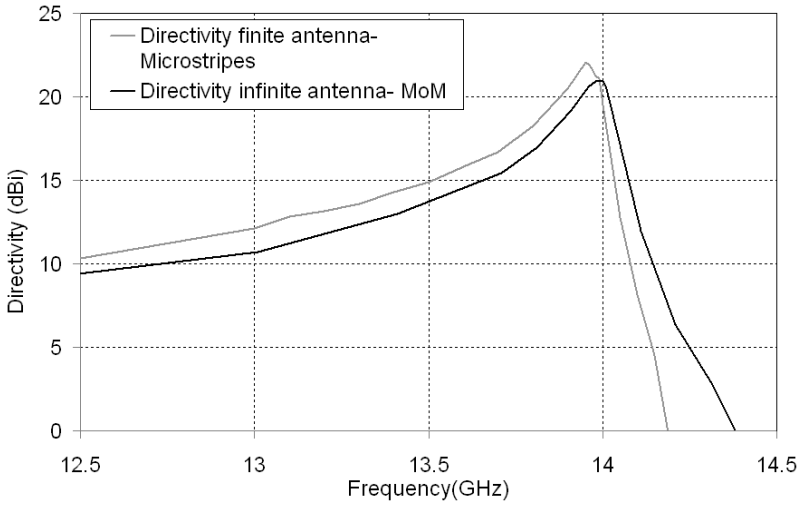

Fig. 4-16 Directivity at boresight vs. frequency for the infinite and finite antenna #2 design using the proposed technique and CST microstripes.

4.3.6 Finite Antenna

The antennas studied in the previous sections have been designed under the consideration of infinite lateral size. In order to check the agreement of the proposed technique with a finite size antenna realization, a finite size model of antenna #2 is simulated using a 3-D electromagnetic simulator (CST Microstripes^{TM} 2009). The lateral dimensions of the antenna are 225 x 225 mm^2, i.e. just over 10λ. These dimensions have been chosen in order to achieve a practical design with minimized edge effects that can be compared with the infinite model. Further studies have shown that smaller antenna sizes shift the resonance to higher frequencies and also degrade the radiation performance in terms of higher sidelobes and lower directivity, with all these effects being more pronounced for sizes less than 5λ. For simulation purposes, a centre fed 3 mm long wire model dipole is used to feed the cavity. The radius of the wire is 0.15 mm and the distance from the HIS substrate is 2.725 mm (i.e. centre of the cavity, z=h/2). Fig. 4-16 shows the boresight directivity as a function of frequency for antenna #2 calculated using the proposed technique as well as the corresponding finite size

model. A very good agreement is observed, with a discrepancy of less than 0.2% in the frequency and 4% in the value of maximum directivity, which can be attributed to numerical tolerances of both techniques. This validates the proposed technique as a fast and accurate tool for the design of the proposed antennas.

4.4 Numerical examples of the complex dispersion analysis

Here we initially demonstrate the application of the proposed method for the calculation of the complex propagation constant in working examples of resonant cavity antennas with a single periodic array and half-wavelength profile. Subsequently, we extend this technique to the case of antennas with two periodic arrays and sub-wavelength profile with unit cell as in Fig. 4-17. The results from the proposed technique are compared with those from a TEN, where a pole and zero method is employed for the estimation of the effective impedance of the arrays. The latter is very well described in [40, 41] and therefore applied here directly.

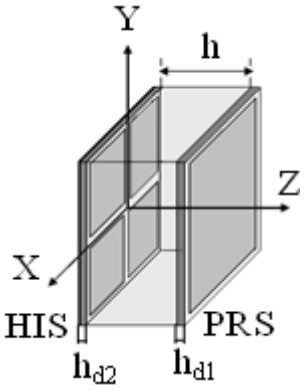

Fig. 4-17 Layout of the resonant cavity leaky-wave antenna unit cell formed by metallodielectric PRS and HIS with excitation source inside the cavity.

4.4.1 Transverse Equivalent Network model

A brief overview of the technique is given in this subsection. The structure of Fig. 4-17 can also be considered for modelling purposes as a leaky parallel-plate waveguide having a plate separation *h*, with the top plate of the waveguide replaced with a shunt admittance screen that acts as a partially reflecting surface (PRS). This realization allows for such structures to be analyzed using a simple transverse equivalent network

(TEN) such as the one shown in Fig. 4-18. The equivalent admittance associated to the PRS is obtained using the pole-zero technique presented in [9]. These admittances are calculated for the E-plane and for the H-plane independently. The Transverse Resonance Equation can be written as,

$$Y_{UP}(f,k) + Y_{DOWN}(f,k) = 0 \tag{4.4-1}$$

from which the unknown leaky-mode propagation constant can be numerically obtained.

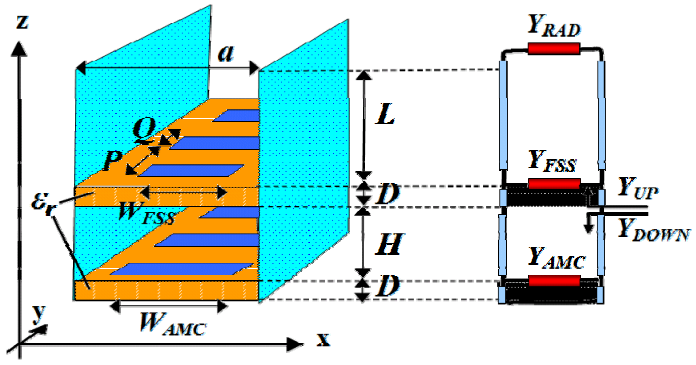

Fig. 4-18 Transverse Equivalent Network to obtain leaky-mode dispersion curves.

4.4.2 Half-wavelength antennas

The structure under consideration involves PRS1 from the previous section printed on the same substrate. The distance between the slab and the ground plane is *h* equal to 9.82 mm this corresponds to approximately half-wavelength at 14GHz, where the antenna produces a broadside pattern. The H- and E- plane radiation patterns for this LWA are obtained by the full-wave method discussed in section 4.2.1 for a range of frequencies between 14GHz and 16.5GHz for the H-plane and between 14GHz and 18GHz for the E-plane. Some examples of these results are presented in Fig. 4-19. Tracking the angle of the maximum, θ, and using Eq. (4.2-7), the dispersion of the phase constant is readily obtained.

In agreement with previous studies of 2-D LWA Fig. 4-19 shows that at broadside a pencil beam is produced with equal 3dB beamwidth in the H- and E-plane [42]. The patterns in the E- and H-plane are increasingly different at higher angles towards

endfire. Further observation of this figure shows that as the beam angle increases, the peak field amplitude increases in the H-plane. The opposite is happening in the E-plane. These observations are in agreement with [42]. Furthermore, the inset in Fig. 4-19 shows the presence of grating lobes that correspond to the -1 FSH from 14.4GHz onwards in the H- and the E-plane.

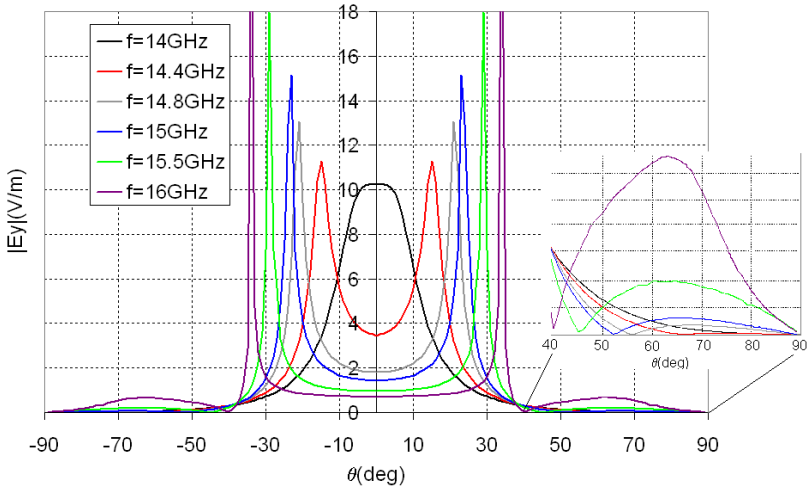

a)

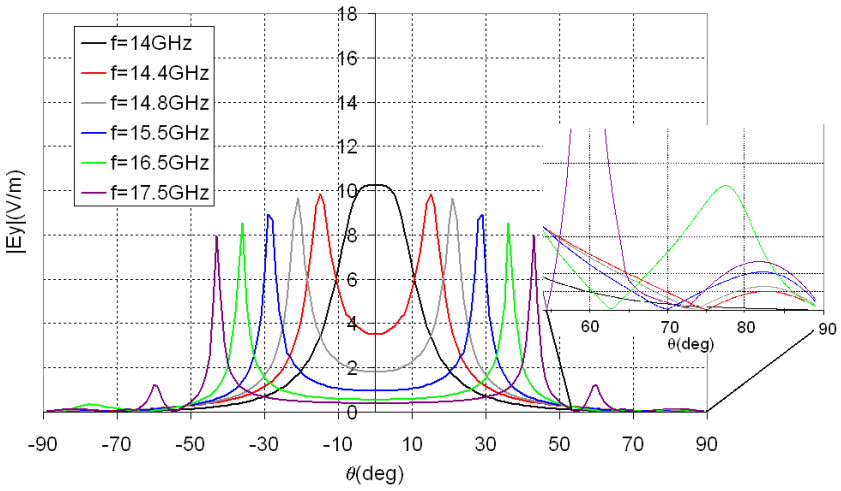

b)

Fig. 4-19 Radiation pattern a) H-plane and b) E-plane of the LWA formed with PRS1 (dimensions (in mm) D= 9.0, L_{PRS}=8, h_{d1}=1.5, h=9.82 and ε_r=2.55).

The dispersion diagrams as obtained from the patterns of Fig. 4-19 in the frequency range studied are shown in Fig. 4-20. Based on Eq. (4.4-6), the H-plane pattern provides the phase constant β_x of a TE mode along x, and the E-plane pattern gives β_y corresponding to a TM mode along y [40]. This figure also shows superimposed the phase constant values as obtained from a TEN model [41]. A comparison of the values for β_x / β_y indicates a very good agreement between the two techniques.

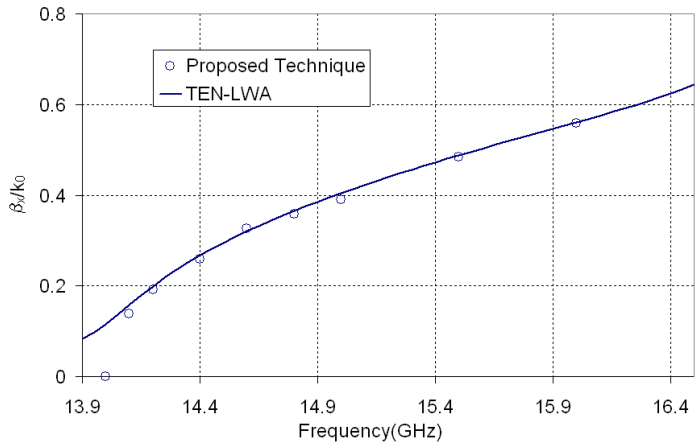

a)

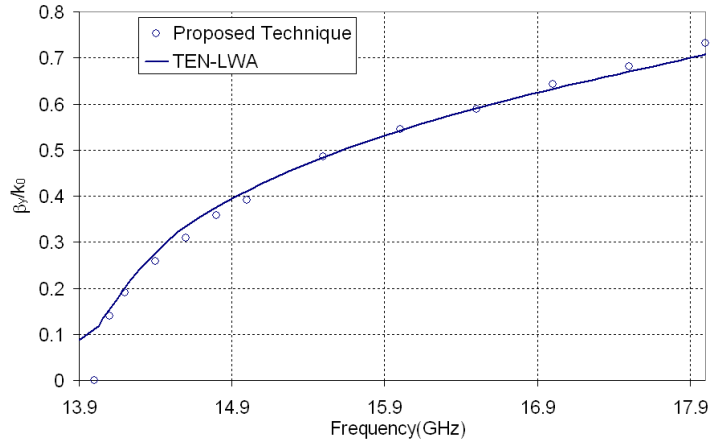

b)

Fig. 4-20 Normalized wavenumber versus frequency for a) the TE mode along x (H-plane) and b) the TM mode along y (E-plane) as obtained by the proposed technique and a Transverse Equivalent Network for the LWA with dimensions as in Fig. 4-19.

Figure 4-21 shows the radiation pattern calculated according to full-wave MoM together with that estimated using the AF approach assuming an infinitely long antenna with the obtained leakage rate, α at 14.4GHz. Since the AF calculation is based on the assumption of a single radiating Floquet space harmonic, it cannot predict the side lobes that emerge as a result of higher Floquet space harmonics in Fig. 4-21b. Therefore, in the calculation of α, the error function will only include the portion of the radiation pattern that is occupied by the main lobe, neglecting the higher values of θ, which correspond to side lobes.

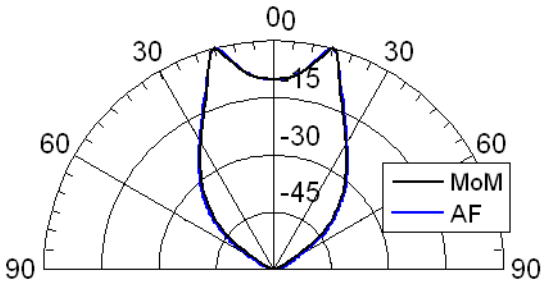

a)

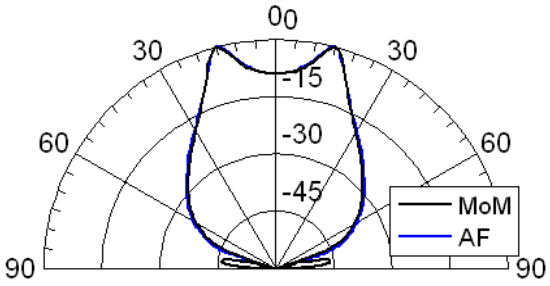

b)

Fig.4-21 a) H- and b) E-plane radiation pattern at 14.4GHz for the half-wavelength antenna of Fig. 4-19 as obtained by full-wave Method of Moments and Array Factor theory.

The computed values of the normalized leakage rate, α, at the H- and E-plane as calculated using the proposed technique as well as the TEN model are shown in Fig. 4-22. The agreement between both techniques is good for the given range of frequencies. As common with LWAs [1], the normalized leakage rate, α/k_0, decreases towards endfire direction. The interference of the side lobes with the main lobe limits the applicability of the proposed technique at higher frequencies.

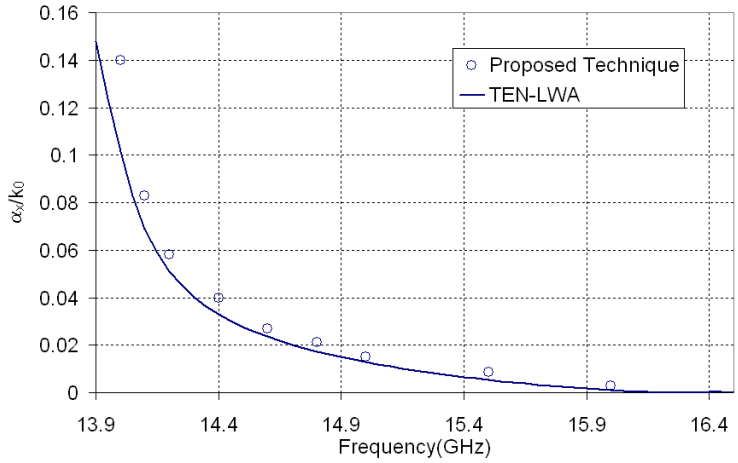

a)

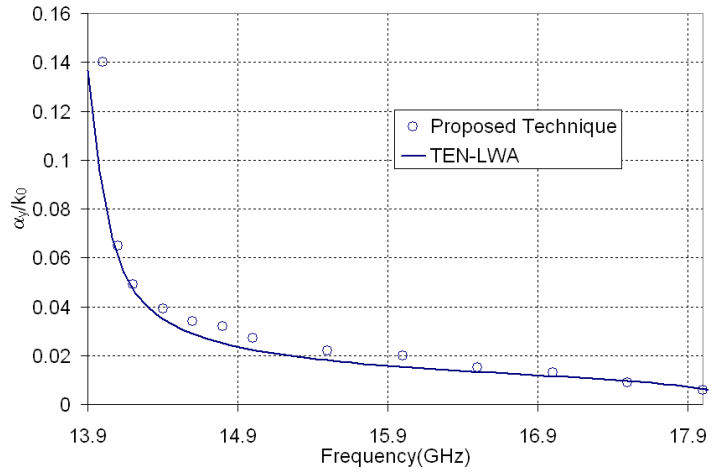

b)

Fig. 4-22 Normalized leakage rate versus frequency, a) H-plane and b) E-plane as obtained by the proposed technique and a Transverse Equivalent Network for the LWA with dimensions as in Fig. 4-19.

4.4.3 Quarter-wavelength antennas

A working example of an antenna such as the one shown in Fig. 4-17 is here employed using PRS1; the slab supporting PRS1 is located at a distance h= 5.46 mm above a HIS array with dimension L_{HIS}=4.1mm. The height of the cavity, h, has been designed for the antenna to produce a broadside pattern at 14GHz. In this example 120 FSH in the x- and y- direction are considered for a convergence better than 1%, chapter 3. A similar study as the one performed for the half-wavelength antenna is carried out.

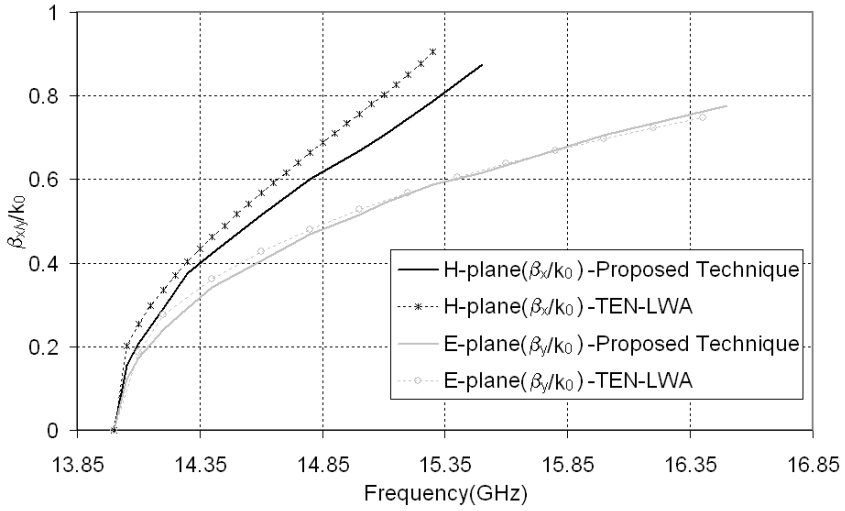

Fig. 4-23 Normalized wavenumber versus frequency for the H- and E-plane as obtained by the proposed technique and a Transverse Equivalent Network for the sub-wavelength antenna of

Fig. 4-17 (PRS1, h_{d1}=1.5mm and ε_r=2.55 and HIS with dimensions: L_{HIS}=4.1mm and D=9mm, printed on a substrate: h_{d2}=1.15mm and ε_r=2.2) operating at 14GHz.

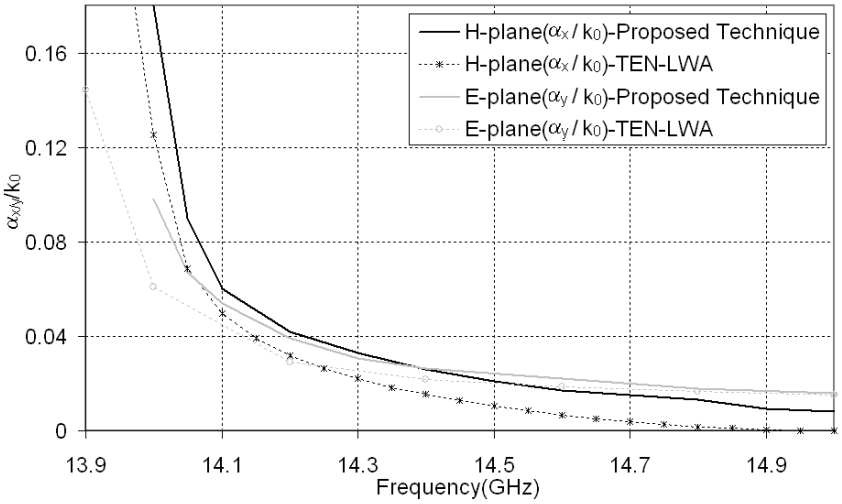

Fig. 4-24 Normalized leakage rate versus frequency for the H-plane and E-plane as obtained by the proposed technique and a Transverse Equivalent Network for the sub-wavelength antenna of Fig. 4-23.

The dispersion of the phase constants are shown in Fig. 4-23 for a range of frequencies between 14GHz and 15.6GHz for the H- and between 14GHz and 16.5GHz for the E-plane. This figure also shows superimposed the phase constant values as obtained from a TEN. The computed values of the leakage rate at the H- and E-plane are also depicted in Fig. 4-24 between 14GHz and 15GHz for the H- and E-plane. The TEN utilised in the calculations only accounts for a single mode, therefore when the antenna profile decreases the accuracy of the method is also reduced. Consequently, as is evident in Fig. 4-23 and 4-24, the agreement between the two methods for this antenna is reduced compared to the half-wavelength antenna, particularly in the H-plane.

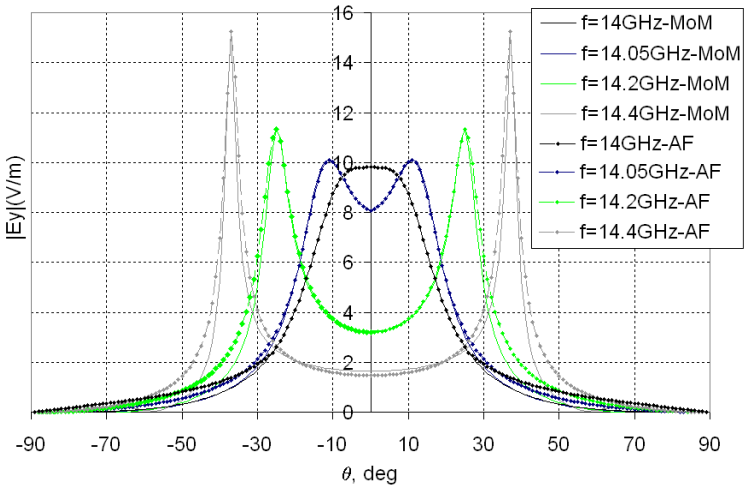

a)

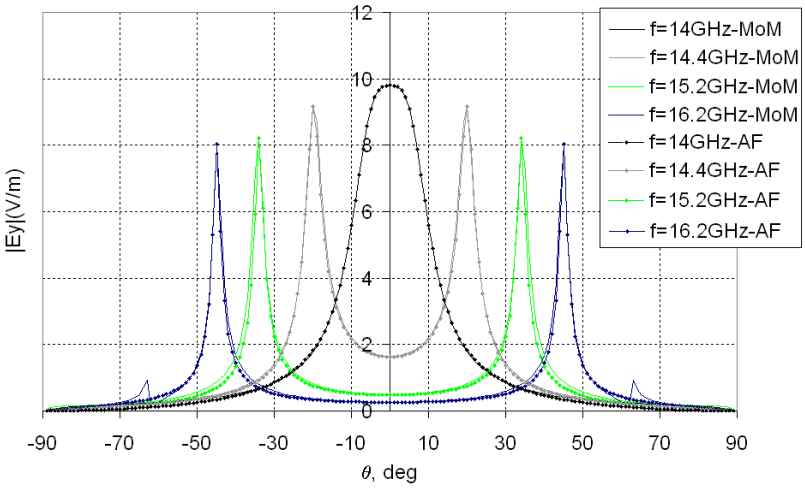

b)

Fig. 4-25 Radiation pattern a) H-plane and b) E-plane of the LWA with dimensions (in mm) h=3.25, PRS1, h_{d1}=1.5 and ε_r=2.55 and for the HIS: square patches L_{HIS}=4.3, h_{d2}=1.15 and ε_r=2.2 operating at 14GHz as obtained using Full-wave MoM and Array Factor procedure.

4.4.4 Dispersion analysis of thin antennas

As the profile of the antenna decreases the interaction of higher order evanescent modes between the two arrays significantly increases. The accuracy of the single mode transverse equivalent network model gradually reduces compared to the half-wavelength profile LWA. The technique proposed here can be directly applied for thin antennas without loss of accuracy. Here we demonstrate this by means of an example involving an antenna with PRS1; the supporting slab of PRS1 is located at a distance h= 3.25mm (~λ/7 at 14GHz) above a HIS array, which consists of patches with L_{HIS}=4.3 mm printed on a dielectric slab of thickness, h_{d2}=1.15mm and relative permittivity 2.2.

The H- and E- plane radiation patterns of the LWA at different frequencies are determined in order to extract the phase constant in either plane. A total number of 170 FSH in each direction has been taken into account for convergence better than 1%. The radiation patterns at both planes as obtained using MoM as well as an AF approach at different frequencies are presented in Fig. 4-25 showing a good agreement between both techniques that validate the AF model accuracy. A pencil beam is obtained at broadside at the frequency of 14GHz. However, a narrower beamwidth is obtained in the E-plane attributed to a lower value of the leakage rate at this plane.

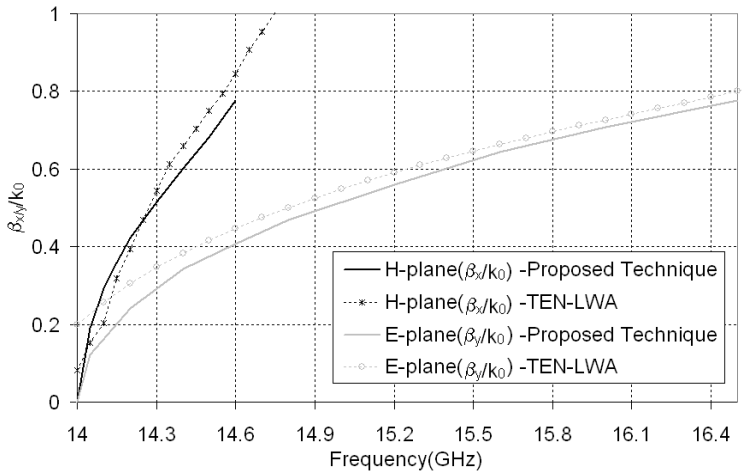

Fig. 4-26 Normalized wavenumber versus frequency for the H-plane and E-plane as obtained by the proposed technique and a Transverse Equivalent Network for the LWA of Fig. 4-25.

The dispersion diagrams for the H- and E-plane are shown in Fig. 4-26 for frequencies between 14-14.6GHz and 14-16.5GHz, respectively. The interference of the side-lobes with the main lobe impedes the application of the proposed technique in this case beyond 14.6 GHz for the H-plane and beyond 16.5 GHz for the E-plane. The computed values of the leakage rate are also depicted in Fig. 4-27 between 14-14.6GHz and 14-15.1GHz for the H- and E-plane, respectively. In both figures, the resulting dispersion parameters as obtained using TEN are depicted clearly showing how the accuracy of the method has reduced even more for the λ/7 antenna, particularly at the H-plane.

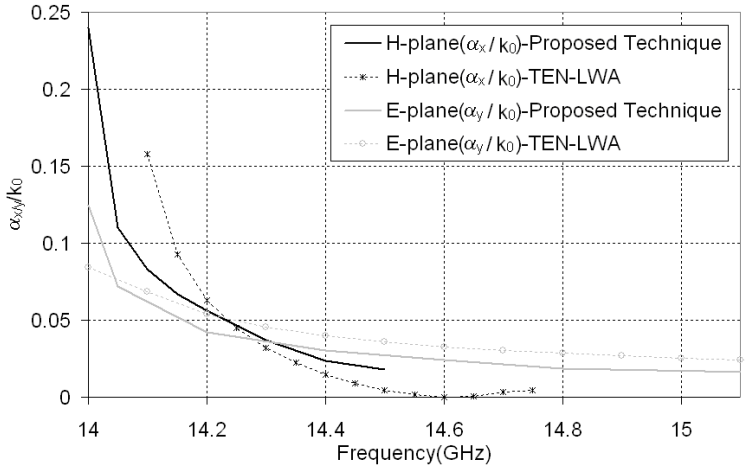

Fig. 4-27 Normalized leakage rate versus frequency for the H-plane and E-plane as obtained by the proposed technique and a Transverse Equivalent Network for the LWA of Fig. 4-25.

As a final remark of the section the following comments can be made. By observation of figures 4-22, 4-24 and 4-27 one can conclude that higher values of the leakage rate are obtained for antennas with reduced profile at the H-plane at broadside (e.g. 14GHz)

for a fixed PRS. This leads to less directive radiation patterns at the H-plane for thinner antennas. However, at the E-plane smaller values of the leakage rate are obtained for antennas with reduced profile leading to more directive radiation patterns. Nevertheless, as the frequency increases the difference between the values of the leakage rate at a fix frequency for antennas with different profiles becomes smaller. Figures 4-20, 4-23 and 4-26 further demonstrate that as the profile reduces (e.g. the dimension of the HIS increases) the dispersion curve varies faster with frequency in both the H- and E- plane. At the same time, the dispersion at the H- and E-plane is similar for half-wavelength antenna (Fig. 4-20a and 4-20b) but increasingly different for thinner antennas.

4.5 Summary

The analysis of sub-wavelength profile high-gain planar leaky-wave antennas employing two periodic surfaces (HIS and PRS) has been presented using MoM and invoking reciprocity. A fast and accurate analysis technique for the estimation of their complex propagation constant with help of array theory has also been shown. The field distribution inside the cavity has demonstrated the operation principles and the radiation characteristics of these antennas. Using these tools, section 4.3 presents design guidelines for tailoring the antenna profile, the HIS dimensions, the directivity and the bandwidth. The trade off between bandwidth and directivity has also been discussed. A study on the effect of the profile thickness on the antenna efficiency has been carried out. The proposed technique has been validated by comparison with 3D full-wave electromagnetic simulatior Microstripes^{TM} 2009.

The method described for the estimation of complex propagation constant was applied to the analysis of a LWA with different profiles. The produced dispersion diagrams were in good agreement with those derived by a TEN. Reactive interaction between adjacent layers due to evanescent higher-order Floquet harmonics limits the validity of single mode TEN, which is based on equivalent impedances of the PRS and HIS arrays obtained under single Floquet mode illumination. The proposed technique overcomes this problem, so that low-profile LWAs can be accurately and efficiently analyzed. The main limitation of the proposed technique is due to the appearance of grating lobes, which limit its applicability.

References

[1] A. Oliner. "Leaky-wave antennas," in Antenna Engineering Handbook, Third Edition, edited by R. C. Johnson, McGraw Hill, 1993.

[2] C. Caloz, T. Itoh, *Electromagnetic Metamaterials: transmission line theory and microwave applications*, John Wiley & Sons, Inc., 2006.

[3] J. R. James, and P. S. Hall, *Handbook of microstrip antennas*, Peter Peregrinus Ltd., 1989.

[4] R. Gardelli, G. Donzelli, M. Albani, and F. Capolino, "Design of Patch Antennas and Thinned Array of Patches in a Fabry-Perot Cavity Covered by a Partially Reflective Surface," in *European Conference on Antennas and Propag*. (EuCAP), Nice, France, 6-10 Nov. 2006.

[5] G.V. Trentini, "Partially reflecting sheet array", *IRE Trans. Antennas Propag.*, vol. AP-4, pp. 666-671, 1956.

[6] A. P. Feresidis, and J. C. Vardaxoglou, "High-gain planar antenna using optimized partially reflective surfaces," *IEE Proc. Microw. Antennas Propag.*, vol. 148, no. 6, Feb. 2001.

[7] Y. J. Lee, J. Yeo, R. Mittra, and W. S. Park, "Design of a high-directivity electromagnetic bandgap (EBG) resonator antenna using a frequency selective surface (FSS) superstrate," *Microwave and Optical Technology Letters*, vol. 43, no. 6, 462-467, 2004.

[8] T. Zhao, D. R. Jackson, J. T. Williams, Hung-Yu D. Yang, and A. A. Oliner, "2-D Periodic Leaky-Wave Antennas-Part I: Metal Patch Design", *IEEE Trans. Antennas and Propag.*, vol. 53, no. 11, pp.3505-3514, Nov. 2005.

[9] T. Zhao, D. R. Jackson, J. T. Williams, Hung-Yu D. Yang, and A. A. Oliner, "2-D Periodic Leaky-Wave Antennas-Part II: Slot Design", *IEEE Trans. Antennas and Propag.*, vol. 53, no. 11, pp. 3515-3524, Nov. 2005.

[10] D. R. Jackson, N. G. Alexopoulos, "Gain enhancement methods for printed circuits antennas," *IEEE Trans. Antennas Propag.*, vol. AP-33, no. 9, pp. 976-987, Sep. 1985.

[11] H. Y. Yang, N. G. Alexopoulos, "Gain enhancement methods for printed circuits antennas through multiple superstrates," *IEEE Trans. Antennas Propag.*, vol. AP-35, no. 7, pp. 860-864, Jul. 1987.

[12] D. R. Jackson, A. A. Oliner, and A. Ip, "Leaky-wave propagation and radiation for a narrow-beam multiple-layer dielectric structure," *IEEE Antennas Propag.*, vol. AP-41, no. 3, pp. 344-348, Mar. 1993.

[13] T. Zhao, D. R. Jackson, J. T. Williams, and A. A. Oliner, "Simple CAD model for a dielectric leaky-wave antenna," *IEEE Antennas Wireless Propag.*, vol. 3, pp. 243-245, April 2004.

[14] R. Gardelli, M. Albani, F. Capolino, "Array thinning by using antennas in a Fabry-Perot cavity for gain enhancement," *IEEE Trans. Antennas Propag.*, vol. 54, no. 7, pp. 1979-90, Jul. 2006.

[15] D. Sievenpiper, Z. Lijun, R.F. Broas, N.G. Alexopoulos and E. Yablonovitch, "High-impedance electromagnetic surfaces with a forbidden frequency band," *IEEE Trans. Microw. Theory and Techniques*, vol. 47, nº11, pp. 2059-2074, Nov. 1999.

[16] Y. Zhang, J. von Younis, C. Fischer and W. Wiesbeck, "Planar artificial magnetic conductors and patch antennas," *Special issue on Metamaterials, IEEE Trans. Antennas Propag.*, vol. 51, no. 10, pp. 2704-2712, Oct. 2003.

[17] A. P. Feresidis, G. Goussetis, S. Wang, and J. C. Vardaxoglou, "Artificial Magnetic Conductor Surfaces and Their Application to Low-Profile High- Gain Planar Antennas," *IEEE Trans. Antennas Propag.*, vol. 53, no. 1, pp. 209-215, Jan. 2005.

[18] G. Goussetis, A.P. Feresidis, J.C. Vardaxoglou, "Tailoring the AMC and EBG Characteristics of Periodic Metallic Arrays Printed on Grounded Dielectric Substrate," IEEE Transactions Antennas and Propagation, vol. 54, No. 1, pp. 82-89, January 2006.

[19] O. Luukkonen, C. Simovski, G. Granet, G. Goussetis, D. Lioubtchenko, A. V. Räisänen, and S. A. Tretyakov, "Simple and accurate analytical model of planar grids and high-impedance surfaces comprising metal strips or patches," *IEEE Trans. Antennas Propag.*, Vol. 56, No. 6, pp. 1624-1632, June 2008.

[20] O. Luukkonen, P. Alitalo, C. R. Simovski and S. A. Tretyakov, "Experimental verification of an analytical model for high-impedance surfaces," *Electronics Letters*, vol. 45, no. 14, pp. 720--721, 2009.

[21] G. Goussetis, A.P. Feresidis and R. Cheung, "Quality factor Assessment of Subwavelength Cavities at FIR Frequencies," Journal of Optics A, Vol. 9, pp. s355-s360, August 2007.

[22] S. Wang, A.P. Feresidis, G. Goussetis, J.C. Vardaxoglou, "High-Gain Subwavelength Resonant Cavity Antennas Based on Metamaterial Ground Planes," *IEE Proc. Antennas and Propagation*, Vol. 153, no. 1, pp.1-6, February 2006.

[23] J. R. Kelly, T. Kokkinos, and A. P. Feresidis, "Analysis and Design of Sub-wavelength Resonant Cavity Type 2-D Leaky-Wave Antennas," *IEEE Trans. Antennas and Propagation*, vol. 56, no. 9, pp. 2817-2825, Sept. 2008.

[24] P. Kosmas, A.P. Feresidis and G. Goussetis, "Periodic FDTD analysis of a 2-D leaky-wave planar antenna based on dipole frequency selective surfaces," *IEEE Transactions on Antenna and Propagation*, Vol. 55, no. 7, pp. 2006-2012, July 2007.

[25] J. L. Gómez, D. Cañete and A. Álvarez-Melcón, "Printed-Circuit Leaky-Wave Antenna with Pointing and Illumination Flexibility," *IEEE Microwave and Wireless Components Lett.*, vol.15, No.8, pp.536-538, August 2005.

[26] J.L. Gómez, G.Goussetis, A.Feresidis, and A.A.Melcón, "Control of Leaky-Mode Propagation and Radiation Properties in Hybrid Dielectric-Waveguide Printed-Circuit Technology: Experimental Results," *IEEE Trans. Antennas Propag.*, vol.54, No.11, pp.3383-3390, Nov. 2006.

[27] S. Maci, M. Casaletti, M. Caiazzo, and C. Boffa, "Dispersion properties of periodic grounded structures via equivalent network synthesis," *IEEE Antennas Propag. Int. Symp.*, vol. 1, pp. 493 – 496, 22-27 June 2003.

[28] J.L. Gómez-Tornero, G. Goussetis, D. Cañete-Rebenaque, F. Quesada-Pereira, and A. Álvarez-Melcón, "Simple and Accurate Transverse Equivalent Network to Model Radiation from Hybrid Leaky-Wave Antennas with Control of the Polarization," *IEEE Antennas Propag. Society Int. Symp.*, pp.1-4, 5-11 July 2008.

[29] G. Goussetis, A. P. Feresidis, and P. Kosmas, "Efficient Analysis, Design, and Filter Applications of EBG Waveguide with Periodic Resonant Loads," *IEEE Trans. Microw. Theory and Tech.*, Vol. 54, No. 11, Nov. 2006.

[30] T. Kokkinos, C. D. Sarris, and G. V. Eleftheriades, "Periodic finite-difference time-domain modeling of leaky-wave structures applied to the analysis of negative-refractive-index metamaterial-based leaky-wave antennas," *IEEE Trans. Microw. Theory Tech.*, vol. 54, pp. 1619–1630, Apr. 2006.

[31] J. R. Kelly, T. Kokkinos, and A. P. Feresidis, "Analysis and Design of Sub-wavelength Resonant Cavity Type 2-D Leaky-Wave Antennas", *IEEE Trans. Antennas Propag.*, vol. 56, nº9, pp. 2817-2825, Sept. 2008.

[32] R. Mittra, C.H. Chan, T. Cwik, "Techniques for analyzing frequency selective surfaces-a review," *Proceedings of the IEEE*, Vol. 76, pp.593- 615, Dec. 1988.

[33] W. Changhua, J.A. Encinar, "Efficient computation of generalized scattering matrix for analyzing multilayered periodic structures," *IEEE Trans. Antennas Propag.*, vol.43, no. 11,Nov. 1995, pp. 1233 - 1242.

[34] J.C. Vardaxoglou, Frequency Selective Surfaces Analysis and Design, John Wiley, 1997.

[35] C. A. Balanis, "Antenna Theory: Analysis and Design," Second edition, New York: John Wiley & Sons Inc, 1997.

[36] C. Mateo-Segura, G. Goussetis, and A. P. Feresidis, "Resonant Effects and Near Field Enhancement in Perturbed Arrays of Metal Dipoles", *IEEE Trans. Antennas Propag.,* in press.

[37] C. Caloz and T. Itoh, "Array factor approach of leaky-wave antennas and application to 1D/2D composite right/left-handed (CRLH) structures," *IEEE Microwave and Wireless Comp. Lett.*, vol.14, No.6, July 2006, pp. 274-276.

[38] G. Lovat, P. Burghignoli, F. Capolino, D. R. Jackson, and D. R. Wilton, "Analysis of directive radiation from a line source in a metamaterial slab with low permittivity," TAP, vol. 54, pp. 1017-1030, Mar. 2006.

[39] D. M. Pozar, Microwave Engineering, 2nd edition, New York: John Wiley & Sons Inc, 1998.

[40] S. Maci, M. Caiazzo, A. Cucini, M. Casaletti, "A Pole-Zero Matching Method for EBG Surfaces Composed of a Dipole FSS Printed on a Grounded Dielectric Slab," *IEEE Trans. Antennas Propag.*, vol. 53, No. 1, Jan. 2005, pp. 70-81.

[41] M. García-Vigueras, J.L. Gómez-Tornero, G. Goussetis, J.S. Gómez-Diaz, and A. Álvarez-Melcón, "A Modified Pole-Zero Technique for the Synthesis of Waveguide Leaky-Wave Antennas Loaded with Dipole-Based FSS", *IEEE Trans. Antennas Propag.,* in press.

[42] T. Zhao, D. R. Jackson, J. T. Williams, and A. A. Oliner, "General Formulas for 2-D Leaky-Wave Antennas," *IEEE Trans. Antennas and Propag.*, vol. 53, No. 11, pp. 3515-3524, Nov. 2005.

Chapter 5

Double layer 2-D periodic arrays for broadband antenna design

"Cada nuevo amigo que ganamos en la carrera de la vida nos perfecciona y enriquece más aún por lo que de nosotros mismos nos descubre, que por lo que él mismo nos da."

Miguel de Unamuno

5.1 Introduction

In this chapter, the technique described in chapter 4 based on MoM together with reciprocity is employed in order to investigate the directivity pattern of double layer two-dimensional periodic arrays acting as partially reflective surfaces (PRS) over a ground plane in the leaky-wave antenna design. The technique proposed for the analysis of these antennas is compared to a ray optics model based on multiple reflections between the PRS and the ground plane to produce the radiation pattern [1].

A parametric study is carried out in section 5.2 using the proposed method in order to study the variation of the radiation intensity and directivity at boresight with frequency

of a double layer antenna array. The study reveals a directivity response which is attributed to the excitation of two different modes, odd and even. By modifying the features of the elements of the arrays, the frequency at which these modes are excited can be modified. Moreover, the variation of the distance between both arrays is shown to affect the level of excitation of the two modes. As a result high gain and wide-band antenna performance can be achieved. An optimised double layer dipole leaky wave antenna design is presented.

In section 5.3 an optimised double layer patch leaky wave antenna design, yielding high gain and broad bandwidth, is produced following the guidelines derived from the parametric study. Finite size leaky-wave antennas are simulated using a 3-D time domain electromagnetic computer simulator, namely CST Microstripes^{TM} 2009 in order to check the accuracy of the proposed method in a more realistic design. In the following section, a finite prototype of the patch PRS broadband leaky-wave antenna is produced in a rigid structure. The antenna is fed by a semi-rigid coaxial cable whose inner connector was bent acting as a dipole placed in the centre of the cavity, between the ground plane and the lower array. The directivity patterns are measured and compared to those obtained for the finite antenna in the full-wave simulations.

5.1.1 Double-layer PRS antenna

The antennas presented in chapter 4 rely on the formation of a resonant cavity between a highly reflective structure and the ground plane. Although in all cases the cavity resonance increases the directivity of simple radiating sources, the strong directivity results in a very small antenna bandwidth [1-5].

A new method for obtaining broadband Fabry-Perot type resonant cavity antennas maintaining the high directivity performance, which is often required in modern communication systems, was reported in [6]. The design was based on a double-layer metallo-dielectric Partially Reflective Surface (PRS) with different array element size (e.g. arrays with dissimilar reflectivity). The second resonance which appears as a result of the second layer array favours a reflection phase of the PRS array response to increase almost linearly with frequency in a certain frequency range. This means that

the resonance condition of the cavity is satisfied at a wide range of frequencies. Therefore, broadband and highly-directive antenna designs can be achieved.

An efficient analysis technique of half-wavelength and sub-wavelength periodic 2-D LWAs has been presented in the previous chapter based on the principle of reciprocity and full-wave spectral domain analysis [4-5, 7]. Here we present for the first time a full-wave periodic analysis of this type of antennas composed of two double PRS layers over a ground plane and its application in the design of broadband LWA. A complete description of the technique has been provided in chapter 4 and it is not presented here to avoid repetition. An optical cavity ray model [1] is also used to analyse these antennas and a comparison between both techniques is presented. The ray optics technique is briefly introduced in the following.

5.1.2 Ray Optics model

A ray-optics analysis can be used to describe the functioning of resonant cavity antennas. This method is approximate as it only considers dominant mode coupling between homogeneous and infinite (i.e. no edge effects) PRSs and ground plane and ignores higher order mode coupling. Although approximate, it gives a valuable insight to the function of highly-directive antennas and resonant cavities. The principle of the analysis is similar to the resonant optical cavity theory [1, 8]. Initially consider an antenna formed by a single layer PRS above a ground plane. This antenna resembles that of a simple Fabry-Perot interferometer, where the reflecting surfaces are now replaced by a highly reflective PRS (or two PRSs) and a ground plane (R_{ground}=1, φ_{ground}=-π). The reflection characteristics of the PRS vary with frequency in contrast to the frequency independent response of partially metallised surfaces used in the interferometer.

The partially reflecting sheet, PRS, is placed at a distance h from the completely reflecting screen (i.e. ground plane). This will introduce multiple reflections with decreasing amplitudes between these two planes. The reflection coefficient of the sheet is $Re^{j\varphi R}$. If there is no transmission losses the amplitude of the directed ray is proportional to $\sqrt{1-R^2}$; the amplitude of the one reflected ray is proportional

to $R\sqrt{1-R^2}$; the amplitude of the twice-reflected ray is proportional to $R^2\sqrt{1-R^2}$ and so on so forth.

The electric field intensity in the Fraunhofer zone is the summation of these partial rays, and it can be written as follows,

$$E = \sum_{n=0}^{\infty} f(\theta) E_0 R^n \sqrt{1-R^2}\, e^{j\varphi_n} \tag{5.1-1}$$

where $f(\theta)$ is the source radiation pattern. The phase angle φ_n is composed of the phase variations during reflections from the PEC. From Fig.5-1 these phases can be derived as,

$$\begin{aligned} \varphi_1 &= \frac{2\pi}{\lambda} 2h\tan(\theta)\sin(\theta) - \frac{2\pi}{\lambda}\frac{2h}{\cos(\theta)} - \pi + \varphi_R \\ \varphi_2 &= \frac{2\pi}{\lambda} 4h\tan(\theta)\sin(\theta) - \frac{2\pi}{\lambda}\frac{4h}{\cos(\theta)} - 2\pi + 2\varphi_R \end{aligned} \tag{5.1-2}$$

…

$$\varphi_n = n\left(\frac{4\pi}{\lambda} h\frac{\sin^2(\theta)}{\cos(\theta)} - \frac{4\pi}{\lambda} h\frac{1}{\cos(\theta)} - \pi + \varphi_R\right) = n\left(\frac{4\pi}{\lambda} h\left(\frac{\sin^2(\theta)-1}{\cos(\theta)}\right) - \pi + \varphi_R\right)$$

$$= n\left(\frac{4\pi}{\lambda} h\left(\frac{-\cos^2(\theta)}{\cos(\theta)}\right) - \pi + \varphi_R\right) = n\left(-\frac{4\pi}{\lambda} h\cos(\theta) - \pi + \varphi_R\right)$$

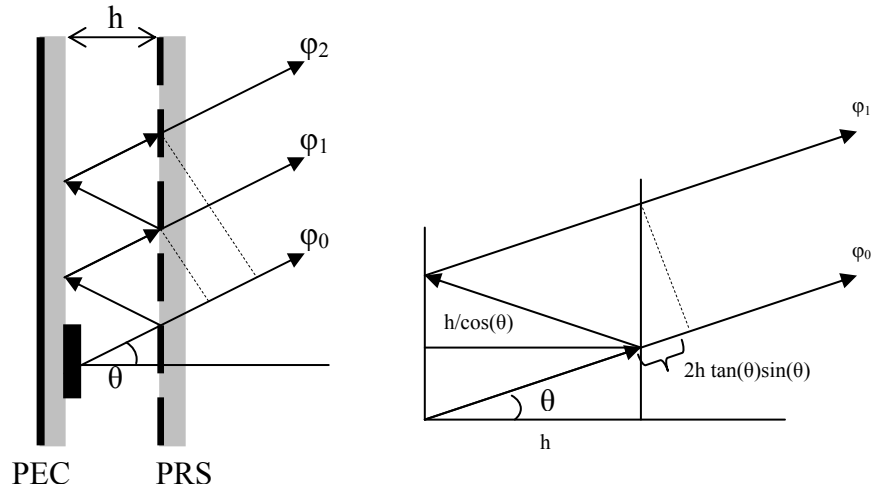

Fig. 5-1 Resonant cavity formed by PEC and PRS with excitation source inside the cavity. Ray diagram of the cavity considering multiple reflections.

Since $R<1$ in (5.1-1), we can rewrite,

$$\sum_{n=0}^{\infty}\left(\mathrm{Re}^{j\psi}\right)^{n}=\frac{1}{1-\mathrm{Re}^{j\psi}} \tag{5.1-3}$$

where $\psi=\left(-\frac{4\pi}{\lambda}h\cos(\theta)-\pi+\varphi_R\right)$. Introducing (5.1-3) in (5.1-1), the absolute value of field strength becomes,

$$|E|=|E_0|f(\theta)\sqrt{\frac{1-R^2}{1+R^2-2R\cos(\psi)}} \tag{5.1-4}$$

Therefore, the power pattern is,

$$P=\frac{|E|^2}{|E_0|^2}=\frac{1-R^2}{1+R^2-2R\cos\left(\varphi_R-\pi-\frac{4\pi}{\lambda}h\cos(\theta)\right)}f^2(\theta) \tag{5.1-5}$$

The amplitude R and the phase φ_R depend on the angle of incident θ. The maximum power, according to (5.1-5), in the normal direction of propagation ($\theta=0$) is obtained when the reflection phase is that described in (5.1-6),

$$\varphi_R-\pi-\frac{4\pi}{\lambda}h_r=2N\pi \tag{5.1-6}$$

and hence, the equation determining the resonance distance h_r of the sheet is,

$$h_r=\frac{\lambda}{4}\left(\frac{\varphi_R}{\pi}-1\right)+\frac{\lambda}{2}N \tag{5.1-7}$$
$$N=0,1,2,...$$

An infinite size PRS and ground plane has been assumed. Inserting Eq. (5.1-7) in (5.1-5) and taking $\theta=0$, yields an expression for the boresight directivity relative to the primary antenna, as a function of the reflection coefficient,

$$D=\frac{P}{F}=\frac{1+R}{1-R} \tag{5.1-8}$$

It can be seen from Eq. (5.1-8) that the directivity increases considerably with R, and high-directivity can be obtained with a highly reflective PRS placed at the resonant distance. The resonant distance and more importantly the reflection phase of the PRS

are function of the frequency (5.1-9). Thus, the resonant condition of the cavity ideally has to be satisfied within a range of frequencies in order to produce high directivity within this range and hence yielding broadband performance. This is shown in (5.1-9),

$$\varphi_R = \frac{4\pi h_r}{c} f - (2N-1)\pi \qquad N = 0,1,2,... \tag{5.1-9}$$

where φ_R is the phase of the PRS reflection coefficient, h_r the distance between the PRS and the ground and f is the frequency. Therefore a linearly increasing (with frequency) phase response will result in a maximum directivity within a wide frequency range. The directivity maximum will be determined from the magnitude of the reflection coefficient of the PRS.

Based on the above analysis, in the following, double-layer arrays of metallic dipoles/patches on a dielectric substrate (Fig. 5-2a) are simulated using the Floquet plane wave modal analysis described in previous chapters. From this simulation the reflection magnitude and phase of the two layer PRS is achieved and subsequently this is used in the formulation above. The antenna is formed by locating the double layer PRS at a resonance distance, h_r, (Fig. 5-2b) and thus the power pattern is readily derived using (5.1-5).

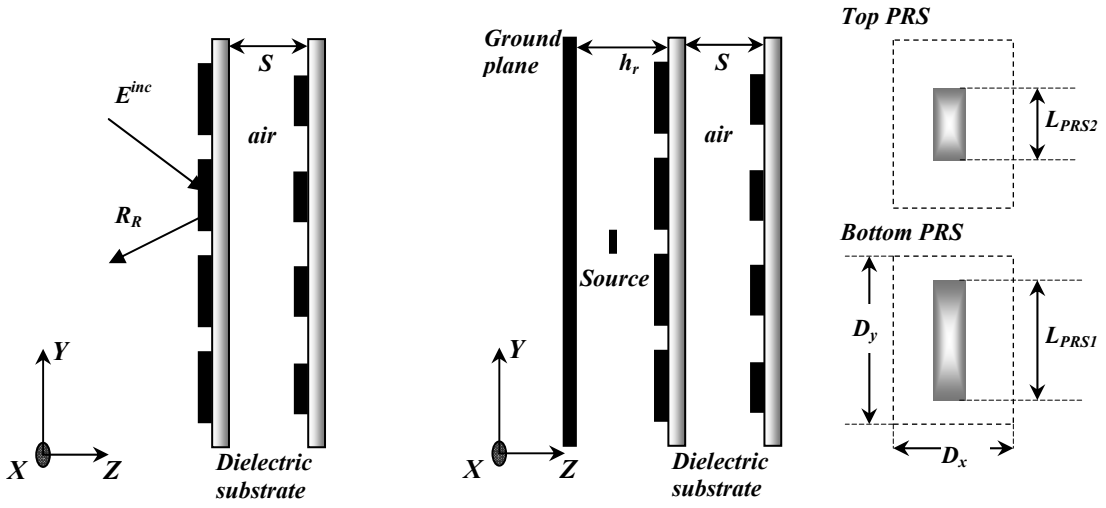

a) b)

Fig. 5-2. Cross-section of a) double layer PRS and b) antenna with double layer dipole PRS.

5.2 Bandwidth optimisation of Double Layer dipole PRS antennas

Initially, a single layer PRS cavity antenna is considered in order to show the bandwidth improvement after adding a second layer PRS. An optimized highly reflective dipole array as the one described in [3] with dimensions l_1=14mm and w_1=0.5mm within a unit cell of D_x=1mm and D_y=14.5mm on a 10mm foamboard (ε_r=1.05) is firstly used as a PRS. Subsequently, the resonant cavity antenna is formed by superimposing the dipole PRS over a ground plane at a distance of h_r=11mm, in the range of half wavelength for a design frequency near 14 GHz. The structure was simulated using Floquet plane wave spectral-domain analysis [7, 9] where five sinusoidal basis functions have been used to expand the current on the unit dipole of the array. Good relative convergence has been achieved with 40 Floquet modes in each direction (x and y). A ray optics model [1] has also been employed to derive the directivity pattern of the antenna. In the full-wave analysis, the directivity pattern is estimated as described in section 4.2.1 of the previous chapter, [4-5]. In the ray optics model, the complex reflection coefficient of the PRS is obtained using the developed code.

At frequencies lower than the resonance the reflection coefficient magnitude of the PRS increases with frequency, its phase is negative and decreases with frequency. At resonance (total reflection) its value becomes $-\pi$, as shown in Fig. 5-3a. Using the reflection coefficient the far field radiation intensity at boresight of the whole antenna can be estimated as described in section 5.1.2, this is presented in Fig. 5-3b which also shows the radiation intensity at boresight estimated using the developed code based on full-wave analysis. The integration of the obtained values in all possible directions can be used as reference in order to obtain the directivity,

$$D(\theta,\varphi)=\frac{4\pi\cdot P(\theta,\varphi)}{\iint\limits_{\theta,\varphi} P(\theta,\varphi)\cdot\sin(\theta)\cdot d\theta\cdot d\varphi} \tag{5.2-1}$$

The maximum directivity for the single layer antenna is 25.7 dBi at about 14.05GHz. The results are shown in Fig.5-4. Full-wave spectral domain MoM results agree relatively well with the ray optics model. In this figure the total power radiated by the antenna has also been depicted as a red line. This corresponds to the value of the denominator in Eq. (5.2-1) which shows the integration of the radiation intensity over

an entire solid angle 4π. The radiation intensity represents the power density associated with the electromagnetic field of an antenna generally calculated in the far-field region. From Fig. 5-4 it can be observed that the value of the power radiated is significantly low at lower frequencies. In fact, at these frequencies the resonant mode of the cavity is below cut-off and thus not excited, the fields are evanescent and are concentrated in the near-field region of the antenna. Due to the inverse relation between total power radiated and directivity, the low values of the power radiated cause the directivity to smoothly decay with frequency and to be higher than the radiated electric field. Despite the high values of the directivity, the low values of the power radiated result however in a low radiation efficiency. The power radiated curve is instructive in determining the frequency at which the cavity mode is excited.

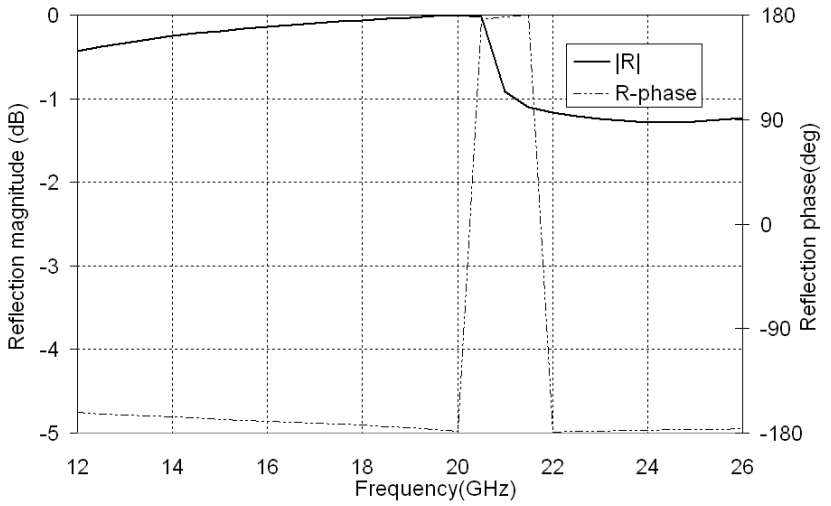

a)

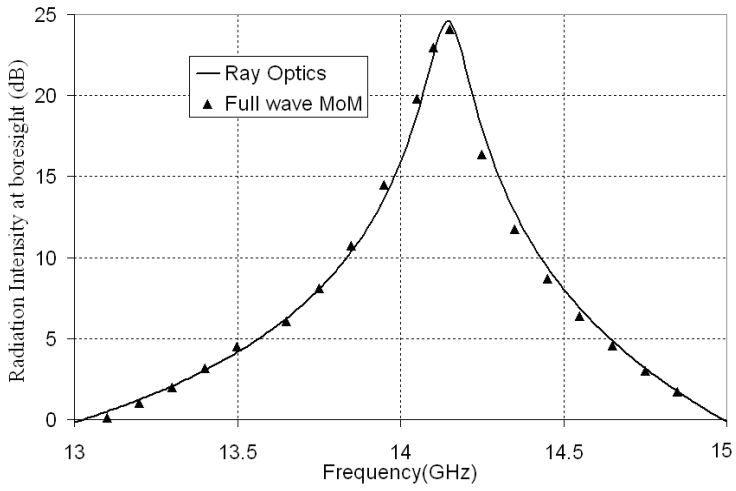

b)

Fig.5-3 a) Reflection coefficient, magnitude and phase, of the dipole PRS for normal incidence and b) Radiation intensity at boresight for the antenna formed using the single dipole PRS, with

dimensions in mm: l_1=14, w_1=0.5, D_x=1 and D_y=14.5 over a 10mm foamboard (ε_r=1.05) located at h_r=11mm from a ground plane.

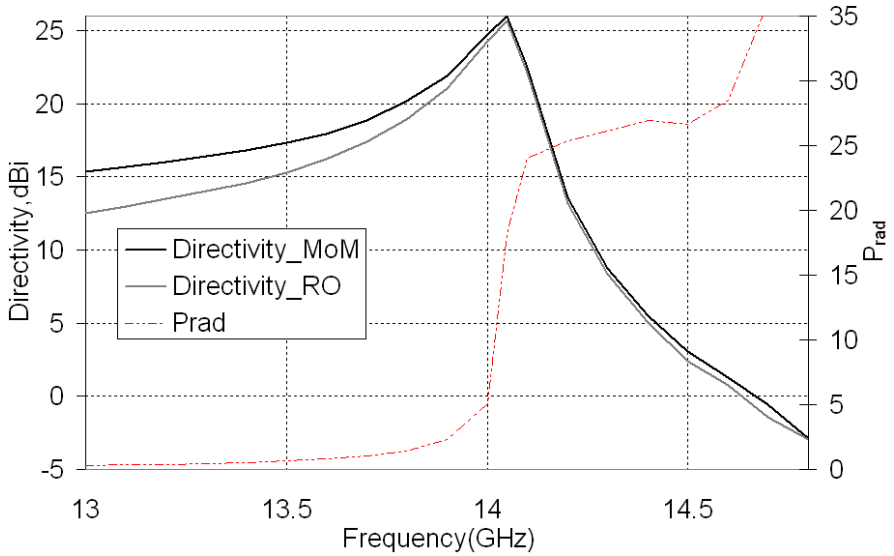

Fig. 5-4 Simulated directivity at boresight of a single layer dipole PRS, with dimensions in mm: l_1=14, w_1=0.5, D_x=1 and D_y=14.5 over a 10mm foamboard (ε_r=1.05) located at h_r=11mm from a ground plane as obtained using Full-wave MoM as well as a ray optics model.

It was argued in section 5.1.2 that a linearly increasing (with frequency) phase response of the PRS yields a broadband antenna performance. Based on this assumption an optimised double-layer metallo-dielectric PRS with dissimilar array element size is considered [3, 9]. The dimensions of the second dipole array are taken as l_2=9mm and w_2=0.5mm. The arrays are considered to be on either side of a flat foamboard (ε_r=1.05) of thickness S=12.6mm. The simulated reflection coefficient (magnitude and phase) of the optimised double layer dipole array is shown in Fig. 5-5a. The minimum reflection value appears at 13.7 GHz. The phase increases with frequency in the range between 13.3 GHz and 14.1 GHz and is close to the optimum PRS phase response as derived from equation (5.1-9), which is also plotted for comparison. For this design, broad bandwidth is expected over the range of frequencies where the reflection phase is close to the optimum (about 13.4 to 14 GHz). In addition, high directivity is also expected due to the relatively high values of the reflection magnitude.

The antenna is formed using the optimised double-layer square patch PRS positioned at a distance h_r=11.4mm above a ground plane. The far-field radiation intensity at boresight versus frequency as calculated using ray optics as well as full-wave MoM - reciprocity is presented in Fig. 5-5b. The 3dB bandwidth performance of the double

layer PRS antenna is over 10% compared to that of the single layer structure, whilst the radiation intensity at boresight is reduced to 17.15dB, 7dB less than the single layer antenna.

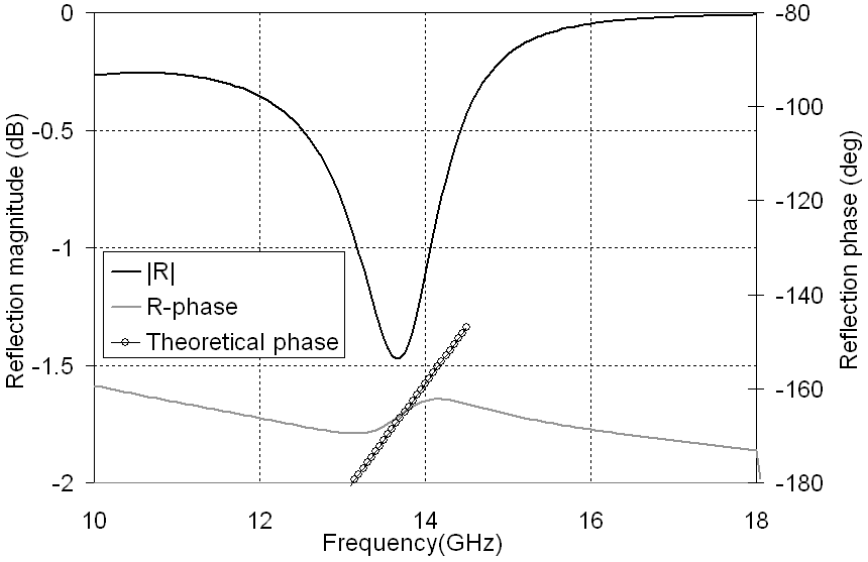

a)

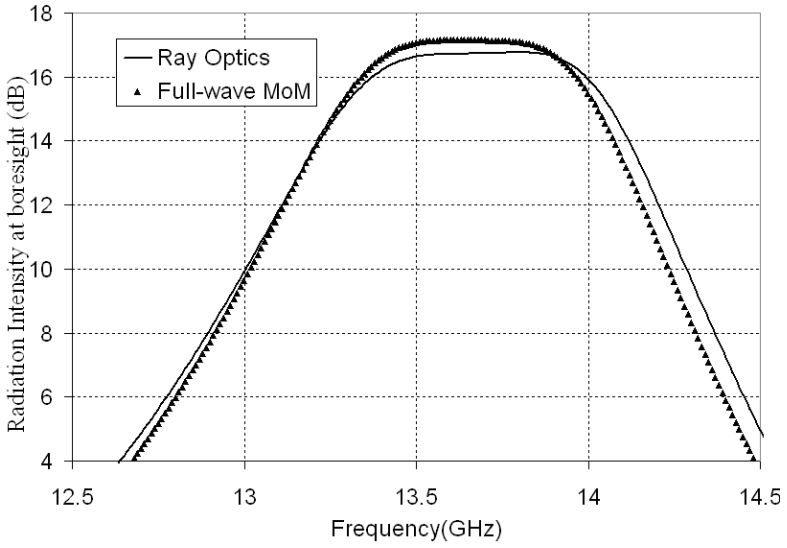

b)

Fig.5-5 a) Reflection coefficient (magnitude and phase) of the double layer dipole PRS, with dimensions in mm: l_1=14, w_1=0.5, l_2=9, w_2=0.5, D_x=1 and D_y=14.5; 12.6mm of foamboard (ε_r=1.05) for normal incidence and b) Radiation intensity at boresight for the antenna formed using the double dipole PRS located at h_r=11.4mm from a ground plane.

Similarly as in the single layer case, the directivity pattern can be obtained. This can be observed in Fig. 5-6 which shows the directivity at boresight for a frequency range between 12.5-14.5 GHz. The maximum directivity is 19.8dBi at 13.2GHz. Good agreement between full-wave and ray optics results for the antenna performance is

observed. In the same figure, the total radiated power as calculated by reciprocity is depicted. As commented before the radiated power is very low at lower frequencies. It can be observed that the leaky mode is excited around 13.2GHz, point of maximum directivity.

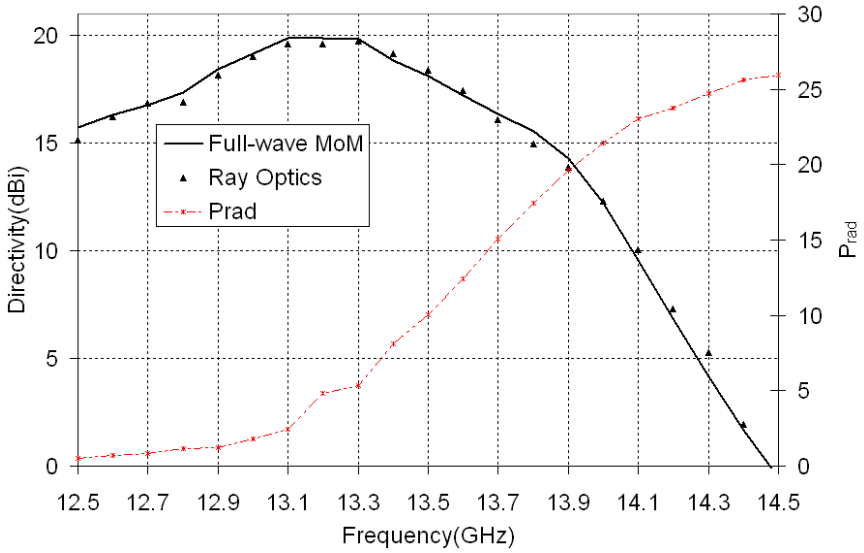

Fig. 5-6 Simulated a) directivity pattern of a double layer dipole PRS cavity antenna, with dimensions in mm: l_1=14, w_1=0.5, l_2=9, w_2=0.5, D_x=1 and D_y=14.5; 12.6mm of foamboard (ε_r=1.05); cavity thickness is 11.4mm, as obtained using Full-wave MoM as well as a ray optics model.

5.2.1 Near-Field excitation on double layer dipole PRS antenna

In the double layer PRS structure apart from the individual resonance of the PRS arrays additional resonances appear as a result of the cavity form between the arrays. In particular, for the double layer PRS antenna two resonant cavities are formed in a similar fashion as in a Fabry-Pèrot cavity. The lower PRS and the ground plane separated approximately half wavelength form a first resonant cavity whilst both two PRSs, separated as well about half wavelength, form a second resonant cavity.

In this section we initially focus on the cavity formed between the two PRSs. The spectral position of the cavity resonances are manifested as sharp peaks in the excited near-fields, it is greatly affected by the distance between the two surfaces and it shows the level of "interaction" (i.e. interference) between both arrays. The plane wave modal analysis based on Floquet theorem discussed in previous chapters is used to compute

accurately the near fields excited in the space between the two cavities formed in the double layer PRS LWA design. The near-fields are computed in the middle point of both cavities for a parametric study related to the frequency and field level.

A single layer PRS as the one in Fig. 5-3 is assumed to be excited by an incident plane wave and the y-component of the excited electric near-field in the vicinity of the surface is shown as an inset in Fig. 5.7. In the single layer PRS the main resonance of the array, due to the dipole elements, is manifested as a null in the near field at 20.2 GHz. Grating lobes appear at frequencies above the resonance because of the array periodicity along y. Subsequently, an incident plane wave is assumed to excite the double layer PRS in Fig. 5-5. The y-component of the excited electric near-field in the middle of the cavity for different separation distances, *S,* between the arrays is shown in Fig. 5-7. It can be observed that the main resonance due to the array elements remains at the same frequency and is not affected by the separation distance. However, the additional resonances, consequence of the cavity, appear at around 5 GHz and 15 GHz as peaks in the near-field and their position in the frequency spectrum is determined by the separation distance. Intuitively as *S* increases it is expected that the interaction between the two arrays decreases and therefore that the peak moves towards lower frequencies. This can be observed in Fig. 5-7. Furthermore, the peak becomes less sharp, due to the lower reflectivity values of the individual dipole array in lower frequencies.

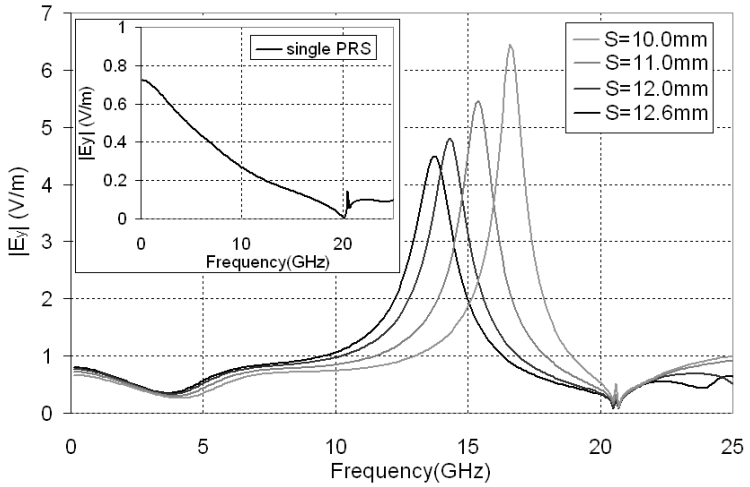

Fig. 5-7 y-component of the electric near-field of a double layer dipole PRS cavity with dimensions in mm: l_1=14, w_1=0.5, l_2=9, w_2=0.5, D_x=1 and D_y=14.5 excited by an incident plane wave for different thickness of foamboard (ε_r=1.05) at z=S/2; the inset shows y-component of the excited electric near-field for the single dipole PRS with dimensions l_1 and w_1 within the same unit cell.

Next, the ground plane is considered at a distance h_r=11.4mm. Initially, the excited electric field is sampled at z=S/2 and z=h_r/2 where S is the thickness of the foamboard (i.e. distance between both arrays) and equal to 12.6mm. The magnitude and phase of the y-component electric near field is shown in Fig. 5-8 between 11GHz and18Ghz. The insertion of the ground plane results in the excitation of two different modes, odd and even, in the two cavities at different frequencies. A null of the excited near-fields in the cavity formed between both PRSs is observed at 13.48 GHz. Inspection of Fig. 5-8 shows that in the lower frequency band, before the null, the fields are out of phase (π rad), corresponding to an odd mode excitation whilst in the upper frequency band the fields are in phase corresponding to the even mode.

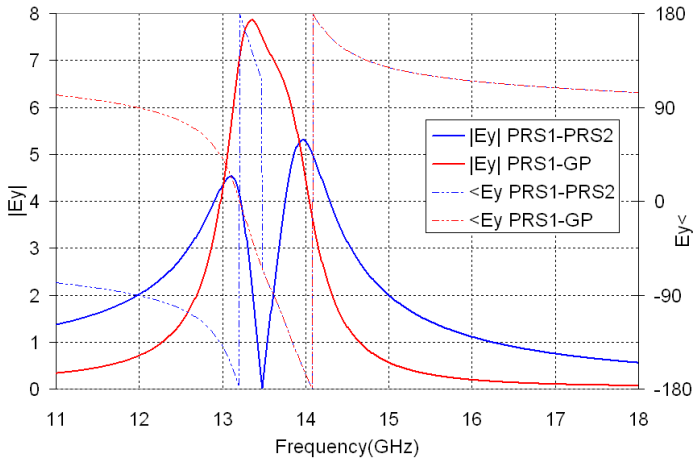

Fig. 5-8 Magnitude and phase of the y-component of the excited electric near-field in a double layer dipole PRS cavity with dimensions in mm: l_1=14, w_1=0.5, l_2=9, w_2=0.5, D_x=1 and D_y=14.5; 12.6mm of foamboard (ε_r=1.05) at z=S/2 (between both PRSs) and z=h_r/2 (between lower PRS and ground plane).

Next, the excited electric near-field of the double layer PRS LWA is studied for different values of S, as shown in Fig. 5-9. This figure shows the magnitude of the y-component of the electric near-field between the two arrays. It can be observed that as S increases the peak of the odd mode moves towards lower frequency values and becomes less sharp, due to the lower reflectivity values of the individual dipole array in lower frequencies. Same observations can be done to the even mode which are in agreement with the conclusions of Fig. 5-7. The point where the fields are null in the cavity formed between both PRSs is not affected by the distance between the two arrays. Fig. 5-9b shows the magnitude of the y-component of the electric near-field between the lower array and the ground plane. It is evident that as the distance between the arrays

decreases, *S*, the interaction between both arrays increases which leads to a higher field level in the lower frequency band (odd mode). On the contrary, as S increases the interaction between the arrays is lower; the field level in the lower frequency band decreases and the field level in the upper frequency band continuously increases.

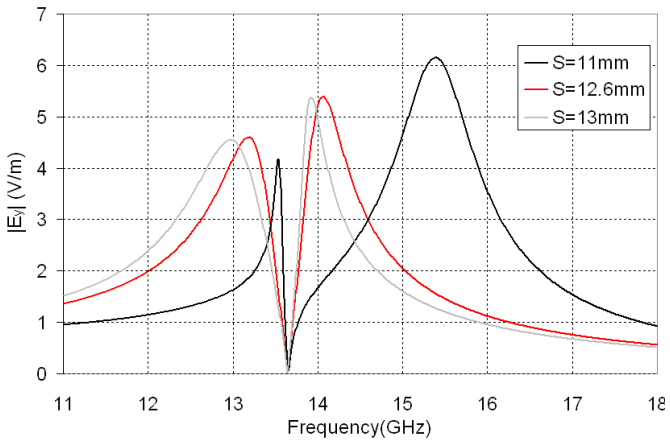

a)

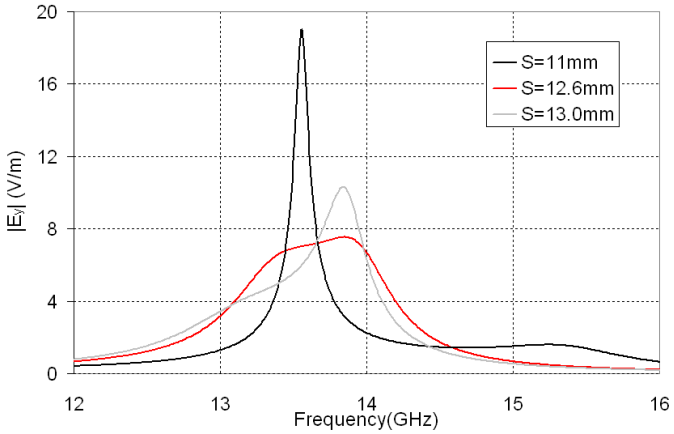

b)

Fig. 5-9 Magnitude of the y-component of the electric near-field of a double layer dipole PRS antenna cavity with dimensions in mm: l_1=14, w_1=0.5, l_2=9, w_2=0.5, D_x=1 and D_y=14.5 at h_r=11.4mm from a ground plane for different thickness of the foamboard, *S*, (ε_r=1.05) at a) z=*S*/2 and b) z=h_r/2.

The same study can be performed by keeping the distance between the arrays and changing the distance between the lower array and the ground plane, h_r. The excited magnitude of the electric near-field is depicted in Fig. 5-10 at the middle point of both cavities. Similar conclusions can be derived from this figure. If the distance between the PRS and the ground plane increases a shift towards lower frequency values is observed for both modes, Fig.5-10a. In this case, the point where the fields are null in the cavity between the two PRSs is greatly affected by the distance between the lower array and

the ground plane. If h_r decreases the even mode is strongly excited and the odd mode level reduces as it can be concluded from Fig. 5-10b.

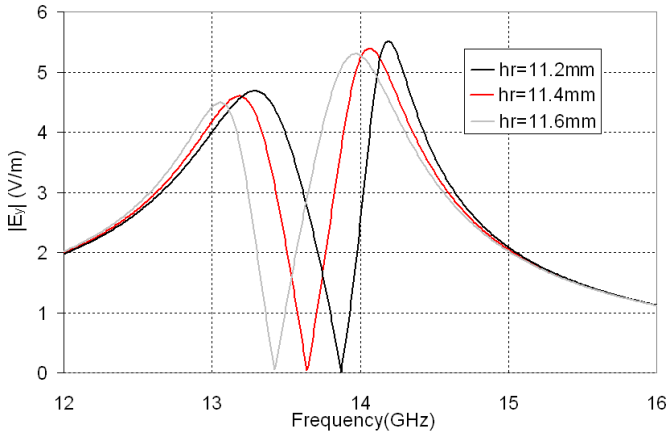

a)

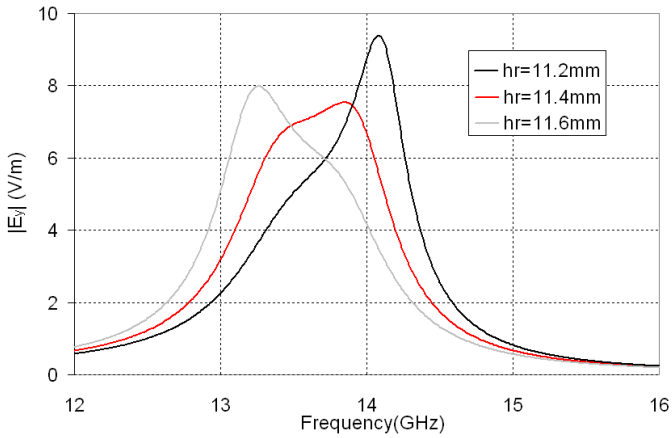

b)

Fig. 5-10 Magnitude of the y-component of the electric near-field of a double layer dipole PRS antenna cavity with dimensions in mm: l_1=14, w_1=0.5, l_2=9, w_2=0.5, D_x=1 and D_y=14.5; 12.6mm of foamboard (ε_r=1.05) for varying resonant distance, h_r from a ground plane at a) z=S/2 and b) z=h_r/2.

5.2.2 Parametric directivity study

In this section the effect of the separation distances between the two 2-D periodic arrays and between the lower array and the ground plane in the directivity and far-field radiation intensity at boresight is presented. Furthermore the consequences of lengthening or shortening the elements that composed both PRSs are also studied. The analysis commences from the structure investigated in Fig. 5-6 with the aim of providing a better directivity bandwidth at boresight. Design guidelines will be given

throughout the section in order to address specific requirements for increasing the bandwidth performance.

5.2.2.a. Distance between lower array and ground plane, h_r

In section 5.2.1 it was shown the effect of varying the resonant length (distance between lower array and ground plane) in the excited fields inside both cavities. Analogous conclusions as the ones exposed there can be derived by observation of the far-field radiation intensity shown in Fig. 5-11a. In this section, the effect of the resonant length on the directivity bandwidth is studied.

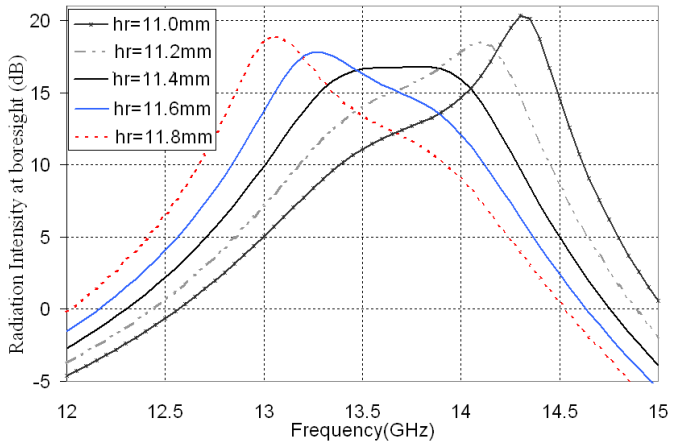

a)

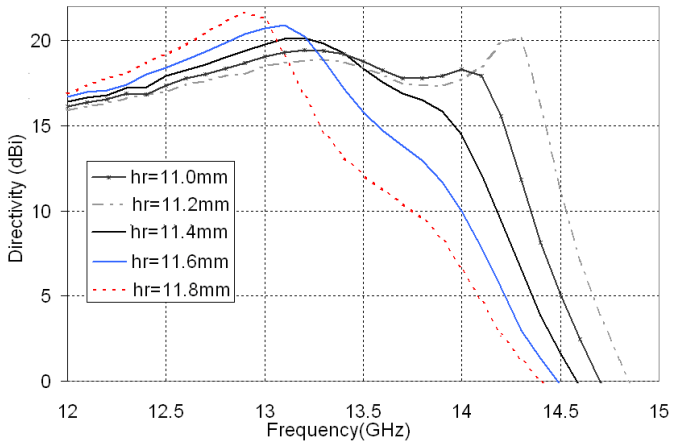

b)

Fig. 5-11 Simulated a) far-field radiation intensity at boresight and b) directivity at boresight of a double layer dipole PRS cavity antenna, with dimensions as in Fig. 5-6 for varying cavity thickness, h_r, as obtained using Full-wave MoM.

The analysis commences from h_r=11.4mm where both modes seem to be equally excited (same field level), Fig. 5-11a. Deriving the directivity at boresight for this resonant distance results in a directivity value higher at the odd mode, frequency 13.4GHz, than at the even mode, frequency 13.8GHz. Although the directivity slightly increases at 13.8GHz the dip between the two frequency points is very steep resulting in a poor bandwidth performance, Fig. 5-11b. Therefore, in order to obtain higher directivity values at the upper frequency band, the even mode should be strongly excited. If the distance between the array and the ground plane is increased the odd mode is more strongly excited than the even mode, as a result, the directivity bandwidth resembles more to the single layer case. Now, notice that if the resonance distance decreases (e.g. h_r=11.2mm) the even mode level is higher than the odd mode level and consequently the directivity at the even mode frequency, 14.1GHz, significantly increases. Thus, the evolution of the directivity at boresight from the odd to the even mode frequency is very smooth which in turn results in a better bandwidth performance of the antenna.

Another interesting characteristic related to the frequency at which the modes are excited can be remarked. When h_r decreases odd and even mode move towards higher frequencies whilst the contrary happens when h_r increases. This can be understood by simple observation of Eq. 5.1-9, if all variables remain constant but the resonant length the frequency can be expressed as,

$$f = \frac{(\varphi_R + (2N-1)\pi)c}{4\pi h_r} = \frac{cst}{h_r} \tag{5.2-2}$$

thus, an inversely proportional relation exists between both variables.

5.2.2.b. Distance between both arrays, S

Next the effect of modifying the distance between both arrays is examined. The analysis starts from S=12.6mm where both modes are excited and have the same magnitude, Fig. 5-12a. It was commented in section 5.2.1 that as the distance between the arrays is reduced the interaction between the two arrays increases; this affects the lower frequency band and therefore the odd mode excitation which results in a higher odd

mode level. The contrary happens if *S* increases. The same observation can be made in the directivity plot at boresight, Fig. 5-12b. Similarly as before better bandwidth performance is achieved when the even mode level is higher than the odd mode (larger *S* values). It is further instructive to note that there is always a common cross frequency point for every value of *S*. This frequency point coincides with the field null observed in Fig. 5-9a which shows that this frequency point is independent of the distance between the arrays. This can also be expected from Eq. 5.2-2.

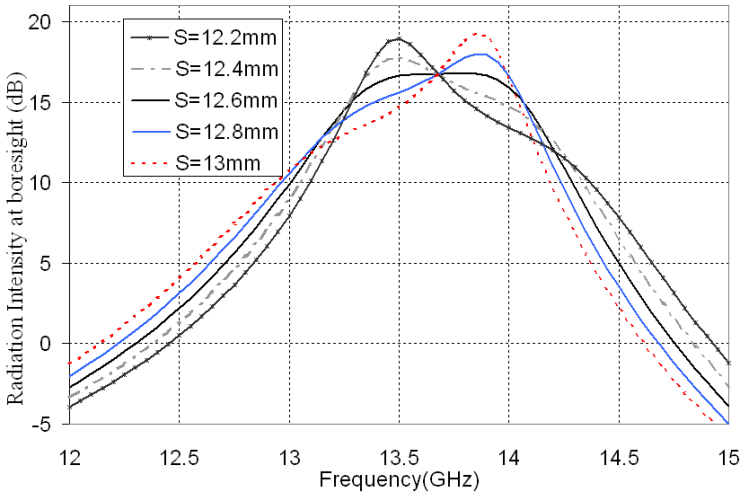

a)

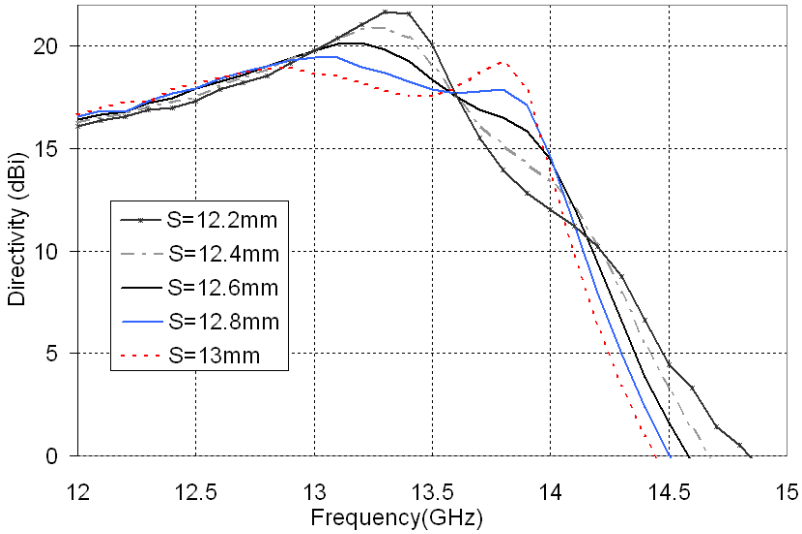

b)

Fig. 5-12 Simulated a) far-field radiation intensity at boresight and b) directivity at boresight of a double layer dipole PRS cavity antenna, with dimensions as in Fig. 5-6 for varying foamboard thickness, *S*, as obtained using Full-wave MoM.

5.2.2.c. Upper array element size, L_2

Using the plane wave modal analysis together with reciprocity, the effect of the reflectivity of the second layer (upper PRS) to the double layer array antenna directivity response has been rigorously studied. The double layer dipole array has been used with a separation distance S=12.6mm between the two layers and a resonance distance of h_r=11.4mm to the ground plane. A parametric study has been carried out by changing the length, L_2, of the unit dipole in the second layer, thus changing the reflectivity of the layer.

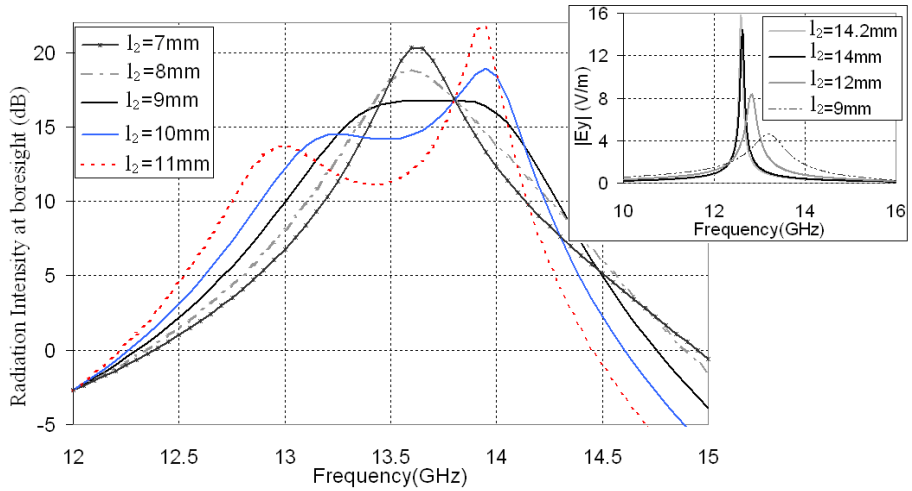

a)

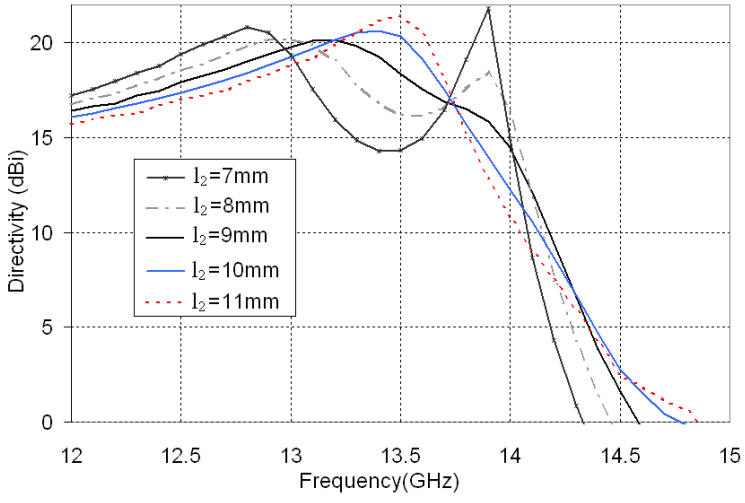

b)

Fig. 5-13 Simulated a) far-field radiation intensity at boresight (inset single layer antenna near-field) and b) directivity at boresight of a double layer dipole PRS cavity antenna, with dimensions as in Fig. 5-6 for varying length of the upper dipole array, L_2, as obtained using Full-wave MoM.

Shorter dipole length, L, in the single layer array, with the same periodicity, results in lower field values, and the peak is smoother and wider in frequency as shown in the inset of Fig. 5-13a. The double layer array antenna far-field radiation intensity for different dipole length in the second layer, L_2, is shown in Fig. 5-13a. For shorter second layer dipole (i.e. lower second layer reflectivity) the maximum near-field at the even mode frequency has lower value. In addition, the odd mode moves towards higher frequencies and has a higher level. The resonance becomes less evident because of the small reflectivity values of the second layer. Thus, one could conclude that when the length of the elements is very short there is almost no resonance in the cavity formed by the two layers being similar to the single layer PRS LW antenna. When the length of the second layer increases the opposite trend occurs leading to apparently larger bandwidth.

Inspection of the directivity at boresight confirms that by lengthening the dipoles of the upper array the even mode is strongly excited, the bandwidth is enlarged but the dip between both frequencies becomes deeper. Therefore, despite the apparent increased bandwidth provided by more reflective arrays the relative -3dB fractional bandwidth is lower. However, this effect could be used for designing dual-band LW antennas.

5.2.2.d. Lower array element size, L_1

If an array of higher reflectivity (i.e. larger values of L_1) is used as the first layer in the double layer cavity antenna, it will produce lower leakage rates which results in a higher directivity [1]. For instance, an array composed of dipoles L_1=14.4mm is 4dB more directive than an array of dipole L_1=13 mm. If the lower array is more reflective the antenna is more weakly coupled to the incoming plane wave and therefore produces a higher external quality factor. As the external quality factor (in case of no ohmic losses) is inversely proportional to the 3 dB fractional bandwidth, a higher external quality factor implies that the 3 dB fractional bandwidth is narrower and also that the reactive power stored in the resonator is higher [10]. This is clearly depicted in Fig. 5-14a which shows the far-field radiation intensity for varying dipole length in the lower array. For larger values of L_1 the antenna behaves as the single layer design. It is also important to highlight the fact that for a specific length the level of both modes are comparable. For

shorter length the coupling is higher and as a result both modes move apart leading to larger bandwidth. The effect on the directivity at boresight is also shown in Fig. 5-14b.

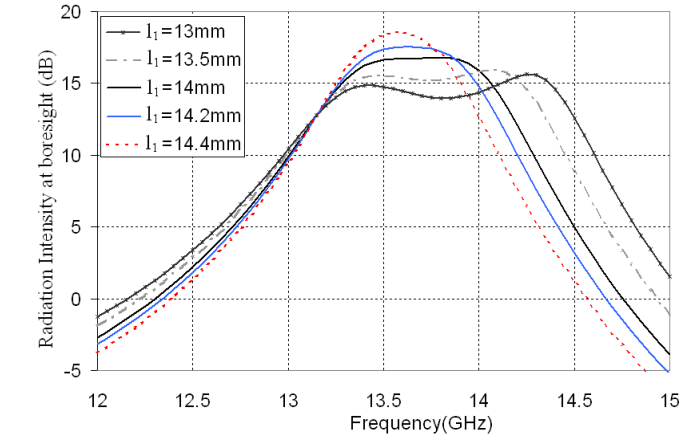

a)

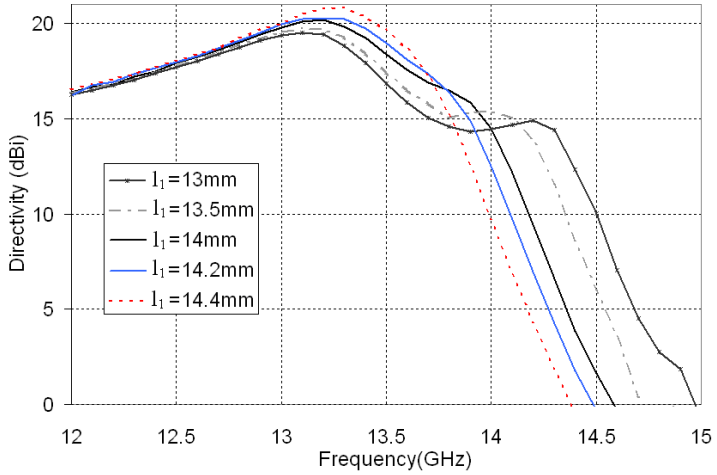

b)

Fig. 5-14 Simulated a) far-field radiation intensity at boresight and b) directivity at boresight of a double layer dipole PRS cavity antenna, with dimensions as in Fig. 5-6 for varying length of the lower dipole array, L_1, as obtained using Full-wave MoM.

5.2.3 Optimised double layer dipole PRS antenna

Following the parametric study some design guidelines can be established:

- The level of excitation of the even mode needs to be higher than the odd mode.
- The level of excitation of the even mode can be increased by:
  · Modifying the length of the upper array (larger values); however the dip between the modes is greatly affected (design of dual-band LW antennas)

· Altering the distance between the arrays (larger S values)

· More significantly by bringing the arrays closer to the ground plane (h_r).

- The bandwidth can be increased by shortening the length of the element in the lower array.

- The dip within the frequency band is greatly affected by the length of the upper array.

- In order to have broad bandwidth performance the transition between odd and even mode should be smooth.

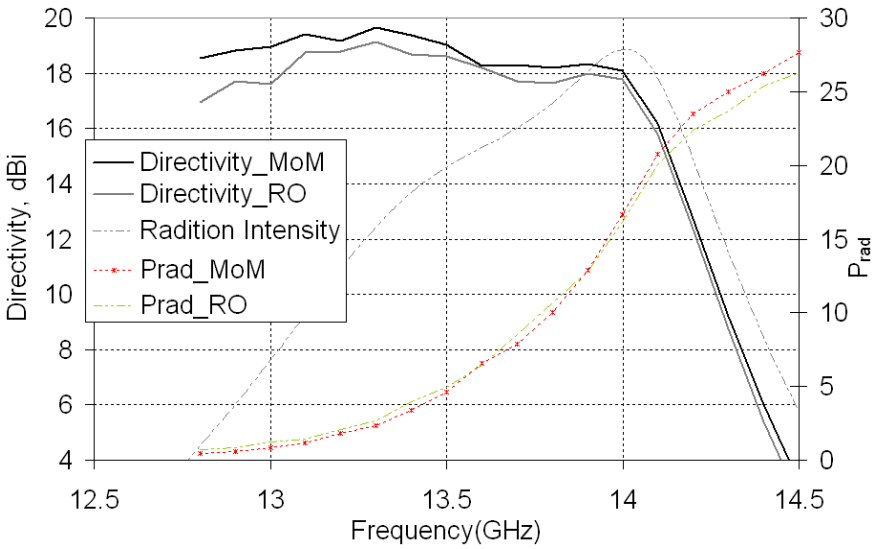

Fig. 5-15 Simulated directivity at boresight of a double layer dipole PRS cavity antenna, with dimensions in mm: l_1=14, w_1=0.5, l_2=9, w_2=0.5, D_x=1 and D_y=14.5; 12.6mm of foamboard (ε_r=1.05); cavity thickness is 11.2mm, as obtained using Full-wave MoM as well as a ray optics model. The radiated power as obtained by Full-wave MoM as well as a ray optics model is also plotted together with the radiation intensity at boresight.

By combining these guidelines optimised designs can be produced for particular requirements. The optimised antenna has been formed using the double layer dipole PRS used in the previous sections, printed on a foamboard of thickness 12.6mm. The distance from the lower array to the ground plane has been reduced to 11.2mm. A broadband antenna performance with high antenna directivity has been obtained and it is presented in Fig. 5-15. The directivity is shown for a frequency range between 12.8-14.5 GHz as obtained from ray optics as well as full-wave MoM with reciprocity. The 1 dB bandwidth is over 7% and the maximum directivity is 19.6dBi at 13.4GHz. There is a good agreement between full-wave and ray optics results for the antenna performance. In the same figure, the far-field radiation intensity and the total radiated power as calculated by reciprocity are depicted. The far-field radiation intensity shows the

stronger excitation of the even mode and the smooth transition between both modes which results in the increased bandwidth as compared with the case in Fig.5-6. The 3-D patterns of the structure in Fig. 5-2b with a directivity response as in Fig.5-15 are shown in Fig. 5-16 at the edges and at the central frequency of the operating bandwidth.

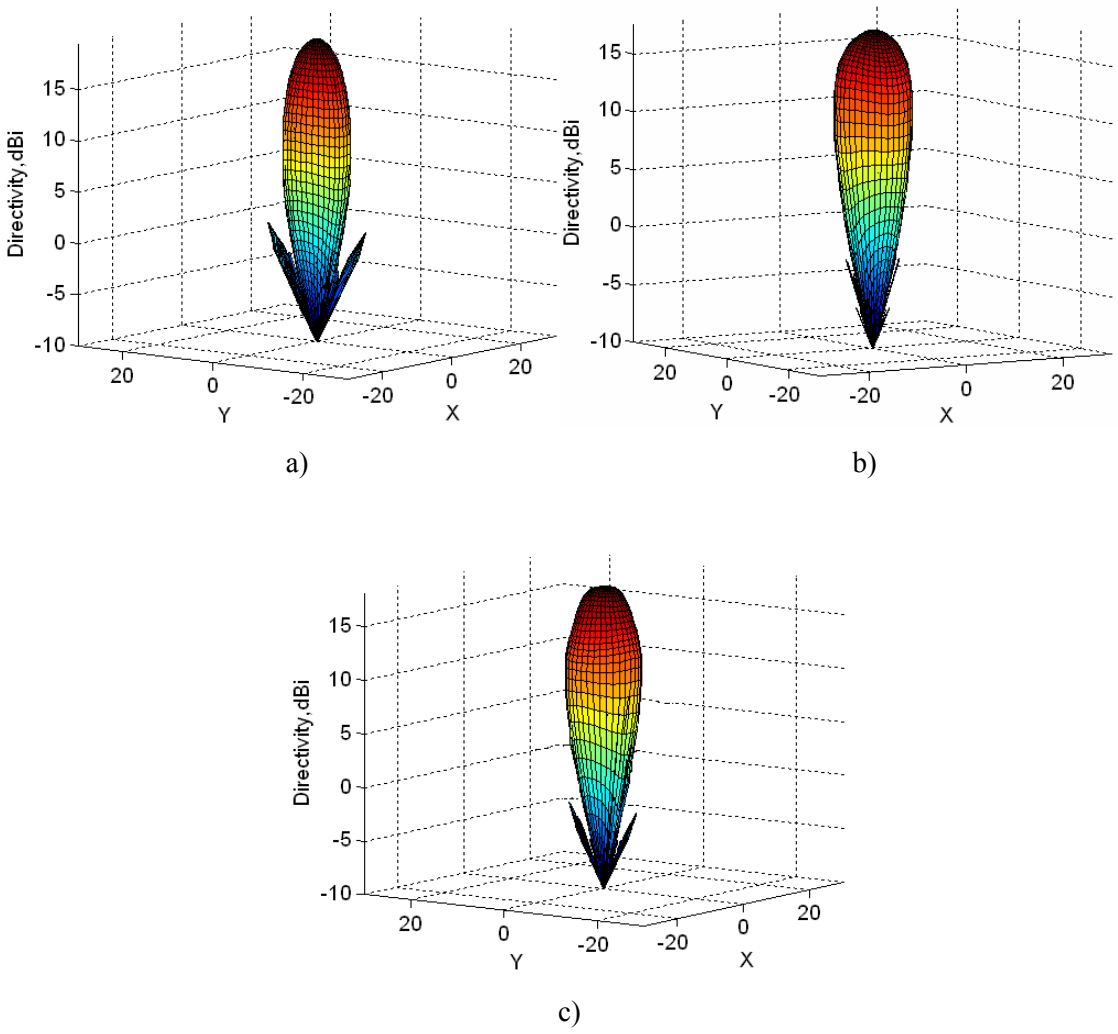

Fig. 5-16 3-D directivity patterns of the antenna in fig. 5-15 at a) 13.1 and b) 13.6GHz and c) 14GHz.

5.3 Antenna with Double Layer patch PRS

A design procedure similar to that of section 5.2 has been carried out, in order to produce a double layer square patch array design with reflection characteristics close to the optimum PRS response for high gain and wideband leaky-wave antenna performance. Both PRS arrays have been printed on a rigid dielectric substrate of 1.5

mm thickness and relative permittivity 2.55. Initially, losses are not considered. The PRS is composed of patches with dissimilar sizes. The square unit cell dimension is D = 11mm for both arrays. The top square patch edge is L_{PRS2}=6.0 mm whilst the bottom array (closer to the ground plane) element is L_{PRS1}=10 mm. The separation distance of the two dielectric boards is S =11 mm. The two boards are separated by air and are located on top of a ground plane at distance h_r. A sketch of the double PRS LW antenna structure is plotted in Fig.5-17.

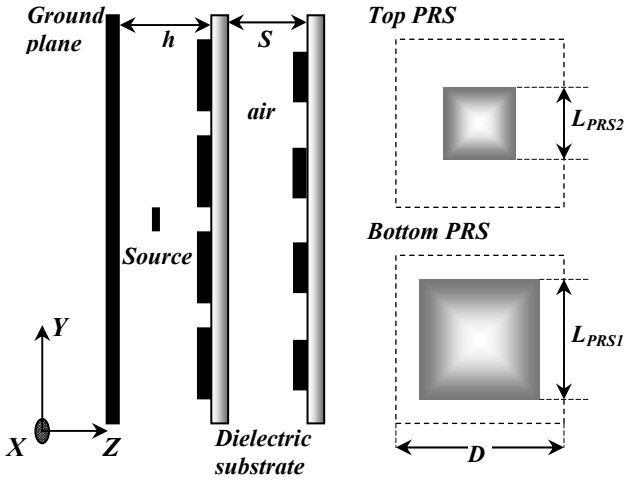

Fig. 5-17 Cross-section of the antenna with double layer square patch PRS.

5.3.1 Design of double layer patch PRS

For the above double layer PRS, Floquet plane wave modal analysis has been used to simulate the (infinite) array response, taking into account the dielectric layers. The patches in the first array are closely spaced together resulting in high reflectivity values. The second layer patch size is smaller in order to exhibit lower reflectivity and thus produce a semi-resonant effect as discussed in [6]. The simulated reflection coefficient of the optimised double layer square patch array is shown in the inset of Fig. 5-18. The minimum reflection value appears at 13.6 GHz and is slightly lower than the one obtained from the double layer dipole PRS. The phase increases with frequency in the range between 13.0 GHz and 14.0GHz. Broad bandwidth is expected over this frequency range and high directivity is also expected due to the relatively high values of the reflection magnitude.

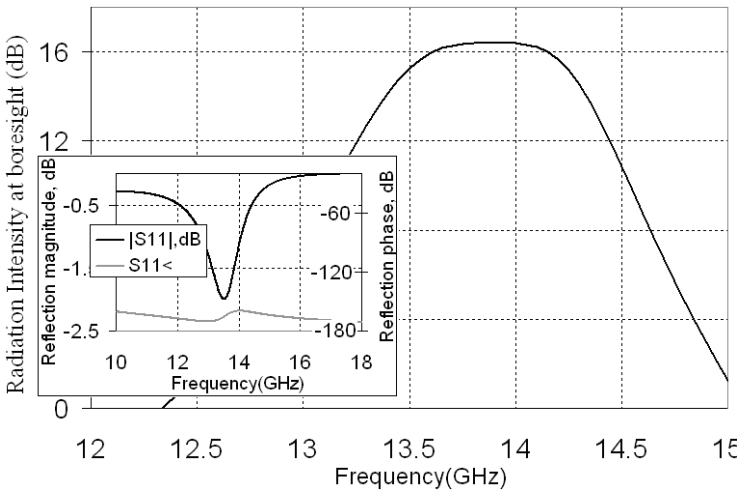

Fig.5-18 Radiation intensity at boresight of the double layer patch PRS, with dimensions in mm: L_{PRS1}=10, L_{PRS2}=6, D=11 printed on a dielectric substrate of 1.5mm and ε_r=2.55 located at h_r=11.3mm from a ground plane. The inset shows the reflection coefficient (magnitude and phase of the double PRS).

An estimation of the far-field radiation intensity of the leaky-wave antenna formed with the double layer square patch PRS is obtained from Eq. (5.1-5) and presented in Fig.5-18. The initial resonant distance h_r is calculated from Eq. (5.1-7) and its value is 11.37mm. A broadband antenna performance is expected. The bandwidth is now larger as compared to the double-layer dipole PRS design but by observation of the radiation intensity the directivity is expected to be lower.

5.3.2 Antenna Performance

As expected from the previous study in section 5.2 the radiation intensity of Fig. 5-18 where odd and even mode are excited with a same magnitude level will produce a narrow directivity bandwidth. Ideally the even mode level should be higher than the odd mode; therefore optimisations need to be performed. After an optimisation study such as the one in section 5.2.3 the leaky-wave antenna has been formed using a double-layer square patch PRS where the length of the upper patch array has been reduced to 5.6mm. The distance between the lower array and the ground plane is reduced to 11 mm and the rest of the variables remain the same.

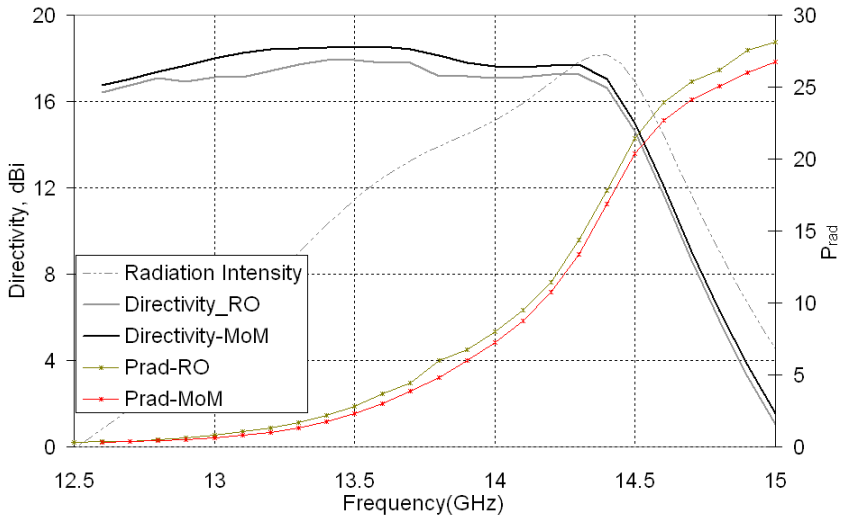

Fig. 5-19 Simulated directivity at boresight of a double layer patch PRS cavity antenna, with dimensions in mm: L_{PRS1}=10, L_{PRS2}=5.6 and D=11; the PRSs are printed on a substrate 1.5mm thick and ε_r=2.55; the air cavity between both arrays is S=11mm thick and the distance between the double layer PRS and the ground plane h_r is 11mm, as obtained using Full-wave MoM as well as a ray optics model. Radiated power and radiation intensity at boresight are also plotted.

For this configuration simulations of the overall antenna have been carried out using full-wave MoM with reciprocity as well as an array optics model. A broadband antenna performance with high antenna directivity has been obtained and it is presented in Fig. 5-19 which shows the directivity for a frequency range between 12.5-15 GHz. The 1 dB bandwidth is over 10% and the maximum directivity is 18.55dBi at 13.6GHz. A good agreement between full-wave and ray optics results for the antenna performance is appreciated. In the same figure, the far-field radiation intensity and the total radiated power as calculated by reciprocity are depicted. The far-field radiation intensity shows the stronger excitation of the even mode which results in the increased bandwidth as compared with the excitation of this mode in Fig.5-18. The 3-D patterns of the optimised double layer patch PRS antenna are shown in Fig. 5-20 at the centre and edges of the operating bandwidth.

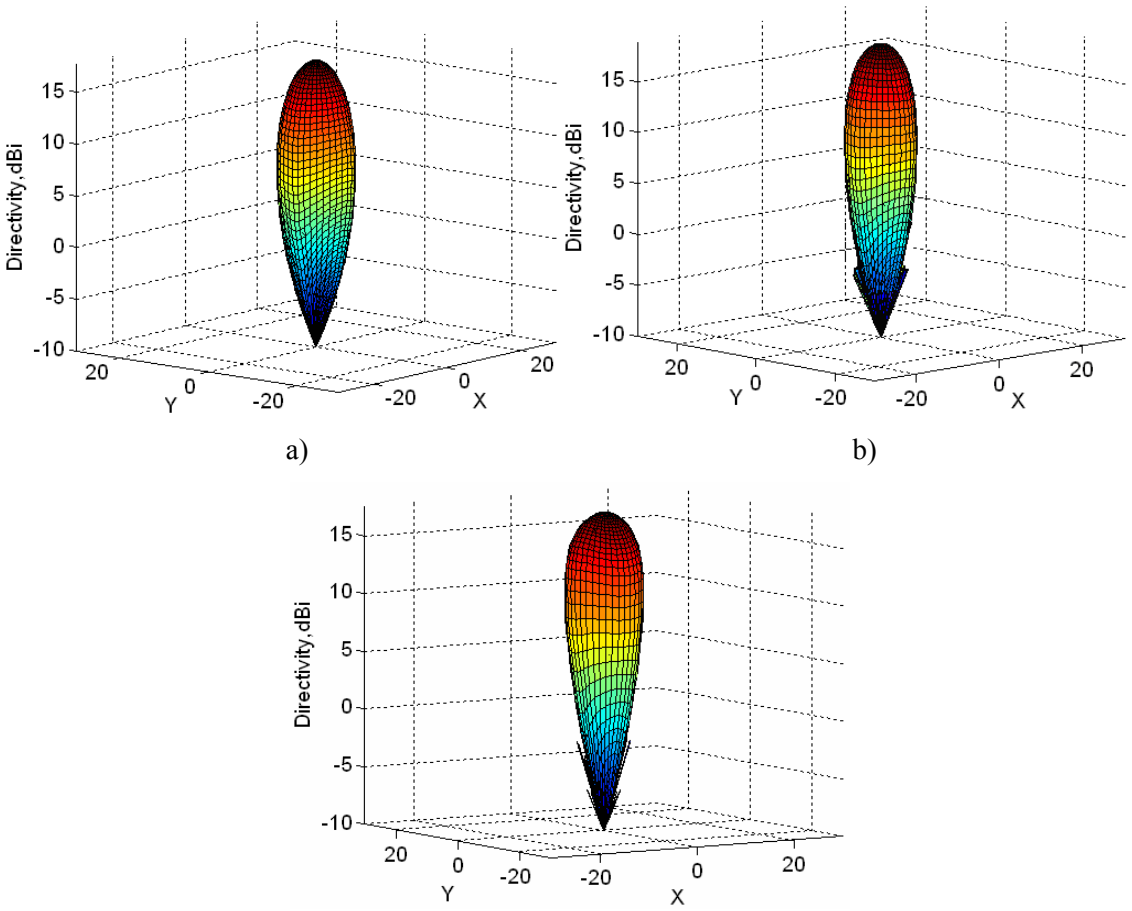

Fig. 5-20 3-D directivity patterns of the antenna in fig. 5-19 at a) the lower end frequency 12.9 b) the central frequency 13.6GHz and c) at the upper end frequency 14.1GHz.

5.3.3 Finite size antenna model

The optimised double layer patch PRS antenna has been modelled in CST Microstripes™ 2009 and simulations of its performance have been carried out. Because of the symmetry of the structure magnetic and electric walls were used, therefore reducing the computational time. In order to use the magnetic and electric walls we assumed that the electric field on either side of the PRS patches is purely vertically polarised. Automatic meshing was employed in the simulation. The model consisted of 3.762 million mesh cells and the simulation required 1700Mb of memory. The simulation process lasted for 42 minutes on an Intel® Core™ i7 CPU 920 @2.67GHz for 30K time steps whilst the developed program needed 4 minutes in the same PC to calculate directivity and radiation pattern for the frequencies presented. The total dimension of the antenna was 23 x 23 cm^2.

For simulation purposes, a 3 mm long wire model dipole located in the middle of the first cavity is used to feed the antenna. The radius of the wire is 0.15 mm and the distance from the lower PRS and the ground plane is 5.5 mm (i.e. centre of the cavity, $z=h_r/2$). The simulated results from the code developed and the simulated antenna directivity using CST Microstripes^{TM} 2009 are shown in Fig. 5-21. The simulation prediction is in satisfactory agreement throughout most of the operating frequency band, apart from the lower end at which Microstripes result seems to slightly deviate from the full-wave MoM technique.

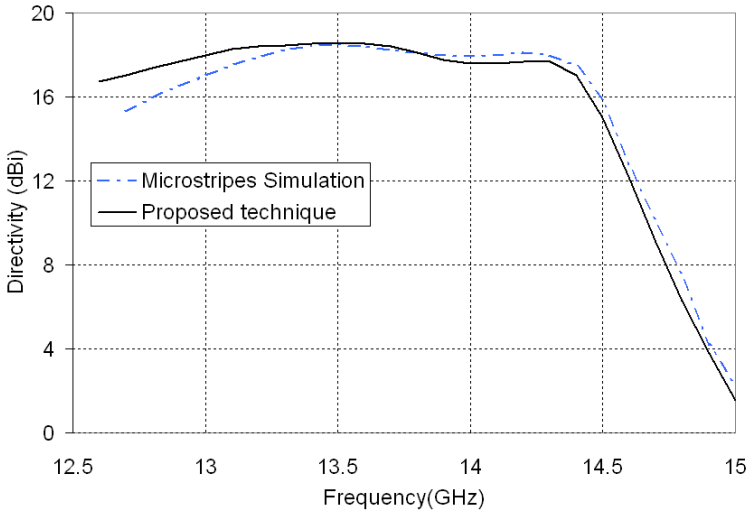

Fig. 5-21 Simulated directivity at boresight of a double layer patch PRS cavity antenna, with dimensions as in Fig.5-19 as obtained using the proposed technique (Full-wave MoM + reciprocity) as well as 3D electromagnetic simulator CST Microstripes^{TM} 2009.

Next, the PRS arrays are printed on a different substrate. In particular, FR-4 substrates of 1.6mm thickness and relative permittivity 4.2 are employed. In this case dielectric losses ($\tan\delta=0.025$) are included in the full-wave simulations. The choice of the substrate was merely due to availability in the material prior to the manufacturing procedure. An optimised double layer patch PRS antenna design is produced for the new substrates by simply modifying the air cavity thickness, S, and the resonant length, h_r. The new values of the distances are 10.1 and 10.9mm, respectively. Further optimisations can be performed by altering the length of the second layer patch PRS thus reducing the dip between the bandwidth edges. Specifically, patches of 5.0mm are employed.

Before the manufacturing procedure, the antenna is modelled in CST Microstripes™ 2009 considering an ideal dipole located in the centre of the cavity as the feeding element. Simulations of the performance of the antenna are investigated. The antenna accepted gain (gain ignoring mismatch, [11]) bandwidth as obtained using the proposed technique as well as the 3D electromagnetic simulator (MS™) is shown in Fig. 5-22 for the above antenna. The antenna presents two gain maximums at 13.5GHz and 14.2GHz with a value of 20.21 and 19.58dBi, the dip between them is smoother and lower than 2dB. The 3dB bandwidth of this antenna is over 8%. The 3-D *gain* patterns obtained using the proposed technique are shown in Fig. 5-23 at the centre and edges of the operating bandwidth.

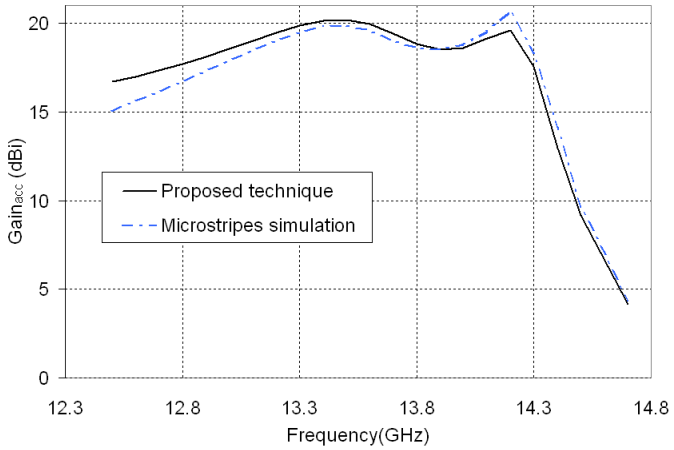

Fig. 5-22 Accepted gain at boresight of a double layer patch PRS cavity antenna, with dimensions in mm (L_{PRS1}=10, L_{PRS2}=5.0 and D=11, dielectric substrate: 1.6mm thick, ε_r=4.2 and tanδ=0.025, air cavity S=10.1mm and resonant distance h_r=10.9mm) as obtained using the proposed technique (Full-wave MoM + reciprocity) as well as 3D electromagnetic simulator CST Microstripes™ 2009 with an ideal dipole as central feed.

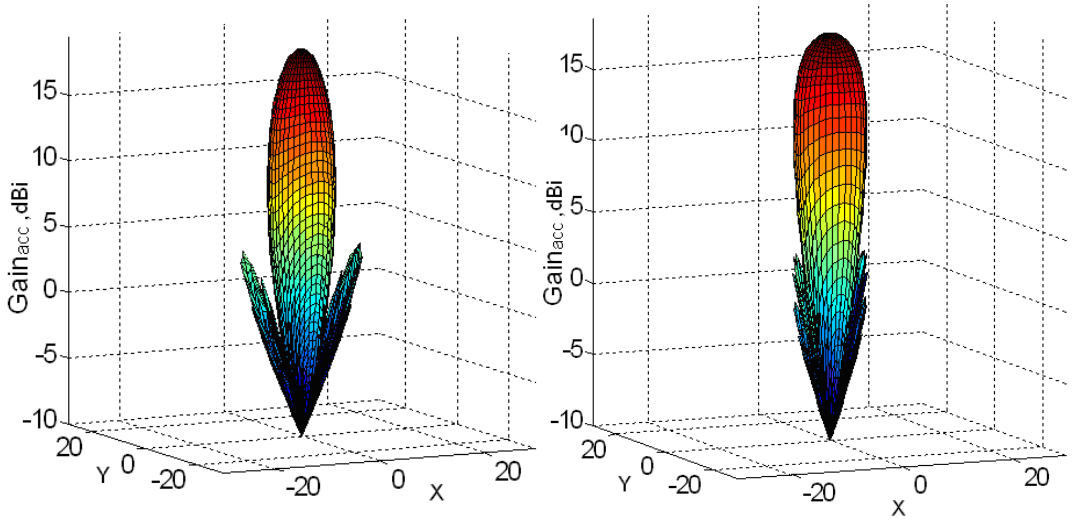

a) b)

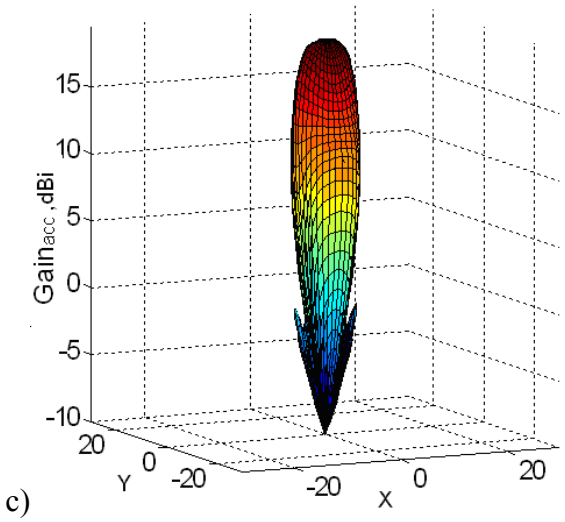

c)

Fig. 5-23 3-D *gain* patterns of antenna in fig. 5-22 at a) 13.2 b) 13.7 and c) 14.2GHz respectively.

5.4 Practical implementation of double layer PRS antennas

The radiation pattern of the excitation source has a fairly significant effect on the radiation pattern of the complete LWA. In this instance, the cavity is fed by a simple dipole. In order to obtain a good level of agreement between the measured and simulated radiation patterns it was necessary to construct an accurate simulation model for the dipole. Therefore, prior to the manufacturing process a different simulation to the one performed in the previous section is carried out on CST Microstripes^{TM} 2009.

5.4.1 Simulation Results

The cavity is fed by a semi-ridged co-axial cable inserted through a drill hole in the ground plane. The hole punctures the ground plane at the centre and the coaxial goes through to the middle of the cavity formed between the lower PRS and the ground plane. For the purpose of these experiments the outer shield of the co-axial cable was insulated from the metallic ground plane. Simulations carried out indicate that soldering the outer shield of the co-axial cable to the ground plane alters the radiation patterns obtained. The inner conductor of the coaxial is extended and bent parallel to the plane of the antenna (XY-plane in Fig. 5-17).

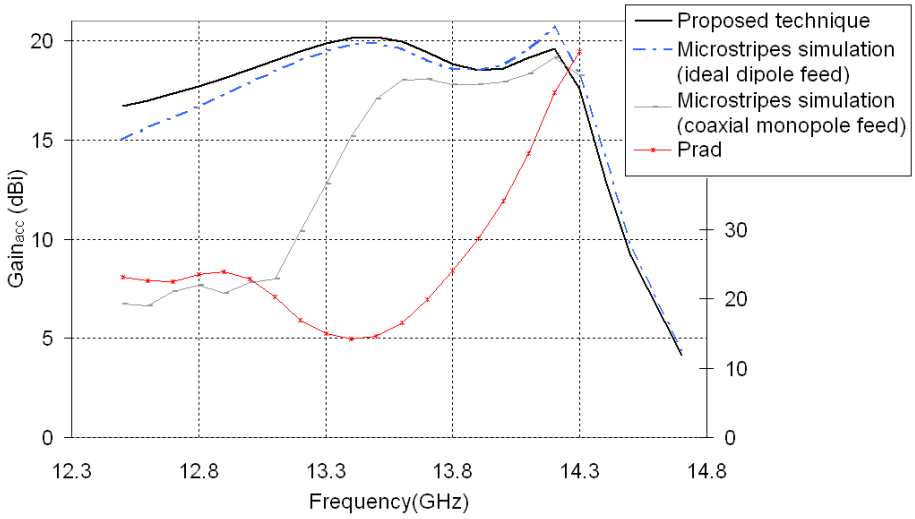

Fig. 5-24 Accepted gain at boresight of the antenna in Fig. 5-22 as obtained using the proposed technique (Full-wave MoM + reciprocity) as well as 3D electromagnetic simulator CST Microstripes^{TM} 2009 with an ideal dipole feed (blue) and a coaxial fed dipole (grey). The radiated power as obtained from Microstripes is also plotted.

The antenna accepted gain bandwidth as obtained using the proposed technique as well as the 3D electromagnetic simulator (MS^{TM}) with an ideal dipole and a coaxially fed dipole is shown in Fig. 5-24 for the antenna presented in Fig. 5-22. The agreement is fairly good at the centre and upper frequency band; however, we observe a disagreement at lower frequencies. Further simulations have been carried out in order to look into this effect. In particular, the near-fields excited at different points along a parallel plane of the array (XY-plane) in the middle of the cavity were obtained for two different cases. Initially, a vertical coaxial monopole puncturing the ground plane is considered (Fig. 5-25a) as a feeding source and it is compared to the case of an ideal dipole excitation (Fig. 5-25b). It is concluded that the currents flowing in the inner coaxial that fed the "realistic" dipole affect the mode excitation on the cavity.

By observation of the near-field it can be seen that for a vertical coaxial monopole, the TEM mode is excited at low frequencies. This is evident by simple inspection of the E_z component of the fields which is much stronger than the E_x and E_y components. As the mode propagates along y (points E1 and E2- Fig. 5-25a (i) and (ii)) we can see that at higher frequencies the TM1 mode starts being excited that is why the magnitude of the E_y component increases around 14.2GHz upwards. As the mode propagates along x (point H1- Fig. 5-25a (iii)) same observations can be made in relation to the magnitude of E_x.

On the contrary, by observation of the near-field for an ideal dipole excitation Fig. 5-25b, the TEM mode is not excited. Below the cut-off frequency of the TM1 mode there is no mode propagating in the cavity. At the cut-off frequency, 13.5GHz, the TM1 mode is excited. By observation of the points E1 (i) and E2 (ii) in Fig. 5-25b we can see the high level of the E_y component. Same observation can be made at point H1 (iii)- Fig. 5-25b.

For the excitation used in the experimental measurements the fields have also been plotted in Fig. 5-26. It is concluded that part of the energy at low frequencies is used for the excitation of the TEM mode given to higher values of the power radiated at low frequencies (refer to Fig. 5-24) which results in lower directivity values than in the ideal dipole excitation case and therefore lower values of the accepted gain.

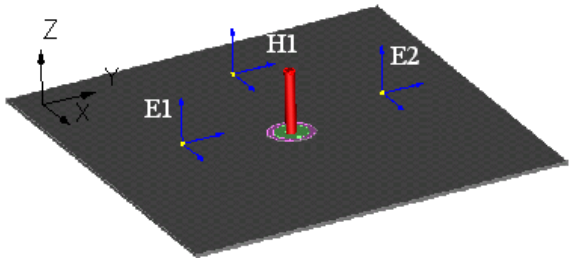

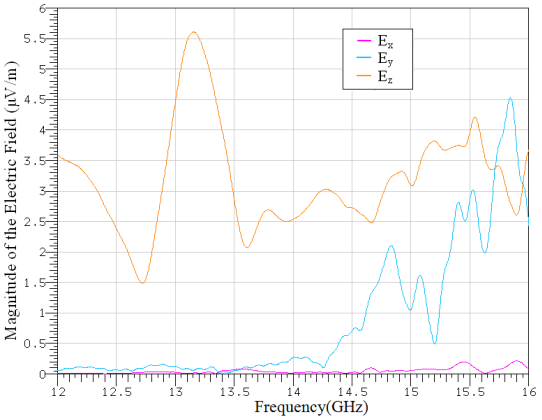

(i)

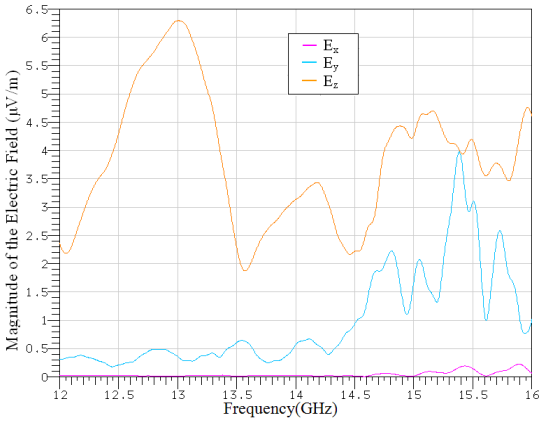

(ii)

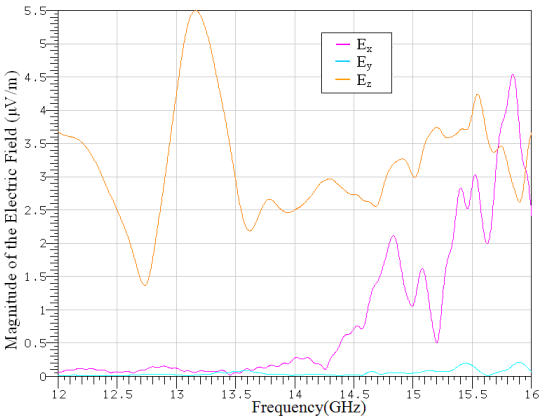

(iii)

a)

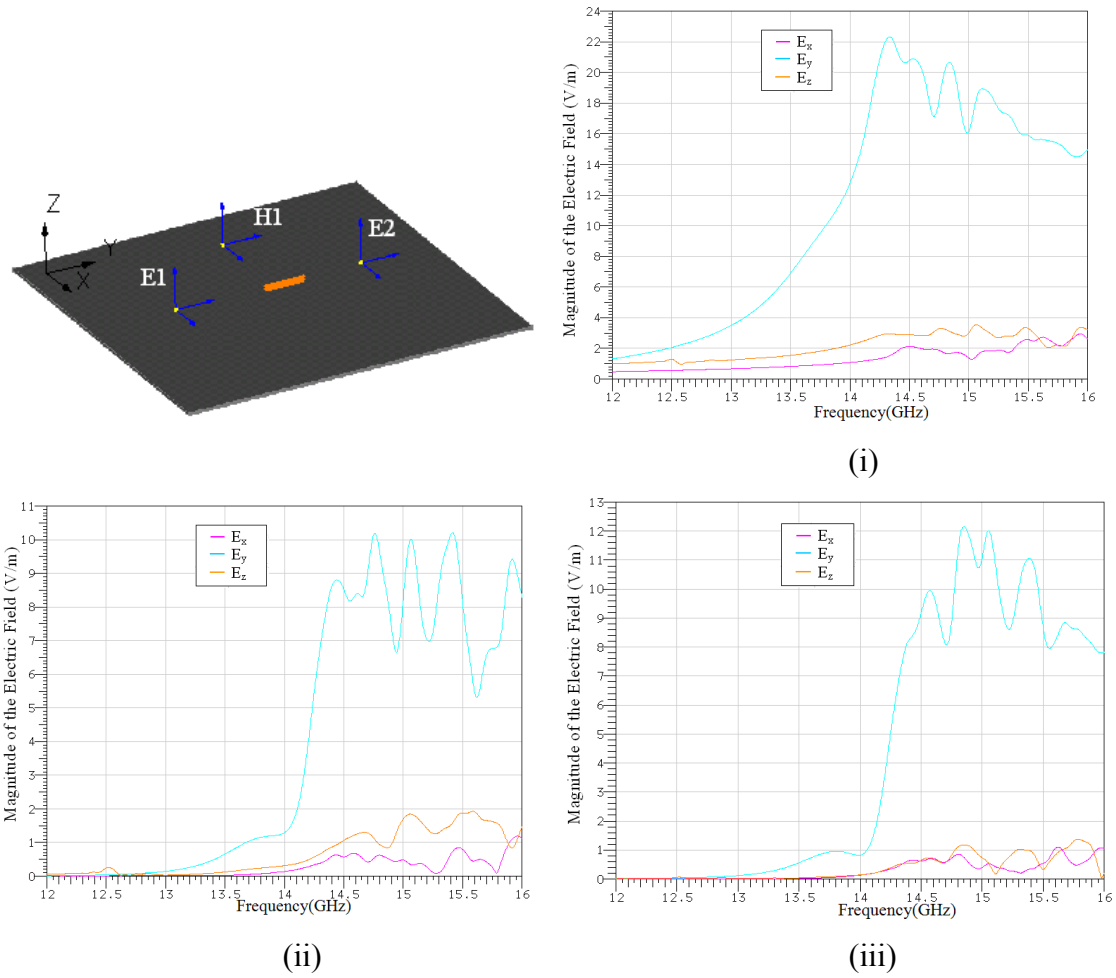

Fig. 5-25 Layout of the antenna for an a) coaxial vertical monopole and b) ideal dipole feed. X-, y- and z- component of the electric near-field at the points i) E1, ii) E2 and iii) H1 depicted in the different models of a) and b) as obtained using the 3D electromagnetic simulator CST Microstripes™ 2009.

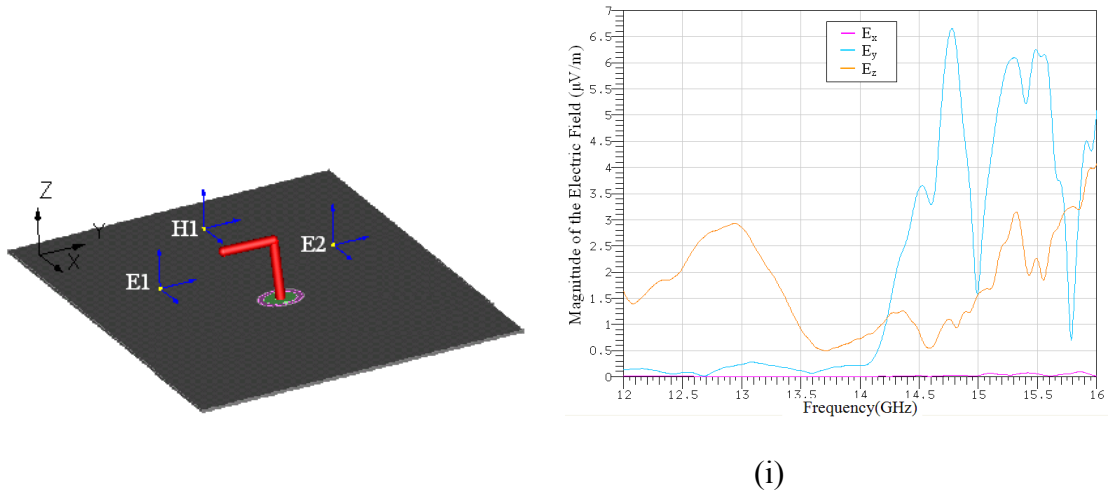

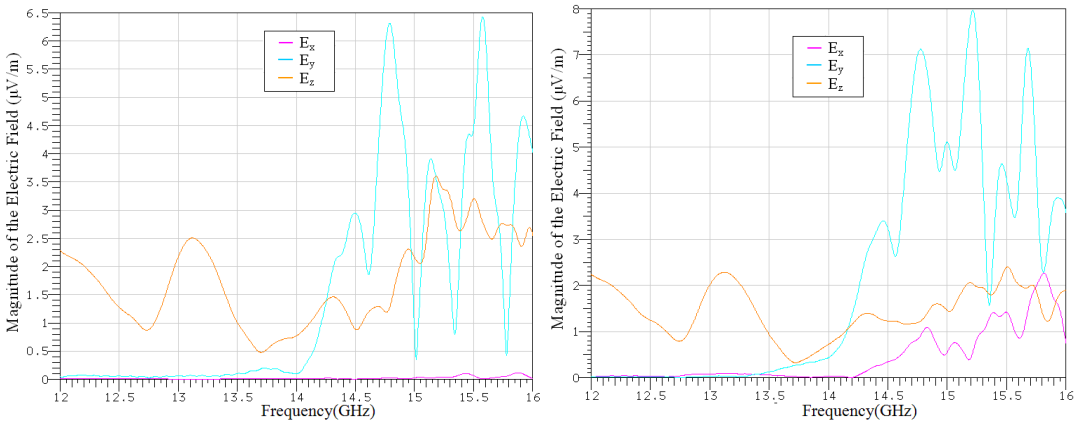

(ii) (iii)

Fig. 5-26 X-, y- and z- component of the electric near-field at the points i) E1, ii) E2 and iii) H1 of the coaxially fed dipole model obtained by the 3-D electromagnetic simulator CST Microstripes™ 2009.

The total surface current (magnitude of current vector) on the square patches of both PRS arrays of the antenna has also been obtained in CST Microstripes™ for an excitation source like in Fig. 5-26. The currents on the square patch array of the second PRS layer (L_{PRS2}=5mm) are shown in Fig. 5-27 for several frequencies and Fig. 5-28 shows the corresponding currents on the patches of the first PRS layer. The figures show the currents on a quarter of the square patch arrays corresponding to the simulation results on that area. The currents on the rest of the patches are symmetrical with respect to both x and y- axes.

At low frequencies, (outside the frequency band, 13.1GHz), almost all the area of the antenna is excited, the currents are high in all patches and high energy reaches the ends of the arrays. This effect results in a considerable directivity reduction as well as the appearance of high level side lobes. As the frequency increases (lower frequency band, 13.5GHz) the currents start concentrating in the central area of the antenna which will produce more directive beams. This effect is observed in all frequencies within the frequency band (for instance at 13.8GHz and 14.1GHz). For higher frequencies (e.g. 14.4 GHz) the currents start increasing in all patches giving to a distorted pattern with high side lobes.

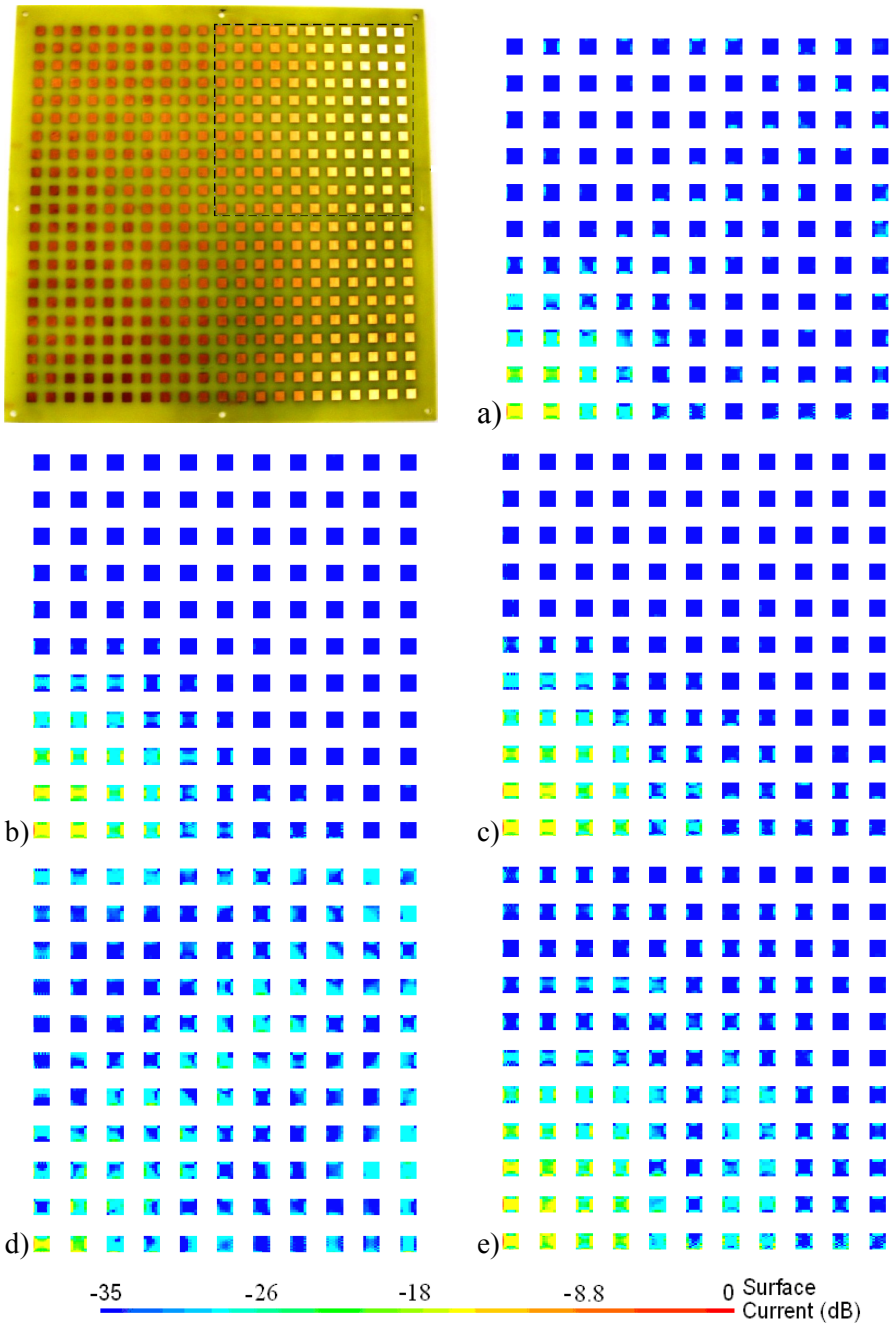

Fig. 5-27 Total surface current density (magnitude) on the half 2nd layer square patch PRS at a) 13.5, b) 13.8, c) 14.1, d) 13.1 and e) 14.4 GHz.

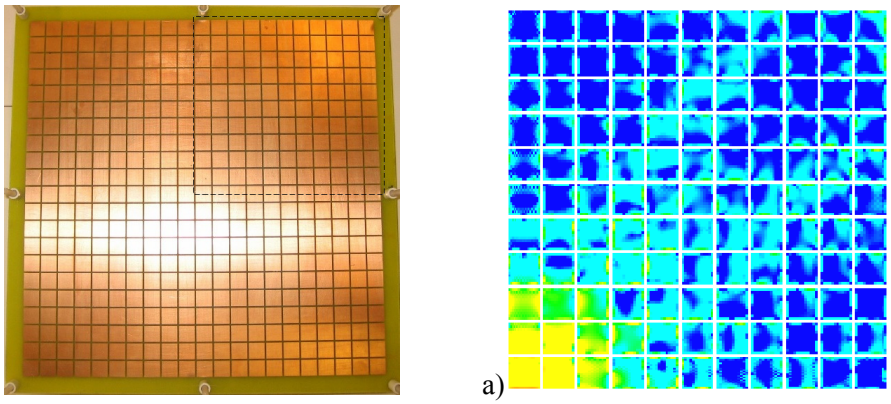

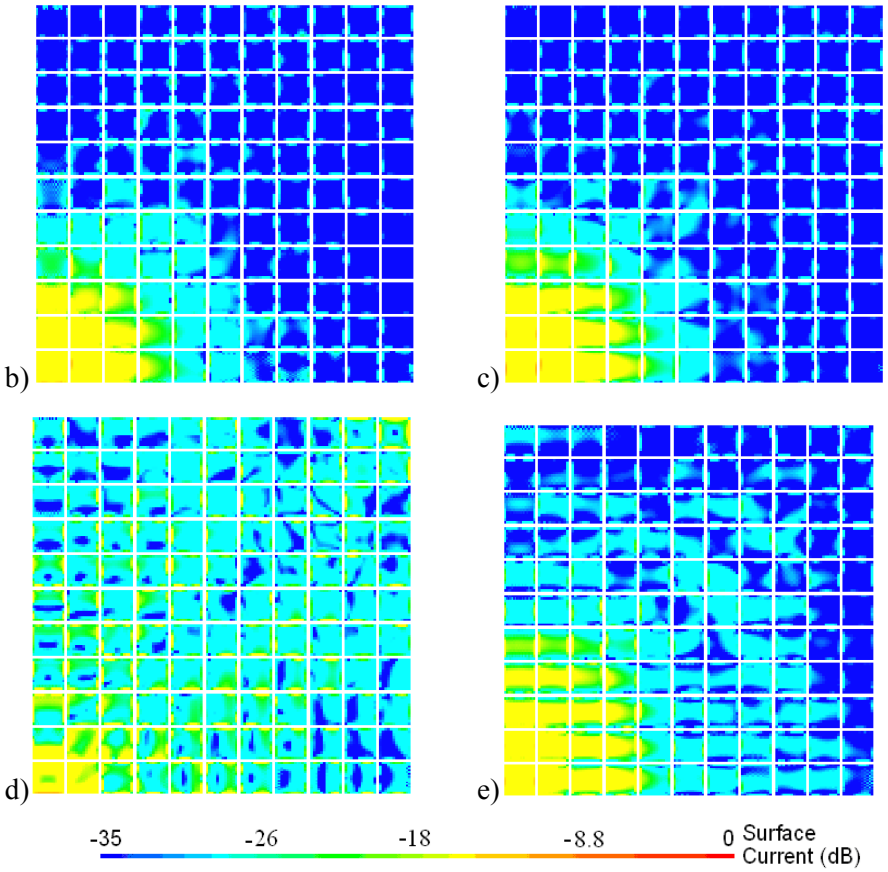

Fig. 5-28 Total surface current density (magnitude) on the half 1st layer square patch PRS at a) 13.5, b)13.8, c) 14.1, d) 13.1 and e) 14.4 GHz.

The near field distribution (magnitude of electric field vector) is shown in Fig. 5-29 for a surface of 28×28 cm^2 at a distance of 1 mm over the front end of the antenna. The field is shown at the centre frequency (13.8 GHz) as well as at the edges of the operating 3dB frequency band (13.5 and 14.1GHz). One frequency outside the band (13.1GHz) is also shown for comparison. The size of the square patch array of the second layer (23.1×23.1 cm^2) is depicted with a dashed line.

At the centre frequency the fields over the PRS are concentrated over the central area of the array; they are high and have a quite uniform distribution. The radiating aperture is slightly larger on the E-plane which will result in a less directive beam at this plane. The diffracted fields can be seen on either side of the PRS and are quite low. At 13.5 GHz the field over the PRS is less uniform; the diffracted fields are higher in the H- and E-plane, which explains the increased level of the side lobes at these planes in the radiation patterns at this frequency. At the upper frequency band the fields are more uniform; the radiating aperture is large and has a square shape distribution which will

result in wider beams in the radiation pattern at the H- and E-plane at this frequency. At low frequencies (13.1GHz) the fields are very high and non uniform in the entire PRS array due to the non-uniform surface currents on PRS_2, this will eventually distort the beam.

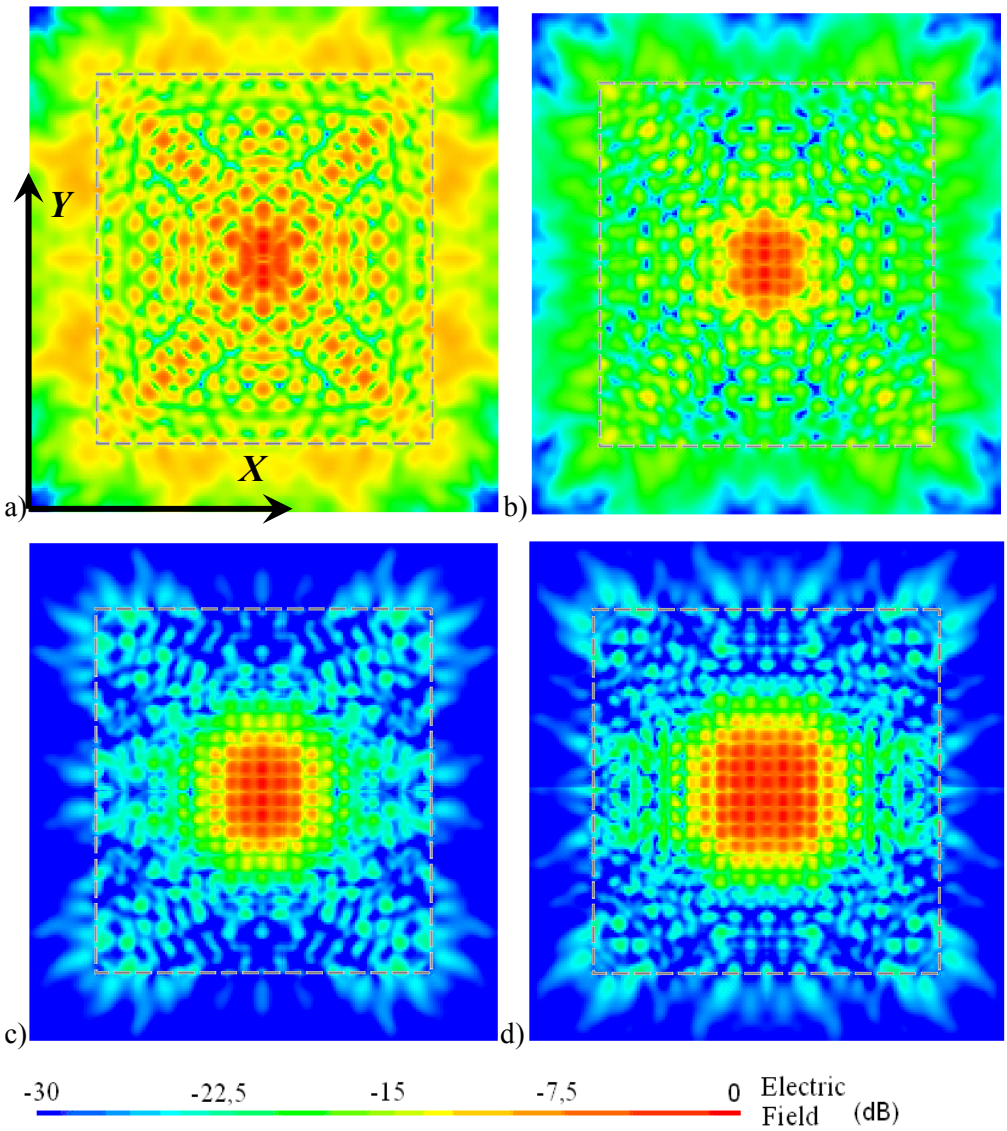

Fig. 5-29 Near Field distribution (magnitude of total electric field) 1 mm above the antenna at a) 13.1, b) 13.5, c) 13.8 and d) 14.1.

5.4.2 Manufacturing process

The optimised double-layer patch array has been manufactured. The patches of each layer were etched on 1.6 mm thick FR-4 substrates of dielectric constant 4.2 at 14GHz and loss tangent 0.025. The arrays have the same periodicity (D = 11 mm) and the patch

dimensions are L_{PRS1} = 10 mm and L_{PRS2} = 5 mm (refer to Fig. 5-17). The two layers were separated by an air cavity and attached to each other by the use of four plastic screws placed in the four corners of the dielectric boards and four at the central part of each side. Plastic spacers were also used to keep the boards parallel and at the specified distances above each other (dimension S= 10.1mm), as shown in Fig. 5-30a.

The antenna has been formed using the optimised double-layer patch PRS attached to a ground plane by the use of the same plastic screws and plastic spacers placed in the four corners of the metallic ground plane board 28 x 28 cm^2 and at the central point of each side, Fig. 5-30a. A central dipole manufactured by bending the inner connector of a semi-rigid coaxial cable was used to form the feeding source, Fig. 5-30b. The limitations in the accuracy of the measurements are mainly related to the misplacement of the PRSs and the flatness of the FR-4 boards.

From Fig.5-29, one can see that it is very important that the distances (S and more importantly h_r) are accomplished in the central part of the antenna as most of the radiation is in that area. For this reason, in the measurements the resonant distance, h_r, was altered to 10.2 mm due to the boards being slightly bowed at the centre.

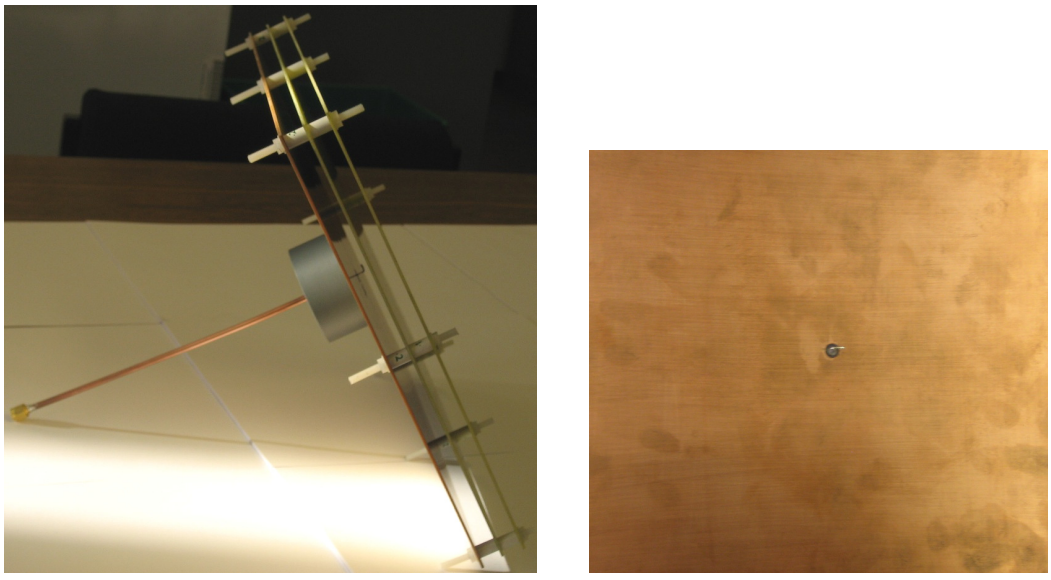

Fig. 5-30 a) Photograph of the antenna prototype and b) coaxially fed dipole source.

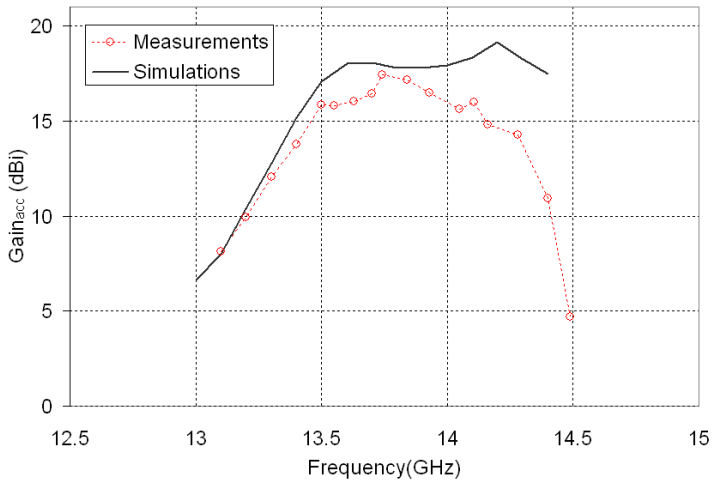

a)

b)

Fig. 5-31 a) Measure and simulated accepted gain vs frequency and b) set-up for the measurement of the S11 parameter and received power.

The accepted gain and the radiation patterns of the antenna were measured in an anechoic chamber, the set-up used for the measurements is shown in Fig. 5-31a. A directional bridge (HP 85027D in the band of 10MHz- 50GHz) was placed between the signal generator (HP 836502) and the antenna to observe the return loss (S11 parameter). A doppelsteg horn antenna (HF 906) was used as a receiver. In order to visualise the received power by the horn antenna a scalar network analyser (HP 8757D) was used. The dynamic range was -35dB. The accepted gain [11] of the transmitting antenna can be calculated by applying Friss equation,

$$G_{acc} = 20 \cdot \log\left(\frac{4\pi d}{\lambda_o}\right) + P_R - P_T - G_R \qquad (5.4\text{-}1)$$

where P_T represents the accepted power which was calculated by (5.4-2), G_R is the gain of the receiver antenna and P_R was the measured received power.

$$P_{acc} = \left(1 - |S11|^2\right) \cdot P_{in} \qquad (5.4\text{-}2)$$

Fig. 5-31a shows the values of the measured accepted gain vs. frequency together with the simulation results. The measurement setup is presented in Fig. 5-31b. As can be observed, a high accepted gain is obtained between 13.4 GHz and 14.1 GHz. The 3dB bandwidth is of approximately 6%. The accepted gain of the single layer PRS_1 antenna is also depicted in Fig. 5-32 for comparison. The small shift in frequency was due to the tolerance of the spacers and the flatness of the boards.

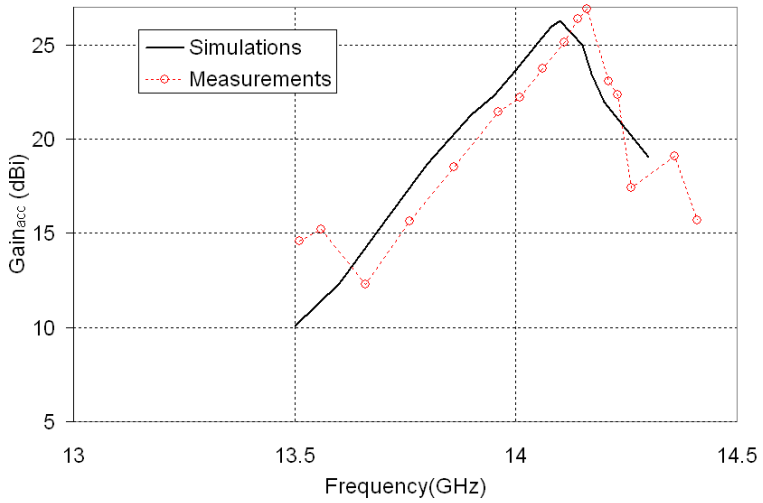

Fig. 5-32 Measure accepted gain vs frequency for the single layer PRS_1 antenna at h_r=10.2 mm over the ground plane.

The H- and E- plane radiation patterns were measured for the antenna at the centre and edges of the frequency band and are shown in Fig. 5-33 and 5-34 respectively. Satisfactory agreement between simulation results and measurements is observed. The side-lobe level (SLL) remains lower than -20 dB in the H-plane and E-plane within the frequency band. The main lobe in the H- and E- plane is distorted in the upper frequency band. The wider main lobe at 14.1 GHz is an indication of the lower gain obtained in the measurement for frequencies at the upper end of the operating band and it has also been predicted in the near-field analysis. At the centre frequency as well as the lower frequency band the beam is slightly wider due to the larger radiating aperture at this plane (as observed in the near field, refer to Fig. 5-29). Cross polarisation level has been measured and is below -28 dB throughout the frequency range studied.

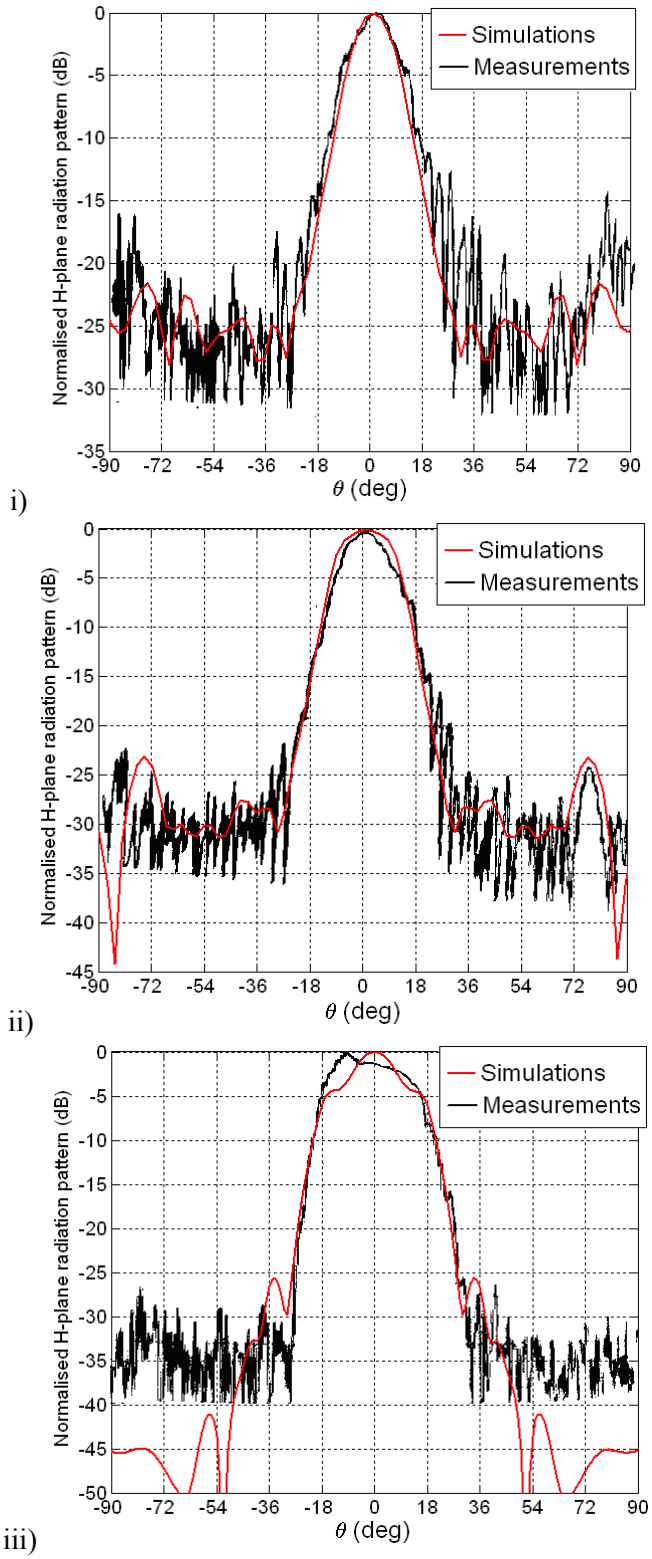

Fig. 5-33 Measured H- radiation pattern at i) 13.5 GHz, ii) 13.9 GHz and iii) 14.1 GHz.

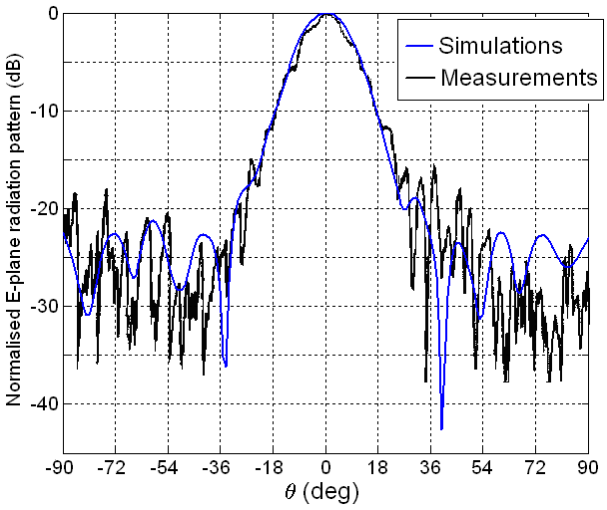

i)

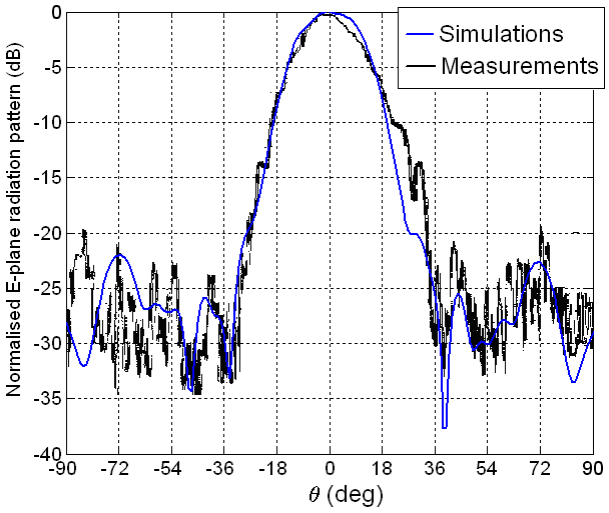

ii)

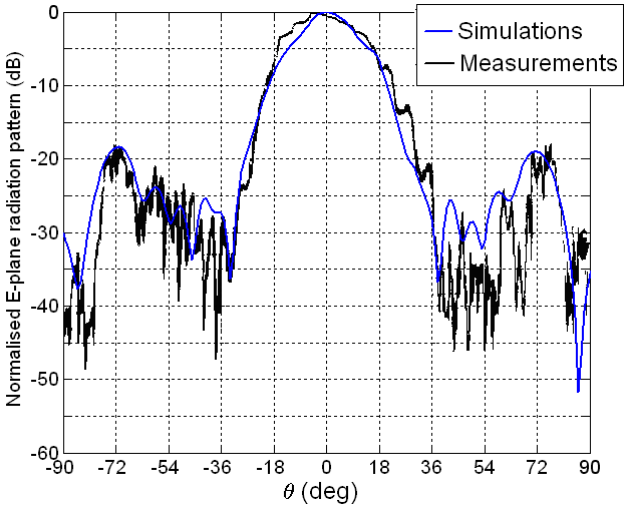

iii)

Fig. 5-34 Measured E- radiation pattern at i) 13.5 GHz, ii) 13.9 GHz and iii) 14.1 GHz.

5.5 Summary

A novel technique for the analysis of double layer arrays in a leaky-wave antenna configuration has been proposed. The antenna is composed of a double layer either dipole or patch PRS over a ground plane. The distance between the arrays as well as the distance from the lower array to the ground plane is of the order of half a wavelength. For specific designs (double layer arrays with different element dimensions in each layer and separation distance of about half wavelength) the phase of the PRS reflection coefficient (under plane-wave illumination) increases with frequency in a certain frequency range. The characteristic phase response resulted in a significant bandwidth enhancement of the leaky-wave antenna. The performance of these double layer PRS antennas has been investigated for different PRS designs.

A double layer dipole PRS leaky wave antenna has been carefully examined in section II. The excited near-fields inside the two cavities formed have been derived. The study reveals that two modes, odd and even, are excited at different frequencies. A parametric study related to the size of the elements employed to form the PRSs, the distance between both PRS arrays as well as the distance between the double layer PRS and the ground plane has been carried out revealing that a higher excitation of the even mode is needed for a better bandwidth performance of the antenna. Design guidelines aiming to increase the bandwidth performance of the antenna have been exposed.

A double layer square patch PRS leaky wave antenna has been designed following the design guidelines in section III. A double layer patch PRS antenna has been studied and simulated in its entirety using the 3D electromagnetic simulator CST Microstripes™ 2009. The directivity bandwidth obtained from the proposed technique for the infinite antenna was in excellent agreement with the finite result when the antenna was excited using an ideal dipole model. Simulations with a realistic feed source (semi-rigid coaxial) revealed that the TEM mode is excited at lower frequencies giving rise to a reduced directivity at low frequencies and therefore a reduced bandwidth. Furthermore, the antenna has been used to form a leaky-wave antenna prototype. A maximum antenna accepted gain of 17.7dBi has been obtained with a broad bandwidth of more than 6%. Simulation results were in satisfactory agreement with measurements and, furthermore, provided a valuable insight into the surface currents and near fields of the antenna.

References

[1] G.V. Trentini, "Partially reflecting sheet array", *IRE Trans. Antennas Propag.*, vol. AP-4, pp. 666-671, 1956.

[2] J. R James, S. J. A Kinany, P.D Peel, and G. Andrasic, "Leaky-wave multiple dichroic beamformers," *Electron. Lett.,* 1989, **25**, pp. 1209-121.

[3] A. P. Feresidis and J. C. Vardaxoglou, "High gain planar antenna using optimised partially reflective surfaces", *IEE Proc. Microw., Antennas and Propag.*, Dec. 2001, vol. 148, (6), pp. 345-350

[4] T. Zhao, D.R. Jackson, J. T. Williams, H. Y. D. Yang, A. A. Oliner, "2-D periodic leaky-wave antennas – Part I:Metal patch design," *IEEE Trans. Antennas Propag.*, vol. 53, no 11, pp. 3505-3514, Nov. 2005

[5] T. Zhao, D.R. Jackson, J. T. Williams, "2-D periodic leaky-wave antennas – Part II: Slot design," *IEEE Trans. Antennas Propag.*, vol. 53, no 11, pp. 3515-3524, Nov. 2005.

[6] A. P. Feresidis, J. C. Vardaxoglou, "A broadband high-gain resonant cavity antenna with single feed", *in Proc. EuCAP 2006*, Nice, France, 2006.

[7] R. Mittra, C.H. Chan, T. Cwik, "Techniques for analyzing frequency selective surfaces-a review," *Proceedings of the IEEE*, Vol. 76, pp.593-615, Dec. 1988.

[8] W. Koechner, Solid state laser engineering", 2nd edition, Springer Verlag, 1988

[9] J.C. Vardaxoglou, Frequency Selective Surfaces Analysis and Design, John Wiley, 1997

[10] D. M. Pozar, Microwave Engineering, 2nd edition, New York: John Wiley & Sons Inc, 1998.

[11] R. Gardelli, M. Albani, and F. Capolino, "Array thinning by using antennas in a Fabry-Perot cavity for gain enhancement", *IEEE Trans. Antennas and Propag.*, vol. 54, no 7, July 2006.

Chapter 6

Conclusions & Future Work

"Man often becomes what he believes himself to be. If I keep on saying to myself that I cannot do a certain thing, it is possible that I may end by really becoming incapable of doing it. On the contrary, if I have the belief that I can do it, I shall surely acquire the capacity to do it even if I may not have it at the beginning."

Mahatma Gandhi

Electromagnetic numerical methods for modelling periodic structures and in particular Frequency Selective Surfaces have been known for many years, as already pointed out in Chap. 1-2. These methods focus on the far-field characterisation of this kind of structures under plane wave excitation. A completely different behaviour of the excited electromagnetic fields dominate at a close distance from the radiating surfaces; therefore, an analysis based on the study of the near fields excited in the vicinity of periodic surfaces is vital for a complete understanding of periodic surfaces. The main scope of this Ph.D. dissertation has been providing a collection of theoretical and numerical results on the different potential applications of these structures in the area of sensoring and antenna systems based on the study of the excited near-fields.

Our analysis has dealt with multiple scenarios, i.e., single periodic planar periodic arrays with unperturbed and perturbed elements in a free-standing configuration or printed over dielectric substrates, double periodic planar periodic arrays printed over grounded dielectric substrates forming highly-directive leaky-wave antennas. The methodology used to analyze the different configurations presented in this Ph.D. dissertation has been briefly introduced in Chap. 2. In particular for all the structures considered, the far and near-fields excited in the proximity of the structures have been derived by means of home made numerical tools based on MoM and then used to design various systems. The reason for using our own tool was primarily due to the necessity of reducing drastically the simulation time needed by commercial tools to analyze such kind of structure.

We have analyzed these electromagnetic problems both from a theoretical perspective, discussing the physical reasons for the behaviour of the structures in the diverse scenarios and a numerical perspective. Initially we showed that a near-field characterisation entails a thorough and rigorous convergence analysis of the calculation of the near-fields. Once the strength and phase relationship between electric and magnetic near-field was known, the power stored and consequently the quality factor of FSSs was presented.

During these years three main topologies have been carefully analysed which I would like to briefly outline in the following.

In Chap. 3 a Frequency Selective Surface consisting of a perturbed periodic planar array of metal dipoles was carefully studied. The far-field characterisation showed a multiband response as a result of the dissimilar size elements used within the unit cell. On the other hand, the near-field study revealed enhanced near-fields. The very strong currents excited on the array elements and thus the very strong near fields excited in the vicinity of the array makes this configuration a good candidate as a biosensing device. Future work will be to accommodate the design to a finite real lab-in structure where characterization of biomolecular specimens is possible.
In Chap. 4 design guidelines of planar Leaky-Wave antennas made by covering an array of patches with a high impedance surface ground plane were shown. This is the first time that this method, which was previously presented by Zhao and Jackson in 2005

Ref. [8] Chap. 4, is used for the calculation of the near-fields in a configuration involving two periodic surfaces in close proximity (<<λ/2) where higher order excited modes from both surfaces increasingly interact. The novelty also comes from using the method in combination with array theory for the estimation of the complex dispersion of sub-wavelength LWA and thus allowing the estimation of the antenna's radiating characteristics. The results achieved can be useful in 2-D periodic leaky-wave antenna design. Future development of this work could analyze the possibility of tunable LW antennas by means of using liquid crystals substrates.

In Chap. 5 a leaky-wave antenna made by using two 2-D periodic arrays with dissimilar elements at ~λ/2 distance apart over a ground plane was considered. The antenna was analysed and designed for a highly-directive broadband response. A prototype has been built and tested to verify the performance of the antenna. In particular the prototype, together with the measurements, proves the feasibility and applicability of the proposed antennas. A future development of this work could analyze the possibility of reducing the profile of the antennas or to incorporate other array layers in order to further increase the bandwidth. In this case, a modelling of the structure by using a Generalised Scattering Matrix approach will result in a more efficient analysis which is currently being undertaken.

The results of this dissertation have been presented at several international conferences such as Days of Diffraction (2007), IEEE Antennas and Propagation Symposium (APS-08-10), European Conference on Antennas and Propagation (EUCAP-10), Metamaterials Congress (Meta-08-10). Part of this work has already been published in IEEE Transaction on Antennas and Propagation.

To conclude, we indeed forecast a widespread uptake in the near-field characterisation of periodic surfaces and of their continuous novel applications.

Appendix A

"Concentrate all your thoughts upon the work at hand.
The sun's rays do not burn until brought to a focus."

Alexander Graham Bell

A.1 Spherical coordinate system

Spherical coordinates are a system of curvilinear coordinates that are natural for describing positions on a sphere. Any point of space is described in spherical coordinates by three values (θ, φ, r) , where φ is the azimuthal angle in the *xy* –plane defined from the *x* -axis with $0 \leq \varphi \leq 2\pi$, θ is the polar angle defined from the *z* -axis with $0 \leq \theta \leq \pi$, and *r* is the distance (radius) from the point to the origin. Figure A.1 shows the commonly used spherical coordinate system.

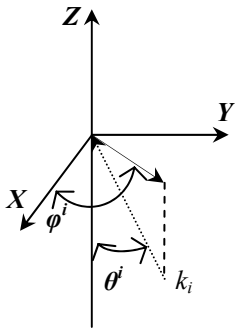

Figure A.1 Spherical coordinate system.

A.2 Derivation of the reflected and transmitted field amplitude at different interfaces

The process of deriving the Electric Field Integral Equation of the problem state in chapter 2 starts with the derivation of the reflected and transmitted field amplitude relationships at each interface of the problem. The procedure begins by matching the fields at different interfaces according to boundary conditions and applying the Floquet modes' orthogonality. Starting from the last interface of Fig 2-7 in chapter 2,

Interface 6(dielectric-air)- $z=z_5$

When $z=z_5$ and a ground plane is considered. The tangential electric and magnetic fields in region 5 must be equal to the fields in region 6 (refer to section 2.4.2). Due to the presence of the ground plane the fields in region 6 ($\boldsymbol{E}^+$) are 0. Therefore,

$$\begin{aligned} &\vec{E}^5(\vec{r}, z_5) = \vec{E}^+(\vec{r}, z_5) = 0 \\ &\sum_{mpq}\left(T^5_{mpq}e^{-j\beta^5_{pq}z_5} + R^5_{mpq}e^{j\beta^5_{pq}z_5}\right)\psi_{pq}(\vec{r})\bar{\kappa}_{mpq} = 0 \end{aligned} \tag{A.2-1}$$

It is possible to simplify this expression by multiplying both sides with $\psi^*_{lm}\bar{\kappa}_{mpq}$ and integrating over the unit cell in order to be able to use the orthogonality of the Floquet phasors. This yields Eq. (A.2-2)

$$\sum_{mpq}\left(T^5_{mpq}e^{-j\beta^5_{pq}z_5} + R^5_{mpq}e^{j\beta^5_{pq}z_5}\right)\iint_A \psi^*_{lm}(\vec{r})\psi_{pq}(\vec{r})ds\bar{\kappa}_{mpq}\bar{\kappa}_{mpq} = 0$$

$$\sum_{mpq}\left(T_{mpq}^{5}e^{-j\beta_{pq}^{5}z_5}+R_{mpq}^{5}e^{j\beta_{pq}^{5}z_5}\right)A\delta_{pl}\delta_{qm}=0$$

$$T_{mpq}^{5}e^{-j\beta_{pq}^{5}z_5}+R_{mpq}^{5}e^{j\beta_{pq}^{5}z_5}=0 \tag{A.2-2}$$

Working with (A.2-2) the relationship between the reflected and transmitted field amplitudes in region 5 is obtained,

$$R_{mpq}^{5}=-e^{-2j\beta_{pq}^{5}z_5}T_{mpq}^{5} \tag{A.2-3}$$

The exponential term refers to the reflection coefficient of this region at $z=z_5$,

$$\rho_{mpq}^{5}=-e^{-2j\beta_{pq}^{5}z_5} \tag{A.2-4}$$

The same procedure can be follow for the rest of the interfaces

Interface 5(dielectric4-dielectric5)- $z=z_4$

When $z=z_4$ the tangential electric and magnetic fields in region 4 must be equal to the fields in region 5.

$$\begin{aligned}&\vec{E}^{4}(\vec{r},z_4)=\vec{E}^{5}(\vec{r},z_4)\\&\sum_{mpq}\left(T_{mpq}^{4}e^{-j\beta_{pq}^{4}z_4}+R_{mpq}^{4}e^{j\beta_{pq}^{4}z_4}\right)\psi_{pq}(\vec{r})\bar{\kappa}_{mpq}\\&=\sum_{mpq}\left(T_{mpq}^{5}e^{-j\beta_{pq}^{5}z_4}+R_{mpq}^{5}e^{j\beta_{pq}^{5}z_4}\right)\psi_{pq}(\vec{r})\bar{\kappa}_{mpq}\end{aligned} \tag{A.2-5}$$

By applying the orthogonality of the Floquet phasors,

$$T_{mpq}^{4}e^{-j\beta_{pq}^{4}z_4}+R_{mpq}^{4}e^{j\beta_{pq}^{4}z_4}=T_{mpq}^{5}e^{-j\beta_{pq}^{5}z_4}+R_{mpq}^{5}e^{j\beta_{pq}^{5}z_4} \tag{A.2-6}$$

Likewise, after imposing the boundary condition for the tangential magnetic field (A.2-7) and applying the orthogonaly of the Floquet phasors (A.2-8) is obtained,

$$\vec{H}^{4}(\vec{r},z_4)=\vec{H}^{5}(\vec{r},z_4) \tag{A.2-7}$$

$$\sum_{mpq}\eta^4_{mpq}\left(T^4_{mpq}e^{-j\beta^4_{pq}z_4}-R^4_{mpq}e^{j\beta^4_{pq}z_4}\right)\psi_{pq}(\vec{r})\vec{z}\times\vec{\kappa}_{mpq}$$
$$=\sum_{mpq}\eta^5_{mpq}\left(T^5_{mpq}e^{-j\beta^5_{pq}z_4}-R^5_{mpq}e^{j\beta^5_{pq}z_4}\right)\psi_{pq}(\vec{r})\vec{z}\times\vec{\kappa}_{mpq}$$
$$\eta^4_{mpq}\left(T^4_{mpq}e^{-j\beta^4_{pq}z_4}-R^4_{mpq}e^{j\beta^4_{pq}z_4}\right)=\eta^5_{mpq}\left(T^5_{mpq}e^{-j\beta^5_{pq}z_4}-R^5_{mpq}e^{j\beta^5_{pq}z_4}\right) \quad \text{(A.2-8)}$$

The ratio of (A.2-8) and (A.2-6) yields (A.2-9)

$$\frac{\eta^4_{mpq}\left(T^4_{mpq}e^{-j\beta^4_{pq}z_4}-R^4_{mpq}e^{j\beta^4_{pq}z_4}\right)}{T^4_{mpq}e^{-j\beta^4_{pq}z_4}+R^4_{mpq}e^{j\beta^4_{pq}z_4}}=\frac{\eta^5_{mpq}\left(T^5_{mpq}e^{-j\beta^5_{pq}z_4}-R^5_{mpq}e^{j\beta^5_{pq}z_4}\right)}{T^5_{mpq}e^{-j\beta^5_{pq}z_4}+R^5_{mpq}e^{j\beta^5_{pq}z_4}} \quad \text{(A.2-9)}$$

The definition of the reflection coefficient in region 5, which relates T^5_{mpq} and R^5_{mpq}, allow us to define the coefficient ζ^5_{mpq},

$$\zeta^5_{mpq}=\frac{e^{-j\beta^5_{pq}z_4}-\rho^5_{mpq}e^{j\beta^5_{pq}z_4}}{e^{-j\beta^5_{pq}z_4}+\rho^5_{mpq}e^{j\beta^5_{pq}z_4}} \quad \text{(A.2-10)}$$

Using (A.2-10) in (A.2-9) yields the relationship between the reflected and transmitted field amplitudes in region 4,

$$\eta^4_{mpq}\left(T^4_{mpq}e^{-j\beta^4_{pq}z_4}-R^4_{mpq}e^{j\beta^4_{pq}z_4}\right)=\eta^5_{mpq}\zeta^5_{mpq}\left(T^4_{mpq}e^{-j\beta^4_{pq}z_4}+R^4_{mpq}e^{j\beta^4_{pq}z_4}\right)$$
$$\left(\eta^4_{mpq}-\eta^5_{mpq}\zeta^5_{mpq}\right)T^4_{mpq}e^{-j\beta^4_{pq}z_4}=\left(\eta^4_{mpq}+\eta^5_{mpq}\zeta^5_{mpq}\right)R^4_{mpq}e^{j\beta^4_{pq}z_4} \quad \text{(A.2-11)}$$
$$R^4_{mpq}=\frac{\left(\eta^4_{mpq}-\eta^5_{mpq}\zeta^5_{mpq}\right)}{\left(\eta^4_{mpq}+\eta^5_{mpq}\zeta^5_{mpq}\right)}e^{-2j\beta^4_{pq}z_4}T^4_{mpq}$$

Likewise, the reflection coefficient of region 4 is,

$$\rho^4_{mpq}=\frac{\left(\eta^4_{mpq}-\eta^5_{mpq}\zeta^5_{mpq}\right)}{\left(\eta^4_{mpq}+\eta^5_{mpq}\zeta^5_{mpq}\right)}e^{-2j\beta^4_{pq}z_4} \quad \text{(A.2-12)}$$

Interface 4(dielectric3-FSS$_2$-dielectric4)- z=z$_3$

Special care needs to be taken at this interface due to the presence of the Frequency Selective Surface (FSS_2) which will affect the boundary condition of the magnetic field (refer to chapter 2 – section 2.2.2). On the other hand, when $z=z_3$ the tangential electric fields in region 3 must be equal to the fields in region 4.

$$\begin{aligned}&\vec{E}^3(\vec{r},z_3)=\vec{E}^4(\vec{r},z_3)\\&\sum_{mpq}\left(T^3_{mpq}e^{-j\beta^3_{pq}z_3}+R^3_{mpq}e^{j\beta^3_{pq}z_3}\right)\psi_{pq}(\vec{r})\bar{\kappa}_{mpq}\\&=\sum_{mpq}\left(T^4_{mpq}e^{-j\beta^4_{pq}z_3}+R^4_{mpq}e^{j\beta^4_{pq}z_3}\right)\psi_{pq}(\vec{r})\bar{\kappa}_{mpq}\end{aligned}\tag{A.2-13}$$

$$T^3_{mpq}e^{-j\beta^3_{pq}z_3}+R^3_{mpq}e^{j\beta^3_{pq}z_3}=T^4_{mpq}e^{-j\beta^4_{pq}z_3}+R^4_{mpq}e^{j\beta^4_{pq}z_3}\tag{A.2-14}$$

The elements that form the FSSs are considered electric sources of perfect electric conductors. Thus, the boundary conditions of the magnetic field must be modified to include the induced linear electric current density $\boldsymbol{J_{s2}}$. The expression for the tangential magnetic field is obtained in (A.2-15),

$$\begin{aligned}&\vec{H}^3(\vec{r},z_3)=\vec{H}^4(\vec{r},z_3)+\hat{z}\times\bar{J}_2(\bar{r},z_3)\\&\sum_{mpq}\eta^3_{mpq}\left(T^3_{mpq}e^{-j\beta^3_{pq}z_3}-R^3_{mpq}e^{j\beta^3_{pq}z_3}\right)\psi_{pq}(\vec{r})\vec{z}\times\bar{\kappa}_{mpq}\\&=\sum_{mpq}\eta^4_{mpq}\left(T^4_{mpq}e^{-j\beta^4_{pq}z_3}-R^4_{mpq}e^{j\beta^4_{pq}z_3}\right)\psi_{pq}(\vec{r})\vec{z}\times\bar{\kappa}_{mpq}+\hat{z}\times\bar{J}_2(\bar{r},z_3)\end{aligned}\tag{A.2-15}$$

LHS and RHS of (A.2-15) are multiply by $\psi^*_{lm}\bar{\kappa}_{mpq}$ and integrated over the unit cell so that the orthogonality of the Floquet phasors can be applied. This yields (A.2-16),

$$\begin{aligned}&\sum_{mpq}\eta^3_{mpq}\left(T^3_{mpq}e^{-j\beta^3_{pq}z_3}-R^3_{mpq}e^{j\beta^3_{pq}z_3}\right)\iint_{A_2}\psi_{pq}(\vec{r})\cdot\psi^*_{lm}(\vec{r})\cdot dS=\\&\sum_{mpq}\eta^4_{mpq}\left(T^4_{mpq}e^{-j\beta^4_{pq}z_3}-R^4_{mpq}e^{j\beta^4_{pq}z_3}\right)\iint_{A_2}\psi_{pq}(\vec{r})\cdot\psi^*_{lm}(\vec{r})\cdot dS\\&+\iint_{A_2}\hat{z}\times J_2(\vec{r},z_3)\cdot\psi^*_{lm}(\vec{r})\cdot\bar{\kappa}_{mpq}\cdot dS\end{aligned}\tag{A.2-16}$$

The current term on the LHS of (A.2-16) represents the Floquet transformation of the electric current excited in the elements. This is presented in (A.2-17) where the tilde signifies the Floquet spectrum of the current distribution.

$$\begin{aligned} \widetilde{J}^2_{pq} &= \iint_{A_2} \vec{J}(\vec{r}, z_3)\psi^*_{pq}(\vec{r}) \cdot ds = \left\langle \vec{J}(\vec{r}, z_3), \psi_{pq}(\vec{r}) \right\rangle_{A2} \\ \widetilde{J}^2_{mpq} &= \widetilde{J}^2_{pq} \cdot \overline{\kappa}_{mpq} \end{aligned} \tag{A.2-17}$$

Therefore, by using (A.2-17) expression (A.2-16) becomes,

$$\eta^3_{mpq}\left(T^3_{mpq}e^{-j\beta^3_{pq}z_3} - R^3_{mpq}e^{j\beta^3_{pq}z_3}\right) = \eta^4_{mpq}\left(T^4_{mpq}e^{-j\beta^4_{pq}z_3} - R^4_{mpq}e^{j\beta^4_{pq}z_3}\right) + \frac{\widetilde{J}^2_{mpq}}{A_2} \tag{A.2-18}$$

were A_2 is the area of the unit cell of the second FSS and $\widetilde{J}^2_{mpq}$ is the excited current on the elements of this array for each Floquet harmonic. The ratio of (A.2-18) and (A.2-14) is,

$$\frac{\eta^3_{mpq}\left(T^3_{mpq}e^{-j\beta^3_{pq}z_3} - R^3_{mpq}e^{j\beta^3_{pq}z_3}\right) - \dfrac{\widetilde{J}^2_{mpq}}{A_2}}{T^3_{mpq}e^{-j\beta^3_{pq}z_3} + R^3_{mpq}e^{j\beta^3_{pq}z_3}} = \frac{\eta^4_{mpq}\left(T^4_{mpq}e^{-j\beta^4_{pq}z_3} - R^4_{mpq}e^{j\beta^4_{pq}z_3}\right)}{T^4_{mpq}e^{-j\beta^4_{pq}z_3} + R^4_{mpq}e^{j\beta^4_{pq}z_3}} \tag{A.2-19}$$

The definition of the reflection coefficient in region 4 allow us to define the coefficient ζ^4_{mpq} in region 3,

$$\zeta^4_{mpq} = \frac{e^{-j\beta^4_{pq}z_3} - \rho^4_{mpq}e^{j\beta^4_{pq}z_3}}{e^{-j\beta^4_{pq}z_3} + \rho^4_{mpq}e^{j\beta^4_{pq}z_3}} \tag{A.2-20}$$

Using (A.2-20) in (A.2-19) gives the relationship between the reflected and transmitted field amplitudes in region 3 as well as the coefficient K^3_{mpq} of the currents (A.2-22),

$$\eta_{mpq}^3\left(T_{mpq}^3 e^{-j\beta_{pq}^3 z_3} - R_{mpq}^3 e^{j\beta_{pq}^3 z_3}\right) - \frac{\tilde{J}_{mpq}^2}{A_2} = \eta_{mpq}^4 \zeta_{mpq}^4 \left(T_{mpq}^3 e^{-j\beta_{pq}^3 z_3} + R_{mpq}^3 e^{j\beta_{pq}^3 z_3}\right)$$

$$\left(\eta_{mpq}^3 - \eta_{mpq}^4 \zeta_{mpq}^4\right) T_{mpq}^3 e^{-j\beta_{pq}^3 z_3} - \frac{\tilde{J}_{mpq}^2}{A_2} = \left(\eta_{mpq}^3 + \eta_{mpq}^4 \zeta_{mpq}^4\right) R_{mpq}^3 e^{j\beta_{pq}^3 z_3} \tag{A.2-21}$$

$$R_{mpq}^3 = \frac{\left(\eta_{mpq}^3 - \eta_{mpq}^4 \zeta_{mpq}^4\right)}{\left(\eta_{mpq}^3 + \eta_{mpq}^4 \zeta_{mpq}^4\right)} e^{-2j\beta_{pq}^3 z_3} T_{mpq}^3 - \frac{\tilde{J}_{mpq}^2}{A_2\left(\eta_{mpq}^3 + \eta_{mpq}^4 \zeta_{mpq}^4\right)} e^{-j\beta_{pq}^3 z_3}$$

$$\rho_{mpq}^3 = \frac{\left(\eta_{mpq}^3 - \eta_{mpq}^4 \zeta_{mpq}^4\right)}{\left(\eta_{mpq}^3 + \eta_{mpq}^4 \zeta_{mpq}^4\right)} e^{-2j\beta_{pq}^3 z_3}$$

$$K_{mpq}^3 = \frac{\tilde{J}_{mpq}^2}{A_2\left(\eta_{mpq}^3 + \eta_{mpq}^4 \zeta_{mpq}^4\right)} e^{-j\beta_{pq}^3 z_3} \tag{A.2-22}$$

Interface 3(dielectric2-dielectric3)- $z=z_2$

The tangential electric and magnetic fields in region 2 equal the tangential electric and magnetic fields of region 3 when $z=z_2$. Therefore, Eq. (A.2-25) and (A.2-26) are obtained after multiplying by $\psi_{lm}^* \bar{\kappa}_{mpq}$ and integrating over the unit cell so that the orthogonality of the Floquet phasors can be used to simplify expressions (A.2-23) and (A.2-24).

$$\vec{E}^2(\vec{r}, z_2) = \vec{E}^3(\vec{r}, z_2)$$

$$\sum_{mpq}\left(T_{mpq}^2 e^{-j\beta_{pq}^2 z_2} + R_{mpq}^2 e^{j\beta_{pq}^2 z_2}\right)\psi_{pq}(\vec{r})\bar{\kappa}_{mpq} \tag{A.2-23}$$

$$= \sum_{mpq}\left(T_{mpq}^3 e^{-j\beta_{pq}^3 z_2} + R_{mpq}^3 e^{j\beta_{pq}^3 z_2}\right)\psi_{pq}(\vec{r})\bar{\kappa}_{mpq}$$

$$\vec{H}^2(\vec{r}, z_2) = \vec{H}^3(\vec{r}, z_2)$$

$$\sum_{mpq}\eta_{mpq}^2\left(T_{mpq}^2 e^{-j\beta_{pq}^2 z_2} - R_{mpq}^2 e^{j\beta_{pq}^2 z_2}\right)\psi_{pq}(\vec{r})\vec{z}\times\bar{\kappa}_{mpq} = \tag{A.2-24}$$

$$\sum_{mpq}\eta_{mpq}^3\left(T_{mpq}^3 e^{-j\beta_{pq}^3 z_2} - R_{mpq}^3 e^{j\beta_{pq}^3 z_2}\right)\psi_{pq}(\vec{r})\vec{z}\times\bar{\kappa}_{mpq}$$

$$T_{mpq}^2 e^{-j\beta_{pq}^2 z_2} + R_{mpq}^2 e^{j\beta_{pq}^2 z_2} = T_{mpq}^3 e^{-j\beta_{pq}^3 z_2} + R_{mpq}^3 e^{j\beta_{pq}^3 z_2} \tag{A.2-25}$$

$$\eta_{mpq}^{2}\left(T_{mpq}^{2}e^{-j\beta_{pq}^{2}z_2}-R_{mpq}^{2}e^{j\beta_{pq}^{2}z_2}\right)=\eta_{mpq}^{3}\left(T_{mpq}^{3}e^{-j\beta_{pq}^{3}z_2}-R_{mpq}^{3}e^{j\beta_{pq}^{3}z_2}\right) \tag{A.2-26}$$

The ratio yields (A.2-27),

$$\frac{\eta_{mpq}^{2}\left(T_{mpq}^{2}e^{-j\beta_{pq}^{2}z_2}-R_{mpq}^{2}e^{j\beta_{pq}^{2}z_2}\right)}{T_{mpq}^{2}e^{-j\beta_{pq}^{2}z_2}+R_{mpq}^{2}e^{j\beta_{pq}^{2}z_2}}=\frac{\eta_{mpq}^{3}\left(T_{mpq}^{3}e^{-j\beta_{pq}^{3}z_2}-R_{mpq}^{3}e^{j\beta_{pq}^{3}z_2}\right)}{T_{mpq}^{3}e^{-j\beta_{pq}^{3}z_2}+R_{mpq}^{3}e^{j\beta_{pq}^{3}z_2}} \tag{A.2-27}$$

Similarly as at other interfaces the definition of the reflection coefficient in region 3 is used to define the coefficient $\zeta^{3}{}_{\mathrm{mpq}}$,

$$\zeta_{mpq}^{3}=\frac{e^{-j\beta_{pq}^{3}z_2}-\rho_{mpq}^{3}e^{j\beta_{pq}^{3}z_2}}{e^{-j\beta_{pq}^{3}z_2}+\rho_{mpq}^{3}e^{j\beta_{pq}^{3}z_2}} \tag{A.2-28}$$

which can be used to derived the relationship between the reflected and transmitted field amplitudes in region 2 as well as the coefficient $\mathrm{K}^{2}{}_{\mathrm{mpq}}$ (A.2-30),

$$\begin{aligned}
&\eta_{mpq}^{2}\left(T_{mpq}^{2}e^{-j\beta_{pq}^{2}z_2}-R_{mpq}^{2}e^{j\beta_{pq}^{2}z_2}\right)-\eta_{mpq}^{3}K_{mpq}^{3}e^{j\beta_{pq}^{3}z_2}\tilde{J}_{mpq}^{2}\\
&=\eta_{mpq}^{3}\zeta_{mpq}^{3}\left(T_{mpq}^{2}e^{-j\beta_{pq}^{2}z_2}+R_{mpq}^{2}e^{j\beta_{pq}^{2}z_2}+K_{mpq}^{3}e^{j\beta_{pq}^{3}z_2}\tilde{J}_{mpq}^{2}\right)\\
&\left(\eta_{mpq}^{2}-\eta_{mpq}^{3}\zeta_{mpq}^{3}\right)T_{mpq}^{2}e^{-j\beta_{pq}^{2}z_2}-\left(1+\zeta_{mpq}^{3}\right)\eta_{mpq}^{3}K_{mpq}^{3}e^{j\beta_{pq}^{3}z_2}\tilde{J}_{mpq}^{2}\\
&=\left(\eta_{mpq}^{2}+\eta_{mpq}^{3}\zeta_{mpq}^{3}\right)R_{mpq}^{2}e^{j\beta_{pq}^{2}z_2}
\end{aligned} \tag{A.2-29}$$

$$\begin{aligned}
R_{mpq}^{2}&=\frac{\left(\eta_{mpq}^{2}-\eta_{mpq}^{3}\zeta_{mpq}^{3}\right)}{\left(\eta_{mpq}^{2}+\eta_{mpq}^{3}\zeta_{mpq}^{3}\right)}e^{-2j\beta_{pq}^{2}z_2}T_{mpq}^{2}\\
&-\frac{\left(1+\zeta_{mpq}^{3}\right)}{\left(\eta_{mpq}^{2}+\eta_{mpq}^{3}\zeta_{mpq}^{3}\right)}\eta_{mpq}^{3}K_{mpq}^{3}e^{j\left(\beta_{pq}^{3}-\beta_{pq}^{2}\right)z_2}\tilde{J}_{mpq}^{2}
\end{aligned}$$

$$\begin{aligned}
\rho_{mpq}^{2}&=\frac{\left(\eta_{mpq}^{2}-\eta_{mpq}^{3}\zeta_{mpq}^{3}\right)}{\left(\eta_{mpq}^{2}+\eta_{mpq}^{3}\zeta_{mpq}^{3}\right)}e^{-2j\beta_{pq}^{2}z_2}\\
K_{mpq}^{2}&=\frac{\left(1+\zeta_{mpq}^{3}\right)}{\left(\eta_{mpq}^{2}+\eta_{mpq}^{3}\zeta_{mpq}^{3}\right)}\eta_{mpq}^{3}K_{mpq}^{3}e^{j\left(\beta_{pq}^{3}-\beta_{pq}^{2}\right)z_2}
\end{aligned} \tag{A.2-30}$$

Interface 2(dielectric1-FSS$_1$-dielectric2)- z=z$_1$

At this interface we find the first Frequency Selective Surface (FSS$_1$), therefore at z=z$_1$ the tangential electric field in region 1 must be equal to the fields in region 2; however, the magnetic field boundary condition must be modified to include the induced linear electric current density $\boldsymbol{J_{s1}}$. The expression for the tangential electric and magnetic field relations are obtained in (A.2-33) and (A.2-34) respectively,

$$\begin{aligned}&\vec{E}^1(\vec{r},z_1)=\vec{E}^2(\vec{r},z_1)\\&\sum_{mpq}\left(T^1_{mpq}e^{-j\beta^1_{pq}z_1}+R^1_{mpq}e^{j\beta^1_{pq}z_1}\right)\psi_{pq}(\vec{r})\bar{\kappa}_{mpq}\\&=\sum_{mpq}\left(T^2_{mpq}e^{-j\beta^2_{pq}z_1}+R^2_{mpq}e^{j\beta^2_{pq}z_1}\right)\psi_{pq}(\vec{r})\bar{\kappa}_{mpq}\end{aligned}\qquad\text{(A.2-31)}$$

$$\begin{aligned}&\vec{H}^1(\vec{r},z_1)=\vec{H}^2(\vec{r},z_1)+\hat{z}\times\bar{J}^1(\bar{r},z_1)\\&\sum_{mpq}\eta^1_{mpq}\left(T^1_{mpq}e^{-j\beta^1_{pq}z_1}-R^1_{mpq}e^{j\beta^1_{pq}z_1}\right)\psi_{pq}(\vec{r})\cdot\hat{z}\times\bar{\kappa}_{mpq}=\\&\sum_{mpq}\eta^2_{mpq}\left(T^2_{mpq}e^{-j\beta^2_{pq}z_1}-R^2_{mpq}e^{j\beta^2_{pq}z_1}\right)\psi_{pq}(\vec{r})\cdot\hat{z}\times\bar{\kappa}_{mpq}+\hat{z}\times\bar{J}^1(\vec{r},z_1)\end{aligned}\qquad\text{(A.2-32)}$$

Multiplying LHS and RHS of (A.2-31) and (A.2-32) by $\psi^*_{lm}\bar{\kappa}_{mpq}$ and integrating over the unit cell so the orthogonality of the Floquet phasors can be applied yields,

$$T^1_{mpq}e^{-j\beta^1_{pq}z_1}+R^1_{mpq}e^{j\beta^1_{pq}z_1}=T^2_{mpq}e^{-j\beta^2_{pq}z_1}+R^2_{mpq}e^{j\beta^2_{pq}z_1}\qquad\text{(A.2-33)}$$

$$\eta^1_{mpq}\left(T^1_{mpq}e^{-j\beta^1_{pq}z_1}-R^1_{mpq}e^{j\beta^1_{pq}z_1}\right)=\eta^2_{mpq}\left(T^2_{mpq}e^{-j\beta^2_{pq}z_1}-R^2_{mpq}e^{j\beta^2_{pq}z_1}\right)+\frac{\widetilde{J}_{mpq}}{A_1}\qquad\text{(A.2-34)}$$

where A$_1$ is the area of the unit cell of the first array and $\widetilde{J}^1_{mpq}$ is the excited current on the elements of the first array for each Floquet harmonic. The ratio of both equations produces (A.2-35),

$$\frac{\eta^1_{mpq}\left(T^1_{mpq}e^{-j\beta^1_{pq}z_1}-R^1_{mpq}e^{j\beta^1_{pq}z_1}\right)-\dfrac{\widetilde{J}^1_{mpq}}{A_1}}{T^1_{mpq}e^{-j\beta^1_{pq}z_1}+R^1_{mpq}e^{j\beta^1_{pq}z_1}}=\frac{\eta^2_{mpq}\left(T^2_{mpq}e^{-j\beta^2_{pq}z_1}-R^2_{mpq}e^{j\beta^2_{pq}z_1}\right)}{T^2_{mpq}e^{-j\beta^2_{pq}z_1}+R^2_{mpq}e^{j\beta^2_{pq}z_1}} \tag{A.2-35}$$

and the definition of the reflection coefficient in region 2 is used to define the coefficient ζ^2_{mpq} which is used to derived the relation between the reflected and transmitted field amplitudes in region 1 as well as the coefficient K^1_{mpq} of the currents of FSS_1 and K^{12}_{mpq} of FSS_2 (A.2-38),

$$\zeta^2_{mpq}=\frac{e^{-j\beta^2_{pq}z_1}-\rho^2_{mpq}e^{j\beta^2_{pq}z_1}}{e^{-j\beta^2_{pq}z_1}+\rho^2_{mpq}e^{j\beta^2_{pq}z_1}} \tag{A.2-36}$$

$$\begin{aligned}
&\eta^1_{mpq}\left(T^1_{mpq}e^{-j\beta^1_{pq}z_1}-R^1_{mpq}e^{j\beta^1_{pq}z_1}\right)-\frac{\widetilde{J}^1_{mpq}}{A_1}-\eta^2_{mpq}K^2_{mpq}e^{j\beta^2_{pq}z_1}\widetilde{J}^2_{mpq}\\
&=\eta^2_{mpq}\zeta^2_{mpq}\left(T^1_{mpq}e^{-j\beta^1_{pq}z_1}+R^1_{mpq}e^{j\beta^1_{pq}z_1}+K^2_{mpq}e^{j\beta^2_{pq}z_1}\widetilde{J}^2_{mpq}\right)\\
&\left(\eta^1_{mpq}-\eta^2_{mpq}\zeta^2_{mpq}\right)T^1_{mpq}e^{-j\beta^1_{pq}z_1}-\left(1+\zeta^2_{mpq}\right)\eta^2_{mpq}K^2_{mpq}e^{j\beta^2_{pq}z_1}\widetilde{J}^2_{mpq}-\frac{\widetilde{J}^1_{mpq}}{A}\\
&=\left(\eta^1_{mpq}+\eta^2_{mpq}\zeta^2_{mpq}\right)R^1_{mpq}e^{j\beta^1_{pq}z_1}
\end{aligned}$$

$$\begin{aligned}
R^1_{mpq}=&\frac{\left(\eta^1_{mpq}-\eta^2_{mpq}\zeta^2_{mpq}\right)}{\left(\eta^1_{mpq}+\eta^2_{mpq}\zeta^2_{mpq}\right)}e^{-2j\beta^1_{pq}z_1}T^1_{mpq}-\frac{\left(1+\zeta^2_{mpq}\right)\eta^2_{mpq}K^2_{mpq}e^{j\left(\beta^2_{pq}-\beta^1_{pq}\right)z_1}}{\left(\eta^1_{mpq}+\eta^2_{mpq}\zeta^2_{mpq}\right)}\widetilde{J}^2_{mpq}\\
&-\frac{\widetilde{J}^1_{mpq}}{A\left(\eta^1_{mpq}+\eta^2_{mpq}\zeta^2_{mpq}\right)}e^{-j\beta^1_{pq}z_1}
\end{aligned} \tag{A.2-37}$$

$$\begin{aligned}
\rho^1_{mpq}&=\frac{\left(\eta^1_{mpq}-\eta^2_{mpq}\zeta^2_{mpq}\right)}{\left(\eta^1_{mpq}+\eta^2_{mpq}\zeta^2_{mpq}\right)}e^{-2j\beta^1_{pq}z_1}\\
K^{12}_{mpq}&=\frac{\left(1+\zeta^2_{mpq}\right)\eta^2_{mpq}e^{j\left(\beta^2_{pq}-\beta^1_{pq}\right)z_1}}{\left(\eta^1_{mpq}+\eta^2_{mpq}\zeta^2_{mpq}\right)}K^2_{mpq}\\
K^1_{mpq}&=\frac{1}{\left(\eta^1_{mpq}+\eta^2_{mpq}\zeta^2_{mpq}\right)}e^{-j\beta^1_{pq}z_1}
\end{aligned} \tag{A.2-38}$$

Interface 1(dielectric1-air)- z=0

Finally at the last interface z=0 the tangential electric and magnetic field in the region 0 must be equal to the tangential electric and magnetic field in region 1. The fields in region 0 include the excited field $T^{inc}{}_{m00}$

$$\vec{E}^{-}(\vec{r},0)=\vec{E}^{1}(\vec{r},0)$$
$$\sum_{m=1}^{2}\left(T_{m00}^{inc}\psi_{00}(\vec{r})\bar{\kappa}_{m00}\right)+\sum_{mpq}R_{mpq}^{-}\psi_{pq}(\vec{r})\bar{\kappa}_{mpq}=\sum_{mpq}\left(T_{mpq}^{1}+R_{mpq}^{1}\right)\psi_{pq}(\vec{r})\bar{\kappa}_{mpq} \quad \text{(A.2-39)}$$

$$\vec{H}^{-}(\vec{r},0)=\vec{H}^{1}(\vec{r},0)$$
$$\sum_{m=1}^{2}\eta_{m00}^{0}\left(T_{m00}^{inc}\psi_{00}(\vec{r})\bar{\kappa}_{m00}\right)-\sum_{mpq}\eta_{mpq}^{0}R_{mpq}^{-}\psi_{pq}(\vec{r})\bar{\kappa}_{mpq} \quad \text{(A.2-40)}$$
$$=\sum_{mpq}\eta_{mpq}^{1}\left(T_{mpq}^{1}-R_{mpq}^{1}\right)\psi_{pq}(\vec{r})\bar{\kappa}_{mpq}$$

Similarly, (A.2-41) and (A.2-42) can be simplified by multiplying $\psi_{lm}^{*}\bar{\kappa}_{mpq}$ and integrating over the unit cell,

$$T_{m00}^{inc}\delta_{p0}\delta_{q0}+R_{mpq}^{-}=T_{mpq}^{1}+R_{mpq}^{1} \quad \text{(A.2-41)}$$

$$\eta_{m00}^{0}T_{m00}^{inc}\delta_{p0}\delta_{0q}-\eta_{mpq}^{0}R_{mpq}^{-}=\eta_{mpq}^{1}\left(T_{mpq}^{1}-R_{mpq}^{1}\right) \quad \text{(A.2-42)}$$

At this point two different cases need to be studied. Initially, the case when either *p* or *q* are different to 0 is analysed. The ratio of (A.2-41) and (A.2-42) becomes (A.2-43) under this assumption,

$$\frac{-\eta_{mpq}^{0}R_{mpq}^{-}}{R_{mpq}^{-}}=\frac{\eta_{mpq}^{1}\left(T_{mpq}^{1}-R_{mpq}^{1}\right)}{T_{mpq}^{1}+R_{mpq}^{1}} \quad \text{(A.2-43)}$$

Using the definition of the reflection coefficient in region 1 the coefficient ζ^{1}_{mpq} is obtained,

$$\zeta_{mpq}^{1}=\frac{1-\rho_{mpq}^{1}}{1+\rho_{mpq}^{1}} \quad \text{(A.2-44)}$$

The relation between the reflected and transmitted field amplitudes in region 0 and the relation with the coefficients of the currents is (A.2-45),

$$\frac{-\eta^0_{mpq}R^-_{mpq}-\eta^1_{mpq}K^{12}_{mpq}\tilde{J}^2_{mpq}-\eta^1_{mpq}K^1_{mpq}\tilde{J}^1_{mpq}}{R^-_{mpq}+K^{12}_{mpq}\tilde{J}^2_{mpq}+K^1_{mpq}\tilde{J}_{mpq}}=\eta^1_{mpq}\zeta^1_{mpq}$$

$$\left(\eta^0_{mpq}+\eta^1_{mpq}\zeta^1_{mpq}\right)R^-_{mpq}=-\eta^1_{mpq}K^{12}_{mpq}\left(1+\zeta^1_{mpq}\right)\tilde{J}^2_{mpq}-\eta^1_{mpq}K^1_{mpq}\left(1+\zeta^1_{mpq}\right)\tilde{J}^1_{mpq}$$

$$R^-_{mpq}=-\frac{\eta^1_{mpq}\left(1+\zeta^1_{mpq}\right)}{\left(\eta^0_{mpq}+\eta^1_{mpq}\zeta^1_{mpq}\right)}\left(K^{12}_{mpq}\tilde{J}^2_{mpq}+K^1_{mpq}\tilde{J}^1_{mpq}\right) \tag{A.2-45}$$

Secondly, the case where *p* and *q* are both equal to 0 is studied. The ratio of (A.2-41) and (A.2-42) is now,

$$\frac{\eta^0_{m00}\left(T^{inc}_{m00}-R^-_{m00}\right)}{T^{inc}_{m00}+R^-_{m00}}=\frac{\eta^1_{m00}\left(T^1_{m00}-R^1_{m00}\right)}{T^1_{m00}+R^1_{m00}} \tag{A.2-46}$$

The reflection coefficient in region 1 is used and the coefficient ζ^1_{m00} is derived,

$$\zeta^1_{m00}=\frac{1-\rho^1_{m00}}{1+\rho^1_{m00}} \tag{A.2-47}$$

The reflected and transmitted field amplitudes relation in region 0 as well as the relation with the coefficients of the currents is obtained when p=q=0,

$$\frac{\eta^0_{m00}\left(T^{inc}_{m00}-R^-_{mpq}\right)-\eta^1_{m00}K^{12}_{m00}\tilde{J}^2_{m00}-\eta^1_{m00}K^1_{m00}\tilde{J}^1_{m00}}{T^{inc}_{m00}+R^-_{m00}+K^{12}_{m00}\tilde{J}^2_{m00}+K^1_{m00}\tilde{J}^1_{m00}}=\eta^1_{m00}\zeta^1_{m00}$$

$$\left(\eta^1_{m00}\zeta^1_{m00}+\eta^0_{m00}\right)R^-_{m00}=\left(\eta^0_{m00}-\eta^1_{m00}\zeta^1_{m00}\right)T^{inc}_{m00}$$
$$-\eta^1_{m00}K^1_{m00}\left(1+\zeta^1_{m00}\right)\tilde{J}^1_{m00}-\eta^1_{m00}K^{12}_{m00}\left(1+\zeta^1_{m00}\right)\tilde{J}^2_{m00}$$

$$R^-_{mpq}=\frac{\left(\eta^0_{m00}-\eta^1_{m00}\zeta^1_{m00}\right)}{\left(\eta^1_{m00}\zeta^1_{m00}+\eta^0_{m00}\right)}T^{inc}_{m00}-\frac{\eta^1_{m00}\left(1+\zeta^1_{m00}\right)}{\left(\eta^0_{m00}+\eta^1_{m00}\zeta^1_{m00}\right)}\left(K^{12}_{m00}\tilde{J}^2_{m00}+K^1_{m00}\tilde{J}^1_{m00}\right) \tag{A.2-48}$$

The reflection coefficient in this region is therefore,

$$\rho^0_{m00}=\frac{\left(\eta^0_{m00}-\eta^1_{m00}\zeta^1_{m00}\right)}{\left(\eta^1_{m00}\zeta^1_{m00}+\eta^0_{m00}\right)} \tag{A.2-49}$$

Putting together the results of (A.2-45) and (A.2-48), the relation between the reflected and transmitted field amplitudes in region 0 for any p and q is,

$$R_{mpq}^{-} = \rho_{m00}^{0} T_{m00}^{inc} \delta_{p0} \delta_{0q} - \frac{\eta_{mpq}^{1}\left(1+\zeta_{mpq}^{1}\right)}{\left(\eta_{mpq}^{0}+\eta_{mpq}^{1}\zeta_{mpq}^{1}\right)}\left(K_{mpq}^{12}\tilde{J}_{mpq}^{2}+K_{mpq}^{1}\tilde{J}_{mpq}^{1}\right) \quad \text{(A.2-50)}$$

A.3 Method of Moment review

The Method of Moments is a numerical computational method of solving linear partial differential equations formulated as integral equations of the general form indicated in (A.3-1),

$$zj = e \quad \text{(A.3-1)}$$

where z is a linear operator, e is a known function (excitation) and j is the unknown function. MoM is the most popular approach to solve Eq. (A.3-1). The application of MoM results in expanding the function j as a series of functions ($j_1, j_2, j_3, \ldots j_n$) in the domain of Z as,

$$j = \sum_{i=1}^{n} c_i j_i \quad \text{(A.3-2)}$$

where c_i are the unknown coefficients of the current to be determined, j_i, are known expansion functions or basis functions (functions considered to describe the currents on the elements of the array). The expansion in (A.3-2) has to satisfy (A.3-1), therefore by substituting (A.3-2) into (A.3-1) the next equation is obtained,

$$\sum_{i=1}^{n} z \cdot c_i j_i = e \quad \text{(A.3-3)}$$

In order to derive the coefficients of the current, c_i, the inner product of equation (A.3-3) with a set of suitable functions, u_j, are taking. The functions u_j chosen in this work are the same as the basic functions employed, this is known as the Galerkin's Method of Moments.

$$\sum_{i=1}^{n} c_i \left\langle u_j, zj_i \right\rangle = \left\langle u_j, e \right\rangle \quad \text{(A.3-4)}$$

Equation (A.3-4) can be written in a matrix form as,

$$\left[Z_{ji}\right]\cdot\left[c_i\right]=\left[e_j\right] \tag{A.3-5}$$

where Z_{ji} is,

$$\left[Z_{ji}\right]=\begin{bmatrix}\langle w_1, zj_1\rangle & \cdots & \langle w_1, zj_n\rangle \\ \vdots & \ddots & \vdots \\ \langle w_n, zj_1\rangle & \cdots & \langle w_n, zj_n\rangle\end{bmatrix} \tag{A.3-6}$$

The coefficients of the current and the fields are,

$$\left[c_i\right]=\begin{bmatrix}c_1 \\ \vdots \\ c_n\end{bmatrix} \tag{A.3-7}$$

$$\left[e_j\right]=\begin{bmatrix}\langle u_1, e\rangle \\ \vdots \\ \langle u_n, e\rangle\end{bmatrix} \tag{A.3-8}$$

Thus, the equation can now be solved by deriving c_i using either direct matrix inversion or an iterative method.